Interfacial Modulation and Optical Properties of Graphene/MoS$_2$ Heterostructures

Inaugural-Dissertation

to obtain the academic degree

Doctor rerum naturalium (Dr. rer. nat.)

submitted to the Department of Biology, Chemistry, Pharmacy

of Freie Universität Berlin

by

Qing Cao

Berlin 2024

The work presented here was conducted from 10/2019 until 04/2024 at the Department of Biology, Chemistry, Pharmacy of the Freie Universität Berlin under the supervision of Prof. Dr. Siegfried Eigler.

1) Referee: Prof. Dr. Siegfried Eigler (Freie Universität Berlin)

2) Referee: Prof. Dr. Kannan Balasubramanian (Humboldt-Universität zu Berlin)

Disputation at: 16.07.2024

Table of Content

1 Summary

1.1 Overview of Presented Topics

In this cumulative dissertation the following topics are presented:

1) Interfacial modulation of MoS_2 with oxo-functionalized graphene and its derivatives

    a. Oxo-functionalized graphene/MoS_2 and reduced oxo-functionalized graphene/MoS_2 heterostructures

    b. Porous oxo-functionalized graphene/MoS_2

2) Interfacial modulation of laser-induced functional graphene/MoS_2 heterostructures

    Oligophenyl-functionalized graphene/MoS_2

The research was conducted in collaboration with the groups of 1) Dr. Patryk Kusch from the Department of Physics at Freie Universität Berlin; 2) Prof. Dr. Hyeon S. Shin from the Department of Chemistry at Ulsan National Institute of Science and Technology. The complete results and experimental details are included in the attached publications in *Chapter 5* and *6*.

To keep the explanation of heterostructures concise, we define the vertical stacking order of the heterostructure layers as (substrate/)bottom layer/upper layer.

1.2 Summary of Results

1.2.1 Interfacial modulation of MoS_2 with oxo-functionalized graphene and its derivatives

    a. Oxo-functionalized graphene/MoS_2 and reduced oxo-functionalized graphene/MoS_2 heterostructures

Tuning the electronic and optical properties of monolayer MoS_2 and gaining

profound insights into the fundamental mechanisms that govern these properties is of utmost significance for the development of efficient optoelectronic devices, such as photodetectors, photodiodes *etc*. Intrinsic structural defects of monolayer MoS_2, such as S vacancies, induce electrons gathering in neighboring Mo atoms, which function as nonradiative traps, thereby impairing the photoluminescence (PL) efficiency. Stacking MoS_2 layers on different two-dimensional (2D) materials, such as hexagonal boron nitride (h-BN) and graphene, provides a way to modulate the PL performance. Oxygen-functionalized graphene (oxo-G), a graphene derivative, has a defective graphene network with oxygen species decorating the edges and the plane. Electron-withdrawing groups, such as hydroxyl, epoxy, and organosulfates, make oxo-G a p-doping material. By reducing oxo-G (r-oxo-G), sp^2-hybridized graphene domains with a lateral size of up to 10 nm are recovered with the removal of most oxygen groups. During the reduction process, in-plane defects such as vacancies, holes, and non-six-membered carbon rings with sp^3 hybridization are formed, which act as structural motifs or active sites and significantly change the electronic and surface properties of r-oxo-G. Therefore, the use of oxo-G and r-oxo-G is suggested for tuning the carrier concentration of MoS_2.

Herein, heterostructures of monolayer MoS_2 with three types of monolayer graphene are fabricated: mechanically exfoliated pristine graphene, oxo-G (a high amount of oxygen of 60%), and r-oxo-G (a defect density of 0.5%). Raman and PL spectroscopy combined with Kelvin probe force microscopy (KPFM, collaboration with the Shin group, Ulsan National Institute of Science and Technology) measurements are carried out to study optoelectronic properties and mechanism of interface interaction. Oxo-G with a work function (WF) of 5.67 eV and r-oxo-G with a WF of 5.85 eV serving as hole injection layers significantly enhance the PL intensity of MoS_2, whereas pristine graphene with

a WF of 5.02 eV resulted in PL quenching of MoS_2. The electron-withdrawing functional groups of oxo-G and the defects in r-oxo-G layers facilitate the recombination of neutral exciton and result in PL enhancement. Furthermore, the r-oxo-G/MoS_2 heterostructure exhibits a higher increase (5-fold) in the overall PL intensity than the oxo-G/MoS_2 (3-fold) heterostructure. Our research demonstrates the PL modulation of monolayer MoS_2 by monolayer graphene with a varying ability in extracting electrons. The enhancement of PL plays a vital role in high performance optoelectronic devices by improving photovoltaic efficiency, sensitivity, and photoresponse etc.

b. Porous oxo-functionalized graphene/MoS_2

The in-plane lattice defects in r-oxo-G can affect the electron transfer between graphene and MoS_2, leading to an enhancement in the PL of MoS_2. To investigate interfacial charge transfer and PL performance, porous graphene with large lattice defects is prepared and stacked with MoS_2. Oxo-G with a low density of initial vacancy defects (0.8%) is used as a precursor to etch pores assisted by a Mn-species at 400 °C in Ar atmosphere. By controlling the reaction conditions, it is possible to gain a certain control over the size of pores on porous oxo-G (Pr-oxo-G) with diameters between 100–200 nm.

The PL of MoS_2 on SiO_2, oxo-G, Pr-oxo-G_{6h} (etching time of 6 h), and Pr-oxo-G_{12h} (etching time of 12 h) are studied. The amplitudes of the PL are increased for oxo-G/MoS_2 (4 times), Pr-oxo-G_{6h}/MoS_2 (3 times), and Pr-oxo-G_{12h}/MoS_2 (10 times), compared to the PL of the pristine MoS_2 monolayer. Overall, Pr-oxo-G_{12h} reflects a p-doped material, as indicated by Raman shifts, achieving the highest PL enhancement. The Pr-oxoG_{12h}/MoS_2 PL intensity map measured by scanning nearfield optical microscopy (s-SNOM) with nano-scale resolution shows a constant PL intensity over the MoS_2 flake, exhibiting no sign of a spatial PL modulation that may arise from free-standing MoS_2. (collaboration with Dr.

Patryk Kusch, FU Berlin) Furthermore, the Pr-oxo-G_{6h}/MoS$_2$ showed slightly lower PL intensity than oxo-G/MoS$_2$. The Mn-impurities in Pr-oxo-G_{6h}/MoS$_2$ are supposed to limit the increase of the PL of MoS$_2$, and the interaction of Mn-species with carbonyl groups may be responsible.

1.2.2 Interfacial modulation of laser-induced functional graphene/MoS$_2$ heterostructures

Oligophenyl-functionalized graphene/MoS$_2$

The electron-withdrawing effects of the functional groups and lattice defects in graphene have been demonstrated to enhance the PL intensity of monolayer MoS$_2$. In addition, Interlayer van der Waals interactions and interlayer distance are very important factors in studying the PL of graphene/MoS$_2$ heterostructures (G/MoS$_2$) as they are only a few atomic thin. Functionalization of graphene with specific functional groups is of great significance for the further development of covalent modification of graphene and the interface construction in G/MoS$_2$ heterostructures, thereby facilitating the study of interlayer coupling of G/MoS$_2$ heterostructures.

Monotopic covalently modified graphene, oligophenyl-functionalized graphene (F-G), are prepared by a laser-induced reaction and stacked with a monolayer MoS$_2$. The functionalization of graphene is regioselective with the assistance of the mapping function of the scanning Raman spectrometer. Through Raman, PL, KPFM and scanning near-field optical microscopy (collaboration with Dr. Patryk Kusch, FU Berlin) measurements, the boundaries and the distinct characteristics of the functionalized and the non-functionalized areas are identified on the heterostructure. More importantly, the layer stacking sequence of F-G and MoS$_2$ brings different interface structures in perpendicular orientation. MoS$_2$ supported by F-G (F-G/MoS$_2$) results in a sandwiched structure consisting of graphene/oligophenyl-groups/MoS$_2$ with an enlarged

interlayer distance of 8 nm between the graphene basal plane and MoS_2. In the case of MoS_2 stacked underneath F-G (MoS_2/F-G) a direct interface is formed between the graphene basal plane and MoS_2, with the oligophenyl-groups located on the top surface of the heterostructure. The different interfaces in the heterostructures result in a significant difference in the PL enhancement of MoS_2. F-G/MoS_2 shows a 5-fold PL enhancement, while MoS_2/F-G only shows a 1.8-fold PL enhancement compared to pristine G/MoS_2. Accordingly, the results indicate that the oligophenyl-groups in F-G/MoS_2 not only have a p-doping effect on MoS_2 but also largely prevent electron donation from the graphene basal plane with the enlarged interlayer distance. Consequently, the PL enhancement is restored with the thermal de-functionalization of F-G. Thus, we conclude that the functional groups can be considered as separate molecular component with the vertical arrangement in the functionalized heterostructure system. The photoactive graphene acts as a template for perpendicular molecular alignment in the heterointerface construction, thus opening more possibilities for the fabrication of heterointerfaces.

In this thesis, the interfaces of G/MoS_2 are engineered through the introduction of oxo-functional groups, structural defects, and laser-induced perpendicular functional-groups on graphene. The interfacial modulation via interlayer charge transfers and interlayer distances results in significant changes in the PL properties of G/MoS_2 heterostructures. These findings offer novel insights into the design and exploration of optoelectronic devices. Furthermore, the PL enhancement of G/MoS_2 opens up numerous possibilities for optoelectronic applications, for instance, wavelength-tunable phototransistors, broadband photodetectors, single-photon emission sites for quantum information science, improved electrical performance for high-speed optoelectronics, and signal enhancement in photodetectors and sensors.

Based on the findings in this thesis, there are still ample opportunities for future

research to continue this study. First, the development of diverse interlayer functional groups with diverse electron transfer capabilities and spatial effects can be achieved through laser-induced functionalization methods to realize a more versatile interface modulation. Second, further investigation into the interface modulation of different 2D materials beyond graphene and MoS_2 is expected. Third, a thorough fundamental understanding of hetero-interfaces is required. A deeper insight into the effects of interface modulation on the electronic structure, band alignment, and van der Waals interactions of heterostructures can be achieved through theoretical studies and techniques such as charge transport measurements, ultrafast optical spectroscopy, and magnetic characterization.

1.3 Zusammenfassung der Ergebnisse

1.3.1 Grenzflächenmodulation von MoS_2 mit Oxo-G und seinen Derivaten

a. Oxo-G/MoS_2 und r-oxo-G/MoS_2

Die Abstimmung der elektronischen und optischen Eigenschaften von einlagigem MoS_2 und die Gewinnung tiefer Einblicke in die grundlegenden Mechanismen, die diese Eigenschaften bestimmen, sind von größter Bedeutung für die Entwicklung effizienter optoelektronischer Bauelemente wie Fotodetektoren, Fotodioden usw. Die intrinsischen Strukturdefekte von Monolayer-MoS_2, wie z.B. Schwefel-Lücken, induzieren Elektronen in benachbarten Mo-Atomen, was die Effizienz der Photolumineszenz (PL) beeinträchtigt. Die Stapelung von MoS_2-Schichten auf verschiedenen 2D-Materialien wie hexagonalem Bornitrid (h-BN) und Graphen bietet eine Möglichkeit, die PL-Intensität zu modulieren. Sauerstoff-funktionalisiertes Graphen (Oxo-G), ein Graphen-Derivat, hat ein defektes Graphen-Gitter das an den Kanten und in der Ebene mit sauerstoffhaltigen Gruppen funktionalisiert ist. Elektronen abziehende Gruppen wie Hydroxyl, Epoxy und Organosulfate

machen Oxo-G zu einem p-dotierenden Material. Durch Reduktion von Oxo-G (r-Oxo-G) werden sp^2-hybridisierte Graphen-Domänen mit einer lateralen Größe von bis zu 10 nm wiederhergestellt, wobei die meisten Sauerstoffgruppen entfernt werden. Während des Reduktionsprozesses bilden sich Defekte im Graphengitter wie zum Beispiel Leerstellen, Löcher und nicht-sechsgliedrige Kohlenstoffringe mit sp^3-Hybridisierung, die als aktive Stellen wirken und die elektronischen und Oberflächeneigenschaften von r-Oxo-G erheblich verändern. Daher wird hier die Verwendung von oxo-G und r-Oxo-G zur Einstellung der Ladungsträgerkonzentration von MoS_2 untersucht.

Hierin werden Heterostrukturen aus einlagigem MoS_2 mit drei Arten von einlagigem Graphen hergestellt: mechanisch exfoliertes Graphen, oxo-G (hoher Sauerstoffanteil von 60%), und r-oxo-G (geringer Sauerstoffanteil von 0.5%). Raman- und PL-Spektroskopie in Kombination mit Raster-Kelvin-Mikroskopie (KPFM, Zusammenarbeit mit der Shin-Gruppe, Ulsan National Institute of Science and Technology) wurden durchgeführt, um die optoelektronischen Eigenschaften und den Mechanismus der Grenzflächeninteraktion zu untersuchen. 1L-oxo-G mit einer Austrittsarbeit (WF) von 5.67 eV und 1L-oxo-G mit einer WF von 5.85 eV, die als Lochinjektionsschichten dienen, erhöhen die PL-Intensität von MoS_2 erheblich, während mechanisch exfoliertes Graphen mit einer WF von 5.02 eV zu einer PL-Abschwächung von MoS_2 führt. Die elektronenziehenden funktionellen Gruppen von oxo-G und die Defekte in r-oxo-G-Schichten erleichtern die Rekombination neutraler Exzitonen und führen zu einer Steigerung der PL. Darüber hinaus wies r-oxo-G/MoS_2 einen stärkeren Anstieg (5-fach) der PL als oxo-G/MoS_2 (3-fach) auf. Unsere Forschung zeigt die PL-Modulation von einlagigem MoS_2 durch einlagige Graphen-Derivate mit unterschiedlichen Fähigkeiten, Elektronen zu extrahieren. Die Verbesserung des PL spielt eine wichtige Rolle für leistungsstarke optoelektronische Geräte, indem sie die

photovoltaische Effizienz, die Empfindlichkeit und die Photoreaktion usw. verbessert.

b. Poröses Graphen/MoS$_2$

Defekte in r-oxo-G können den Elektronentransfer zwischen Graphen und MoS$_2$ beeinflussen, was zu einer Verbesserung der PL von MoS$_2$ führt. Um den Ladungstransfer an der Grenzfläche und die PL-Intensität zu untersuchen, wird poröses Graphen mit großen Gitterdefekten hergestellt und mit MoS$_2$ gestapelt. Oxo-G mit einer geringen Dichte an anfänglichen Defekten (0.8%) wird als Präkursor verwendet, um die Poren mit Hilfe einer Mn-Spezies bei 400 °C unter Ar-Atmosphäre zu ätzen. Durch die Steuerung der Reaktionsbedingungen ist es möglich, eine gewisse Kontrolle über die Größe der Poren auf porösem Oxo-G (Pr-Oxo-G) mit Durchmessern zwischen 100-200 nm zu erlangen.

Die PL von MoS$_2$ auf SiO$_2$, Oxo-G, Pr-oxo-G$_{6h}$ (Ätzzeit von 6 h) und Pr-oxo-G$_{12h}$ (Ätzzeit von 12 h) wird untersucht. Die Amplituden der PL sind bei oxo-G/MoS$_2$ (4-fach), Pr-oxo-G$_{6h}$/MoS$_2$ (3-fach) und Pr-oxo-G$_{12h}$/MoS$_2$ (10-fach) im Vergleich zur PL der ursprünglichen MoS$_2$-Monolage erhöht. Insgesamt ist Pr-oxo-G$_{12h}$ ein p-dotiertes Material, wie aus den Raman-Verschiebungen hervorgeht, und erzielt die höchste Steigerung der PL. Die ortsaufgelöste PL-Intensität von Pr-oxoG12h/MoS$_2$, gemessen mit optischer Rasternahfeldmikroskopie (s-SNOM) mit nanoskaliger Auflösung zeigt eine konstante PL-Intensität über die gesamte Fläche der MoS$_2$-Flocke, ohne Anzeichen einer räumlichen PL-Modulation, die bei freistehendem MoS$_2$ auftreten kann. (Zusammenarbeit mit Dr. Patryk Kusch, FU Berlin) Außerdem zeigt Pr-oxo-G$_{6h}$/MoS$_2$ eine etwas geringere PL-Intensität als oxo-G/MoS$_2$. Es wird vermutet, dass die Mn-Verunreinigungen in Proxo-G$_{6h}$/MoS$_2$ den Anstieg des PL von MoS$_2$ begrenzen, und dass die Wechselwirkung von Mn-Spezies mit Carbonylgruppen dafür verantwortlich sein könnte.

1.3.2 Grenzflächenmodulation von laserinduzierten funktionalisiertem Graphen/MoS$_2$-Heterostrukturen

Oligophenyl-funktionalisiertes Graphen/MoS$_2$

Die elektronenziehenden Effekte der Funktionalisierung und der Gitterdefekte in Graphen erhöhen nachweislich die PL-Intensität von einlagigem MoS$_2$. Darüber hinaus sind die Van-der-Waals-Wechselwirkungen zwischen den Schichten und der Abstand zwischen den Schichten sehr wichtige Faktoren bei der Untersuchung der PL von Graphen/MoS$_2$-Heterostrukturen (G/MoS$_2$), da sie nur wenige Atomlagen dünn sind. Die regioselektive Funktionalisierung mit spezifischen funktionellen Gruppen ist von großer Bedeutung für die weitere Entwicklung der kovalenten Modifikation von Graphen und den Aufbau von Grenzflächen in G/MoS$_2$-Heterostrukturen, wodurch die Untersuchung der Zwischenschichtkopplung von G/MoS$_2$-Heterostrukturen erleichtert wird.

Monotopisches kovalent modifiziertes Graphen, oligophenylfunktionalisiertes Graphen (F-G), wird durch eine laserinduzierte Reaktion hergestellt und mit einer Monolage MoS$_2$ zu einer Heterostruktur zusammengesetzt. Die Funktionalisierung von Graphen erfolgt regioselektiv mit Hilfe der Mapping-Funktion des Raman-Spektrometers. Durch Raman-, PL-, KPFM- und Scanning-Nahfeldmikroskopie-Messungen (in Zusammenarbeit mit Dr. Patryk Kusch, FU Berlin) identifizieren wir die Grenzen und die unterschiedlichen Eigenschaften der funktionalisierten und nicht-funktionalisierten Bereiche der Heterostruktur. Noch wichtiger ist, dass die Schichtabfolge von F-G und MoS$_2$ unterschiedliche Grenzflächenstrukturen in senkrechter Orientierung hervorbringt. MoS$_2$ auf F-G (F-G/MoS$_2$) ergibt eine Sandwich-Struktur aus Graphen/Oligophenyl-Gruppen/MoS$_2$ mit einem vergrößerten Zwischenschichtabstand von 8 nm zwischen der Graphen-Basalebene und MoS$_2$. Im Falle von MoS$_2$, das unter F-G gestapelt ist (MoS$_2$/F-G), bildet sich

eine direkte Grenzfläche zwischen der Graphen-Basalebene und MoS_2, wobei sich die Oligophenylgruppen auf der oberen Oberfläche der Heterostruktur befinden. Die unterschiedlichen Grenzflächen in den Heterostrukturen führen zu einem signifikanten Unterschied in der PL-Verstärkung von MoS_2. F-G/MoS_2 zeigt eine 5-fache PL-Verstärkung, während MoS_2/F-G nur eine 1,8-fache PL-Verstärkung aufweist. Die Ergebnisse deuten darauf hin, dass die Oligophenylgruppen in F-G/MoS_2 nicht nur einen p-Dotierungseffekt auf MoS_2 haben, sondern auch den Elektronen-donierenden Effekt aus der Graphen-Basalebene durch den vergrößerten Zwischenschichtabstand weitgehend verhindern. Folglich wird die PL-Verbesserung durch die thermische Defunktionalisierung von F-G wiederhergestellt. Daraus schließen wir, dass die funktionellen Gruppen als separate molekulare Komponente mit vertikaler Anordnung im funktionalisierten Heterostruktursystem betrachtet werden können. Das photoaktive Graphen dient als Templat für die senkrechte Anordnung der Moleküle in der Heterogrenzflächenkonstruktion und eröffnet somit weitere Möglichkeiten für die Herstellung von Heterogrenzflächen.

In dieser Arbeit werden die Grenzflächen von G/MoS_2 durch die Einführung von oxo-funktionellen Gruppen, strukturellen Defekten und laserinduzierten senkrechten funktionellen Gruppen auf Graphen modifiziert. Die Modulation der Grenzflächen durch Ladungstransfers zwischen den Schichten und Abständen zwischen den Schichten führt zu signifikanten Veränderungen der PL-Eigenschaften von G/MoS_2-Heterostrukturen. Diese Erkenntnisse bieten neue Einblicke in das Design und die Erforschung von optoelektronischen Bauelementen. Darüber hinaus eröffnet die PL-Verbesserung von G/MoS_2 zahlreiche Möglichkeiten für optoelektronische Anwendungen, z. B. wellenlängenabstimmbare Phototransistoren, Breitband-Photodetektoren, Einzelphotonen-Emissionsstellen für die Quanteninformatik, verbesserte elektrische Leistung für Hochgeschwindigkeits-Optoelektronik und

Signalverstärkung in Photodetektoren und Sensoren.

Ausgehend von den in dieser Arbeit gewonnenen Erkenntnissen gibt es noch zahlreiche Möglichkeiten für künftige Forschungsarbeiten. Erstens kann die Entwicklung verschiedener funktioneller Zwischenschichtgruppen mit unterschiedlichen Elektronentransferfähigkeiten und räumlichen Effekten durch laserinduzierte Funktionalisierungsmethoden erreicht werden, um eine vielseitigere Schnittstellenmodulation zu realisieren. Zweitens wird eine weitere Untersuchung der Grenzflächenmodulation verschiedener 2D-Materialien über Graphen und MoS_2 hinaus erwartet. Drittens ist ein gründliches grundlegendes Verständnis von Hetero-Grenzflächen erforderlich. Ein tieferer Einblick in die Auswirkungen der Grenzflächenmodulation auf die elektronische Struktur, die Bandausrichtung und die van-der-Waals-Wechselwirkungen von Heterostrukturen kann durch theoretische Studien und Techniken wie Ladungstransportmessungen, ultraschnelle optische Spektroskopie und magnetische Charakterisierung gewonnen werden.

2 Introduction

2.1   From   Two-dimensional   Materials   to   Two-dimensional   Heterostructures

Since graphene was exfoliated in 2004, two-dimensional (2D) materials have emerged.[1] With ultrathin layered structures, 2D materials exhibit unique properties that have attracted the attention of researchers worldwide.[2] In the pursuit of graphene, more than one thousand structures of 2D materials have been investigated, such as graphene analogs (including black phosphorus (BP),[3] hexagonal boron nitride (h-BN),[4] etc.), transition metal dichalcogenides (TMDCs, including molybdenum disulfide (MoS_2), tungsten disulfide (WS_2), molybdenum diselenide ($MoSe_2$), *etc.*),[5] metal-organic frameworks (MOFs),[5a, 6] covalent-organic frameworks (COFs),[7] MXenes,[8] layered metal oxides,[9] and layered double hydroxides (LDHs),[10] forming a large family of 2D materials (**Figure 1**).[11]
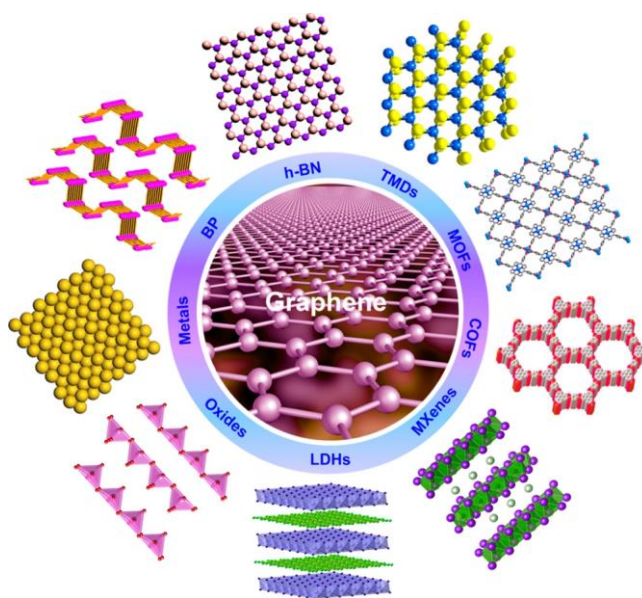

Figure 1 Schematic illustration of different kinds of typical ultrathin 2D materials. Reproduced from ref.[11a] with permission from the American Chemical Society, Copyright 2015.

These 2D materials exhibit new properties distinct from those of bulk

materials.[12] 2D materials can be conductors, semiconductors, or insulators; they can be chemically inert, or chemically reactive, e.g. on the surfaces. To summarize, 2D materials have several crucial advantages compared to their bulk counterparts: 1) Highly exfoliated 2D materials have a high surface-to-volume ratio. Nearly all atoms are exposed to the outer surfaces, especially in materials with only one atom thickness such as graphene, h-BN, and phosphorene. This high specific surface area facilitates maximum adsorption sites for sensing or catalytic applications and accommodates hetero-species directly bound to the surface.[13] 2) 2D materials show rapid charge transport characteristics, benefitting from the 2D confinement at the atomic level that prevents the unnecessary scattering of charge carriers, and therefore offer intriguing properties in many different types of electronics. By controlling the thickness and elemental doping, the band structure and electrical properties can be more easily tuned.[14] 3) 2D materials show flexibility and transparency, with attractive prospects in the fields of wearable smart devices.[15] 4) 2D materials exhibit notable photothermal conversion effects due to their photonic and electronic properties. Semiconducting 2D materials (TMDCs, phosphorene) create electron-hole pairs upon light absorption, resulting in radiative and nonradiative recombination. Metallic 2D materials exhibit localized surface plasmon resonance, leading to energy transfer to the lattice phonons. The notable photothermal effect of 2D materials can be beneficial in the antiviral/bacterial textiles and light-driven soft actuators.[16]

Infinite opportunities appear when combining different 2D crystals in one vertical stack that are held together by van der Waals forces.[13b, 15a, 17] Andre Konstantin Geim, the discoverer of graphene, described the stacking of multilayer van der Waals heterostructures as building atomic-scale Lego.[18] As the family of 2D crystals is expanding day by day, so does the complexity of fabricated heterostructures with atomic precision (**Figure 2**).[19]
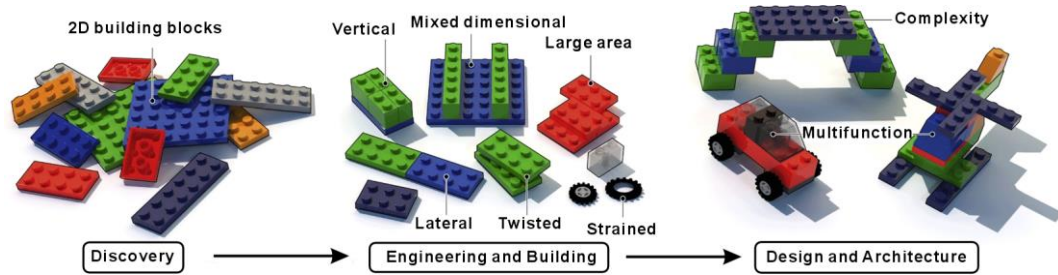
Figure 2 The development from 2D atomic building blocks to their heterostructures. Adapted from ref.[19] with permission from the by Elsevier, Copyright 2023.

Pioneering work on van der Waals heterostructures began with h-BN/graphene in 2010. Hone *et al.* transferred mechanically exfoliated monolayer and bilayer graphene on single-crystal h-BN substrates by polymethyl-methacrylate (PMMA) assisted wet-transfer method. Owing to the atomically surface flatness of h-BN, the mobility of graphene devices on h-BN substrates were almost an order of magnitude higher than those on SiO_2.[20] Beyond that, thin h-BN crystals further served as isolation and encapsulation layers for graphene devices.[21] Wang *et al.* for the first-time encapsulated graphene between two h-BN sheets through the dry transfer method. The resulting heterostructures exhibited carrier mobilities close to the theoretical phonon-scattering limit at room temperature.[22] Epitaxially growing graphene on top of h-BN using catalysis-free chemical vapor deposition (CVD) resulted in Moiré pattern superlattice, a minor lattice mismatch, forming sub-Dirac cones at superlattice zone boundaries.[23]

Inspired by the development of h-BN/graphene heterostructures and the fabrication techniques, the permutation of 2D van der Waals heterostructures consisting of various 2D materials is thriving, offering a rich stage for fundamental studies as well as novel device concepts. For example, the p-type tungsten diselenide (WSe_2) and n-type MoS_2 were assembled to a p–n junction at the ultimate thickness, which displayed efficient photon harvesting. [24] Vertical graphene/MoS_2 (G/MoS_2) heterostructures have enabled the

fabrication of unique gated photodiodes.[25] MoS$_2$/h-BN quantum well structures have been used to fabricate light-emitting diodes.[26]

The integration of dissimilar materials underlies most functional devices, implying the near ubiquity of interfaces in applied technologies. At the ultrathin limit, the characteristics and functionalities of 2D heterostructures are dominated by surface chemistry and interface coupling.[13b] Nobel laureate Herbert Kroemer coined the famous phrase, "the interface is the device".[27] Therefore, methods for comprehensively characterizing and precisely controlling surfaces and interfaces are required to realize the full technological potential of 2D materials.

The interface in 2D van der Waals heterostructures can be controlled by designing interlayer stacking configurations, which rely on the relatively weak van der Waals interaction between neighboring layers.[13b] Van der Waals coupled materials can have various stacking configurations controlled via interlayer twist angle or introduction of guest species (atoms, molecular, or dielectric layers) between neighboring layers.[28] Instead of assuming a fixed orientation as in the bulk materials, the homo- or heterolayers can be stacked at desired azimuthal angles between their lattices, which opens up new freedom in van der Waals heterostructures. The twisted 2D heterostructures possess angle-induced periodic superlattices which can be characterized by scanning tunneling microscope and high-resolution transmission electron microscopy.[29] In 2018, twisted bilayer graphene was first assembled with a subtle twist angle of about 1.1° (the first 'magic' angle) and exhibited flat bands near zero Fermi energy.[2a] This unique structure appeared unconventional superconductivity at 1.7 K.[2a, 30] Since then, twist angle as an emerging property has attracted unprecedented attention. By precisely adjusting the twist angels, new characteristics appear in 2D heterostructures, such as flat bands,[30b, 31] interlayer ferromagnetism,[32] moiré excitons,[33] topological polaritons,[34] and

15

soliton superlattices.[35] Moreover, the van der Waals gap between layers in 2D materials has the potential to accommodate the introducing of atomic and molecular species. Intercalation has been exploited to modify the interfacial interaction in 2D heterostructures. For example, $FeCl_3$ intercalation of mechanically exfoliated few-layer graphene has been reported to result in an extraordinarily large charge doping (up to 9×10^{14} cm^{-2}) with a record low electrical resistivity (<8 Ω sq^{-1}) and high optical transparency in the visible wavelength (>84%), which makes this material attractive for applications requiring transparent electrodes.[36] In addition to intercalation with atoms and molecules, the insertion of dielectric layers into existing 2D vertical heterostructures can affect interfacial interactions. The strong interlayer spatially indirect recombination in the WSe_2/MoS_2 heterostructure was decreased by inserting a single layer of h-BN and fully suppressed by a trilayer h-BN spacer.[37]

The above examples of 2D van der Waals materials are some representative highlights of the almost infinite number of reported novel physical effects. As new ideas emerge, in addition to studying the properties of 2D materials themselves, more and more artificially designed van der Waals systems come into play to meet corresponding challenges in the field of electronics (transistors, integrated circuits, flexible electronic devices, etc.),[38] optoelectronics (photovoltaic devices, photodetectors, light-emitting diodes, optical communications, etc.),[38-39] magnetoelectronics (magnetic storage, magnetic sensors, etc.),[40] energy storage and conversion (lithium-ion batteries, supercapacitors, photovoltaic cells, fuel cells, etc.),[41] quantum technology (quantum computing, quantum communication, and quantum sensing),[42] biomedical engineering (biosensor, drug delivery, and bioimaging)[43] and the emerging filed, such as smart fibers,[44] softrobotics,[45] neuromorphic computing[46] and single atom catalysts,[47] etc.[16]

2.2 Structures of Graphene and Graphene Derivatives

2.2.1 Crystal and Electronic Band Structures of Pristine Graphene

Graphene is a crystal material composed of a closely packed single layer of carbon atoms. The carbon atoms in graphene are sp^2 hybridized and bonded in a hexagonal honeycomb lattice as shown in **Figure 3a**.[48] The unit cell of a graphene crystal contains two carbon atoms, labelled A and B. The unit cell vectors a_1 and a_2 have the same lattice constant of 0.246 nm. **Figure 3c** illustrates the reciprocal lattice of graphene, and the hexagon is the corresponding Brillouin zone. Because of the two sublattice in the real lattice structure, the vertex points in Brillouin zone are equivalent, and called the K and K' point.[49] Γ point is the center of the Brillouin zone.
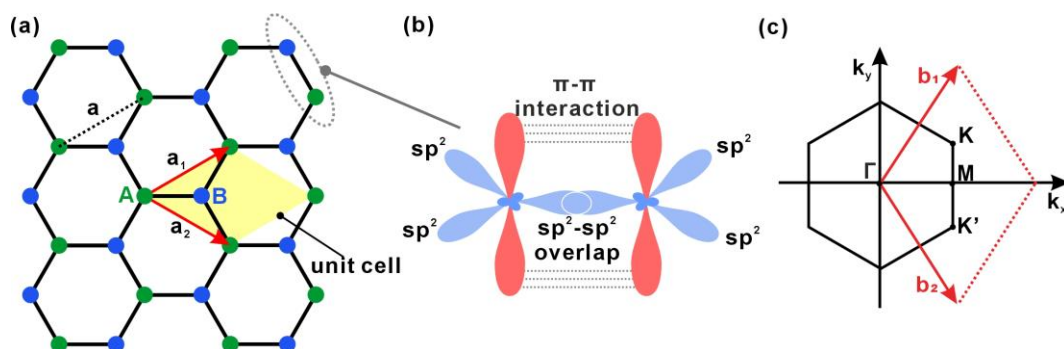
Figure 3 (a) Lattice structure of graphene, which is composed of two triangular sublattices highlighted by blue and green carbon atoms. The primitive lattice vectors are represented by a_1 and a_2. The unit cell is highlighted in the yellow area, and a is the lattice constant (0.246 nm). (b) Hybridization of the s, p_x and p_y orbitals to sp^2 orbitals and the sp^2 orbitals of neighboring atoms overlap to form σ bonds in graphene, while the p_z orbitals form π bonds. (c) Corresponding Brillouin-zone with marked high symmetry points. The reciprocal lattice vectors are represented by b_1 and b_2.

In each carbon atom of graphene, one *2s* orbital and two *2p* orbitals (p_x and p_y) hybridize to form three sp^2 hybrid orbitals oriented 120º to each other in one plane. The two neighboring carbon atoms form an in-plane σ-bond by head-on overlapping of two sp^2 orbitals. The length of the σ-bond is 0.142 nm.[50] The unhybridized p_z orbital lies perpendicular to the planar structure and interacts with the p_z orbitals of adjacent carbon atom, forming an out-of-plane π-bond

and antibonding π*-bond (**Figure 3b**). These π (π*) bonds permit free-moving electrons which contribute to high electron mobility in graphene.[51] Furthermover, the π-bonds provide a weak van der Waals interaction between adjacent graphene layers stacked together, which form bulk graphite with an interlayer spacing of 0.335 nm.[50b]

In graphene, the valence band formed by π-bonds and conduction band formed by π*-bonds meet at the Dirac points, which locate at the K and K' points of the Brillouin zone. At these Dirac points, the valence band and conduction band exhibit linear dispersion (**Figure 4a-b**).[52] Thus, graphene is a semimetal or referred to as a zero-gap semiconductor. In the undoped graphene, the Dirac point is energetically identical to the Fermi level (E_F). The position of the E_F determines the majority charge carriers in graphene which can be altered by doping (**Figure 4c**).
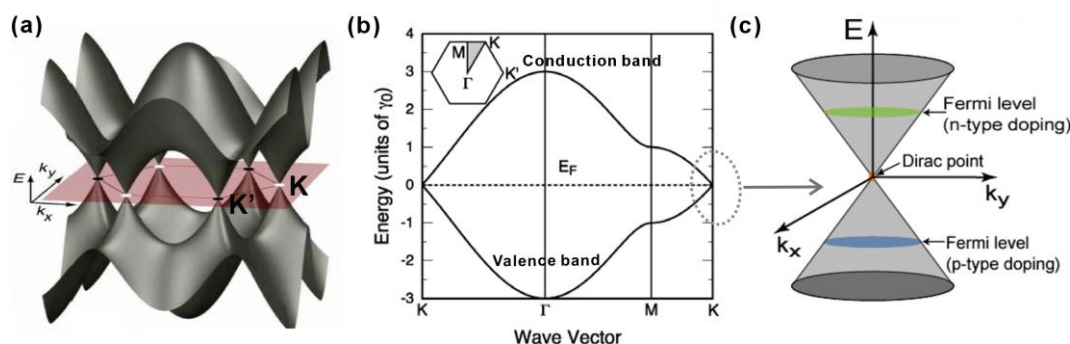
Figure 4 (a) The 3D band structure of graphene. (b) Dispersion of the states of graphene. (c) Approximation of the low energy band structure as two cones touching at the Dirac point. The position of the E_F determines the nature of the doping and the transport carrier. Reproduced from ref.[52] with permission from the American Chemical Society, Copyright 2010.

2.2.2 Dynamic Structure Model of Graphene Oxide

Graphene oxide (GO) is the oxidized form of graphene, containing oxygen functional groups such as epoxides, alcohols, and carboxylic acids etc.[53] Every GO layer consists of a single atomic layer of carbon atoms with oxygen functionalities extending out of the plane and decorating the carbon grid. These

oxygen functionalities are attached to the carbon lattice from both sides. The composition of functional groups in GO are influenced by reaction conditions, including factors like preparation time, temperature, and processing methods. In general, GO consists of approximately 45 wt% carbon.[54] Despite several structural models that have been proposed, GO remains a polydisperse material, making it difficult to precisely define its structure.

The most advanced structural model of GO is the dynamic structure model (DSM), illustrated in **Figure 5**. [55] In the DSM, GO does not contain any significant quantity of preexisting acidic functional groups, but gradually generates them through interaction with water. In the GO fragment shown in **Figure 5**, a hole is positioned at the boundary between a graphenic domain (lower right corner) and an oxidized domain (upper left corner). Various structural features are denoted by different numbers and colors. The main functional groups on the basal planes are epoxides and tertiary alcohols. The DSM suggests that in aqueous solutions GO constantly interacts with water. Water molecular or hydroxide ions can attack the 1,2-dihydroxy moieties ends up with the C-C bond cleavage and formation of carbonyl groups on the newly formed edges. The hydroxide can further react with carbonyl group at edges of defects and further cleave C−C bonds forming carboxylic acids, which may decarboxylate forming CO_2. Additionally, organic sulfates can be found in GO samples prepared in a sulfuric acid medium by esterification.[56] The density of organic sulfates depends on the washing procedures, which is about one organic sulfate per 90 carbon atoms for thoroughly washed GO samples. Although the DSM explains the dynamic transfer and acidity of GO in aqueous solution, the local structure of GO, in particular at defect sites, remains unclear.[57]
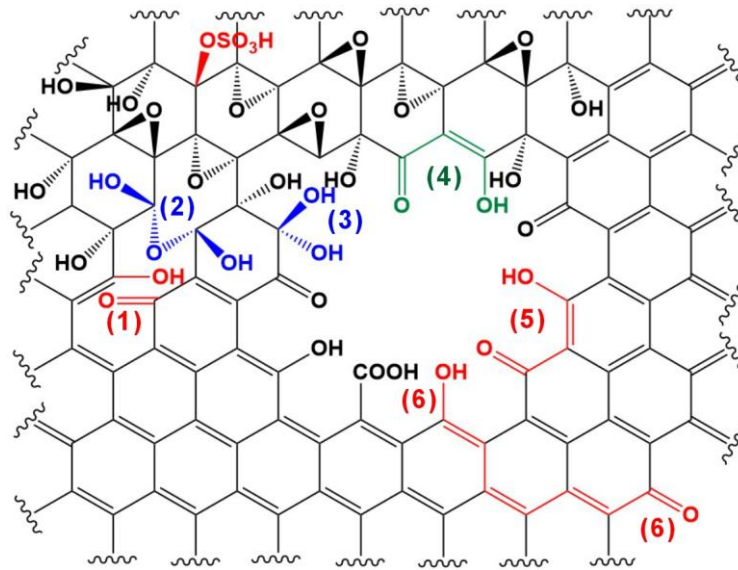
Figure 5 DSM of GO, accounting for defects in the carbon lattice.

2.2.3 Chemical Structure of Oxo-functionalized Graphene

In the preparation of GO, defects can easily form upon overoxidation, with the release of CO_2. The Eigler group achieved the almost complete avoidance of defect formation by maintaining the entire preparation temperature below 10 °C.[58] This resulted in the synthesis of oxo-functionalized graphene (oxo-G), a subclass of GO. Oxo-G preserves the complete carbon framework to a large extent, with only minimal loss of carbon, leading to a residual defect density as low as approximately 0.01%.[54] As shown in **Figure 6**, main oxo-functional groups are hydroxyl and epoxy groups, which are located on both sides of the carbon framework. The degree of oxidation for carbon atoms is estimated to around 50%. what means that about every second carbon atom in oxo-G is sp^3-hybridized.[59]
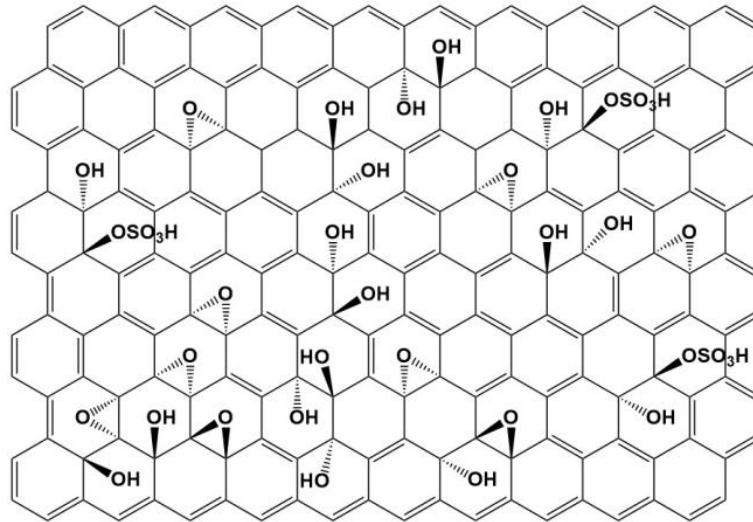
Figure 6 Schematic illustration of the chemical structure of oxo-G.

By chemical reduction of oxo-G (r-oxo-G), the majority of oxygen groups are reductively removed, resulting in restoration of sp^2-hybridized graphene domains with lateral dimensions of up to 10 nm.[60] However, few residual oxo-groups persistently adhere to the edges and defect sites. It's imperative to note that the decomposition and recombination of carbon atoms during the reduction process bring various in-plane defects, including vacancies, holes, and non-six-membered carbon rings with sp^3 hybridization. High-resolution TEM image of thermally reduced oxo-G at 300 °C is depicted in **Figure 7**.[57] Vacancy defects with a few missing carbon atoms and hole defects are visible. It's important to note that a vacancy defect doesn't always result in a hole, as functional groups at the edges of the material can fill the space left by the missing carbon atoms. However, multiple vacancy defects can collectively form a hole defect as marked in the red area in **Figure 7**.[57] These defects, serving as structural motifs or active sites, exert significant influence over the electronic and surface properties of r-oxo-G.[61] The Eigler group investigated the relationship between structural defects and transport capacities of single-layer r-oxo-G with defect densities from 0.2 % to 1.5 %. The corresponding field-effect mobility values ranged from 0.3 cm^2 V^{-1} s^{-1} to 33.2 cm^2 V^{-1} s^{-1}, showing an inverse relationship

to defect density.[61a]
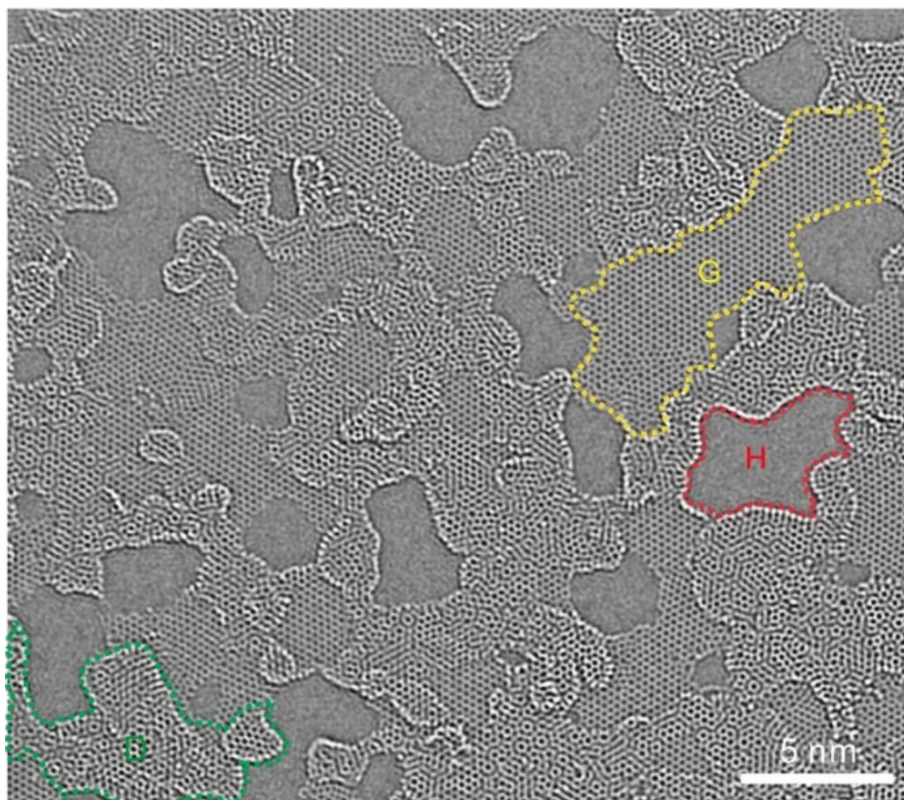
Figure 7 High-resolution TEM image of thermally reduced oxo-G at 300 °C, showing holes, areas of stacked carbon layers, and grain boundaries. The striking features are marked: holes (H), intact single-layer graphene (G), and double-layer carbon (D). Reproduced from ref.[60] with permission from Wiley-VCH Verlag GmbH & Co, Copyright 2020.

2.3 Preparation Methods of Graphene

One of the key challenges in graphene research and applications is the cost-effective, large-scale production of graphene with controllable quality. Currently, the main preparation methods for graphene are mechanical exfoliation, chemical vapor deposition (CVD), chemical oxidation-reduction method, pyrolysis of silicon carbide, and liquid phase exfoliation etc.[11a, 62] In this thesis, mechanical exfoliation, CVD, and chemical oxidation-reduction method were used to prepare graphene-based samples. The detailed methods are introduced in the following *sections 2.3.1-2.3.3*.

2.3.1 Synthesis of Graphene by Mechanical Exfoliation
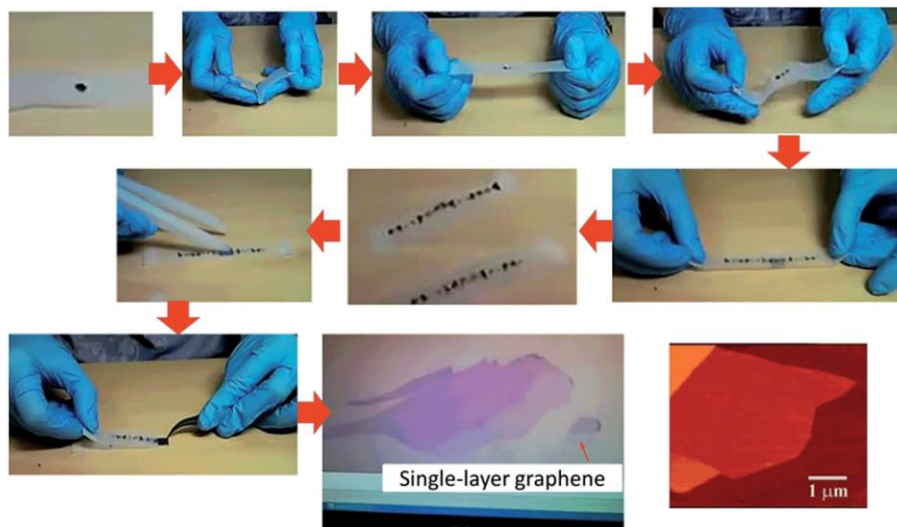
Figure 8 The procedure of the Scotch-tape based micromechanical cleavage of HOPG. Reproduced from ref.[63] with permission from Royal Society of Chemistry, Copyright 2013.

Mechanical exfoliation is a conventional technique to isolate 2D flakes by carefully separating layers from bulk crystals.[1, 64] This process relies on mechanical forces to disrupt the van der Waals forces between the neighboring layers. A typical mechanical exfoliation procedure is shown in **Figure 8**, a bulk graphite is initially attached to a strip of adhesive tape (Scotch tape from 3M). Another piece of tape is then applied to the other side of the crystal and gently pulled apart. This sequence is repeated several times to create thin flakes suitable for transfer to a desired substrate, such as Si/SiO$_2$ wafers. Afterward, the Scotch tape is peeled off from the substrate. With the assistance of an optical microscope, single or few-layer nanosheets like graphene can be identified on the substrate by optical contrast. Finally, Raman spectroscopy is used to prove the single layer nature of the material, which is discussed in *section 3.1.1*.

In 2004, Novoselov Gaim and Andre Konstantin Geim *et al*. successfully used mechanical exfoliation to prepare monolayer graphene from graphite.[1] Based

on their work, this approach was used to prepare other 2D crystals from layered bulk crystals, including h-BN, MoS_2, niobium diselenide ($NbSe_2$), and $Bi_2Sr_2CaCu_2O_x$.[64a] Drawing inspiration from these results, researchers further developed a variety of monolayer or few-layer nanosheets, including 2D TMDCs, BP, and MOF.[64-65]

Graphene crystals obtained through mechanical exfoliation from graphite maintain their crystal structure with high quality and minimal defects, making them ideal candidates for investigating intrinsic properties and applications in electronic devices. However, production yields are limited, and a supporting substrate is always necessary. To fully harness the potential of this technology, the key lies in improving the technique to enhance production efficiency. Lee *et al* reported the largest exfoliated monolayer graphene ever reported with a lateral size of a millimeter, which was exfoliated by layer-engineered exfoliation. A 60 nm thick Au film was thermally evaporated onto the graphite flake to induce tensile stress. Using spin-coated PMMA and thermal release tape as handling layers, an external bending moment generated cracks formed at domain boundaries within the graphite flake. These cracks propagated parallel to the Au-graphene interface, resulting in large-area exfoliation. Moreover, large-area graphene with a controlled number of layers was achieved by depositing metal films (Pd, Ni, and Co) with higher interfacial toughness than Au.[66] In addition, sonication, ball milling, and fluid dynamics methods also have been used for the large-scale production of graphene.[63] Coleman *et al* demonstrated a high-shear mixing exfoliation method for producing graphene at rates exceeding 0.4 g h^{-1}, coupled with low defects (Raman I_D/I_G below 0.65).[67] The variations in shear forces and mixing conditions lead to inconsistencies in layer thickness and quality, making uniform exfoliation challenging.

2.3.2 Synthesis of Graphene by Chemical Vapor Deposition

CVD is one of the most widely used material deposition techniques in the semiconductor industry.[68] In a typical CVD process, the chosen substrate is exposed to reactive precursor materials under high temperatures. These precursor materials react and/or decompose on the surface of the substrate, resulting in the formation of ultrathin 2D flakes or large-area ultrathin films.
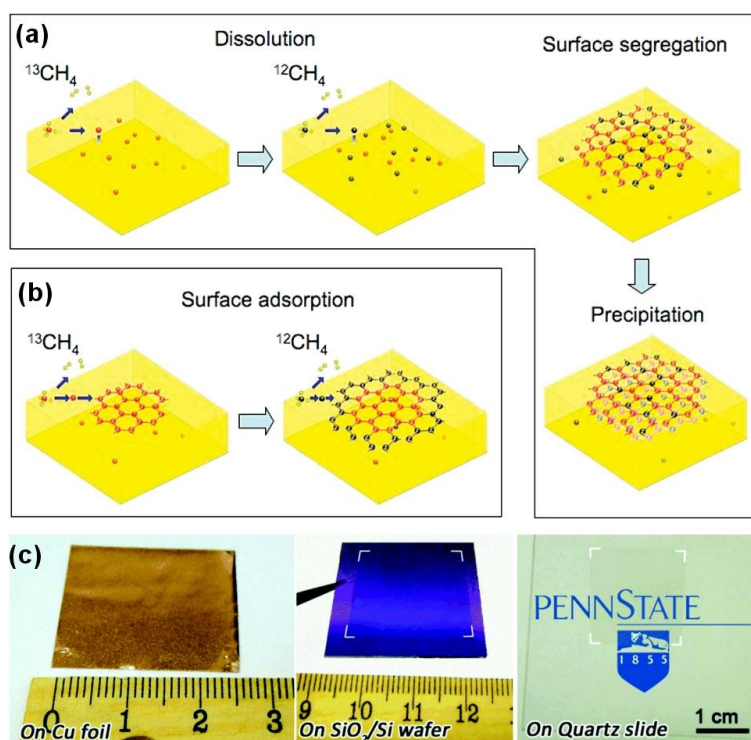
Figure 9 (a-b) Schematic of the CVD growth method of graphene based on the two different growth mechanisms. Reproduced from ref.[69] with permission from the American Chemical Society, Copyright 2009. (c) CVD graphene on different substrates. Adapted from ref.[70] with permission from Wiley-VCH Verlag GmbH & Co, Copyright 2014.

The quality of the generated thin film can be regulated by controlling parameters such as chamber pressure, reaction temperature, gas flow rates, gas composition ratios, and deposition time. To date, this approach has been successfully applied to produce a wide range of ultrathin 2D nanomaterials, including graphene,[71] TMDCs such as MoS_2, WS_2, $MoSe_2$, tungsten diselenide (WSe_2), rhenium disulfide (ReS_2), gallium sulfide (GaS_2),[72] h-BN,[73]

topological insulators like indium(III) selenide (In_2Se_3) and bismuth selenide (Bi_2Se_3),[74] as well as metal oxides.[75]

The mechanism of graphene preparation by CVD method can be divided into two categories: 1) the carbon diffusion and precipitation mechanism (**Figure 9a**), and 2) the surface growth mechanism (**Figure 9b**). Carbon diffusion and precipitation mechanism primarily involves high-carbon-solubility metal substrates such as nickel (Ni). During high temperatures, carbon atoms from the carbon source, such as methane (CH_4), diffuse into the metal substrate. The carbon atoms precipitate from the metal with the subsequent cooling and crystallize into graphene. The surface growth mechanism refers to the process in which, at high temperatures, gaseous carbon sources decompose into carbon atoms that adsorb onto metal surfaces with lower carbon solubility. These carbon atoms autonomously grow into "graphene islands", which gradually increase in number and size. When the entire substrate is covered, the graphene islands stop growing, eventually forming a large-area monolayer graphene. In 2009, the Ruoff group pioneered the use of low-carbon-solubility copper (Cu) foils as substrates to successfully produce large-area, high-quality graphene, mainly in monolayer form.[69, 76] This method yields graphene with fewer layers, fewer defects, and larger sizes, making it suitable for applications in high-quality electronic nanodevices. The CVD-grown graphene on the metal substrates can be transferred to different substrates for various applications (**Figure 9c**).

To further improve the quality of CVD graphene, continuous optimization and improvement of CVD techniques are ongoing.[71a, 77] The large-scale synthetic graphene films are typically polycrystalline, consisting of multiple single-crystalline grains with inherent grain boundaries. The grain boundaries are structural defects and degrade the electrical and mechanical properties of the

resulting films.[78] Centimeter-scale single-layer single-crystalline graphene without grain boundaries have been achieved through proper substrate engineering, including using substrates such as oxygen-rich Cu, Cu–Ni alloy, single-crystal Cu(111), Ge(110) *etc*.[79] In addition, to avoid the defects and contaminations from the transfer process, graphene are directly synthesized on insulators, such as SiO_2, h-BN, quartz, and Al_2O_3.[80] This is achieved by additionally introducing of a gaseous promotor that catalyzes the decomposition of carbon feedstock on the surface of the insulating substrate. Moreover, progress has also been reported on graphene growth at low-temperature, with controlled thickness and stacking twist angles.[81]

2.3.3 Synthesis of Graphene by Chemical Oxidation and Reduction

The chemical oxidation-reduction method stands out as the predominant approach for macroscopic production of graphene. It enables the production of graphene in large quantities suitable for applications in catalysis, energy storage, etc.

In 1859, chemist Benjamin C. Brodie pioneered this method by successfully creating graphite oxide from graphite using potassium chlorate and fuming nitric acid. Several iterative oxidation steps yielded "paper-like foils" with a thickness of 0.05 mm.[82] In 1898, Staudenmaier improved the oxidation method by introducing potassium chlorate in small portions and subsequently acidifying the mixture with concentrated sulfuric acid (H_2SO_4).[83] In 1957, Hummers and Offeman introduced the renowned "Hummers' method" as an improved technique for producing GO.[84] Indeed, the credit for "Hummers' method" should be given to Charpy. He had used the combination of potassium permanganate ($KMnO_4$) and H_2SO_4 and published a similar method in 1909.[85] The Graphite was oxidized to graphite oxide by treating it with a water-free mixture of concentrated H_2SO_4, sodium nitrate ($NaNO_3$), and $KMnO_4$. The

reaction was cooled in an ice-bath and the KMnO₄ was gradually added in portions to maintain the temperature below 20 °C. The ice-bath was then removed. The temperature of the suspension was raised to 35°C and kept for 30 minutes. causing a temperature rise to 98°C. After 15 minutes, more water was added to dilute the mixture, and the remaining permanganate was neutralized with hydrogen peroxide. This method is extensively utilized, often with some modifications, to synthesize GO due to its relative safety and efficiency in exfoliating graphite into thin layered sheets.
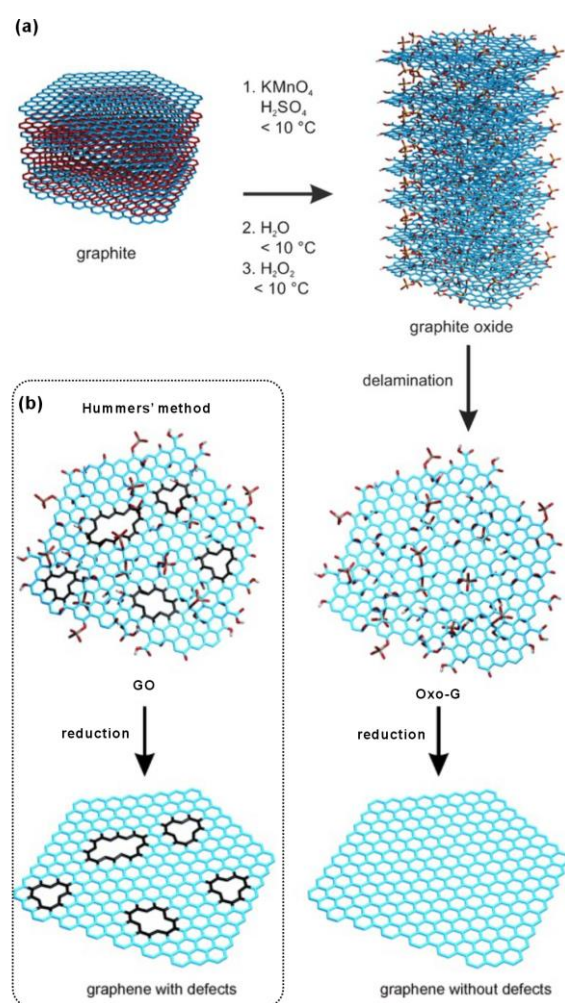

Figure 10 Synthesis and reduction of (a) oxo-G and (b) GO. Adapted from ref.[59] with permission from Wiley-VCH Verlag GmbH & Co, Copyright 2014.

The Eigler group modified this method by maintaining a reaction temperature below 10 °C and extending the oxidation time to 16 h to minimize CO_2 formation during oxidation (**Figure 10a**).[54] The reaction was terminated by slowly adding

cold water to avoid heating with concentrated H_2SO_4. Subsequent purification and exfoliation remained consistent with Hummers' method, but with a temperature threshold of less than 10 °C. The new form of GO, named oxo-G (**Figure 10a**), obtained through this method exhibits very few defects and demonstrates better stability against degradation compared to GO (**Figure 10b**). The temperature control is indispensable for preserving the carbon framework, and is the crucial difference to Hummers' method. The detailed structures of GO and oxo-G are discussed in *Section 2.2.2* and *2.2.3*.

To convert GO to graphene, various reduction methods are employed, including thermal annealing, electrochemical reduction, and chemical reduction with reducing agents, such as borohydrides, hydrohalic acid, and hydrazine *etc*.[86] During reduction, oxygen-containing functional groups, such as hydroxyl, epoxy, and carboxyl groups, are removed or chemically modified to form carbon-carbon bonds, thereby reducing the oxygen content and restoring the sp^2 carbon network characteristic of graphene. The quality of the reduced GO (r-GO) can be controlled by adjusting reaction parameters such as temperature, reaction time, choice of reducing agent, and also depending on the initial degree of defect in GO.[87] In contrast to GO, oxo-G has an almost intact carbon framework and, therefore, can be chemically reduced to high-quality graphene (defect density below 1%, as discussed in *Section 2.2.3*) (**Figure 10**).[58]

2.4 Covalent Functionalization of Graphene

2.4.1 Covalent Functionalization Method

Pristine graphene is a zero-bandgap semimetal, as its conduction and valence bands meet at the Dirac point, as discussed in *Section 2.2.1*.[50a] Covalent functionalization of the graphene is to form covalent bonds between functional groups and carbon atoms within the graphene lattice. This covalent bonding process utilizes π electrons, thereby altering the charge carrier properties of

graphene and leading to the opening of its bandgap (**Figure 4c**).[88] Consequently, graphene undergoes a transition from a semimetal to a semiconductor.[89] This is crucial for applying graphene in micro- and nano-electronic devices.[90]

Various approaches have been employed for the covalent modification of graphene, which include the addition of free radicals to sp^2 carbon atoms, the addition of dienophiles to carbon–carbon bonds, hydrogenation, and fluorination of graphene *etc* (**Figure 11**).[91] Among these methods, radical reactions generating reactive species, such as nitrene, carbene, and aryl intermediates, are most prominent in covalent functionalization of graphene.
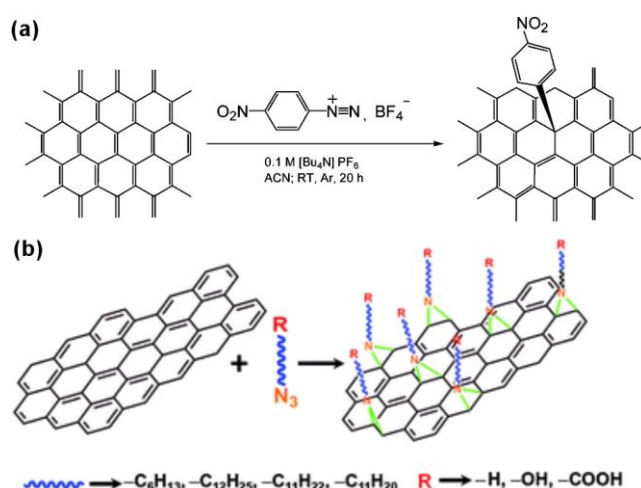
Figure 11 (a) Functionalization of graphene by (p-nitrophenyl) diazonium tetrafluoroborate. Reproduced from ref.[92] with permission from the American Chemical Society, Copyright 2009. (b) Functionalization of graphene by alkyl nitrenes. Reproduced from ref.[91d] the Royal Society of Chemistry, Copyright 2011.

Aryl diazonium salt molecules with a range of functionalities have been effectively used to modify graphene. For example, the Haddon group first used diazonium salts ((p-nitrophenyl) diazonium tetrafluoroborate) to modify graphene sheets (**Figure 11a**).[92] The epitaxial graphene was functionalized with nitrophenyl-groups, leading to an increase in electrical resistance. The Yang group applied aryl diazonium salts with different types and quantities of

reactive end groups (-Cl, -NO$_2$, or -NH$_2$) to functionalize graphene nanosheets by electrochemical methods. Depending on the types (charge states) of reactive terminal groups and target analytes, selective and sensitive detections of three inorganic ions (lead, nitrite, sulfite ions) have been realized.[93] In addition to the direct functionalization of monolayer graphene, Hirsch group reported on a two-step covalent bulk functionalization of graphene. It started with the reduction of graphite using alkaline metals in dimethoxyethane yielding negatively charged graphenides, followed by the quenching it with diazonium salts, iodonium salts, or alkyl halides leads to the covalently functionalized graphene.[94]

2.4.2 Laser-induced Selective Functionalization Method

Through the aforementioned covalent modifications, the carbon lattice of graphene undergoes a *sp^2-sp^3* transition. These initial studies constitute the first stage of covalent modification of graphene chemistry, focusing on the binding of functional groups, with less regard to the regioselectivity. [95] Moreover, most methods demand specific experimental conditions, including long reaction times and harsh reaction temperatures. Laser-induced functionalization achieves high regioselectivity for functionalization on graphene surfaces, introducing functional groups primarily at irradiated locations or structures. This method does not require direct contact with the graphene surface, avoiding damage or contamination, and minimizing the introduction of external impurities. By adjusting parameters such as laser power, wavelength, and irradiation time, precise control over the modification process can be achieved to obtain the desired modification structures and properties. By introducing functional groups in specific surface regions, the chemical properties, such as hydrophilicity, hydrophobicity and catalytic activity, [92, 96] and physical properties of graphene, such as electronic conductivity and

bandgap,[88, 97] can be tailored.

Focused laser writing is an effective technique for selective functionalization of graphene. As shown in **Figure 12a**, the procedure initiates with the deposition of a photosensitizer onto the graphene surfaces. Subsequently, laser-induced photolysis of the photosensitizer occurs, generating free radicals that react with graphene. Notably, the radical reaction is confined to the region illuminated by the laser. Related research started in 2009, Brus *et al*. reported the laser-triggered photochemical reaction between graphene and benzoyl peroxide (BPO), realizing the covalent modification of graphene.[98] Graphene on a Si wafer was immersed in a BPO solution, and the reaction was initiated by focusing an Ar-ion laser beam (λ = 514.5 nm, 0.4 mW) onto the graphene flake in the solution. As BPO is transparent at the laser wavelength, direct photolysis is unlikely. However, the process can be initiated by photoexcited graphene, which absorbs light and transfers an electron to BPO, leading to its decomposition to phenyl radical and CO_2. The phenyl radical then forms a covalent bond with the unbonded free electron in graphene. In addition, the phenyl radicals likely also react with phenyl groups that are already bound on the graphene surface, resulting in the formation of polymeric dendritic structures. Moreover, Hirsch *et al* controlled the covalent bonding of phenyl groups on graphene with a designed 2D-pattern, which was guided by Raman mapping techniques. The 2D-functionalized patterns on graphene can be erased by de-functionalization through thermal treatment.[99]
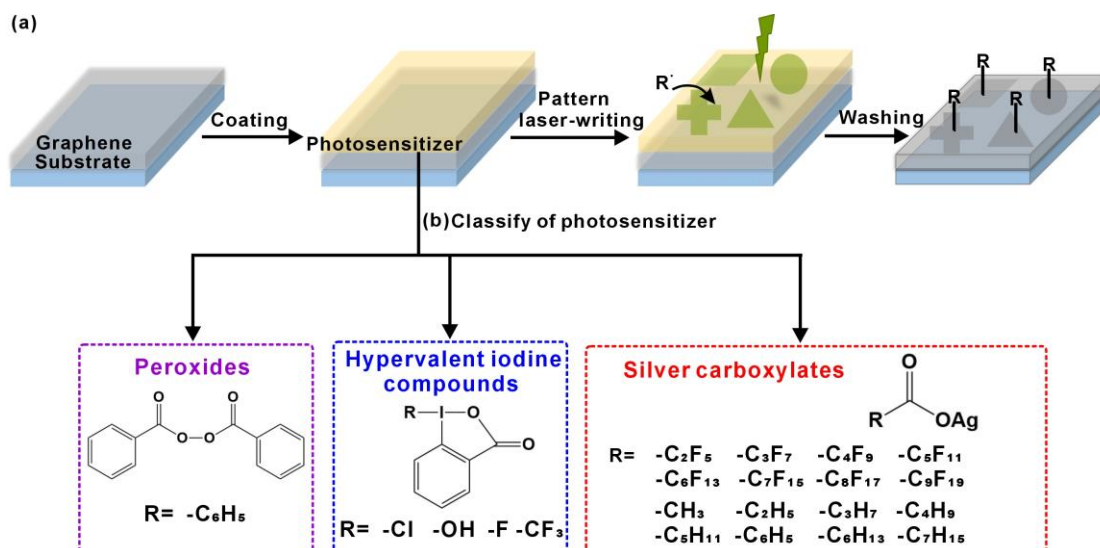
Figure 12 (a) Schematic illustration of the reaction sequence for the laser-induced 2D-functionalization of monolayer graphene. (b) Classify of reported photosensitizer.

In addition to BPO, the Hirsch group used hypervalent iodides as photosensitizers, including 1-chloro-1,2-benziodoxol-3(1H)-one, 1,3-dihydro-1-hydroxy-3,3-dimethyl-1,2-benziodoxole, 1-fluoro-3,3-dimethylbenziodoxole, and 3,3-dimethyl-1-(trifluoromethyl)-1,2-benziodoxole to introduce various functional groups to pattern graphene.[100] Recent studies have shown that silver trifluoroacetate, a novel photosensitizer for laser writing on graphene, can achieve extremely high degrees of functionalization.[101] Moreover, a series of silver carboxylates were used to bind 16 kinds of fluoroalkyl and alkyl groups to graphene surface to achieve the p-doping and n-doping of graphene, respectively (**Figure 12b**).[102] The degrees of functionalization are above 1%.[100] In addition, the laser-induced covalent bonds can be broken by high-temperature annealing treatments, and the functionalization of graphene is reversible, which makes the graphene surface adjustable.[100-102, 103] The laser-induced functionalization method provides us with a precise and controllable way to modify the surface of 2D materials, which brings new ideas for designing the chemical interfaces of the 2D heterostructures.

2.5 Structures and Optical Properties of MoS$_2$

2.5.1 Atomic and Electronic Band Structures of MoS$_2$
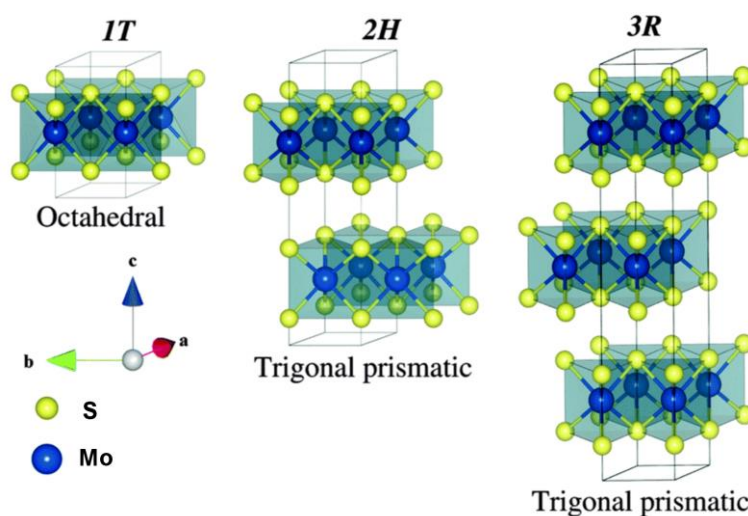
Figure 13 Lattice structures of 2H, 3R, and 1T phase MoS$_2$. Adapted from ref.[104] the Royal Society of Chemistry, Copyright 2015.

MoS$_2$ is a typical TMDCs with a layered structure. A monolayer of MoS$_2$ is a sandwich structure consisting of three atomic layers: a central layer of Mo atoms sandwiched between two layers of S atoms. In each layer, Mo atoms form covalent bonds with six S atoms.[105] However, Mo and S atoms cannot form perfect bonds at the edges, leading to numerous dangling bonds, consequently, resulting in high energy levels at the edges. Multilayer MoS$_2$ is formed by stacking these "tri-atomic-layer sandwich" structures through relatively weak van der Waals forces, with an interlayer spacing of 0.650 nm.[106] Therefore, the intralayer forces within MoS$_2$ are strong, while the interlayer interactions are relatively weak.

Different atomic arrangements between S and Mo atom layers lead to different MoS$_2$ structures, such as 2H phase, 3R phase, and 1T phase (**Figure 13**).[107] The metallic phase 1T has a triangular S-atomic layer at the top and a 180° rotated S-atomic layer at the bottom, forming a hexagonal arrangement of S atoms.[108] In the semiconductor 2H phase, each Mo atom extends six branches

in two tetrahedra in the Z directions forming hexagonal symmetry. The 2H phase have ABAB stacking between layers. The 3R phase is a rhombohedral symmetric crystal system with ABCABC stacking between layers.
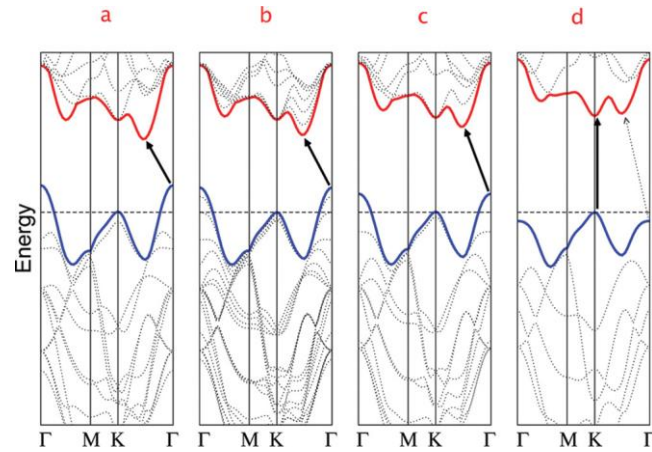
Figure 14 Calculated band structures of (a) bulk MoS_2, (b) four-layer MoS_2, (c) bilayer MoS_2, and (d) monolayer MoS_2. Reproduced from ref.[109] with permission from the American Chemical Society, Copyright 2010.

Figure 14 is a schematic energy band diagram for the bandgap transitions of bulk, four-layer, bilayer and monolayer MoS_2, which is based on the density functional theory (DFT).[109] The variation in the band structure with the number of layers arises from quantum confinement and the resulting hybridization changes between the p_z orbitals on S atoms and the d orbitals on Mo atoms.[109-110] DFT calculations indicate that the conduction band states at the K point primarily originate from the localized d orbitals on Mo atoms in the S-Mo-S region, which are relatively unaffected by interlayer coupling.[111] However, the states near the Γ point originate from the combination of the antibonding p_z orbitals on S atoms and the d orbitals on Mo atoms, exhibiting strong interlayer coupling effects.[109] Consequently, as the number of layers decreases, the direct excitonic states near the K point remain relatively stable, while the indirect transitions near the Γ point increases monotonically. As shown in **Figure 14d**, the monolayer MoS_2 changes into a direct bandgap semiconductor as the positions of both valence band maximum and conduction band minimum shift

to the K point. [111]

2.5.2 Photoluminescence of MoS$_2$

The phenomenon of photoluminescence (PL) arises from the process of excitation and recombination of non-equilibrium carriers in semiconductor materials. The process begins when incident light illuminates the semiconductor material with a higher energy than the band gap of the material. In this case, electrons in the valence band vertically jump to the conduction band after absorbing the photon energy, forming a pair of non-equilibrium carriers with holes in the valence band. This excited state carrier pair is unstable as it tends to return to the ground state by undergoing a recombination process. The recombination of the carriers in the excited state leads to the release of energy, which is emitted in the form of light, resulting in PL.

Wang *et al*.[109] first proposed in 2010 that monolayer MoS$_2$ is a direct bandgap material with strong PL. Nevertheless, bulk MoS$_2$ is an indirect bandgap semiconductor with negligible PL. The PL quantum efficiency from such a direct excitonic state in MoS$_2$ can be approximated by $\eta_{Lum} \approx k_{rad}/(k_{rad} + k_{defect} + k_{relax})$, where k_{rad}, k_{defect}, and k_{relax} are, respectively, rates of radiative recombination, defect trapping, and electron relaxation rate of intraband relaxation to band minimum. In bulk MoS$_2$, the k_{relax} is extremely high. Therefore, PL from direct excitonic transitions is usually not observable in bulk MoS$_2$. With the increase of the indirect bandgap in thinner MoS$_2$, the intraband relaxation rate from the excitonic states decreases. However, k_{rad} is not likely to change as the direct excitonic transitions remain at the same energy, as discussed in *section 2.5.1*. In the case of monolayer MoS$_2$, a qualitative change into a direct bandgap semiconductor renders $k_{relax} = 0$. Therefore, the enhanced PL in monolayer has to be attributed to a dramatically slower electronic relaxation k_{relax}.[109]
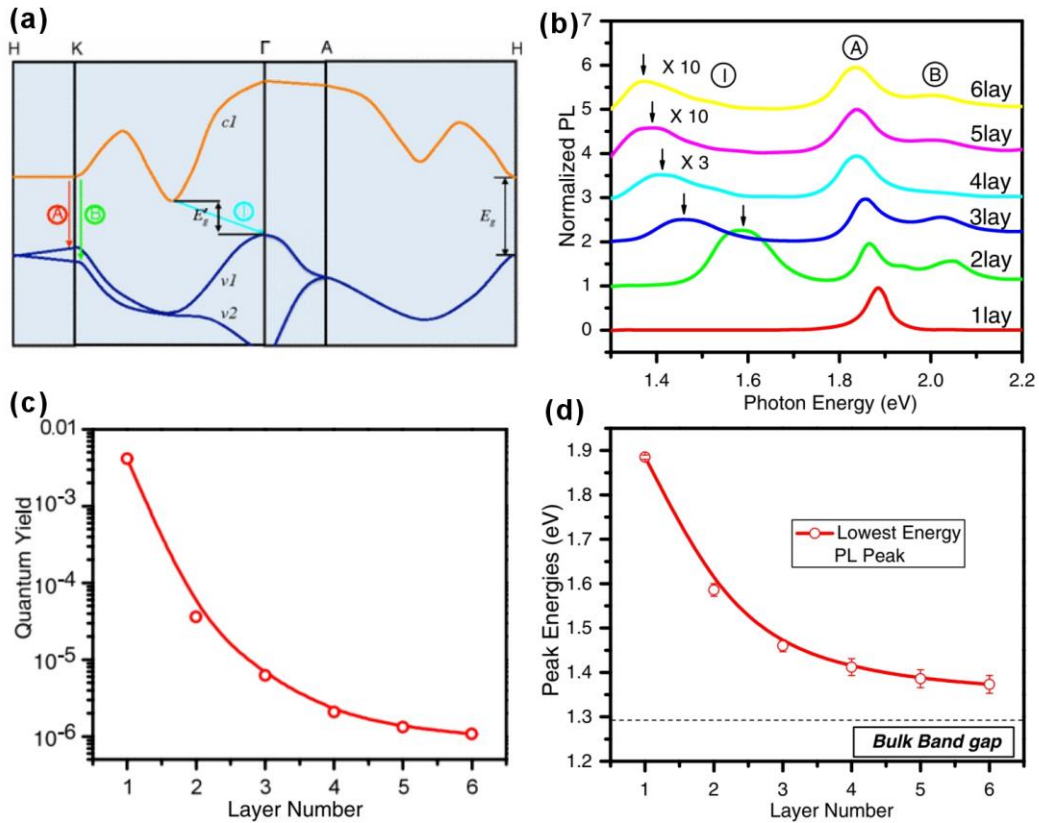
Figure 15 (a) Simplified band structure of bulk MoS$_2$. (b) Normalized PL spectra by the intensity of peak A of 1-6 layers MoS$_2$. Feature I for 4–6 layers are magnified for clarity. (c) PL quantum yield of 1-6 layers MoS$_2$. (d) Bandgap energy of thin layers of MoS$_2$, inferred from the energy of the PL feature I for 2-6 layers and from the energy of the PL peak A for monolayer MoS$_2$. The dashed line represents the indirect bandgap energy of bulk MoS$_2$. Adapted from ref.[110] with permission from the American Physical Society, Copyright 2010.

Figure 15a shows the simplified band structure of MoS$_2$, where Γ indicates the Brillouin zone center, *c1* is the conduction band, *v1* and *v2* are the two split valence bands. A and B represent the direct-gap transitions with the energy split from *v1* and *v2*, and I represents indirect-gap transition from the conduction band to the valence band, which corresponds to the A, B, and I peaks in the PL spectra in **Figure 15b**. E'$_g$ is the indirect energy band gap, and E$_g$ is the direct band gap.[110] The PL intensity of suspended 1-6 layers MoS$_2$ samples varies significantly depending on the number of layers when excited at the same energy of 2.33 eV (**Figure 15c**). The PL quantum yields for 2-6 layers MoS$_2$ are on the order of 10^{-5}–10^{-6}, while a value as high as 4×10^{-3} was observed in

monolayer MoS_2. The normalized PL spectra for suspended 1-6 layers MoS_2 are shown in **Figure 15b**. The PL spectrum of monolayer MoS_2 exhibits a single peak centered at 1.90 eV, which is attributed to direct-gap transition A. In contrast, in few-layer samples, multiple emission peaks are observed, labeled as A, B, and I. Peak A coincides with the monolayer emission peak but redshifts and broadens slightly with an increasing number of layers. Peak B lies about 150 meV above peak A. The broad feature I lies below peak A and systematically shifts to lower energies. It approaches the indirect-gap energy of 1.29 eV and becomes less prominent with an increasing number of layers (**Figure 15d**).
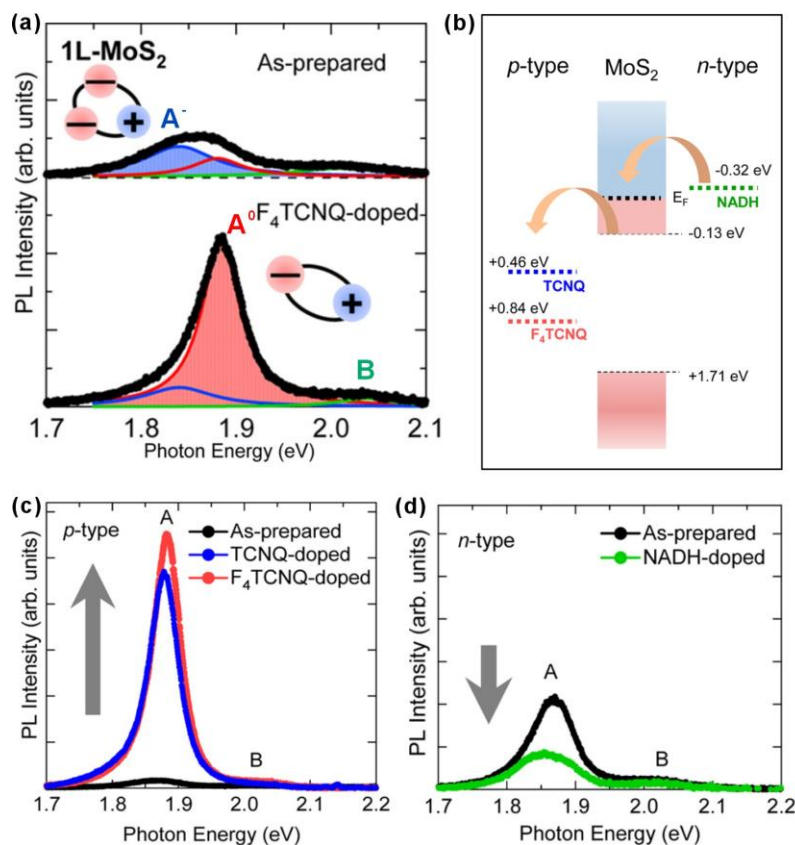
Figure 16 (a) Peak fittings using Lorentz functions of as-prepared and F_4TCNQ-doped monolayer MoS_2. (b) Schematic of relative potentials (vs SHE) of monolayer MoS_2 and n- and p-type dopants. (c) PL spectra of monolayer MoS_2 before and after p-doping by TCNQ and F_4TCNQ, respectively. (d) PL spectra of 1L-MoS_2 before and after n-doping NADH. The PL spectra were measured at 532 nm excitation. Adapted from ref.[112] with permission from the American Chemical Society, Copyright 2013.

Most of the monolayer MoS$_2$ obtained by mechanical exfoliation or CVD method displays n-type behavior, which results in multiple peaks in the PL spectra. As shown in **Figure 16a**, the PL emissions of monolayer MoS$_2$ mainly stem from neutral excitons (A^0, one electron and one hole) and other excitonic complexes such as trions (A$^-$, two electrons and one hole) and biexcitons (B, two electrons and two holes). By controlling the electric field[113] and chemical doping, the concentration of electrons in MoS$_2$ can be changed, leading to the modulation of intrinsic behavior. This change enables the transition of different excitons thus to adjust the PL behavior of MoS$_2$.[112]

Mouri *et al*. successfully achieved tunable PL of 1L-MoS$_2$ vis n-type and p-type chemical doping, respectively.[112] They utilized 2,3,5,6-tetrafluoro-7,7,8,8-tetracyanoquinodimethane (F$_4$TCNQ) and 7,7,8,8-tetracyanoquinodimethane (TCNQ) as p-type dopants, leading to a notable enhancement in the PL of 1L-MoS$_2$ (**Figure 16c**). Additionally, the introduction of n-type dopant, nicotinamide adenine dinucleotide (NADH), resulted in PL quenching (**Figure 16d**). Schematic of relative potentials (vs SHE) of monolayer MoS$_2$ and dopants are shown in **Figure 16b**. The flat band potential of few-layer MoS$_2$ is −0.13 eV (vs SHE), which is smaller than the reduction potentials of 0.84 eV (vs SHE) for F$_4$TCNQ and 0.46 eV (vs SHE) for TCNQ, and larger than the low oxidation potential of −0.32 eV (vs SHE) for NADH. Therefore, the F$_4$TCNQ and TCNQ function as electron acceptors (p-type dopants) and the NADH functions as an electron donor (n-type dopant) for monolayer MoS$_2$. The difference in chemical potential between monolayer MoS$_2$ and p-type (n-type) dopants induces the electron extraction (injection) in MoS$_2$. As displayed in **Figure 16a**, the PL spectral weight of the A$^-$ at ~1.84 eV is greater than that of the A^0 peak at ~1.88 eV in the as-prepared monolayer MoS$_2$. However, the PL spectra of F$_4$TCNQ-doped MoS$_2$ are dominated by A^0 exciton peak at ~1.88 eV, which indicates that the excitons can recombine from trions to neutral excitons due to the

decrease in the number of excess carriers in MoS$_2$ (**Figure 16a**).[114] In addition to surface doping, various approaches, including local surface plasmon resonance,[115] strain engineering,[116] and defect engineering,[117] are used to adjust the PL performance of MoS$_2$.

2.6 Interfacial Charge Transfer and Optical Properties of Graphene-based/MoS$_2$ Heterostructures

2.6.1 Research Status of Graphene/MoS$_2$

Since the discovery of graphene in 2004, the properties of graphene have been extensively studied, and many of its properties exceed those of any other material: ultrahigh room-temperature electron mobility of $1.5 \times 10^4\,cm^2\ V^{-1}\ s^{-1}$ (10 times to Si);[1] a Young's modulus of 1 TPa and intrinsic strength of 130 GPa;[2b] very high thermal conductivity (above $3000\,W\ mK^{-1}$);[118] complete impermeability to any gases;[119] ability to sustain extremely high densities of electric current (a million times higher than copper)[120]. However, the absorption of incident light by monolayer graphene is only 2.3%,[121] which is insufficient for high-performance optoelectronic devices that require strong light absorption. The zero bandgap of graphene leads to a short photocarrier lifetime, limiting effective photocurrent generation.[122] Consequently, the optical properties of graphene greatly limit its applicability in optoelectronics.

Stacking graphene with other 2D materials to form van der Waals heterostructures is one way to open the bandgap (about 2 meV) of graphene besides chemical modification. Such heterostructures not only overcome the limitations of individual materials but also introduce novel properties through their effective combination.[123] Compared to the semimetal graphene, monolayer MoS$_2$ has a direct band gap of 1.9 eV with a high absorption coefficient and efficient electron-hole pair generation under photoexcitation.[124] The G/MoS$_2$ integrate the superior light-matter interaction in MoS$_2$ and high

charge mobility in graphene, providing potential for high-performance optoelectronic devices.[125] Zhang *et al*. fabricated MoS$_2$/G photodetector by transferring graphene onto a large continuous MoS$_2$ monolayer film. They found that the photogenerated electron-hole pairs in MoS$_2$ could be separated across the hetero-interlayers, and the photoelectrons were injected into graphene rather than trapped in MoS$_2$ due to the presence of a perpendicular effective electric field. The MoS$_2$/G photodetector exhibited an ultrahigh optical responsivity of more than 10^7 A W $^{-1}$ at room temperature and an optical gain of ~10^8, whereas the highest photoresponsivity for the pristine monolayer MoS$_2$ is only around 780 A W^{-1}.[126] Pala *et al*. reported that the photo-generated holes traveled from graphene to MoS$_2$ over the Schottky barrier under illumination. The p-type MoS$_2$ formed a Schottky junction with graphene with a barrier height of 139 meV, which provided a broad spectral range of detection.[127] Strano *et al*. proposed that the junction in G/MoS$_2$ was a Schottky barrier, whose height was artificially controlled by gating or doping of graphene.[128] Xu *et al*. made one step further. They found that the insertion of CVD-grown monolayer h-BN between G/MoS$_2$ efficiently blocked the interlayer coupling and therefore restored its photovoltaic effect. The photocurrent of MoS$_2$/h-BN/graphene heterostructure increased by over three orders, demonstrating a responsivity of 0.36 A W^{-1} at 532 nm illumination and an ultra-high detectivity of 6.7 × 10^{10} Jones.[129]

As discussed above, the current research focus of G/MoS$_2$ heterostructures is on interface modulation.[130] In this thesis, we use chemical ways to construct the interface for adjusting the Fermi level of graphene and regulating the charge transfer at the interface, promoting the high optical performance of G/MoS$_2$ heterostructures in optoelectronic applications.

2.6.2 Atomic and Electronic Band Structures of Graphene/MoS$_2$
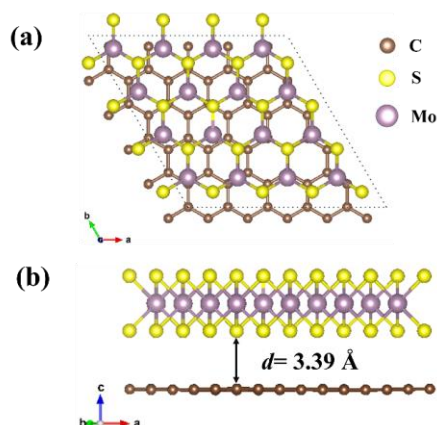
Figure 17 Optimized structure of G/MoS$_2$ from (a) top view and (b) side view.

Figure 17 shows the atomic structure G/MoS$_2$ heterostructure with supercell geometry of 5:4 (graphene: MoS$_2$) obtained by DFT calculations. The DFT based first principles calculations were carried out using the projector augmented-wave (PAW) method as implemented in the VASP code. MoS$_2$ sheet was compressed by 0.3%, whereas the graphene sheet was stretched by 1.16% from the optimized pristine cell parameters. Mo-S bond length is 2.38 Å and C-C bond length is 1.44 Å. The thickness of the MoS$_2$ monolayer (the vertical distance between S-S planes) is 3.13 Å.[131] The interlayer spacing between graphene and MoS$_2$ sheets is 3.39 Å, which is in good agreement with the experimentally reported interlayer distance of 3.40 Å. [132]

The calculated electronic band structures of the isolated MoS$_2$ monolayer, pristine graphene, and G/MoS$_2$ heterostructure are shown in **Figure 18**.[133] The electronic band structure of G/MoS$_2$ heterostructure appears to be a simple sum of the electronic band structures of the graphene and MoS$_2$. The linear dispersion bands of graphene appear in the large energy gap of MoS$_2$, and the electronic band structure features of pristine graphene seem to be preserved, indicating that the van der Waals interaction between graphene and MoS$_2$ is relatively weak. As displayed in the inset of **Figure 18c**, the linear bands at the

Dirac point of graphene are slightly changed by the interactions between graphene and MoS_2, and a band gap of about 2 meV opens in G/MoS_2 interfaces.[134]
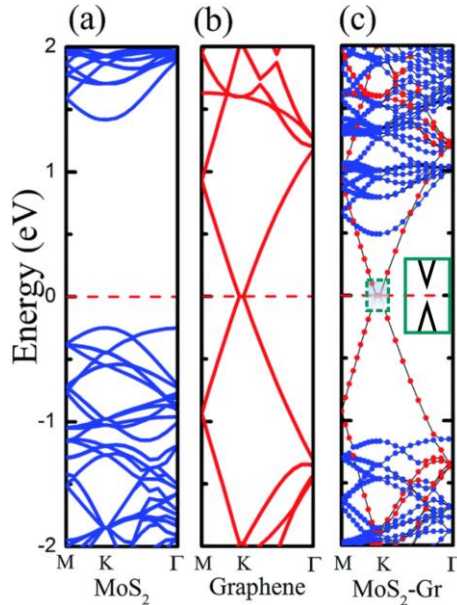
Figure 18 Electronic band structures of (a) MoS_2 (b) graphene, and (c) G/MoS_2 heterostructure. Inset of (c) shows the zoom in of the band structure near Fermi Energy. The Fermi level is set to zero and marked by red dotted lines. Adapted from ref.[133] the Royal Society of Chemistry, Copyright 2016.

One of the key parameters in the design of a heterostructure is the determination of the band offset, which is the relative alignment of the energy bands of heterostructure. Anderson's rule is used to construct energy band diagrams for two semiconductor heterojunctions. The rule states that the vacuum of the semiconductors on both sides of the heterojunction should be equal when plotting the energy band diagram.[135] Based on Anderson's rule and the calculated electronic band structures (relative to vacuum E_{VAC}), the schematic band alignment for graphene, MoS_2, as well as the G/MoS_2 heterostructure are shown in **Figure 19a**. The band alignment diagram demonstrates the emergence of interlayer excitons. For semiconductors, the E_F lies within the band gap. The position of E_F depends on factors such as temperature and doping level. At absolute zero temperature (0 K), E_F is located in the middle of the band gap for intrinsic (undoped) semiconductors. When the

semiconductor is doped, E_F shifts toward the conduction band for n-type (electron-doped) semiconductors or toward the valence band for p-type (hole-doped) semiconductors. Due to the difference between the E_F of MoS$_2$ (E_{F1}) and graphene (E_{F2}), the excited electrons migrate from graphene to MoS$_2$, while the holes move in the opposite direction. The charge difference of the G/MoS$_2$ heterostructure was calculated. As expected, the charge redistribution occurs mainly at the interface between the two layers, with electrons accumulating on the MoS$_2$ layer and charges being depleted on the graphene layer (**Figure 19b**).
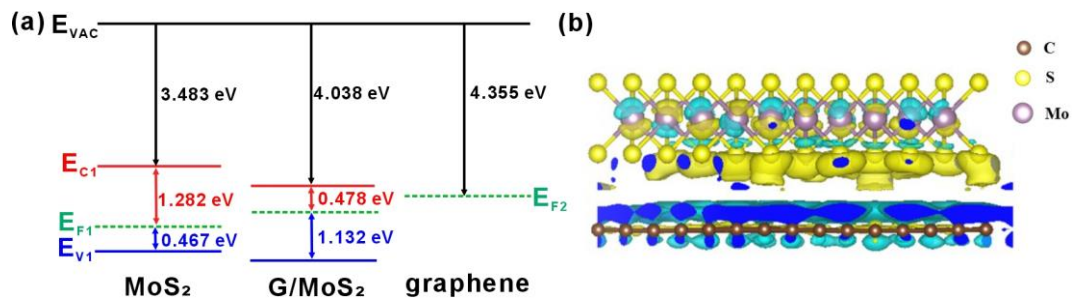
Figure 19 (a) Schematic band alignment for monolayer MoS$_2$, graphene, and G/MoS$_2$ heterostructure.[136] (b) three dimensional isosurface of the charge density difference of G/MoS$_2$ heterostructure (The yellow and blue areas represent electron accumulation and depletion, respectively).

2.6.3 Effects of Interlayer Distance on Interfacial Charge Transfer of Graphene/MoS$_2$

Changing the interlayer distance is an effective way to modulate the electronic properties of van der Waals heterostructures. The interlayer distance in van der Waals heterostructures can be controlled experimentally by vacuum thermal annealing, nanomechanical pressure, intercalation, diamond anvil units, and chemical functionalization.[137] Therefore, it is necessary to consider the effect of interlayer distance on the electronic properties of G/MoS$_2$ heterostructures.
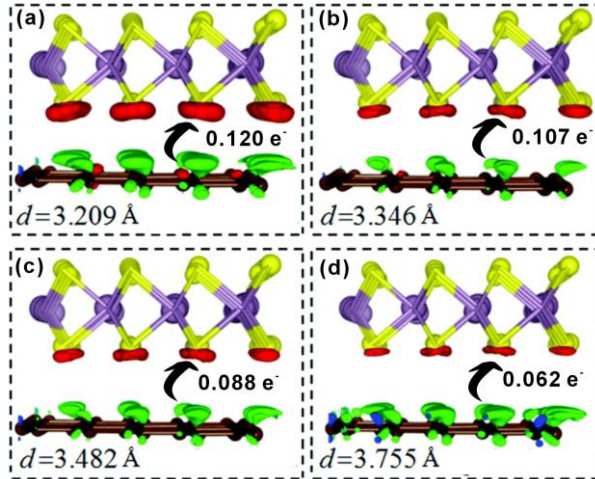
Figure 20 Three dimensional isosurface of the charge density difference of G/MoS$_2$ heterostructure at various interlayer distances. Reproduced from ref.[136] The Royal Society of Chemistry, Copyright 2022.

Figure 20 illustrates that the fluctuation of the charge density difference curves increases as the interlayer distance of the G/MoS$_2$ heterostructure decreases from 3.755 Å to 3.209 Å, which indicates that the graphene layer is transferring more charge to the MoS$_2$ layer. When the interlayer distances were 3.209 Å, 3.346 Å, 3.482 Å, and 3.755 Å, 0.120 e$^-$, 0.107 e$^-$, 0.088 e$^-$, and 0.062 e$^-$ of charge were transferred from the graphene layer to the MoS$_2$ layer, respectively. Due to the charge transfer to the MoS$_2$ layer, the Fermi level of graphene is shifted downward, while the band structures of pristine graphene and MoS$_2$ monolayers are preserved. The band gaps of the MoS$_2$ layer in the heterostructure are 1.747 eV, 1.737 eV, 1.747 eV, and 1.757 eV, when the interlayer distances are 3.209 Å, 3.346 Å, 3.482 Å, and 3.755 Å respectively.[136] All of these results indicate that the interlayer distance can effectively control the charge transfer but plays a limited role in regulating the electronic structure.

2.6.4 Effect of Interfacial Charge Transfer on Photoluminescence of Graphene/MoS$_2$

When 2D materials are stacked to form van der Waals heterostructures, the interfacial coupling between adjacent layers significantly influences their

physical characteristics. Lattice vibrations and PL emissions offer valuable insights into lattice structure, electronic band structure, and interlayer coupling. Excitons in heterostructures exhibit diverse behaviors, which are influenced by electron-electron interactions and charge transfer at the hetero-interface.[138]
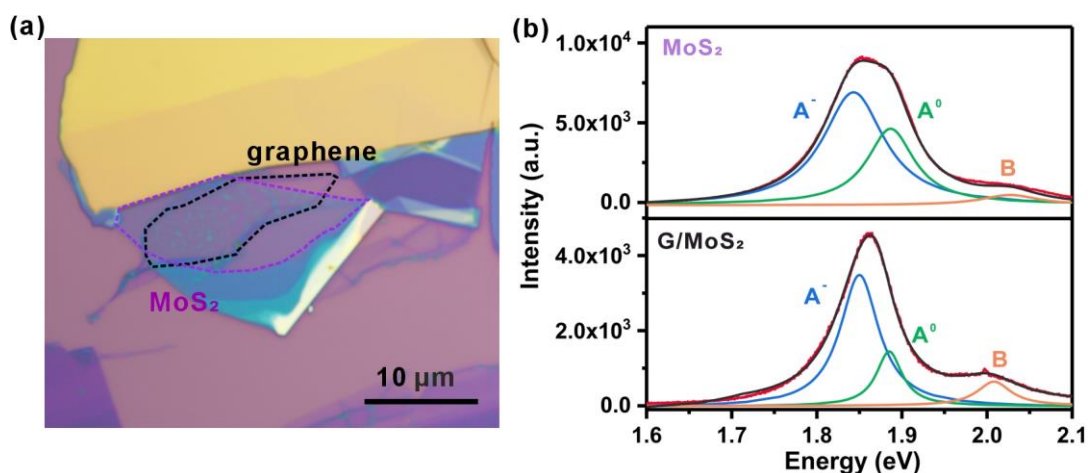
Figure 21 (a) Microscope image and (b) PL spectra of MoS_2/G heterostructures.

For pristine G/MoS_2, the interactions between graphene and MoS_2 leads to the band gap opens of graphene (**Figure 18c**). The upward shift of the Dirac point of graphene with respect to the Fermi level indicates that holes are donated by the MoS_2 monolayer.[139] Specifically, due to the Schottky barrier at the interface, the photogenerated holes are injected from the valence band of MoS_2 to graphene, whereas the photogenerated electrons in the conductance band of MoS_2 are prohibited to diffuse to graphene because of the built-in barrier formed at the hetero-interface.[125] Therefore, the exciton recombination efficiency and the resultant PL intensity of MoS_2 in G/MoS_2 significantly decreased with the increase in the spectral weight of the A$^-$ trion peak (**Figure 21**). Zhen *et al*. systematically investigated the PL characteristics of MoS_2/G heterostructures by electrochemical gate modulation.[138] The results indicated that the PL intensity of excitons can be adjusted by more than two orders of magnitude, with an observed blue shift of the exciton peak up to 40 meV. Under negative gate bias, the tunability of MoS_2 carrier density played a dominant role in focal

adjustment, while under positive gate bias, exciton splitting driven by the built-in electric field at the Schottky contact became the primary influence. They further inserted different thicknesses of insulating self-assembled monolayers (SAMs: octyltrichlorosilane C8-OTS, ca. 0.8 nm, and trichlorooctadecylsilane C18-OTS, ca. 1.8 nm) at the MoS_2/G interface. The insulating SAMs increased the tunneling barrier between MoS_2 and graphene, and further impeded the splitting of excitons. Thus, the significant PL quenching was not observed at positive gate biases, which verified the impact of heterostructure interfaces on PL modulation in G/MoS_2 systems. However, this modulation requires complex device fabrication process and can only be applied in specific situations.
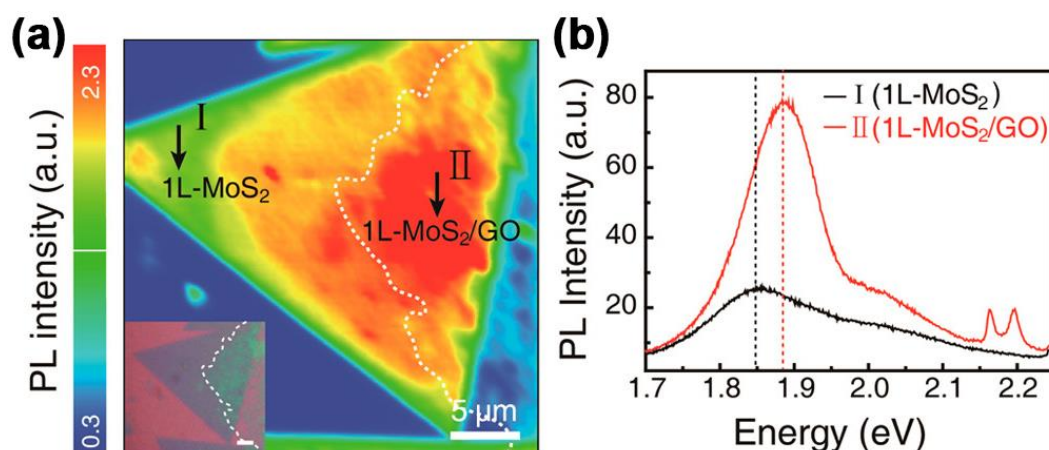
Figure 22 Spatially resolved optical properties of 1L-MoS_2/GO. (a) Confocal PL intensity image of 1L-MoS_2/GO. The inset is an optical image of 1L-MoS_2/GO used for the measurements. (b) Local PL spectra obtained from points I and II in (a). Adapted from ref.[140] with permission from the American Chemical Society, Copyright 2016.

As we discussed in *section 2.4*, graphene can be functionalized with different groups, which can offer various chemical interfaces when assembled with monolayer MoS_2. In this case, graphene can act as a flexible template, and interfacial design with tunable charge transfer is possible. Jeong *et al*. reported the tuning of the electronic properties of monolayer MoS_2 by coating with GO.[140] The abundant electron-withdrawing characteristics from various oxygen functional groups of GO sheets induce the p-doping effect of MoS_2

(**Figure 22**). This process is simple and low-cost, and it allows large-scale fabrication and modulation of the electronic properties. Depending on the needs of monolayer MoS_2 in optoelectronic applications, a variety of functional groups with different electron-accepting and electron-withdrawing capabilities are required. However, the constitute and distribution of the functional groups in GO vary depending on the synthesis method and processing conditions. Consequently, GO may not provide the desired functional groups to meet the specific requirements in fabrication heterointerface with monolayer MoS_2. More synthesis strategies are required to achieve the desired functional groups in G/MoS_2 heterostructures.

Covalently bound functional G/MoS_2 heterostructures are fabricated beyond van der Waals materials. Pérez *et al*. covalently link 2H-MoS_2 flakes with graphene monolayers by a bifunctional molecule featuring a maleimide and a diazonium functional group, which are known to connect to sulfide- and carbon-based materials, respectively.[141] Electronic transport of the linked material was measured in field-effect transistors. The electronic characteristics of the functionalized devices are primarily influenced by the chemical interface. Consequently, the devices exhibit p-doping owing to the electron-withdrawing character of the diazonium linker. The extent of doping can be modulated by increasing the degree of functionalization. However, the device prepared without diazonium linkers indicates n-doping of graphene as a consequence of the direct interactions with MoS_2. They conducted preliminary photoresponsivity experiments using an ultraviolet laser source (365 nm) on the covalent functionalized heterostructure. The initial results show a similar photoresponse to the G/MoS_2 van der Waals heterostructures. Further studies are necessary to understand the role of the linker in the photoresponsivity of the covalent heterostructure. Chen *et al*. designed a covalently linked MoS_2/G heterostructure, inducing PL quenching in monolayer MoS_2.[142] Initially, a layer

of 4-bromophenyl functionalized MoS_2 is prepared on a Si/SiO_2 substrate by reacting negatively charged MoS_2 with 4-bromobenzenediazonium tetrafluoroborate. Subsequently, a graphene layer was transferred on top. The graphene layer was covalently attached from the interior to the functionalized MoS_2 through a laser-triggered free radical reaction of 4-bromophenyl groups. The covalent heterostructure exhibited significant PL quenching, which was similar to the PL performance of pristine G/MoS_2.

Existing reports on the construction of G/MoS_2 interfaces are relatively scarce, and the preparation processes of such structures are complex. The previous examples inspire us to modulate the interface between graphene and MoS_2 by chemical functionalization. The carrier densities and band structure changes in both counterparts, which affect the PL properties of the heterostructures. It is essential to recognize that 2D heterostructures with few atomic thicknesses are not only sensitive to charge-transfer doping but also susceptible to van der Waals interactions and interlayer distance,[143] which play crucial roles in studying the PL of G/MoS_2 heterostructures. In this thesis, graphene-based/MoS_2 heterostructures are fabricated including oxo-G/MoS_2, r-oxo-G/MoS_2, porous oxo-G/MoS_2, and selectively functionalized G/MoS_2 with different functional groups and interlayer distances. The effects of functional groups and porous defects of graphene, and different interlayer distances on the interlayer charge transfer, interlayer van der Waals interactions, and PL properties of G/MoS_2 are investigated.

3 Analytical Methods

3.1 Raman Spectroscopy

Raman spectroscopy, a non-destructive analytical technique, can offer detailed insights into the chemical structure, phases, crystallinity, defects or strain and molecular interactions of 2D materials. It relies on light-matter interaction,

through non-elastic scattering of photons, resulting in Raman scattering. Utilizing a monochromatic light source, commonly derived from lasers in the visible, near-infrared, or near-ultraviolet range, laser photons couple to molecular vibrations or phonons in materials. This light-matter interaction results in an upward or downward shift of scattered photons, providing valuable information about the vibrational modes of the system.
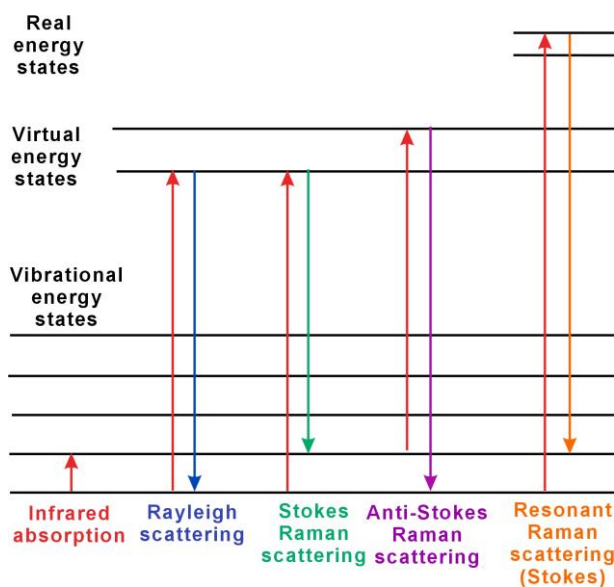
Figure 23 Energy-level diagrams of different states in Raman spectroscopy.

As shown in **Figure 23**, the Raman process can involve resonant or non-resonant excitation. For non-resonant Raman excitation, a photon excites the molecule from the ground state to a virtual energy state. If the excitation is resonant, a real excited state is reached. The virtual or real excited state is not stable and the photon is re-emitted almost immediately, as scattered light. Most of the scattered light is at the same wavelength as the laser source and does not provide useful information, which is called Rayleigh scattering. However, a small amount of light (typically 0.0000001%) is scattered at different wavelengths (Raman scattering), which is an inelastic scattering process with a transfer of energy between the molecule and scattered photon. If the molecule gains energy from the photon during the scattering, it is known as Stokes

Raman scattering. Conversely, Anti-Stokes Raman scattering occurs when a molecule loses energy by relaxing to a lower vibrational level. In most cases the matter is in ground state and excitation in a virtual state occurs. The interaction of light and molecular vibrations leads to Stokes scattering which is normally interpreted.

3.1.1 Raman Spectra of Graphene
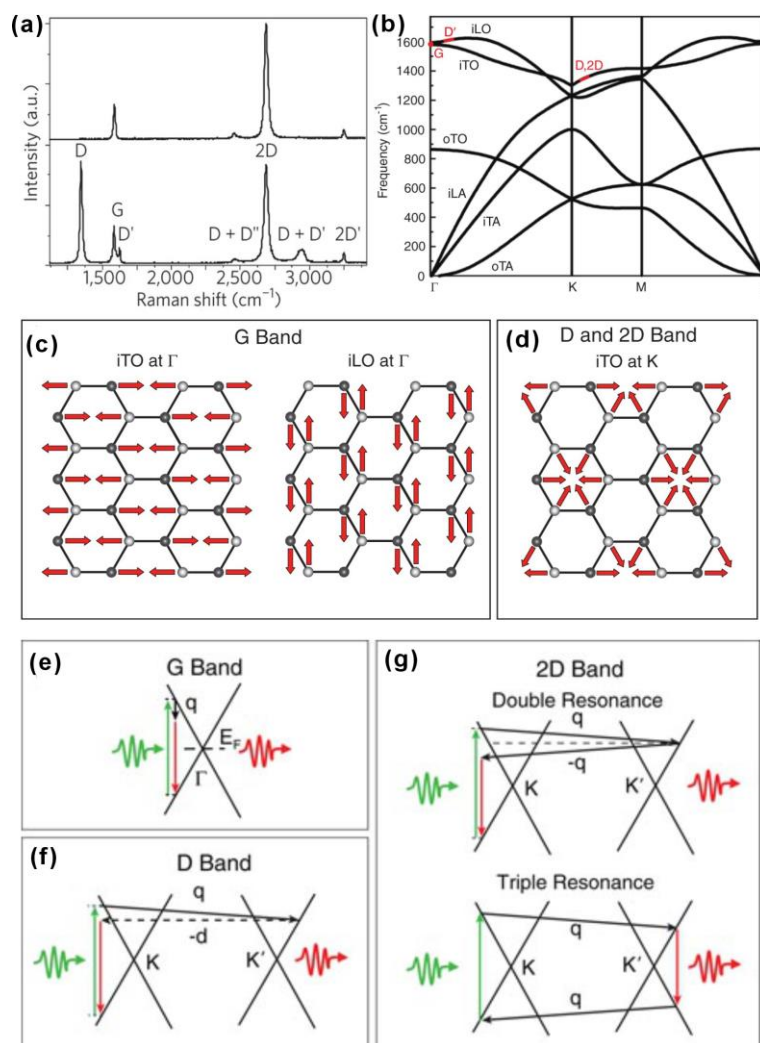
Figure 24 (a) The Raman spectra of graphene measured at 514 nm excitation. Reproduced from ref.[144] with permission from Springer Nature, Copyright 2013. (b) Phonon dispersion of graphene. The phonons associated with important Raman bands are highlighted. (c-d) Schematic diagram of phonon vibration in graphene. (e-g) Illustrations of the excitation and emission in G band, D band, and 2D band. Adapted from ref.[145] with permission from IOP Publishing, Copyright 2015.

The Raman spectrum of graphene was first measured in 2006.[146] The absence

of a bandgap in graphene makes all wavelengths of incident radiation resonant. **Figure 24b-d** depict the optical phonon dispersions and vibration in graphene, which are relevant for interpreting the Raman spectra of graphene (**Figure 24a**). The G-band (at ~1580 cm^{-1}) is associated with doubly-degenerate in-plane stretching vibrations of C-C bonds, involving transverse optical (TO) and longitudinal optical (LO) modes (**Figure 24e**). The G-band is sensitive to the structural properties of graphene because it reflects the *sp²* hybridization of carbon atoms in the graphene lattice. Any changes in the lattice structure, such as strain or defects, can alter the vibrational characteristics of the C-C bonds, leading to shifts or broadening of the G-band peak in the Raman spectrum. The 2D-band (at ~2700 cm^{-1}), sensitive to the number of graphene layers, is ralated to a second-order double resonance (DR) mode, activated by interval scattering of an excited electron. The DR mode is particularly affected by the electronic structure of graphene. As the number of layers changes, the electronic properties of graphene, such as band structure and Fermi level, change accordingly. These changes influence the scattering processes that give rise to the 2D-band, making it sensitive to the number of graphene layers. The D-band (at ~1350 cm^{-1}), also involving a DR process, is triggered by defects like sp^3-defects, and its intensity serves as an estimate for the defect density in graphene, as explained in *section 3.1.2*.[147] DR can also happen as an intravalley process, that is, connecting two points belonging to the same cone around K (or K'). This gives the D' peak (at ~1620 cm^{-1}) and 2D' peak (at ~3250 cm^{-1}) associated with the D peak and 2D peak, respectively (**Figure 24f-g**). Their combination D+D' peak at ~2950 cm^{-1} and D+D" peak at ~2450 cm^{-1} also appear. The D+D" band originates from intervalley scattering induced by phonons, showing a negative curvature due to longitudinal acoustic (LA) dispersion.

3.1.2 Determinate the Degree of Functionalization of Graphene
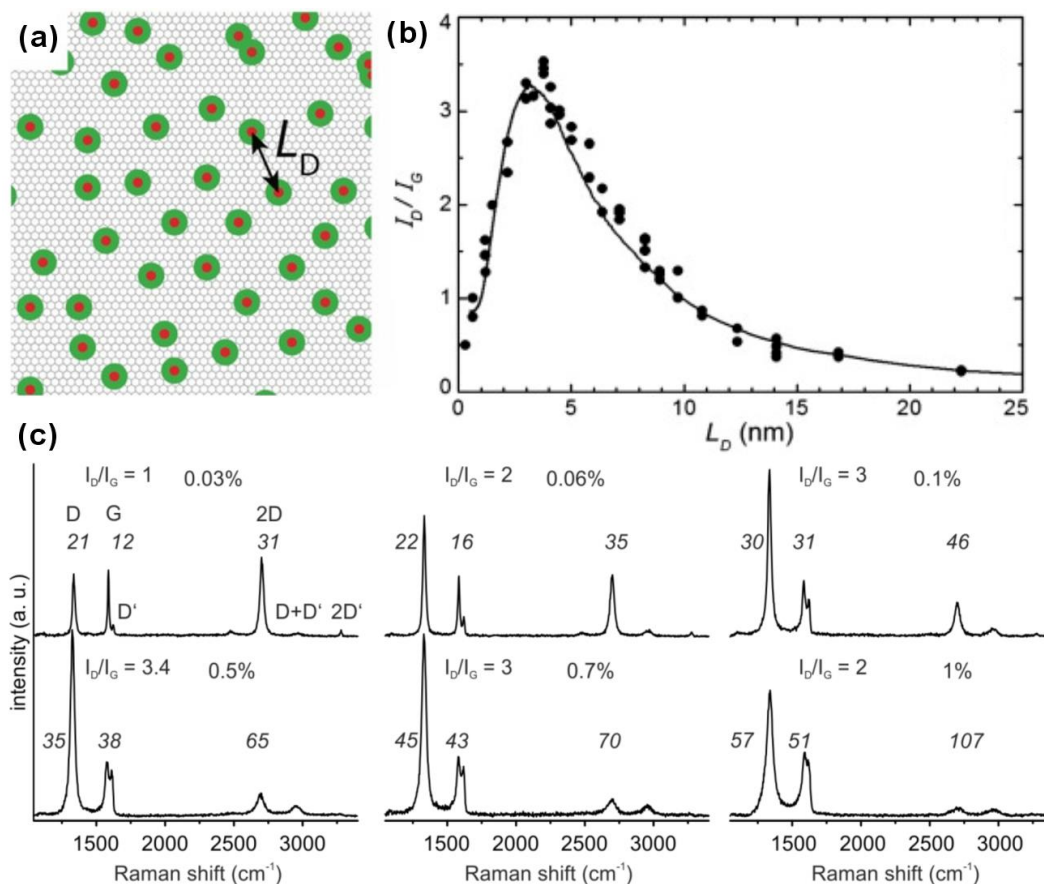
Figure 25 (a) The distance of point defects L_D, with a defect size marked in red and a disturbance area marked in green. Reproduced from ref.[57] with permission from Wiley-VCH Verlag GmbH & Co, Copyright 2018. (b) The I_D/I_G data points of different graphene samples as a function of the average distance L_D between defects. Reproduced from ref.[148] with permission from Elsevier, Copyright 2010. (c) Raman spectra of specially prepared r-GO with a variable of defects measured at an excitation wavelength of 532 nm. For the D, G and 2D peak the FWHM values are given in italic numbers. Reproduced from ref.[56] with permission from Wiley-VCH Verlag GmbH & Co, Copyright 2016.

Raman spectroscopy is a well-established tool for determining the quality of graphene. As discussed in *Section 3.1.1*, the main peaks observed in graphene Raman spectra are the D (at ~1350 cm⁻¹), G (at ~1580 cm⁻¹), and 2D (at ~2700 cm⁻¹) peaks. D peak is only visible when active by a defect. These defects can be structural nature, such as disorder within the carbon framework, missing atoms, or even substituted atoms. The chemical functionalization of graphene

leads to a sp^2-to-sp^3 rehybridization of lattice carbon atoms, which is another possible reason for the evolution of a D peak. This process leads to creating π-conjugated domains with diverse shapes and sizes.[149]

Although Raman spectroscopy cannot determine the type of defects, the origin of the D peak can be estimated based on the starting material. The evolution of Raman spectra was studied with Ar^+ ion bombardment on graphene that bears originally no defects.[148] As illustrated in **Figure 25a**, the distance between two nearest point defects (L_D), can be determined by the ratio of the integrated area or amplitude of the D and G peak (I_D/I_G). The I_D/I_G ratio is an important indicator to estimate the defects density. Furthermore, the relationship between I_D/I_G vs. L_D can distinguish between high-degree regime ($L_D < 3$ nm) and low-degree regime ($L_D \geq 3$ nm) (**Figure 25b**).[148, 150] In addition, the full width at half maximum (FWHM) of D, G, and 2D peaks all broaden with the introduction of defects. The FWHM of the peaks is taking into account to discriminate high degree of defects and low degree of defects. A set of Raman spectra of r-GO is depicted in **Figure 25c**. FWHM values of D peak between 21 and 57 cm^{-1} are found in an I_D/I_G ratio range between 1 over about 4 and down to about 2 again. The FWHM values of G peak are between 12 and 51 cm^{-1} and FWHM values of 2D are between 31 and 107 cm^{-1}. The density of defects between 0.03% and 1% can be estimated.[56]

The interpretation limit for the I_D/I_G ratio is confined to defect distances smaller than 1 nm or defect densities out of 1-3%. Therefore, for graphene that the defect density exceeding this threshold, such as GO, it is necessary to use the amplitude or integrated area of the D and G peaks to determine the density of surface-functionalized defects and in-plane vacancy defects.[57, 151] As depicted in **Figure 26**, a new model is offered to identify the density of defects (θ) with ratio of the Raman modes, I_D/I_G. Moreover, θ can also be determined in a wide range up to 50–60%, which is relevant for graphene oxide, by utilizing non-

linear regression and the formulas provided in **Figure 26**.

(a) $I_D(\theta) \approx D_0 \theta^{k_D} e^{-\gamma_D \theta}$ **(b)** $I_G(\theta) \approx I_0 + G_0 \theta^{k_G} e^{-\gamma_G \theta}$
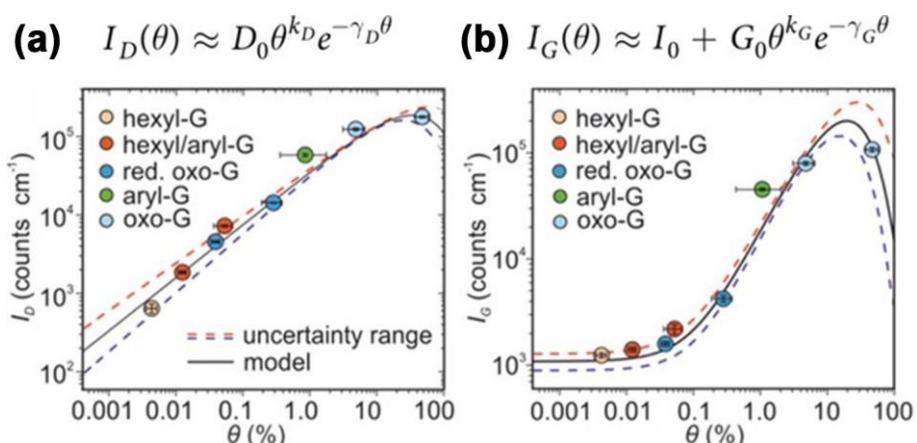
Figure 26 Dependence of the density of defects (θ) on the intensity of Raman peaks (D_0, G_0, k_D, k_G, γ_D, γ_G depend on the experimental setup). (a) I_D *vs.* θ and (b) I_G *vs.* θ. Reproduced from ref.[149] with permission from Springer Nature, Copyright 2017.

3.1.3 Raman Spectra of MoS$_2$
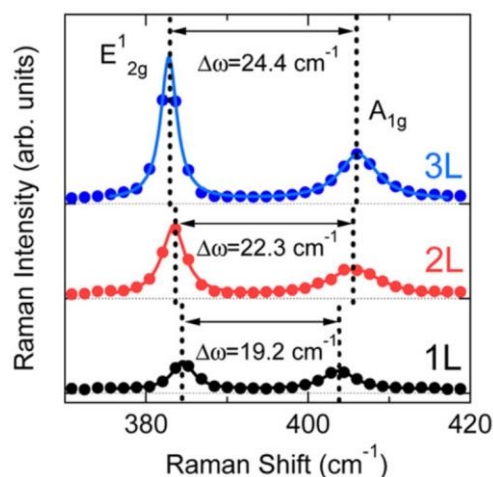
Figure 27 Raman spectra of monolayer, bilayer, and trilayer of MoS$_2$ measured at 532 nm excitation. Adapted from ref.[112] with permission from the American Chemical Society, Copyright 2013.

For MoS$_2$ Raman spectra, two typical phonon modes of MoS$_2$, E$^1_{2g}$ due to in-plane vibrations (at ~385 cm^{-1}) and A$_{1g}$ due to out-of-plane vibrations (at ~404 cm^{-1}), exhibit a strong dependence on the number of MoS$_2$ layers. Specifically, the phonon frequency of E$^1_{2g}$ decreases with an increasing number of layers, while the phonon frequency of A$_{1g}$ increases with an increasing number of layers. As displayed in **Figure 27**, the distance between E$^1_{2g}$ and A$_{1g}$ is about

19.2 cm^{-1} for monolayer MoS$_2$, which increases to 22.3 cm^{-1} and 24.4 cm^{-1} for bilayer and trilayer MoS$_2$, respectively. The different trends in the phonon frequencies of E$^1_{2g}$ and A$_{1g}$ with the number of layers can serve as a reliable method for checking the number of layers in MoS$_2$. This contributes to further researches on the optical properties of both single-layer and multilayer MoS$_2$ thin films.
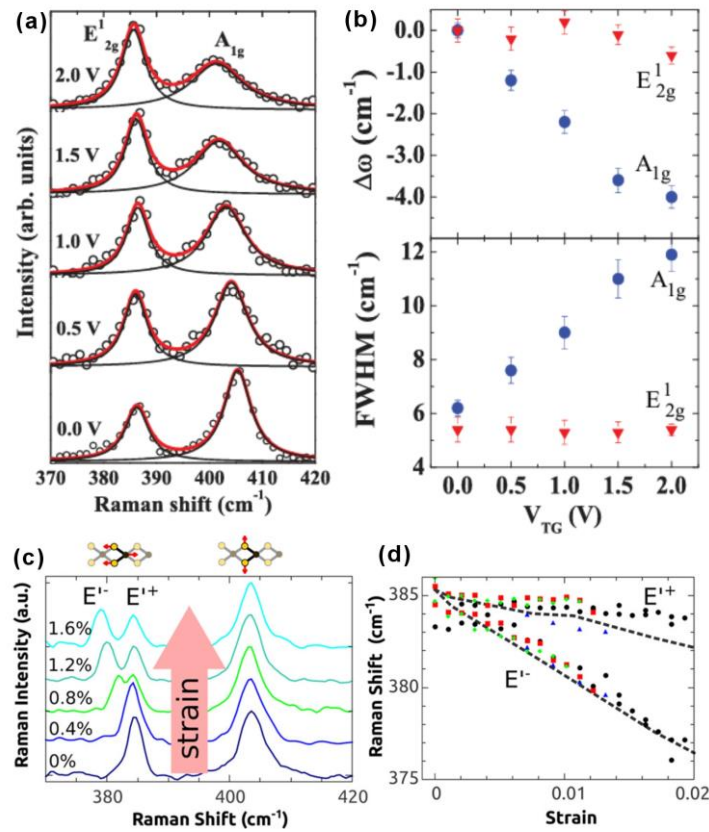
Figure 28 (a) Raman spectra of monolayer MoS$_2$ at different top-gate voltages. Open circles are experimental data points, the gray (red) lines are Lorentzian fits to the total spectrum, and the black lines are the Lorentzian fit to individual peak. Change in the (b) phonon frequency ω and FWHM of A$_{1g}$ and E$^1_{2g}$ modes as a function of top-gate voltages. Raman spectra were recorded with 514 nm laser excitation. Reproduced from ref.[152] with permission from American Physical Society, Copyright 2012. (c) Evolution of the Raman spectrum as a device is strained from 0 to 1.6% measured at a 532 nm laser excitation. (d) The peak location of the *E'$^+$* and *E'$^-$* Raman modes, extracted by fitting the peaks to a Lorentzian, as their degeneracy is broken by straining MoS$_2$. Reproduced from ref.[5d] with permission from American Chemical Society, Copyright 2013.

In addition, it is reported that the E$^1_{2g}$ mode is sensitive to strain and the A$_{1g}$ is

sensitive to doping in MoS_2.[153] Sood *et al.* reported an *in situ* Raman study of a top-gated single-layer MoS_2 transistor. As displayed in **Figure 28a**, the A_{1g} mode showed a strong doping dependence. The phonon frequency decreased by 4 cm^{-1} and the line width broadened by 6 cm^{-1} for a maximum electron doping of 1.8 ×10^{13} cm^{-2}. The phonon frequency of the E^1_{2g} mode decreased by only ~0.6 cm^{-1} and the linewidth of it showed no appreciable change.[152] Bolotin *et al.* investigate the influence of uniaxial tensile strain from 0% to 2.2% on the Raman spectra of monolayer MoS_2 by employing a four point bending apparatus (**Figure 28b**).[5d] With increased strain, the A_{1g} mode showed no measurable shift in position and maintained its intensity, while the degenerate E^1_{2g} peak split into two subpeaks (label as E'^+ and E'^-), as strain breaks the symmetry of the crystal. The E'^- peak shifted by 4.5 ± 0.3 cm^{-1}/% strain, while the E'^+ peak shifts by 1.0 ± 1 cm^{-1}/% strain.
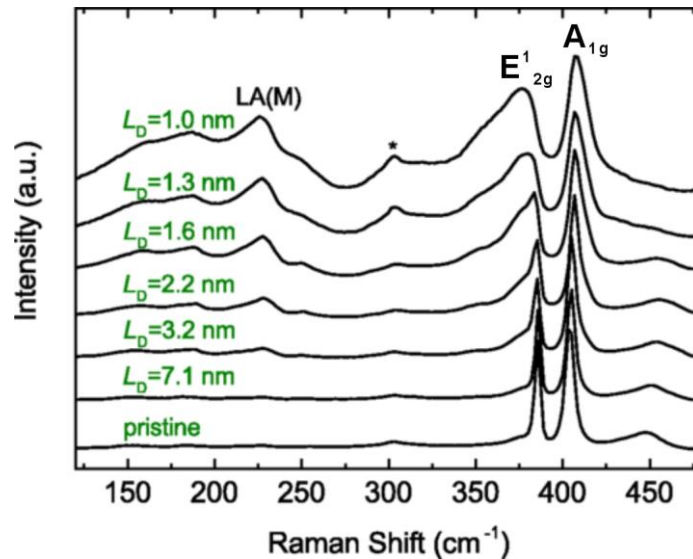
Figure 29 Raman spectra of monolayer MoS_2 with varying defect distances L_D. The spectra were measured at 532 nm excitation and normalized to the intensity of the A_{1g} peak. Reproduced from ref.[154] with permission from American Physical Society, Copyright 2015.

The introduction of structural disorder results in the observation of specific Raman signatures. **Figure 29** shows the development of representative Raman spectra of monolayer MoS_2 flakes, bombarded with Mn$^+$, for an increasing

density of defects.[154] The Raman spectrum gradually evolves as a function of L_D. The E^1_{2g} and A_{1g} Raman modes show changes in both their widths and positions. The E^1_{2g} peak and the A_{1g} peak broaden upon increasing the defect density, which is accompanied by a downshift of the position of the E^1_{2g} peak and an upshift of the position of the A_{1g} peak. Moreover, the introduced disorder activates new Raman modes in the spectral region $\sim$140-420 cm^{-1}. Among these, the most prominent is the LA(M) peak at $\sim$227cm^{-1} and its intensity is found to be proportional to the density of defects.[154] The Raman spectroscopy allows a fast and practical quantification of defects in monolayer MoS_2.

3.1.4 Interfacial Coupling of Graphene/MoS$_2$ Heterostructures
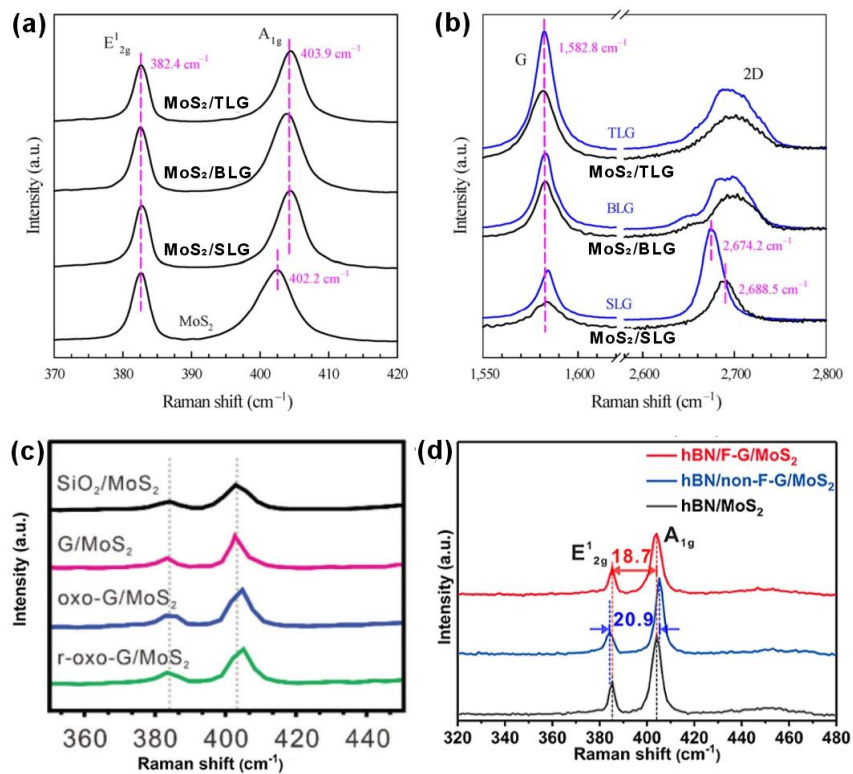
Figure 30 Raman spectra of (a)MoS_2 and (b) graphene in MoS_2/G (1-3 layers) heterostructures. Reproduced from ref.[125] with permission from Springer Nature, Copyright 2021. Raman spectra of MoS_2 in (c) pristine G/MoS_2, oxo-G/MoS_2, r-oxo-G/MoS_2 and (d) oligophenyl-functionalized G/MoS_2 (F-G/MoS_2). The Raman spectra were measured using a 532 nm laser.

The interfacial coupling between neighboring layers of van der Waals heterostructures greatly affects their physical properties and device performance. Owing to the weak van der Waals interlayer coupling of G/MoS_2, it is difficult to directly detect interfacial coupling between neighboring layers of graphene and MoS_2 using scanning electron microscopy or transmission electron microscopy. The effects of interfacial coupling in G/MoS_2 can be determined by the shift of Raman and PL peaks, as well as the changes in the peak intensities. The effects of interfacial charge transfer on MoS_2 PL spectra are discussed in *Section 2.6.5*. As the A_{1g} modes of $MoS_2$ are sensitive to carrier transfers (discussed in *Section 3.1.3*),[153] the shift of A_{1g} modes in G/MoS_2 heterostructures is normally detected owing to the interlayer charge transfer. **Figure 30a** displays the Raman spectra of MoS_2/G heterostructures prepared by transferring 1–3 layers of graphene onto monolayer MoS_2. A upshift of A_{1g} mode from 402.2 cm^{-1} (pristine MoS_2) to 403.9 cm^{-1} is observed for all the Raman spectra of MoS_2/G heterostructures but there is no apparent shift exhibited in all of the E^1_{2g} modes.[125] **Figure 30b** shows the G mode and 2D mode of pristine 1-3 layers graphene and corresponding graphene in MoS_2/G heterostructures. There is a upshift by about 15 cm^{-1} observed for 2D mode in MoS_2/monolayer graphene (MoS_2/SLG), but no noticeable shift for G mode. However, for multilayer graphene heterostructures, there is no changes for G mode and 2D mode. This means the 2D bands in multilayer graphene were less sensitive to the interfacial coupling due to their band structures different from SLG.[125] As depicted in **Figure 30c**, when MoS_2 is stacked on graphene (G/MoS_2), the A_{1g} frequency of MoS_2 shifts downward by ~2 cm^{-1} with increasing electron density generated by charge transfer from MoS_2 to graphene, which exhibits the opposite shift direction to that of the MoS_2/G heterostructure shown in **Figure 30a**. The Raman shift for functionalized G/MoS_2 heterostructures are also investigated. There is an upshift of A_{1g}

frequency of MoS_2 in oxo-G/MoS_2 and r-oxo-G/MoS_2 owing to the electron-withdrawing groups in oxo-G and the defects in r-oxo-G. The E^1_{2g} mode of MoS_2 is more related to the external strains or lattice distortions.[155] For the Raman spectrum of oligophenyl-functionalized G/MoS_2, there is a slight downshift of E^1_{2g} due to strain generated by the large oligophenyl-groups, resulting in decreased distance between E^1_{2g} mode to A_{1g} by 2.2 cm^{-1} (**Figure 30d**). As discussed above, the changes in Raman spectra can provide information of interlayer coupling. However, there are still debates regarding the shift of Raman modes and exciton peaks in G/MoS_2 due to the numerous possibilities in creating van der Waals heterostructures with varying thickness, stacking sequence, and interface engineering.[125, 156]

3.2 Atomic Force Microscopy

Atomic force microscopy (AFM) is an influential surface analysis technique to probe surfaces and gain information about the surface morphology, surface roughness, and thickness etc. The key component of AFM is a microscopic cantilever with a sharp probe on its head that scans the surface of the sample. This cantilever is tens to hundreds of microns in size and the radius of curvature of the tip of the probe is on the nanometer scale. The lateral resolution of the AFM image can be as small as the tip radius (typically 5-15 nm), and the vertical resolution can be on the order of angstroms. The vertical resolution is typically better than 1 nm. When the probe is placed near the sample surface, the probe head on the cantilever will bend and deflect according to Hooke's law due to the force on the sample surface. Under different circumstances, the force measured by AFM may be mechanical contact force, van der Waals force, hair attraction force, chemical bond, orientation force, electrostatic force, magnetic force, Casimir effect force, solvent force, etc. Typically, deflection is measured by reflecting a laser beam on a microcantilever to a photodiode array. Thin cantilever surfaces are often coated with a reflective material (such as

aluminum) to enhance its reflection. Other methods include optical interference, capacitance and piezoelectric effect methods. These probes are usually made from deformation gauges that use the piezoelectric effect. Through the Wheatstone bridge, the deformation of the probe can be measured, but this method is not as sensitive as the laser reflection method or the interference method.
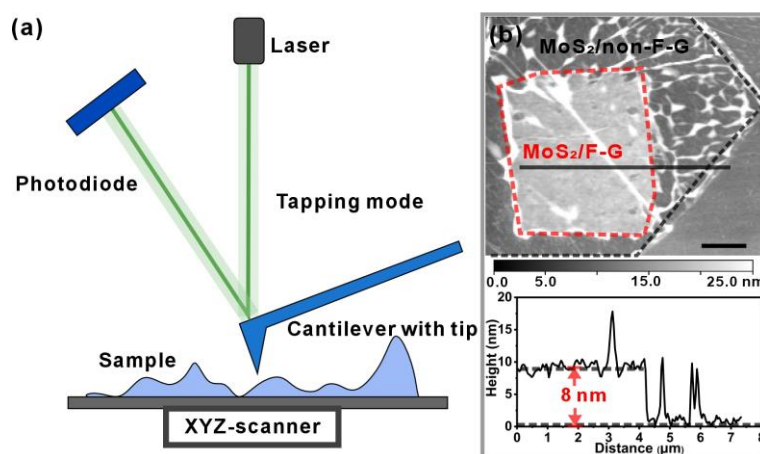
Figure 31 (a) AFM measurement with tapping mode. (b) AFM image of functionalized G/MoS$_2$ heterostructure.

AFM can operate in different modes. These modes can be divided into static mode (also called contact mode), or a series of other dynamic modes (such as non-contact mode, tapping mode, lateral force mode). Among those modes, tapping mode (also called AC mode) has become the most widely used AFM working mode today because it effectively avoids lateral friction and reduces the abrasion of probe and samples. In tapping mode, the cantilever vibrates up and down through tiny piezoelectric elements loaded on the probe (**Figure 31a**). The frequency is near its resonance frequency, but the amplitude is much larger than 10 nm, probably between 100 and 200 nm. As the probe gets closer to the sample surface, the van der Waals force, dipole-dipole interaction and electrostatic force between the probe and the sample surface will cause the amplitude to become smaller and smaller. The electronic automatic servo controls the distance between the cantilever and the probe through a

piezoelectric actuator. When the cantilever scans the sample surface, the servo machine adjusts the distance between the probe and the sample to maintain the preset amplitude of the cantilever, while the imaging interaction force obtains the AFM tapping mode image. For a single layer of exfoliated graphene, the average thickness varies from 0.4 nm to 0.9 nm.[157] In comparison, the thickness of chemically derived graphene (such as GO) is approximately 0.8-1.2 nm due to the presence of oxo-functional groups on the carbon plane. **Figure 31b** exhibits a height difference of 8 nm of oligophenyl-functionalized G/MoS$_2$ heterostructure to the pristine G/MoS$_2$.

3.3 Scanning Near-field Optical Microscopy
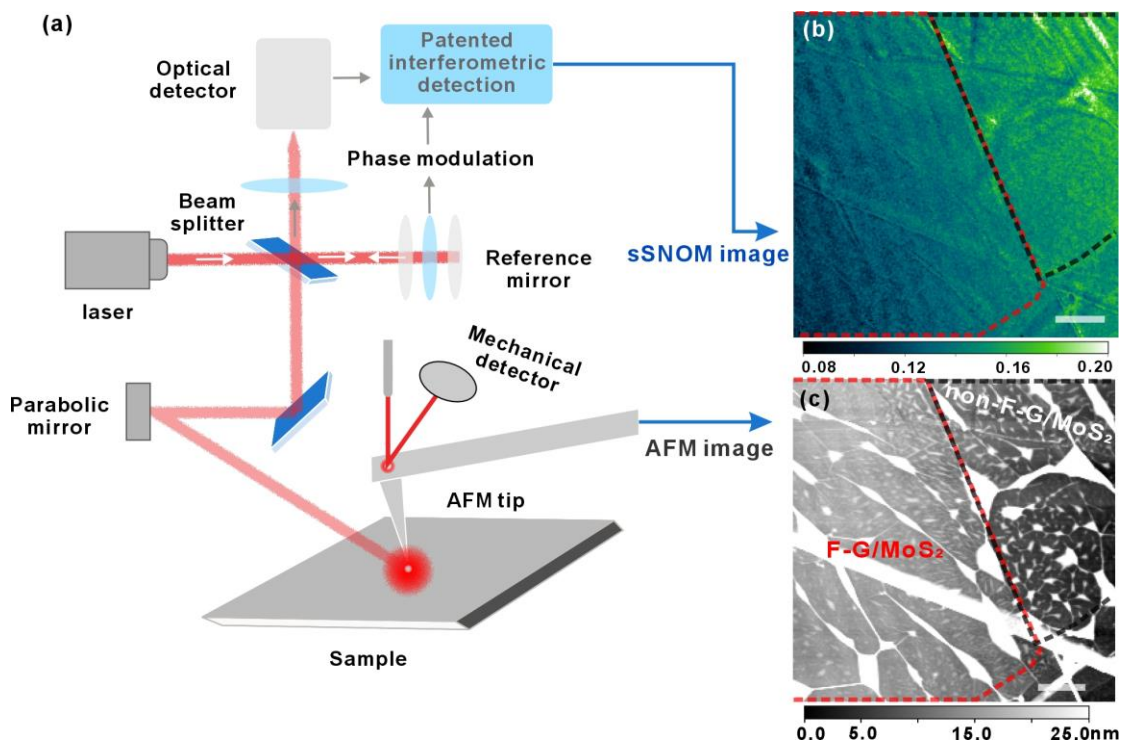
Figure 32 (a) Schematic illustration of SNOM measurement. (b) S-SNOM images together with (c) AFM topography of oligophenyl-functionalized G/MoS$_2$ heterostructure. The scale bars in (a–f) are 5 μm.

Optical spectroscopy offers great versatility, but typically has diffraction-limited spatial resolution. However, when it is combined with localized optical excitation or detection with a scanning probe tip, the diffraction limit (about 300 nm) can be exceeded. Scanning near-field optical microscopy (SNOM) utilizes a

standard metal-coated AFM probe and illuminates it with laser light. As shown in **Figure 32**, the illuminated probe forms a nanoscale focus at its tip, serving as a very small light source, and is then employed to locally scan the sample. Optical imaging is achieved by recording the scattered light formed by the probe during the sample surface scan. The probe tip of an AFM serves as a scattering source to enhance the localized electric field between the tip and the sample. Topography, near-field light field intensity, and phase images can be simultaneously recorded at multiple wavelengths through technologies such as heterodyne interference, probe modulation, and optical path design. This technology can be used to detect the optical properties of nanomaterials and changes in electromagnetic fields caused by nanostructures with nanometer-scale, which makes a significant contribution to the studies of 2D materials. As indicated in **Figure 32b-c**, the identified features (such as wrinkles and bubbles) in AFM image can be identified in the s-SNOM images. Despite the influence of wrinkles and bubbles on the s-SNOM images, there is a distinct and uniform contrast from the oligophenyl-functionalized G/MoS$_2$ (F-G/MoS$_2$) to pristine G/MoS$_2$ (non-F-G/MoS$_2$) heterostructures. The functionalization leads to doping and thus to an increase in the dielectric function.

3.4 Kelvin Probe Force Microscopy
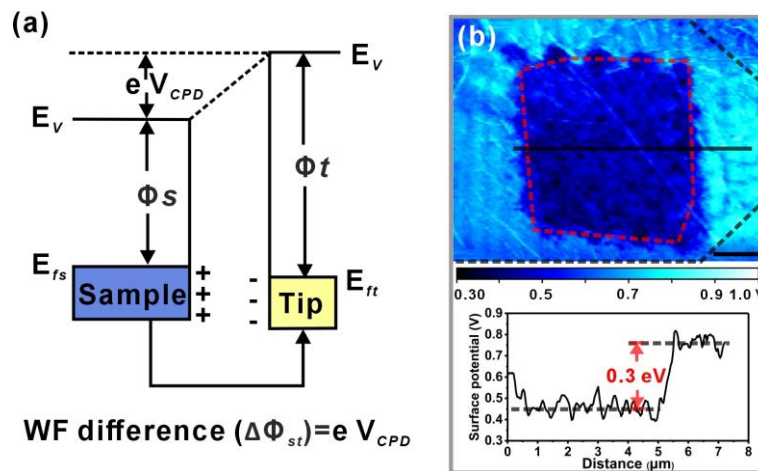
Figure 33 (a) Energy level diagram of two materials with different work function

representing the tip Φ_t and sample Φ_s. (b) KPFM image of functionalized G/MoS$_2$ heterostructure.

Kelvin probe force microscopy (KPFM) is a surface-sensitive technique based on AFM. Its operating principle involves using a non-contact probe for vibrational scanning over the surface of a sample. When the probe approaches regions with charge distribution or potential differences, electrostatic interactions cause changes in the probe's vibrational frequency. The KPFM system can infer the potential distribution on the sample surface, generating high-resolution surface potential images. The work function (WF) of the samples (Φ_{sample}) is defined by the following formula: $\Phi_{sample} = e\ V_{CPD} + \Phi_{tip}$, where V_{CPD} is the contact potential difference measured by the KPFM, Φ_{tip} is the work function of the tip, and e is the elementary charge (**Figure 33a**). **Figure 33b** shows a surface potential increase of 0.3 eV of G/MoS$_2$ heterostructure after surface functionalization. The potential profile is measured by maintaining a constant distance of 50 nm between the tip and the sample surface. The KPFM is widely applicable in studying the electrical properties of materials, nano-electronic devices, and biological samples, providing a powerful tool for revealing charge distribution, surface charge states, and charge transport, among other phenomena.

3.5 Langmuir-Blodgett Technique

The Langmuir-Blodgett (LB) technique is a process that deposits molecular layers from a liquid surface onto a solid substrate at the air-water interface. This technique enables the self-assembly of highly ordered films, and is named after the two inventors, Irvine Langmuir and Katharine Burr Blodgett. Due to the amphiphilic nature and surface chemistry of oxo-G, it can be deposited onto a solid substrate in a controlled way by LB technique. To use this technique, the substrate is fully immersed in a water-filled sink, and then the oxo-G dispersion is deposited onto the water surface (**Figure 34a**). The compression of the

barrier at the edges of the trough reduces the distance between surface oxo-G, which changes the surface tension of water and creates a dense floating film. The condition of the assembled film can be controlled by parameters such as surface pressure and the pH value of the solution. By slowly lifting the surface under a surface pressure ranging from 3-6 mN m^{-1}, nearly closed arrays of oxo-G films are formed, which can be used as supporting layers for heterostructure assembling with other 2D materials. **Figure 34b** shows an optical image of deposited oxo-G flakes on a Si/SiO$_2$ wafer by LB process.
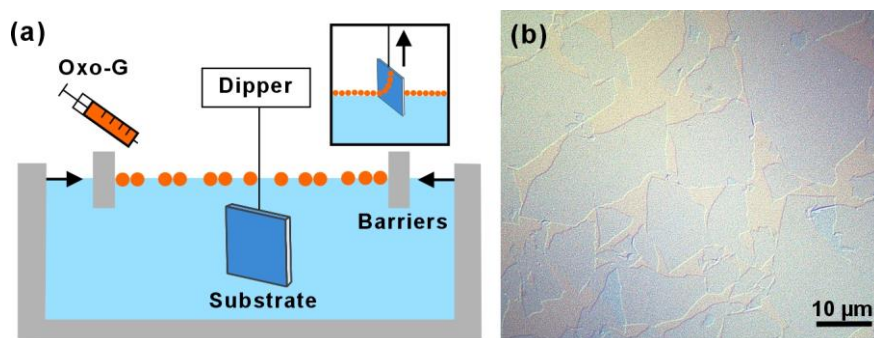
Figure 34 (a) Schematic illustration of LB device. The inset shows the deposition process after compression proceeded in a simplified way. (b) Optical image of deposited oxo-G flakes on a Si/SiO$_2$ wafer by LB process.

3.6 Transfer Technique for Assembling Graphene-based/MoS$_2$

In this thesis, a dry transfer system is used for the precise alignment and stacking of a polydimethylsiloxane (PDMS) stamp with target materials onto a substrate. The dry transfer method using a PDMS stamp was first reported by Rogers *et al.* in 2005. As depicted in **Figure 35a**, the integrated system comprises an optical microscope equipped with a series of objectives (5x, 10x, 20x, and 100x), a mechanical stage with high resolution micromanipulators and a heater. The transfer stage is capable of movement along the X, Y, and Z directions, facilitating the accurate alignment of flakes during the construction of 2D-based heterostructures. Different heterostructures have been fabricated, such as oxo-G/MoS$_2$, r-oxo-G/MoS$_2$, G/MoS$_2$, porous G/MoS$_2$, h-BN/G/MoS$_2$,

h-BN/F-G/MoS$_2$, and MoS$_2$/F-G. Here, the transfer process of G/MoS$_2$ is explained as an example.
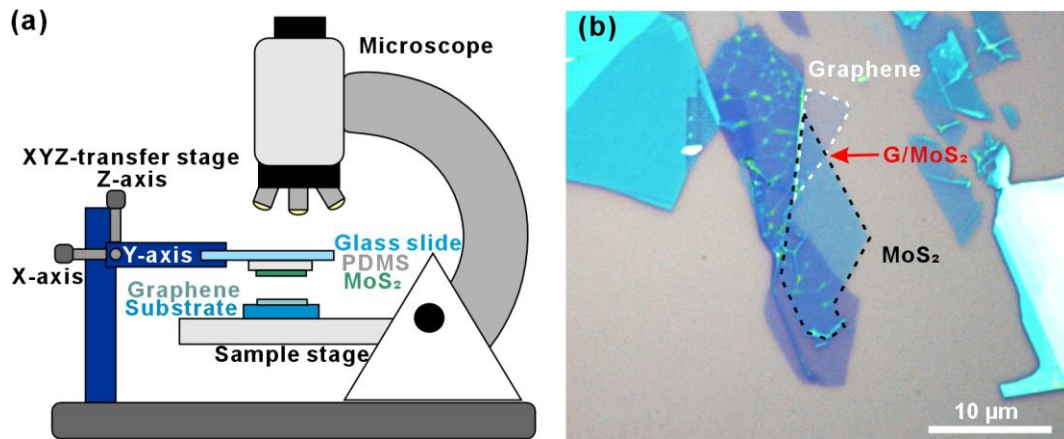
Figure 35 (a) Setup of the 2D-dry transfer system. (b) Optical microscope image of the G/MoS$_2$ heterostructure.

Firstly, the graphene G flake is mechanically exfoliated on one side of a thin polydimethylsiloxane (PDMS, X4, Gelpak) film. The other free side of the PDMS was stacked onto a thick PDMS layer on a glass slide, which is called transfer slide. The transfer slide is holed above the fixed Si/SiO$_2$ substrate and slowly approaches until contact. The stacked wafer and the glass slide are heated at 50 °C for around 5 minutes. Afterwards, the transfer slide is slowly lifted up until it is away from the wafer. The same process is used for transferring the second layer. The transfer slide with a monolayer of MoS$_2$ is assembled on top of the pre-transferred graphene. The positions of the MoS$_2$ onto the graphene flake are corrected repeatedly under the optical microscope to make sure the two flakes overlap. By screwing the Z-axis of the transfer stage, the glass slide contacts the graphene flake. After heating at 50 °C for 5 minutes, the PDMS is picked up with the glass slide and the MoS$_2$ deposits to form G/MoS$_2$ heterostructure on the wafer. The heterostructure is annealed at 100-200 °C in a vacuum for 2 hours to remove impurities from the transfer process. **Figure 35b** shows an optical microscope image of the G/MoS$_2$ heterostructure fabricated by dry transfer in air.

Direct transfer of 2D heterojunctions onto a substrate often leads to unstable materials that are highly susceptible to be washed off from the substrate during solvent treatment, such as isopropanol cleaning and subsequent liquid-phase functionalization. Therefore, in heterostructure or nano-device fabrication, few-layered h-BN is utilized as a substrate to effectively shield transferred 2D materials from environmental influences. h-BN exhibits chemical inertness and no dangling bonds or surface charge traps due to the strong in-plane ionic bonding within its planar hexagonal lattice structure. It was reported that the atomically planar surface of h-BN serves as a flat and stable substrate to suppress graphene corrugation.[158] As a result, h-BN is preferred over commonly used substrates like SiO_2, which can overcome various limitations such as substrate surface roughness, charge traps, surface optical phonons, and inhomogeneity.[158a, 159] In addition, h-BN, as an insulator with a band gap of 5.97 eV[160] and a minimum lattice mismatch of 1.7% with graphite,[161] can preserve the energy band structure of graphene near the Dirac point, which significantly enhances the mobility of graphene devices.[15a, 123, 159a, 162]

4 Synopsis of Results

For most MoS_2 monolayers, intrinsic structural defects, such as sulfur vacancies, can cause unsaturated electrons in the surrounding Mo atoms and act as electron donors, which make the MoS_2 n-doped. However, the existence of defective states acting as nonradiative traps deteriorates the PL efficiency.[163] Thus far, several strategies, including electrical gating,[164] chemical doping,[112] defect engineering,[117, 165] covalent functionalization,[117] and plasma treatment,[166] have been exploited to modulate the PL emissions of monolayer MoS_2. However, these approaches either require complicated methods, are sensitive to chemical contamination, or cause structural damage to the structure.

Stacking MoS$_2$ layers onto different 2D materials, such as h-BN, graphene, or other TMDCs, have inspired new approaches for modulating the PL performance.[167] As discussed in *Section 2.6.2*, semi-metallic graphene has a highly symmetric band structure and an adjustable Dirac point lying within the bandgap of MoS$_2$, making it an ideal electron–hole acceptor. Unfortunately, PL quenching occurs in G/MoS$_2$ heterostructures as a result of charge transfer from graphene to MoS$_2$. The carrier densities of both counterparts and the band alignment in the heterostructures determine the PL properties.

In this thesis, different G-based/MoS$_2$ heterostructures are fabricated to modulate the PL properties of MoS$_2$. The research focus is the effect of heterointerface on the PL properties of MoS$_2$. Factors including the functional groups and defects of graphene, the interlayer charge transfer, and the interlayer distance are investigated. There are three publications covering these topics showing in this section. For the publication in *section 4.1.1*, I have a major contribution (50%). I prepared all the samples used in the manuscript, did the Raman and PL measurement, and participated in writing of the manuscript. For the publications in *section 4.1.2*, my contribution is minor (15%). I used the porous graphene prepared by Yiqing Wang to assemble the porous-graphene/MoS$_2$ heterostructures and did the PL measurements. For the publication in *section 4.2*, I have a major contribution (80%). I participated the generation of the concept, prepared all the samples used in the manuscript, did the characterization (except for SNOM), and wrote the manuscript. The detailed contributions are displayed in *Section 5.1, 5.2* and *6.1*. In *Section 4.1.1*, interlayer electron modulation in van der Waals heterostructures assembled by stacking monolayer MoS$_2$ onto oxo-G/MoS$_2$, r-oxo-G/MoS$_2$ and pristine graphene are studied. It was confirmed that the functional-groups of oxo-G and the defects on r-oxo-G withdrew electrons from MoS$_2$, which facilitated the switch from trion to neutral exciton recombination and thus significantly

increase the PL intensity of MoS$_2$. In *Section 4.1.2*, porous graphene prepared by wet-chemical method using oxo-G as a starting material were assembled with monolayer MoS$_2$. It was found that porous graphene as a novel highly temperature-stable electron-accepting 2D material enhanced the PL of MoS$_2$ by 10-times. In *Section 4.2*, the regioselective oligophenyl-functionalized graphene were prepared by the laser-induced radical reaction to investigate the G/MoS$_2$ interface with only one specific functional-group. It was found that the oligophenyl-groups not only have a p-doping effect on MoS$_2$ but also largely prevent electron donation from the graphene basal plane with an enlarged interlayer distance of 8 nm. The detailed results are discussed in *Section 4.1* and *4.2*.

4.1 Interfacial Modulation of MoS$_2$ with Oxo-functionalized Graphene and Its Derivatives

4.1.1 Oxo-functionalized graphene/MoS$_2$ and Reduced Oxo-functionalized Graphene/MoS$_2$ Heterostructures

Z. Wang,[1] Q. Cao,[1] K. Sotthewes, Y. Hu, H. Shin, and S. Eigler Interlayer electron modulation in van der Waals heterostructures assembled by stacking monolayer MoS$_2$ onto monolayer graphene with different electron transfer ability *Nanoscale*, **2021**,*13*, 15464-15470 [1]Z. Wang and Q. Cao contribute equally to this work.	5.1

As explained in *Section 2.2.3*, oxo-G is a graphene derivative decorated with oxygen species on the edges and the plane. Electron-withdrawing groups, such as hydroxyl, epoxy, and organosulfates, make oxo-G an electron acceptor, resulting a p-doping of material.[168] Therefore, oxo-G can work as an electron extraction layer for tuning the carrier concentration of MoS$_2$. The r-oxo-G prepared by removing oxygen groups through chemical reduction results in the recovery of *sp^2*-hybridized graphene domains with a lateral size of up to 10

nm.[60] However, few residual oxo-groups, such as electron-withdrawing carbonyl groups, remain firmly attached at the edges and defect sites.[57, 60] It is important to note that during the reduction process of oxo-G, various in-plane defects such as vacancies, holes, and non-six-membered carbon rings with sp^3 hybridization are formed.[57] These defects act as structural motifs or active sites, and significantly impact the electronic and surface properties of r-oxo-G.[61]
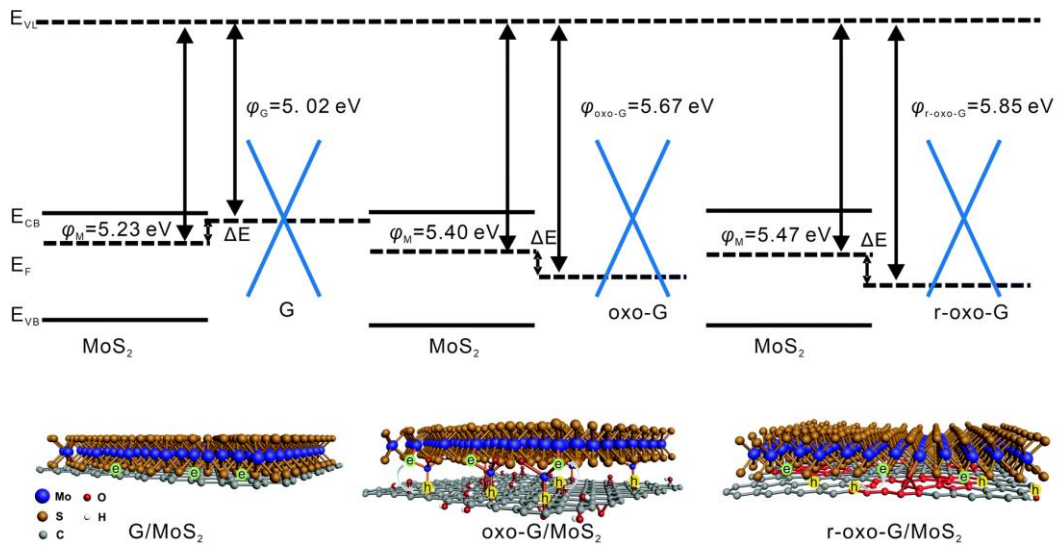
Figure 36 Energy-level diagrams of MoS$_2$ on the pristine graphene, oxo-G, and r-oxo-G layers, and interfacial interaction mechanism in the three heterostructures.

To investigated the effect of oxo-functional groups and defects on the interfacial properties, monolayer MoS2 were stacked on oxo-G and r-oxo-G, and compared with mechanically exfoliated graphene. Raman and PL spectroscopy combined with KPFM measurements were carried out to study the optoelectronic properties and mechanism of interface interaction. The work function (WF) of the three heterostructures were measured by KPFM. As displayed in **Figure 36**, oxo-G (a high amount of oxygen of 60%) with a WF of 5.67 eV and its lowly oxidized reduction product (r-oxo-G, a defect density of 0.1%), with a WF of 5.85 eV act as electron extraction layers by withdrawing electrons from MoS2, which facilitate the switch from trion to exciton recombination and thus significantly increase the PL intensity of MoS2.

Conversely, pristine graphene with a WF of 5.02 eV results in PL quenching of MoS_2. The p-doping to MoS_2 leads to the increased WF of oxo-G/MoS_2 (5.40 eV) and r-oxo-G/MoS_2 (5.47 eV) heterostructures. In addition, r-oxo-G/MoS_2 exhibits a higher increase (5-fold) in PL than oxo-G/MoS_2 (3-fold) owing to the defects with effective electron-accepting abilities on r-oxo-G. Our research provides a controllable approach to tune the optoelectronic properties of atomically thin TMDCs, which have promising applications in optoelectronic devices.

4.1.2 Porous-graphene/MoS_2

Y. Wang, C. Neumann, M. Hußmann, Q. Cao, Y. Hu, O. Garrity, P. Kusch, A. Turchanin, and S. Eigler Synthesis of wet-chemically prepared porous-graphene single layers on Si/SiO_2 substrate increasing the photoluminescence of MoS_2 in heterostructures *Adv. Mater. Interfaces* **2021**, *8*, 2100783	6.1

Section 4.1.1 has shown that defects in r-oxo-G can affect the electron transfer between graphene and MoS_2 and thus enhance the PL of MoS_2. In this chapter, porous-graphene with large lattice defects was prepared by Y. Wang. I prepared the porous-graphene/MoS_2 heterostructure to investigate the interfacial charge transfer and PL performance.

Wet-chemical generation of pores in graphene is a challenging synthetic task. GO was used as a precursor for etching pores.[169] However, due to the excessive lattice defect sites existing in GO, which are the origin of the etched pores, the produced pores are not uniform in size and are limited to a few nanometers. Thus, the formation of larger pores is not possible since flakes start to disintegrate.[170] Oxo-G with a low density of initial vacancy defects (0.8%, as determined by Raman spectroscopy) was used as a precursor to etch pores assisted by a Mn-species at 400 °C in Ar atmosphere. By controlling the

reaction conditions, it is possible to gain a certain control over the formation of pores with diameters between 100–200 nm in majority. The porous-graphene (Pr-oxo-G) are highly temperature stable since they are synthesized at 400 °C.
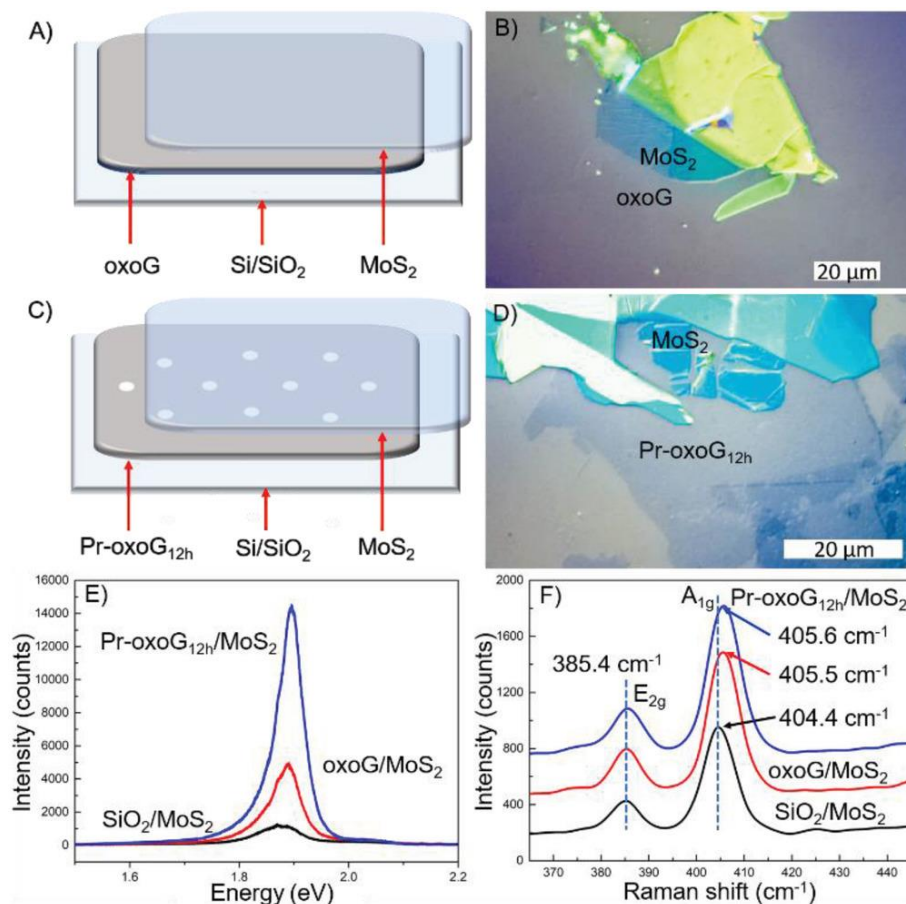
Figure 37 a) Illustration and b) optical microscopy image of the oxoG/MoS$_2$ heterostructure. c) Illustration and (d) optical microscopy image of the realized Pr-oxoG$_{12h}$/MoS$_2$ heterostructure. e) PL spectra and (f) Raman spectra of monolayer MoS$_2$ on SiO$_2$, oxoG/MoS$_2$, and Pr-oxoG$_{12h}$/MoS$_2$.

The as-prepared porous graphene has good stability and no wrinkles, which was further used as a bottom material to prepare heterostructures with MoS$_2$. The PL of MoS$_2$ on SiO$_2$, oxo-G, Pr-oxo-G$_{6h}$ (etching time of 6 h), and Pr-oxo-G$_{12h}$ (etching time of 12 h) were studied. As shown in **Figure 37**, the amplitudes of the PL are increased for oxo-G/MoS$_2$ (4 times), Pr-oxo-G$_{6h}$/MoS$_2$ (3 times), and Pr-oxo-G$_{12h}$/MoS$_2$ (10 times), compared to the PL of the pristine MoS$_2$ monolayer. Overall, the highest PL enhancement is achieved by using Pr-oxo-G$_{12h}$. The Raman spectroscopy detects that the A$_{1g}$ mode of MoS$_2$ is blue-

shifted from 404.4 cm^{-1} to 405.6 cm^{-1} for MoS$_2$ on Pr-oxo-G$_{12h}$, which indicates the p-doping of MoS$_2$. Moreover, Pr-oxo-G$_{12h}$ reflects a p-doped material, as indicated by Raman shifts of the G and 2D peaks. Furthermore, the Pr-oxo-G$_{6h}$/MoS$_2$ showed slightly lower PL intensity than oxo-G/MoS$_2$. It is supposed that the Mn-impurities limit the increase of the PL of MoS$_2$ in the Pr-oxo-G$_{6h}$/MoS$_2$ heterostructure, and the interaction of Mn-species with carbonyl groups may be responsible.

4.2 Interfacial Modulation of Laser-induced Functionalized Graphene/MoS$_2$ Heterostructures

Oligophenyl-functionalized Graphene/MoS$_2$

Q. Cao, M. Kreßler, M. Hußmann, Y. Hu, P. Kusch, and S. Eigler Photoluminescence modulation of graphene/MoS$_2$ heterostructures separated by laser-induced functionalization *Chem. Mat.*, **2024**, *36*, 3267-3276	5.2

As discussed in *section 4.1*, derivatives of graphene, such as GO, oxo-G, r-oxo-G, and porous graphene, have been used to enhance the PL intensity of 1L-MoS$_2$. However, the binding of covalent additives without controllability of the precise binding positions. To achieve regioselective functionalization with defined structures is of great significance for the further development of covalent modification of graphene and the interfaces construction of G/MoS$_2$ heterostructures. In addition, 2D materials are not only sensitive to charge-transfer doping but also susceptible to interlayer interactions as they are atomically thin.[133, 136, 143]

Monotopic oligophenyl-functionalized graphene was prepared by a laser-induced reaction between mechanically exfoliated graphene and photosensitizer BPO. The functionalization of graphene is regioselective with the assistance of the mapping function of the scanning Raman instrument. The
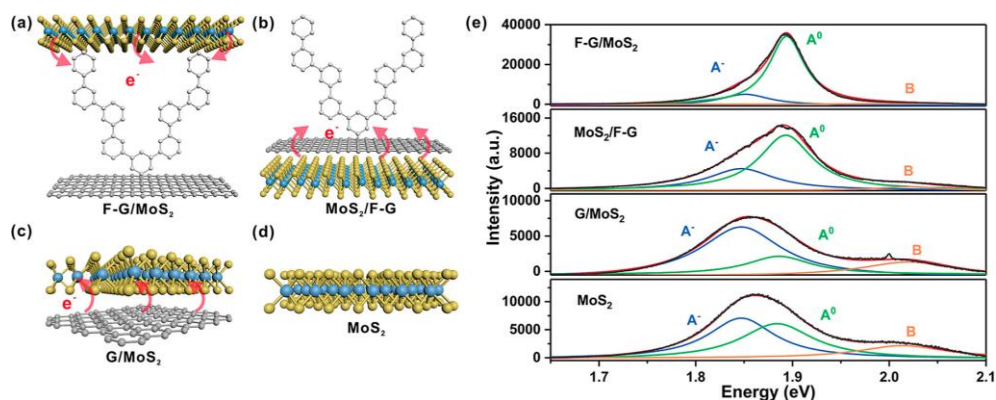
Figure 38 Sketch illustrating the interfacial interaction mechanism in the four heterostructures: (a) F-G/MoS$_2$, (b) MoS$_2$/F-G, (c) G/MoS$_2$, and (d) MoS$_2$. (e) Peak fittings using Lorentz functions for the four structures.

areas that were irradiated by laser were functionalized (F-G), while the non-irradiated areas remained as pristine structures of graphene (non-F-G). The oligophenyl-functionalized graphene was stacked with MoS$_2$ on top to form a heterostructure ((non-)F-G/MoS$_2$). Through Raman, PL, s-SNOM, and KPFM, the boundaries and the distinct characteristics of the F-G and the non-F-G were identified on the heterostructure. In (non-)F-G/MoS$_2$, the functionalized area of graphene (F-G/MoS$_2$) exhibits a 5-fold enhancement in the PL intensity of MoS$_2$ compared to the non-functionalized area of graphene. As depicted in **Figure 38**, more importantly, the layer stacking sequence of F-G and 1L-MoS$_2$ brings different interface structures in perpendicular orientation, resulting in a significant difference in the PL enhancement. The reverse stacked MoS$_2$/F-G heterostructure was fabricated by *in situ* functionalizing MoS$_2$/G/BPO through photochemical reaction and only shows a 1.8 times PL increase compared to pristine G/MoS$_2$. Accordingly, the results indicate that the oligophenyl-groups in F-G/MoS$_2$ not only have a p-doping effect on MoS$_2$ but also largely prevent electron donation from the graphene basal plane with an enlarged interlayer distance of 8 nm. Consequently, the PL enhancement was restored with the thermal de-functionalization of F-G. Thus, we conclude that the functional groups can be considered as separate molecular components with the vertical arrangement in the functionalized heterostructure system.

5 Publications - Major Contributions

5.1 Interlayer Electron Modulation in van der Waals Heterostructures Assembled by Stacking Monolayer MoS$_2$ onto Monolayer Graphene with Different Electron Transfer Ability

Authors	Zhenping Wang,[1] Qing Cao,[1] Kai Sotthewes, Yalei Hu, Hyeon S. Shin, and Siegfried Eigler
Journal	*Nanoscale*, **2021**,*13*, 15464-15470
DOI	10.1039/D1NR03708K
Links	https://doi.org/10.1039/D1NR03708K
Detailed scientific contribution	The concept of this manuscript was elaborated by Z. Wang and Prof. Dr. S. Eigler. The heterostructures shown in the manuscript were prepared by Q. Cao and Y. Hu. The Raman and PL measurements were done by Q. Cao. K. Sotthewes, Prof Dr. H. Shin and Prof. Dr. S. Eigler provided help and suggestions on projects. The manuscript was mainly written by Z. Wang and Q. Cao. [1]Z. Wang and Q. Cao contribute equally to this work.
Estimated own contribution	~50%

5.2 Photoluminescence Modulation of Graphene/MoS$_2$ Heterostructures Separated by Laser-induced Functionalization

Authors	Qing Cao, Mira Kreßler, Marleen Hußmann, Yalei Hu, Patryk Kusch, and Siegfried Eigler
Journal	*Chem. Mater.* **2024**,*36*, 3267−3276
DOI	10.1021/acs.chemmater.3c03166
Links	https://doi.org/10.1021/acs.chemmater.3c03166
Detailed scientific contribution	The concept of this manuscript was elaborated by Q. Cao and Prof. Dr. S. Eigler. All samples used in the manuscript were prepared by Q. Cao. The Raman and PL measurements were performed by Q. Cao. M. Kreßler and P. Kusch performed the KPFM and s-SNOM measurement. M. Hußmann and Y. Hu provided help and suggestions on projects. Prof. Dr. S. Eigler. supervised the project. All authors discussed the results and commented on the manuscript. The manuscript was mainly written by Q. Cao and Prof. Dr. S. Eigler.
Estimated own contribution	~80%

Article

Photoluminescence Modulation of Graphene/MoS$_2$ Heterostructures Separated by Laser-Induced Functionalization

Qing Cao, Mira Kreßler, Marleen Hußmann, Yalei Hu, Patryk Kusch, and Siegfried Eigler*

Read Online

ACCESS | Metrics & More | Article Recommendations | Supporting Information

ABSTRACT: Tuning the optoelectronic properties of monolayer MoS$_2$ (1L-MoS$_2$) is highly desired for optoelectronic applications. Gaining profound insights into the fundamental mechanisms that govern optoelectronic properties is of utmost significance. Here, we demonstrate that the photoluminescence (PL) of 1L-MoS$_2$ can be modulated by photochemically functionalized graphene (F-G), which is covalently modified by oligophenyl groups. More importantly, the layer stacking sequence of F-G and 1L-MoS$_2$ brings different interface structures, resulting in a significant difference in the PL enhancement. MoS$_2$ supported by F-G (F-G/MoS$_2$) has a 5-fold PL enhancement, while it only shows a 1.8-fold PL enhancement if stacked underneath F-G (MoS$_2$/F-G). Accordingly, the results indicate that the oligophenyl groups in F-G/MoS$_2$ not only have a p-doping effect on MoS$_2$ but also largely prevent electron donation from the graphene basal plane with an enlarged interlayer distance of 8 nm. Consequently, the PL enhancement is lost with the thermal defunctionalization of F-G. Thus, we conclude that the functional groups can be considered as separate molecular components with the vertical arrangement in the functionalized heterostructure system. The photoactive graphene acts as a template for perpendicular molecular alignment in the heterointerface construction. The F-G/MoS$_2$ heterostructures bring new perspectives to the design and investigation of optoelectronic devices.
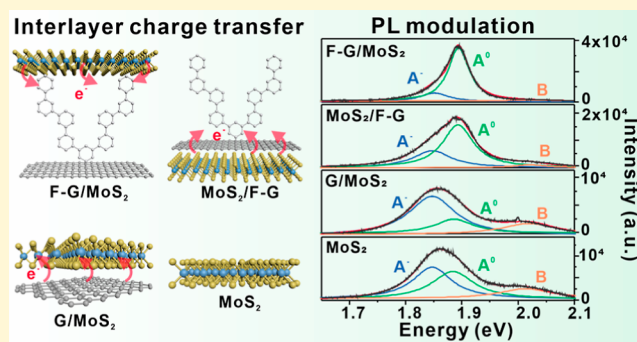
Two-dimensional transition-metal dichalcogenides (2DTMDs) monolayers have attracted massive research attention over the past decade due to their unique electronic, optical, and mechanical properties, which remarkably differ from the properties of their respective bulk materials.[1−3] As a prototypical 2DTMD, monolayer molybdenum disulfide (1L-MoS$_2$) transforms from an indirect band gap (1.2 eV) semiconductor in its bulk form to a direct band gap (1.8 eV) semiconductor, owing to which photoluminescence (PL) emerges in 1L-MoS$_2$ with sensitive photo response.[4,5] Optically generated electron−hole pairs in 1L-MoS$_2$ form stable excitonic states due to large Coulomb interactions in atomically thin layers.[6] Many-body bound states, such as charged exciton (trion), can be formed through the interplay between an exciton and a charge carrier by tuning the electron densities in 1L-MoS$_2$, thereby enabling variable PL properties to meet different optoelectronic applications, such as photodetectors, photovoltaics, sensors, and light emitters.[7] Various approaches, including electrical gating,[8] chemical doping,[6] defect engineering,[9] covalent functionalization,[10,11] and plasma treatment,[12] have been employed to realize the PL enhancement or quenching of 1L-MoS$_2$. Nevertheless, these approaches either require complicated methods, are sensitive to chemical contamination, or cause structural damage to the structure.[9]

Stacking of 1L-MoS$_2$ with different 2D materials, such as graphene, hBN, or other TMDs by van der Waals forces, also makes the excitonic states of MoS$_2$ adjustable through quantum coupling.[13,14] Among which, graphene is a semimetal composed of sp^2-hybridized carbon atoms in a honeycomb lattice array, exhibiting outstanding properties such as high carrier mobility up to 10^5 cm^2 V$^{−1}$ s$^{−1}$ at room temperature, quantum electronic transport, high optical transparency (∼97.7%), and large tunability of the Fermi level.[15−17] These superiorities make it an ideal heterogeneous layer to change the excitonic states in MoS$_2$ via interlayer charge transfer. It is reported that the PL of 1L-MoS$_2$ becomes quenched when stacked with pristine graphene.[18,19] Due to the Schottky barrier at the interface, the photogenerated holes are injected from the valence band of MoS$_2$ to graphene, while the photogenerated electrons in the conductance band of MoS$_2$ are not allowed to diffuse to graphene.[19,20] Derivatives of graphene, such as
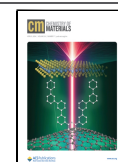
Scheme 1. Schematic Illustration of the Laser-Induced Functionalization Process for Fabricating hBN/(non-)F-G/MoS$_2$ Heterostructure
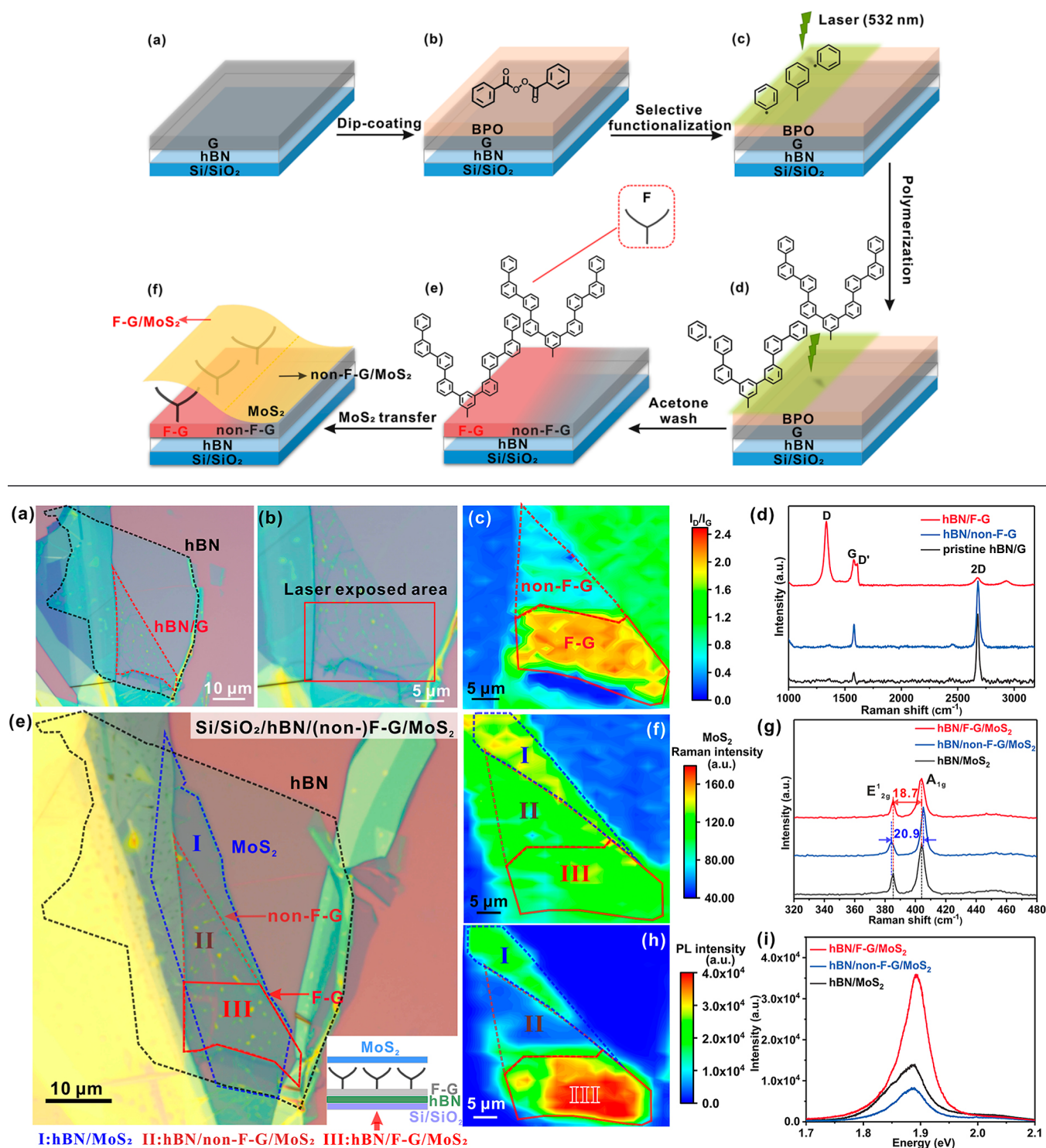
Figure 1. (a) Optical microscopy images of the hBN/G heterostructure. (b) Laser-exposed area on hBN/G/BPO as marked in the red box. (c) I_D/I_G Raman mapping of hBN/G after functionalization. (d) Average Raman spectra of pristine hBN/G, hBN/non-F-G, and hBN/F-G. hBN/(non-)F-G/MoS$_2$ heterostructure. (e) Optical microscopy image, insert of (e) schematic structure of hBN/F-G/MoS$_2$, (f) MoS$_2$ Raman intensity mapping, (g) MoS$_2$ Raman spectra, (h) MoS$_2$ PL intensity mapping, and (i) PL spectra.

graphene oxides (GO),[21] oxo-functionalized graphene (oxo-G),[22] reduced oxo-functionalized graphene (r-oxo-G),[22] and porous graphene,[23] have been used to enhance the PL intensity of 1L-MoS$_2$. Owing to the rich electron-withdrawing groups in GO and oxo-G, such as hydroxyl, epoxy, and organosulfates, or

the defective sites in r-oxo-G and porous graphene, a p-doping effect with a PL enhancement of the neutral exciton is observed in 1L-MoS$_2$.[21−23] In addition to the noncovalent heterostructures, Chen et al. fabricate a covalently linked MoS$_2$/graphene heterostructure generating PL changes in 1L-

MoS$_2$.[11] First, a 4-bromophenyl functionalized MoS$_2$ layer is prepared on a Si/SiO$_2$ substrate by reacting the generated negatively charged MoS$_2$ with 4-bromobenzenediazonium tetrafluoroborate. Subsequently, a graphene layer is transferred on top. Through the laser-triggered free radical reaction of 4-bromophenyl groups, the overlaying graphene is covalently attached from underneath to functionalized MoS$_2$. However, the covalent heterostructure shows remarkable PL quenching, which is due to the efficient charge transfer at the covalently bonded interface. Structures like those require complex preparation processes, and the PL changes are considered as a result of charge transfer. However, 2D materials are not only sensitive to charge-transfer doping but also susceptible to interlayer interactions as they are atomically thin.[24] Interlayer van der Waals interactions and interlayer distance are very important factors but are rarely considered in studying the PL of graphene/MoS$_2$ heterostructures (G/MoS$_2$).

Herein, we report on the effect of functional groups interacting with MoS$_2$ in the perpendicular orientation. PL modulation of 1L-MoS$_2$ is realized via the monotopic covalent photochemical functionalization of graphene in G/MoS$_2$ heterostructures. Through Raman, PL, dual scanning near-field optical microscopy (dual s-SNOM), and Kelvin probe force microscopy (KPFM), we identify the boundaries and the distinct characteristics of the selectively functionalized regions and the pristine regions on the heterostructures. In G/MoS$_2$, the functionalized area of graphene (F-G/MoS$_2$) exhibits a 5-fold enhancement in the PL intensity of MoS$_2$ compared to the nonfunctionalized area of graphene. Furthermore, the reverse stacked MoS$_2$/F-G heterostructure is fabricated by in situ functionalizing MoS$_2$/G/benzoyl peroxide (BPO) through photochemical reaction and only shows a 1.8-fold PL increase compared to pristine G/MoS$_2$. This observation demonstrates the role of monotopic functionalization in differentiating surfaces of 2D materials. We conclude on the flexible role of F-G in the PL modulation of 1L-MoS$_2$.

■ RESULTS AND DISCUSSION

Fabrication and Characterization of the hBN/(non-)F-G/MoS$_2$ Heterostructure. To keep the explanation of heterostructures concise, herein, we define the vertical stacking order of the heterojunction layers as (substrate/)bottom layer/upper layer. As shown schematically in Scheme 1a and Figure 1a, few-layer hBN with a thickness of 6 nm (Figure S1) was exfoliated and transferred to a Si/SiO$_2$ (300 nm) wafer substrate. Then, a monolayer of graphene exfoliated from HOPG was transferred to the hBN flake (hBN/G). The hBN/G structure was subsequently annealed in vacuum at 150 °C for 2 h to remove water and organic residues originating from the transfer process.[25] The utilization of the hBN layer is to stabilize the flat structure of the graphene flake during repeated solution treatments because hBN has a superior flatness compared to Si/SiO$_2$.[26] Then, a thin film of BPO was formed by dip-coating hBN/G to yield hBN/G/BPO (Scheme 1b). The photochemical functionalization of graphene was carried out by a 532 nm Raman laser treatment at a power of 1 mW. Under laser irradiation, the BPO decomposes to phenyl radicals and CO$_2$ by accepting a hot electron from photo-excited graphene. The phenyl radicals subsequently attack the basal plane of graphene (Scheme 1c).[27] Following the establishment of phenyl-functional sites on the basal plane, the phenyl radicals are likely to attack the bound phenyl groups, resulting in the formation of polymerized dendritic

structures (Scheme 1d).[27−29] To exclude any damaging effect from the laser energy input or in combination with solvent residues, we conducted reference experiments for pristine graphene and graphene treated with acetone. Therefore, the reference structures were treated for accumulated laser irradiation times from 1 to 300 s. According to the Raman spectra of nondefective graphene displayed in Figure S2, the graphene is stable under the used laser irradiation conditions and acetone treatment. For hBN/G/BPO, we find that the degree of functionalization of graphene is radiation time-dependent. Accordingly, with accumulated laser acquisition time from 1 to 50 s, the maximum functionalization density was indicated by the Raman spectra (Figure S3). Thus, for further experiments, we used 50 s irradiation time for the monotopic functionalization of hBN/G. By using the mapping function of the scanning Raman instrument, regioselective laser irradiation can be performed to illuminate only half of the graphene sheet, as marked by the green area in Scheme 1c and the red box in Figure 1b. After laser-induced functionalization, the residual BPO film was washed with acetone (Scheme 1e). The readout process of Raman spectra of the as-functionalized hBN/G was accomplished at a lower laser power of 0.5 mW and 1 s irradiation time. As can be seen in the I_D/I_G Raman intensity mapping in Figure 1c, the illuminated region can be clearly distinguished as a result of functionalization (F-G), unlike the rest of the graphene flake (non-F-G). The average Raman spectra of pristine hBN/G before functionalization, hBN/F-G, and hBN/non-F-G are depicted in Figure 1d, respectively. There are two dominant peaks in the Raman spectra of pristine hBN/G and hBN/non-F-G: G-band (at 1580 cm^{-1}) and 2D-band (at 2680 cm^{-1}). The absence of a D-band (at 1340 cm^{-1}) indicates the defect-free graphene in hBN/G and hBN/non-F-G. For F-G, the D and D′ peaks appear in the Raman spectra. A uniform functionalization with an average I_D/I_G of 2.2 is indicated, representing that the functionalization degree is around 1%.[30]

After functionalization of hBN/G, mechanically exfoliated 1L-MoS$_2$ was directly transferred on top of the hBN/G to form the areas of hBN/F-G/MoS$_2$ and hBN/non-F-G/MoS$_2$ (Scheme 1f and Figure 1e). Afterward, hBN/(non-)F-G/MoS$_2$ was annealed in vacuum at 200 °C for 2 h to enhance the interlayer contact since low-weight molecular contaminants are known to be eliminated from the interior.[31] As shown in Figure 1f, the Raman intensity of MoS$_2$ on hBN/(non-)F-G is uniform, although the MoS$_2$ Raman signal on hBN (hBN/MoS$_2$), as marked in region I, is slightly increased owing to the electric neutral characteristic of hBN.[32] The Raman spectra of heterojunction areas display the typical vibration modes of 1L-MoS$_2$ and 1L-graphene, which indicates the effective formation of the heterostructure (Figure S4). The magnified Raman spectra of MoS$_2$ in the range of 300−500 cm^{-1} are shown in Figure 1g. Two peaks, the in-plane E$_{2g}^1$ (385.4 cm^{-1}) and the out-of-plane A$_{1g}$ (404.1 cm^{-1}) appear in the Raman spectrum of the hBN/MoS$_2$ layer. The frequency difference between E$_{2g}^1$ and A$_{1g}$ is 18.7 cm^{-1}, confirming the monolayer characteristic of the MoS$_2$ flake.[6] It has been reported that the A$_{1g}$ mode is sensitive to charge-doping and the E$_{2g}^1$ mode is sensitive to lattice distortions or strain in MoS$_2$.[33]

The frequency difference between E$_{2g}^1$ and A$_{1g}$ in hBN/non-F-G/MoS$_2$ is 20.9 cm^{-1}, which is 2.2 cm^{-1} higher than the value of hBN/MoS$_2$ due to the electron donation from graphene to MoS$_2$.[33] However, after the functionalization, the E$_{2g}^1$ and A$_{1g}$ modes in hBN/F-G/MoS$_2$ with a difference of 18.7
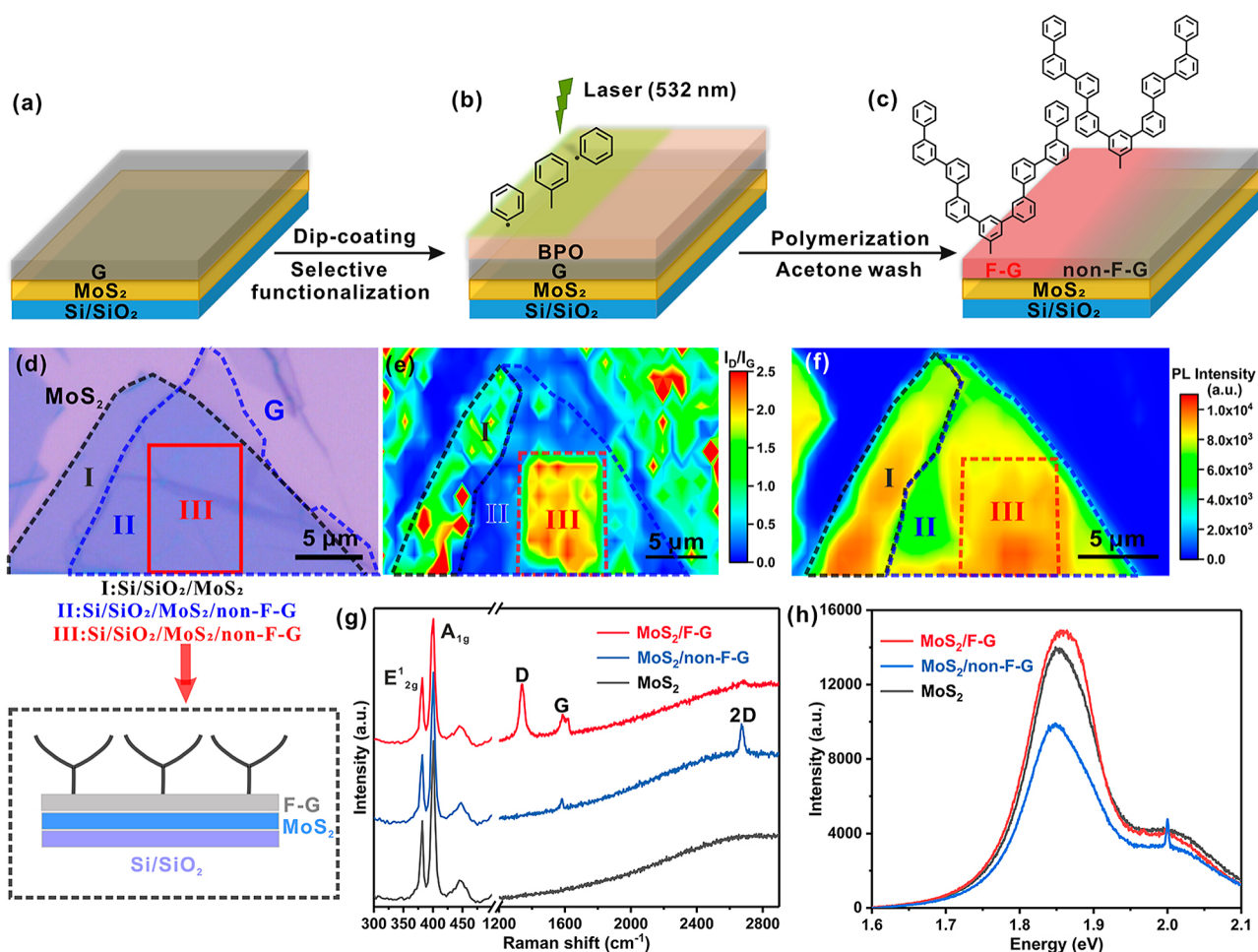
Figure 2. MoS_2/(non-)F-G heterostructure: (a–c) schematic illustration of the process for fabrication. (d) Optical microscopy image and schematic structure, (e) I_D/I_G Raman intensity mapping, (f) MoS_2 PL intensity mapping, (g) Raman spectra, and (h) PL spectra.

cm^{-1} have no obvious shift compared to the hBN/MoS_2. We deduce that there are two possible reasons: on the one hand, the weak electron-withdrawing effect from the oligophenyl groups cannot generate a large shift of the A_{1g} Raman mode of MoS_2. On the other hand, the oligophenyl functional groups effectively separate the graphene basal plane and MoS_2 interface with an increased interlayer distance, which impairs the electron transfer from the carbon plane to MoS_2. The MoS_2 in hBN/F-G/MoS_2 is mainly supported by the phenyl groups instead of the graphene surface, resulting in partly free-standing MoS_2. Figure 1h depicts the MoS_2 PL intensity mapping of the hBN/(non-)F-G/MoS_2 heterostructure. The F-G with a high I_D/I_G shows an enhanced PL intensity of MoS_2 (region III), which is 5 times and 3 times increased compared to hBN/non-F-G/MoS_2 (region II) and hBN/MoS_2 (region I), respectively. The PL maximum of the hBN/F-G/MoS_2 structure (1.89 eV) is red-shifted by 0.01 eV compared to hBN/non-F-G/MoS_2 and hBN/MoS_2 (1.88 eV), respectively, due to the p-doping effect of the phenyl groups (Figure 1i). In addition, laser-induced effects can be excluded, since the laser radiation did not generate PL changes for pristine MoS_2 and MoS_2/G, respectively (Figures S5a and S6). Moreover, the potential BPO residues on the surface cannot vary the PL properties of MoS_2 under the operational laser energy, as reference experiments revealed (Figure S5b). The profile maps corresponding to Figure 1c,f,h are displayed in Figure S7. The frequency distribution centers are consistent with the different

intervals on the relevant mapping images. In addition, since the PL intensity of MoS_2 is sensitive to the variations in samples, such as bubbles, strain, contamination, and measurement environment, several (hBN)/(non-)F-G/MoS_2 samples have been prepared, as shown in Figure S8, demonstrating the reproducibility of fabrication and measured properties. Based on the results, it is confirmed that the F-G layer significantly enhances the PL of MoS_2.

Fabrication and Characterization of the MoS_2/(non-)F-G Heterostructure. Compared to the electron-withdrawing groups in GO, such as hydroxyl, epoxy, and organosulfates,[34,35] the phenyl groups have a very weak electron-withdrawing effect. Nevertheless, the F-G/MoS_2 shows comparable PL enhancement for MoS_2 to that of GO/MoS_2, as we reported in previous works,[21,22] demonstrating that the electronic effect of the functional groups is not the only factor in the PL enhancement of MoS_2. To elucidate further effects, a reversely stacked MoS_2/F-G heterostructure was fabricated. The F-G placed on top of MoS_2 can keep the electron-withdrawing effect induced by the oligophenyl groups, but it has better interlayer contact with the graphene lattice compared to the F-G/MoS_2. Figure 2a–c illustrates the fabrication process of the MoS_2/F-G heterostructure. First, a mechanically exfoliated 1L-MoS_2 was transferred onto a Si/SiO_2 (300 nm) wafer. Then, a monolayer of graphene was transferred to the 1L-MoS_2 to form a MoS_2/G heterostructure. The MoS_2/G heterostructure was annealed in vacuum at 200
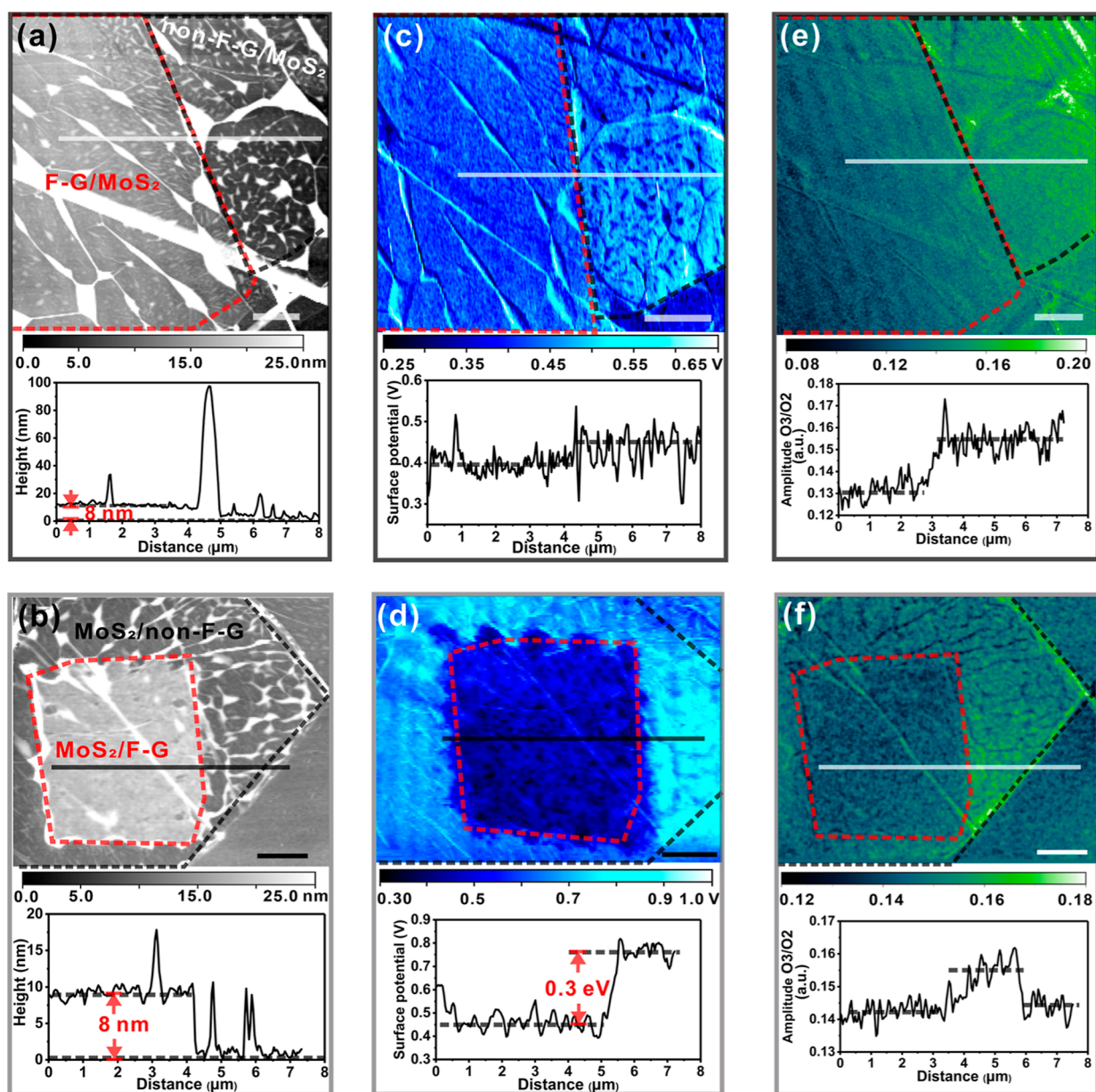
Figure 3. (a,b) AFM topography together with (c,d) KPFM images and (e,f) s-SNOM images at the same sample area for (non-)F-G/MoS$_2$ and MoS$_2$/(non-)F-G, respectively. The scale bars in (a−f) are 5 μm.

°C for 2 h, and then a thin layer of BPO was deposited on the graphene surface of the heterostructure by dip-coating (5 mM, in acetone) to fabricate MoS$_2$/G/BPO. The laser functionalization process is identical to the previously described procedure for the functionalization of hBN/G/BPO (Scheme 1b−e). However, here, in situ functionalization is directly carried out on the surface of the MoS$_2$/G heterostructure without further transfer process compared to F-G/MoS$_2$. The laser irradiation area on MoS$_2$/G is marked by the green area in Figure 2b and the red box (region III), as shown in the optical microscopy image (Figure 2d). After 50 s of laser exposure and acetone washing, the functionalized area on MoS$_2$/G (MoS$_2$/F-G) marked as region III shows a high I_D/I_G intensity of around 2.2 (Figure 2e) with a slight increase in the PL intensity of MoS$_2$ (Figure 2f). In contrast, the non-functionalized area of MoS$_2$/G (MoS$_2$/non-F-G) marked as region II shows PL quenching of MoS$_2$. In Figure 2g, the average Raman spectra of MoS$_2$/F-G (region III), MoS$_2$/non-

F-G (region II), and isolated MoS$_2$ (region I) from the three different areas on the MoS$_2$/G heterostructure are shown. The E$_{2g}^1$ (385.4 cm^{-1}) and A$_{1g}$ (404.1 cm^{-1}) peaks in the Raman spectrum of the isolated 1L-MoS$_2$ layer confirm the monolayer characteristic of the MoS$_2$ flake. Vibrational modes of both 1L-MoS$_2$ and 1L-graphene appear in the Raman spectra of the MoS$_2$/F-G and MoS$_2$/non-F-G regions, indicating the formation of heterostructures. The D peak appears in MoS$_2$/F-G after functionalization with the attenuation of the 2D peak, and the degree of functionalization is around 1%, which is consistent with that of hBN/F-G/MoS$_2$ (Figure 1c). However, as the PL spectra in Figure 2h reveal, the PL intensity of MoS$_2$ only increases marginally by 1.1 and 1.8 times in comparison with isolated MoS$_2$ and MoS$_2$/non-F-G, respectively. Owing to the p-doping effect induced by F-G, the PL maximum of MoS$_2$/F-G shows a redshift compared with the pristine MoS$_2$, however, the MoS$_2$/F-G displays much lower PL enhancement than hBN/F-G/MoS$_2$.
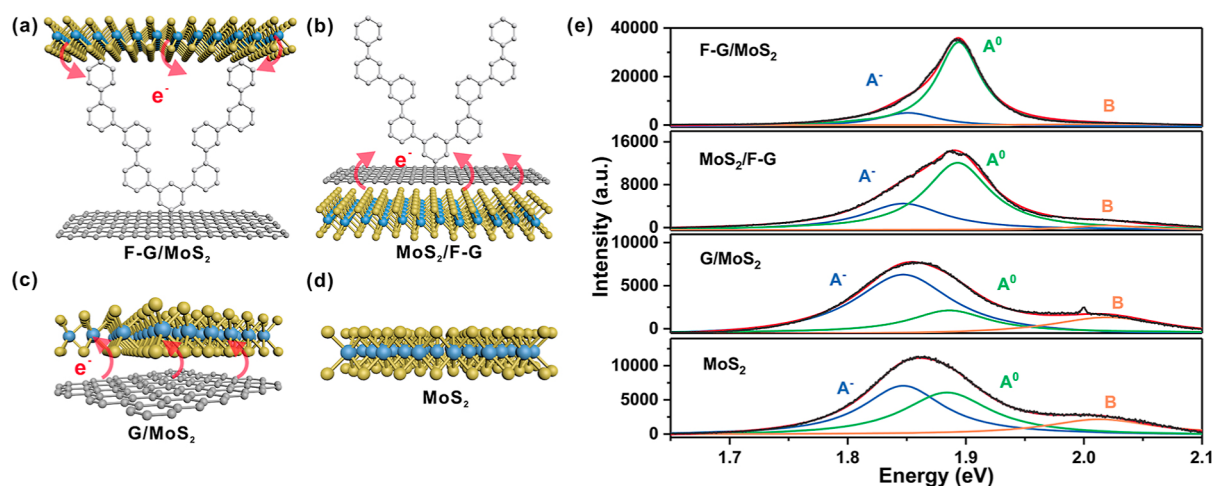
95

Figure 4. Sketch illustrating the interfacial interaction mechanism in the four heterostructures: (a) F-G/MoS$_2$, (b) MoS$_2$/F-G, (c) G/MoS$_2$, and (d) MoS$_2$. (e) Peak fittings using Lorentz functions for the four structures.

Effect of Functionalization on the Dielectric Function and Surface Potential. One way to accurately describe the electrical and optical features of nanoscale materials is to analyze their complex dielectric function, which is a measure of the transmission and absorption of light through a material as a function of frequency.[36] By employing Raman/PL spectroscopy, we investigated the effect of the functionalized groups on the photoelectric characteristics of G/MoS$_2$ heterostructures. However, the spatial resolution of these techniques is bound by the diffraction limit of light and does not provide information on the homogeneity of the prepared samples on the nanometer scale. Here, we use the dual s-SNOM as an advanced tool for nanoimaging that combines near-field optical microscopy, KPFM, Raman, and PL spectroscopy, enabling to spatially resolve the variation of the dielectric function and the surface work function with nanometer-scale resolution. In detail, to begin with, we measured the KPFM of the (non-)F-G/MoS$_2$ and MoS$_2$/(non-)F-G. In KPFM, we determine a topography image by the AFM together with the surface work function as a function of tip position that varies, for example, with doping levels. Consequently, the sample height, surface roughness, boundaries, and charge transfer influence on the surface work function can be characterized. As depicted in the AFM images in Figure 3a,b, F-G regions on both (non-)F-G/MoS$_2$ and MoS$_2$/(non-)F-G exhibit an 8 nm height difference compared with the non-F-G regions. The thickness is induced by the functional component, which further proves our speculation described in Scheme 1 that photochemical functionalization leads to the formation of polymerized or oligomerized phenyl chain structures. In addition, the functionalized areas display flatter surfaces with fewer wrinkles and bubbles compared to the nonfunctionalized areas of the heterostructures, which proves the homogeneity of the functionalization. We suppose that the dendritic functional structures support the surface of the sample away from the bubbles and contaminations introduced by the transfer process. Consistent with the AFM images, on both heterostructures, the functionalized region exhibits darker KPFM contrast (lower surface potential) than the non-functionalized region (Figure 3c,d), which can be ascribed to the anchoring of electron-withdrawing phenyl groups.[37,38] The detection of functionalization on the surface of MoS$_2$/F-G is more feasible using KPFM, as it is a surface-sensitive method

that exclusively probes the surface and near-surface areas. There is a significant variation of 0.3 V in surface potential between MoS$_2$/F-G and MoS$_2$/non-F-G. The KPFM images are in perfect agreement with our input selective functionalization patterns as well as the respective MoS$_2$ PL mappings, as shown in Figure S9 [(non-)F-G/MoS$_2$] and Figure 2d−f [MoS$_2$/(non-)F-G].

To support the data, we take near-field images by s-SNOM. The detected signal is related to the tip−sample distance and the dielectric function. In the s-SNOM, the tip−sample distance is kept the same during the scan. Indeed, wrinkles and bubbles may influence and vary slightly the tip−sample distance; however, on flat areas, it is around held at 1 nm. Thus, strong changes in the near-field contrast are a result of changing dielectric function due to doping, straining, and defects. We find that the s-SNOM images are in excellent agreement with the KPFM. As indicated in Figure 3e,f, all the previously identified features can be identified in the s-SNOM images. Despite the influence of wrinkles and bubbles on the s-SNOM images, there is a distinct and uniform contrast from the F-G to non-F-G heterostructures for both (non-)F-G/MoS$_2$ and MoS$_2$/(non-)F-G. The functionalization leads to doping and thus to an increase in the dielectric function. In addition, s-SNOM images of the pristine MoS$_2$ and G/MoS$_2$ structures are shown in Figure S10. Monolayer and bilayer MoS$_2$, as well as different regions of G/MoS$_2$, show clear near-field contrast arising from variations in the local dielectric value. Therefore, based on the KPFM and s-SNOM findings, we prove that the PL enhancements of MoS$_2$ are attributed to the photofunctionalization of graphene rather than any external factors like contaminants or bubbles.

Electron Transfer in Heterostructures. The differentiated PL characteristics of F-G/MoS$_2$ and MoS$_2$/F-G prove that the structural disparity notably affects the PL of MoS$_2$. Normalized average PL spectra extracted from the four different structures of F-G/MoS$_2$, MoS$_2$/F-G, G/MoS$_2$, and pristine 1L-MoS$_2$ on Si/SiO$_2$ were compared (Figure S11). Corresponding statistics of PL map profiles and mapping are listed in Figure S12. To gain a better understanding of the spectral changes, peaks were fitted using Lorentzian functions. Corresponding to the three typical excitonic states of neutral exciton (A^0, 1.89 eV), negatively charged trion (A$^−$, 1.85 eV), and B exciton (2.02 eV), the PL spectra of F-G/MoS$_2$, MoS$_2$/
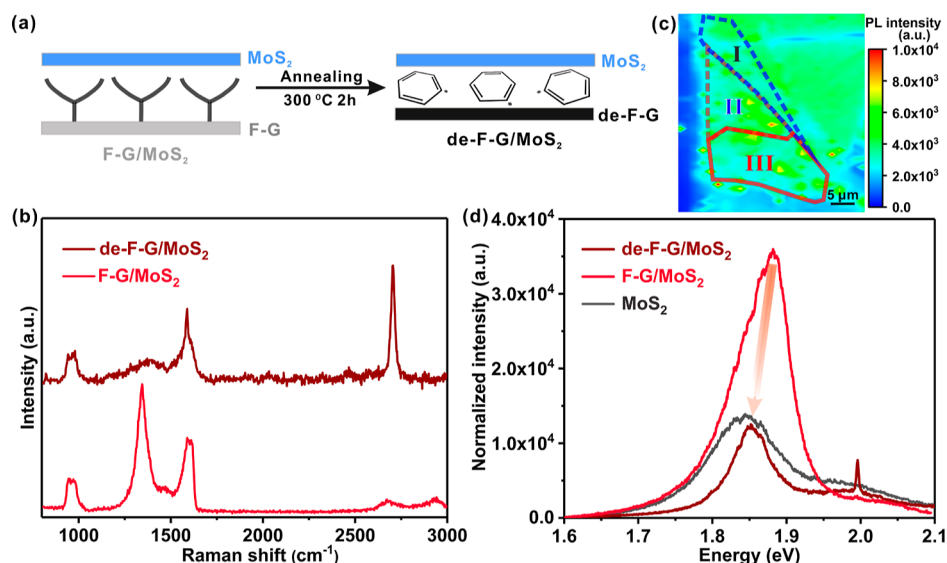
Figure 5. Defunctionalization of the hBN/(non-)F-G/MoS_2 heterostructure. (a) Schematic illustration of the defunctionalization process. (b) Raman spectra of F-G/MoS_2 and de-F-G/MoS_2, (c) MoS_2 PL mapping image of the de-F-G/MoS_2 heterostructure, and (d) normalized PL spectra of de-F-G/MoS_2, F-G/MoS_2, and pristine MoS_2.

F-G, G/MoS_2, and MoS_2 were fitted by three Lorentzian functions (Figure 4e). Detailed parameters of fitted PL peaks by Lorentz functions are summarized in Table S1. In pristine 1L-MoS_2, the PL spectrum is dominated by the trion state, which arises from reduced dielectric screening in gapped 2D crystals and the relatively heavy particle band masses associated with the Mo *d*-manifolds.[8] In contrast to pristine MoS_2, the A^- peak increases in G/MoS_2 and the A^0 peak is obviously weakened. Conversely, the A^0 excitons are the dominant contributors in the PL emission, with a 1.8-fold enhancement in MoS_2/F-G and a 5-fold enhancement in F-G/MoS_2 compared to isolated MoS_2, which indicates charge transfer from MoS_2 to F-G. The A^0 exciton peak intensity in F-G/MoS_2 is 11 times higher than that in G/MoS_2. The additional peak at 2.0 eV in the PL spectrum of G/MoS_2 corresponds to the sharp 2D peak of monolayer graphene, which vanished in the PL spectra of F-G/MoS_2 and MoS_2/F-G because of the functionalization of graphene. Figure 4a−c illustrates the electron transfer from MoS_2 to F-G for F-G/MoS_2 and MoS_2/F-G. For G/MoS_2, pristine graphene donates electrons to MoS_2. Even though F-G shows electron-withdrawing ability, there is a significant difference in the effect on enhancing the PL of MoS_2 whether it is placed on top or under MoS_2. This result indicates that the p-doping is not the only reason for the PL increase of MoS_2. In F-G/MoS_2, the MoS_2 is supported directly by the oligophenyl groups due to the high functionalization degree on the graphene surface, which increases the interlayer distance and decreases the van der Waals interaction between the graphene basal plane and MoS_2. Compared to G/MoS_2, there is no interlayer contact possible between MoS_2 and the graphene basal plane of F-G/MoS_2, hindering also the electron transfer from the carbon plane to MoS_2 and consequently enhancing the PL intensity.

Thermal Defunctionalization of the hBN/(non-)F-G/MoS_2 Heterostructure. Moreover, the reversibility of the functionalization effect on the PL enhancement of MoS_2 is investigated. The hBN/(non-)F-G/MoS_2 heterostructure was annealed at 300 °C for 2 h in a vacuum to break the C-Aryl bond for restoring graphene (Figure 5a). As shown in the

Raman spectra in Figure 5b, the Raman signal of de-F-G recovers the narrow and most intense 2D peak. The sharp D peak vanishes, although a broad peak remains, most likely resulting from trapped dissociated polyphenyl or oligophenyl groups between graphene and MoS_2. The 8 nm height resulting from the oligophenyl structures (Figure 3a) is largely reduced to about 0.8 nm after annealing, as depicted in Figure S13.

Accordingly, the PL enhancement from F-G also disappears after defunctionalization (Figure 5c,d). The PL intensity of de-F-G/MoS_2 is slightly lower than that of the isolated MoS_2 area because of the interlayer Schottky barrier. Compared to the vanished 2D peak of F-G/MoS_2, the appearance of the 2D peak after annealing indicates the defunctionalization and restoration of graphene. However, the maximum of the PL peak of de-F-G/MoS_2 is red-shifted on account of the decoupled phenyl groups (Figure 5c). The absence of LA(M) peak at 227 cm^{-1} in the MoS_2 Raman spectra (Figure S14) indicates that the annealing process in vacuum (1×10^{-3} mbar) does not generate defects to MoS_2. The loss of PL enhancement is mainly because of the annealing process, which breaks the covalent bonds of the oligophenyl groups oriented perpendicular to the graphene plane, leading to the free orientation of the dissociated oligophenyl groups.

■ CONCLUSIONS

The PL of 1L-MoS_2 is demonstrated to be tunable by laser-induced oligophenyl-functionalized graphene. The s-SNOM, combined with AFM, KPFM, and Raman, allows us to characterize and understand the fabricated heterostructures. The monotopic functionalized graphene stacked on top or bottom of MoS_2 differentiates the heterointerface between graphene and MoS_2, thus generating varied PL modulation. In addition, the MoS_2 supported on top of F-G results in significant increases of dominant A^0 excitons compared to the MoS_2 with direct interlayer interaction to the graphene basal plane (pristine G/MoS_2 and MoS_2/F-G). The results indicate that the enlarged interlayer distance by the oligophenyl groups hinders the electron transfer from the graphene carbon plane

to MoS$_2$. Moreover, the PL enhancement of MoS$_2$ is lost by thermally induced defunctionalization with the restoration of interlayer distances. Our findings prove that the interface designed by functional components and the accompanied tailoring of the interlayer distance of heterostructures provide major effects on the PL modulations. The graphene carbon plane acts as an active reaction template for the covalent attachment of perpendicular molecules, thus opening more possibilities for the fabrication of heterointerfaces. With that knowledge in mind, we change our way of thinking about functionalized 2D heterostructures.

■ EXPERIMENTAL SECTION/METHODS

Materials. Si wafers with a 300 nm thick SiO$_2$ layer were purchased from the Fraunhofer Institut für Integrierte Systeme und Bauelementetechnologie IISB in Erlangen. BPO and acetone (HPLC) were purchased from Sigma-Aldrich Co. (Germany) and used without further treatment. Polydimethylsiloxane (PDMS) was purchased from Gel-Pack.

Characterization. Optical imaging and transfer processes were performed using a Nikon LV100ND microscope equipped with a self-built transfer stage.[39] Raman and PL characterizations were conducted using a confocal Raman microscope (Horiba Explorer, 532 nm excitation wavelength, 0.7 μm laser spot, 1200/2400 gratings, 0.5 and 1 mW, 100× objectives) in air. The 1 mW laser power was used for the functionalization process. The 2400 gratings were used for precise Raman characterization of MoS$_2$. The general readout of Raman and PL maps was carried out by 1200 gratings and 0.5 mW power. AFM images were recorded on a JPK Nanowizard 4 equipped with NSG10/Au probes using a Tap300-G AFM probe, and intermittent contact mode was chosen. Annealing of the samples was carried out using a tube furnace (Nabertherm GmbH, 30−3000 °C).

For the s-SNOM and KPFM, we used the neaSNOM from neaSPEC, which is coupled to a fully tunable visible laser (Hübner). The neaSNOM provides near-field imaging, KPFM, and AFM. In s-SNOM, a metallic tip is illuminated by light, and plasmons are generated that promote a near-field between the tip and sample. The near-field enhances both the incoming and backscattered light by a factor f and is detected by a single-line CCD. The enhancement factor f is given by the tip−sample distance and the dielectric function of the sample. By scanning the tip across the sample and measuring the near-field signal as a function of it, the optical properties of the sample can be studied qualitatively. To achieve background suppression, the tip was oscillated with an amplitude of 50 nm and a frequency Ω of approximately 250 kHz. The resulting signal was demodulated using the higher harmonics of the tip frequency $n\,\Omega$. To further reduce noise, a pseudoheterodyne interferometer was employed, which utilized a reference mirror oscillating at a much lower frequency $M \ll \Omega$. This caused the length of the reference beam path to change, leading to interference with the scattered signal. As a result, sidebands were generated around the fundamental harmonics at frequencies equal to plus or minus an integer multiplied by the reference frequency $f = n\,\Omega + m\,M$. In this detection method, both the amplitude and phase information were recorded from the sample, resulting in near-field amplitude and phase images at different sidebands of the fundamental harmonic. Increasing the sideband index, (m), contributed to a reduction in noise present in the s-SNOM images. The dual s-SNOM technique was used to characterize the sample, employing a commercial s-SNOM (NeaSNOM from Neaspec GmbH, Germany). The platinum−iridium-coated AFM tips (23 nm coating thickness) from NanoWorld were used, featuring a tip apex radius of less than 25 nm. To excite the sample, a wavelength-tunable cw laser (Hübner C-Wave, 450−650 nm wavelength) was used, and it was guided through a beam expander onto a parabolic mirror with a high NA of 0.7. The parabolic mirror collects the backscattered light, and the laser light is focused onto the AFM tip, which then acts as a near-field probe in the visible spectral range. The

laser power used for all s-SNOM image measurements was approximately 1 mW at the tip, with an integration time of 16 ms. The tip amplitude was 53.5 nm, with a tapping frequency of 243 kHz. The neaSNOM also can measure the surface potential by KPFM. For KPFM, we used the Pt-Ir-coated Si tips (ACCESS-EFM probes, AppNano, k = 2.7 N m^{-1}). AM-KPFM was operated, which is sensitive to electrostatic force. The work function of the samples (Φ_{sample}) is defined by the following formula, $\Phi_{sample} = q\,V_{CPD} + \Phi_{tip}$, where V_{CPD} is the contact potential difference measured by the KPFM, Φ_{tip} is the work function of the tip, and q is the elementary charge. The potential profile is measured by maintaining a constant distance of 50 nm between the tip and the sample surface.

Fabrication of Heterostructures. *Preparation of the hBN/G Heterostructure.* Few-layer hBN was mechanically exfoliated from bulk hBN via PDMS and transferred onto a Si/SiO$_2$ wafer. Monolayer graphene was mechanically exfoliated from HOPG via PDMS and transferred to the few-layer hBN flake. According to the transfer method reported previously, the transfer process was carried out under a microscope equipped with a self-built transfer stage.[39] The thicknesses of the exfoliated hBN and graphene were determined by optical contrast, Raman spectroscopy, and AFM. After every transfer step, the sample was mildly annealed in vacuum (10^{-3} mbar) at 150 °C for 2 h to remove water and residuals stemming from the transfer process.

Photochemical Reaction of BPO on the hBN/G Heterostructure. First, a 5 mM BPO solution in acetone was prepared. The wafer with the hBN/G sample was vertically held by a clean tweezer and slowly dipped in the BPO solution for 2 s and then carefully moved out and deposited on a glass slide. Within 5 min, the acetone evaporated under ambient conditions, and an optically uniform thin film of BPO formed on top of the hBN/G structure. A photochemical reaction was initiated by the 532 nm green Raman laser with a spot size of 0.7 μm and 1 mW energy. The selective functionalization on hBN/G was realized using the point-by-point mapping function of the scanning Raman instrument with incremental steps of 0.7 μm. The irradiation time of every point was calculated accumulatively. The laser illuminated the bottom half part of the graphene flake by defining a rectangular map of 20 μm × 15 μm. The illumination time at every step was 10 s, and the mapping was repeated five times so that the total illumination time accumulated to 50 s. After laser functionalization, the residual BPO molecule film was removed by acetone washing. The Raman spectra of the whole hBN/G structure were measured by a mapping function using an increment of 0.7 μm at 532 nm laser excitation with 1 s irradiation time at a lower energy of 0.5 mW, and other parameters remained the same.

Preparation of the hBN/(non-)F-G/MoS$_2$ Heterostructure. Monolayers of MoS$_2$ were mechanically exfoliated, and a single-layer flake was selected (identified by optical contrast and Raman spectroscopy, 18.7 cm^{-1} wavenumber difference of A$_{1g}$−E$^1_{2g}$) and transferred to the as-prepared hBN/G via PDMS, covering both the functionalized area (F-G) and the nonfunctionalized area of graphene (non-F-G). The heterostructure was annealed at 200 °C for 2 h in vacuum (10^{-3} mbar) to enhance the interlayer contact between MoS$_2$ and hBN/G. The PL and Raman measurements were performed afterward. F-G/MoS$_2$ heterostructure was also fabricated directly on a Si/SiO$_2$ wafer without hBN for comparison studies. For determining the Raman shifts of MoS$_2$, the 2400 grating was used.

Preparation of the MoS$_2$/F-G Heterostructure. Exfoliated 1L-MoS$_2$ was transferred onto a Si/SiO$_2$ wafer, followed by a monolayer of graphene (MoS$_2$/G). Then, the whole wafer with the MoS$_2$/G heterostructure was dip-coated with a thin BPO layer (compare section "Photochemical Reaction of BPO on the hBN/G Hetero-structure"). The laser-induced functionalization was carried out on the top of the upper graphene layer using the same parameters as for the preparation of F-G/MoS$_2$.

Defunctionalization Studies. The heterostructures were annealed in a vacuum (10^{-3} mbar) at 300 °C for 2 h with a heating rate of 2 °C/min. The total processing time, including cooling to ambient, was 9 h.

■ ASSOCIATED CONTENT

ⓢ Supporting Information

The Supporting Information is available free of charge at https://pubs.acs.org/doi/10.1021/acs.chemmater.3c03166.

AFM image of the hBN/G heterostructure; stability test of graphene under laser irradiation and acetone solvent; Raman spectra of G/BPO after an accumulated laser irradiation time; Raman spectra of the hBN/(non-)F-G/MoS₂ heterostructure; PL spectra of pristine MoS₂ and MoS₂/BPO after accumulated laser irradiation; PL spectra of G/MoS₂ after accumulated laser irradiation; Raman, PL map profiles, and corresponding intensity frequency distribution; reproducibility of the heterostructure and PL enhancement; functionalization of hBN/G/BPO and PL enhancement of hBN/(non-)F-G/MoS₂; optical microscopy, AFM, and s-SNOM images of Si/SiO₂/MoS₂ and G/MoS₂ heterostructures; comparison of PL spectra of different structures; PL map profile and mapping of different heterostructures on Si/SiO₂ wafers; AFM and PL mapping of hBN/(non-)F-G/MoS₂ after annealing; Raman spectra of MoS₂ over the de-F-G/MoS₂ heterostructure; and parameters about fitted PL peaks by the Lorentz function (PDF)

■ AUTHOR INFORMATION

Corresponding Author

Siegfried Eigler − *Institute of Chemistry and Biochemistry, Freie Universität Berlin, 14195 Berlin, Germany;* ⓞ orcid.org/0000-0002-0536-8256; Email: siegfried.eigler@fu-berlin.de

Authors

Qing Cao − *Institute of Chemistry and Biochemistry, Freie Universität Berlin, 14195 Berlin, Germany;* ⓞ orcid.org/0000-0001-5691-5427

Mira Kreßler − *Department of Physics, Freie Universität Berlin, 14195 Berlin, Germany*

Marleen Hußmann − *Institute of Chemistry and Biochemistry, Freie Universität Berlin, 14195 Berlin, Germany*

Yalei Hu − *Institute of Chemistry and Biochemistry, Freie Universität Berlin, 14195 Berlin, Germany;* ⓞ orcid.org/0000-0001-6708-944X

Patryk Kusch − *Department of Physics, Freie Universität Berlin, 14195 Berlin, Germany;* ⓞ orcid.org/0000-0001-9180-786X

Complete contact information is available at:
https://pubs.acs.org/10.1021/acs.chemmater.3c03166

Author Contributions

Q. C. performed the experiments and wrote the manuscript. M. K. and P. K. performed the KPFM and s-SNOM measurement. M. H. and Y. H. provided help and suggestions on projects. S. E. supervised the project. All authors discussed the results and commented on the manuscript.

Notes

The authors declare no competing financial interest.

■ ACKNOWLEDGMENTS

■ REFERENCES

(1) Duan, X.; Wang, C.; Pan, A.; Yu, R.; Duan, X. Two-Dimensional Transition Metal Dichalcogenides as Atomically Thin Semiconductors: Opportunities and Challenges. *Chem. Soc. Rev.* **2015**, *44*, 8859−8876.

(2) Yu, S.; Wu, X.; Wang, Y.; Guo, X.; Tong, L. 2D Materials for Optical Modulation: Challenges and Opportunities. *Adv. Mater.* **2017**, *29*, 1606128.

(3) Moses Badlyan, N.; Pettinger, N.; Enderlein, N.; Gillen, R.; Chen, X.; Zhang, W.; Knirsch, K. C.; Hirsch, A.; Maultzsch, J. Oxidation and Phase Transition in Covalently Functionalized MoS₂. *Phys. Rev. B* **2022**, *106*, 104103.

(4) Splendiani, A.; Sun, L.; Zhang, Y.; Li, T.; Kim, J.; Chim, C. Y.; Galli, G.; Wang, F. Emerging Photoluminescence in Monolayer MoS₂. *Nano Lett.* **2010**, *10*, 1271−1275.

(5) Mak, K. F.; Lee, C.; Hone, J.; Shan, J.; Heinz, T. F. Atomically Thin MoS₂: a New Direct-Gap Semiconductor. *Phys. Rev. Lett.* **2010**, *105*, 136805.

(6) Mouri, S.; Miyauchi, Y.; Matsuda, K. Tunable Photoluminescence of Monolayer MoS₂ via Chemical Doping. *Nano Lett.* **2013**, *13*, 5944−5948.

(7) Ross, J. S.; Wu, S.; Yu, H.; Ghimire, N. J.; Jones, A. M.; Aivazian, G.; Yan, J.; Mandrus, D. G.; Xiao, D.; Yao, W.; Xu, X. Electrical Control of Neutral and Charged Excitons in a Monolayer Semiconductor. *Nat. Commun.* **2013**, *4*, 1474.

(8) Mak, K. F.; He, K.; Lee, C.; Lee, G. H.; Hone, J.; Heinz, T. F.; Shan, J. Tightly Bound Trions in Monolayer MoS₂. *Nat. Mater.* **2013**, *12*, 207−211.

(9) Nan, H.; Wang, Z.; Wang, W.; Liang, Z.; Lu, Y.; Chen, Q.; He, D.; Tan, P.; Miao, F.; Wang, X.; Wang, J.; Ni, Z. Strong Photoluminescence Enhancement of MoS₂ through Defect Engineering and Oxygen Bonding. *ACS Nano* **2014**, *8*, 5738−5745.

(10) Chen, X.; Kohring, M.; Assebban, M.; Tywoniuk, B.; Bartlam, C.; Moses Badlyan, N.; Maultzsch, J.; Duesberg, G. S.; Weber, H. B.; Knirsch, K. C.; Hirsch, A. Covalent Patterning of 2D MoS₂. *Chem.—Eur. J.* **2021**, *27*, 13117−13122.

(11) Chen, X.; Assebban, M.; Kohring, M.; Bao, L.; Weber, H. B.; Knirsch, K. C.; Hirsch, A. Laser-Triggered Bottom-Up Transcription of Chemical Information: Toward Patterned Graphene/MoS₂ Heterostructures. *J. Am. Chem. Soc.* **2022**, *144*, 9645−9650.

(12) Kang, N.; Paudel, H. P.; Leuenberger, M. N.; Tetard, L.; Khondaker, S. I. Photoluminescence Quenching in Single-Layer MoS₂ via Oxygen Plasma Treatment. *J. Phys. Chem. C* **2014**, *118*, 21258−21263.

(13) Buscema, M.; Steele, G. A.; van der Zant, H. S. J.; Castellanos-Gomez, A. The Effect of the Substrate on the Raman and Photoluminescence Emission of Single-Layer MoS₂. *Nano Res.* **2014**, *7*, 561−571.

(14) Fang, H.; Battaglia, C.; Carraro, C.; Nemsak, S.; Ozdol, B.; Kang, J. S.; Bechtel, H. A.; Desai, S. B.; Kronast, F.; Unal, A. A.; Conti, G.; Conlon, C.; Palsson, G. K.; Martin, M. C.; Minor, A. M.; Fadley, C. S.; Yablonovitch, E.; Maboudian, R.; Javey, A. Strong Interlayer Coupling in van der Waals Heterostructures Built from Single-Layer Chalcogenides. *Proc. Natl. Acad. Sci. U.S.A.* **2014**, *111*, 6198−6202.

(15) Novoselov, K. S.; Geim, A. K.; Morozov, S. V.; Jiang, D.; Zhang, Y.; Dubonos, S. V.; Grigorieva, I. V.; Firsov, A. A. Electric Field Effect in Atomically Thin Carbon Films. *Science* **2004**, *306*, 666−669.

(16) Wassei, J. K.; Kaner, R. B. Graphene, a Promising Transparent Conductor. *Mater. Today* **2010**, *13*, 52−59.

(17) Hu, Z.; Zhao, Y.; Zou, W.; Lu, Q.; Liao, J.; Li, F.; Shang, M.; Lin, L.; Liu, Z. Doping of Graphene Films: Open the way to Applications in Electronics and Optoelectronics. *Adv. Funct. Mater.* **2022**, *32*, 2203179.

(18) Yang, M.; Wang, L.; Hu, G.; Chen, X.; Gong, P. L.; Cong, X.; Liu, Y.; Yang, Y.; Li, X.; Zhao, X.; Liu, X. Optical Identification of Interlayer Coupling of Graphene/MoS₂ van der Waals Heterostructures. *Nano Res.* **2021**, *14*, 2241−2246.

(19) Li, Y.; Xu, C.-Y.; Qin, J.-K.; Feng, W.; Wang, J.-Y.; Zhang, S.; Ma, L.-P.; Cao, J.; Hu, P. A.; Ren, W.; Zhen, L. Tuning the Excitonic States in MoS$_2$/Graphene van der Waals Heterostructures via Electrochemical Gating. *Adv. Funct. Mater.* **2016**, *26*, 293−302.

(20) Shih, C. J.; Wang, Q. H.; Son, Y.; Jin, Z.; Blankschtein, D.; Strano, M. S. Tuning On-Off Current Ratio and Field-Effect Mobility in a MoS$_2$-Graphene Heterostructure via Schottky Barrier Modulation. *ACS Nano* **2014**, *8*, 5790−5798.

(21) Oh, H. M.; Jeong, H.; Han, G. H.; Kim, H.; Kim, J. H.; Lee, S. Y.; Jeong, S. Y.; Jeong, S.; Park, D. J.; Kim, K. K.; Lee, Y. H.; Jeong, M. S. Modulating Electronic Properties of Monolayer MoS$_2$ via Electron-Withdrawing Functional Groups of Graphene Oxide. *ACS Nano* **2016**, *10*, 10446−10453.

(22) Wang, Z.; Cao, Q.; Sotthewes, K.; Hu, Y.; Shin, H. S.; Eigler, S. Interlayer Electron Modulation in van der Waals Heterostructures Assembled by Stacking Monolayer MoS$_2$ onto Monolayer Graphene with Different Electron Transfer Ability. *Nanoscale* **2021**, *13*, 15464−15470.

(23) Wang, Y.; Neumann, C.; Hußmann, M.; Cao, Q.; Hu, Y.; Garrity, O.; Kusch, P.; Turchanin, A.; Eigler, S. Synthesis of Wet-Chemically Prepared Porous-Graphene Single Layers on Si/SiO$_2$ Substrate Increasing the Photoluminescence of MoS$_2$ in Hetero-structures. *Adv. Mater. Interfaces* **2021**, *8*, 2100783.

(24) Rao, R.; Islam, A. E.; Singh, S.; Berry, R.; Kawakami, R. K.; Maruyama, B.; Katoch, J. Spectroscopic Evaluation of Charge-Transfer Doping and Strain in Graphene/MoS$_2$ Heterostructures. *Phys. Rev. B* **2019**, *99*, 195401.

(25) Ni, Z. H.; Wang, H. M.; Luo, Z. Q.; Wang, Y. Y.; Yu, T.; Wu, Y. H.; Shen, Z. X. The Effect of Vacuum Annealing on Graphene. *J. Raman Spectrosc.* **2010**, *41*, 479−483.

(26) Man, M. K. L.; Deckoff-Jones, S.; Winchester, A.; Shi, G.; Gupta, G.; Mohite, A. D.; Kar, S.; Kioupakis, E.; Talapatra, S.; Dani, K. M. Protecting the Properties of Monolayer MoS$_2$ on Silicon Based Substrates with An Atomically Thin Buffer. *Sci. Rep.* **2016**, *6*, 20890.

(27) Liu, H.; Ryu, S.; Chen, Z.; Steigerwald, M. L.; Nuckolls, C.; Brus, L. E. Photochemical Reactivity of Graphene. *J. Am. Chem. Soc.* **2009**, *131*, 17099−17101.

(28) Kariuki, J. K.; McDermott, M. T. Nucleation and Growth of Functionalized Aryl Films on Graphite Electrodes. *Langmuir* **1999**, *15*, 6534−6540.

(29) Tahara, K.; Kubo, Y.; Lindner, B.; Hashimoto, S.; Hirose, S.; Brown, A.; Hirsch, B.; Daukiya, L.; De Feyter, S.; Tobe, Y. Steric and Electronic Effects of Electrochemically Generated Aryl Radicals on Grafting of the Graphite Surface. *Langmuir* **2019**, *35*, 2089−2098.

(30) Vecera, P.; Eigler, S.; Koleśnik-Gray, M.; Krstić, V.; Vierck, A.; Maultzsch, J.; Schäfer, R. A.; Hauke, F.; Hirsch, A. Degree of Functionalisation Dependence of Individual Raman Intensities in Covalent Graphene Derivatives. *Sci. Rep.* **2017**, *7*, 45165.

(31) Kim, Y.; Herlinger, P.; Taniguchi, T.; Watanabe, K.; Smet, J. H. Reliable Postprocessing Improvement of van der Waals Hetero-structures. *ACS Nano* **2019**, *13*, 14182−14190.

(32) Illarionov, Y. Y.; Rzepa, G.; Waltl, M.; Knobloch, T.; Grill, A.; Furchi, M. M.; Mueller, T.; Grasser, T. The Role of Charge Trapping in MoS$_2$/SiO$_2$ and MoS$_2$/hBN Field-Effect Transistors. *2D Mater.* **2016**, *3*, 035004.

(33) Hong, S.; Fu, D.; Hou, J.; Zhou, D.; Wang, B.; Sun, Y.; Liu, P.; Liu, K. Robust Photoluminescence Energy of MoS$_2$/Graphene Heterostructure Against Electron Irradiation. *Sci. China Mater.* **2018**, *61*, 1351−1359.

(34) Naumov, A.; Grote, F.; Overgaard, M.; Roth, A.; Halbig, C. E.; Nørgaard, K.; Guldi, D. M.; Eigler, S. Graphene Oxide: a One- versus Two-Component Material. *J. Am. Chem. Soc.* **2016**, *138*, 11445−11448.

(35) Gao, W.; Alemany, L. B.; Ci, L.; Ajayan, P. M. New Insights into the Structure and Reduction of Graphite Oxide. *Nat. Chem.* **2009**, *1*, 403−408.

(36) Garrity, O.; Rodriguez, A.; Mueller, N. S.; Frank, O.; Kusch, P. Probing the Local Dielectric Function of WS$_2$ on an Au Substrate by

Near Field Optical Microscopy Operating in the Visible Spectral Range. *Appl. Surf. Sci.* **2022**, *574*, 151672.

(37) Al-Fogra, S.; Yang, B.; Jurkiewicz, L.; Hauke, F.; Hirsch, A.; Wei, T. Spatially Resolved Janus Patterning of Graphene by Direct Laser Writing. *J. Am. Chem. Soc.* **2022**, *144*, 19825−19831.

(38) Bao, L.; Zhao, B.; Yang, B.; Halik, M.; Hauke, F.; Hirsch, A. Hypervalent Iodine Compounds as Versatile Reagents for Extremely Efficient and Reversible Patterning of Graphene with Nanoscale Precision. *Adv. Mater.* **2021**, *33*, No. e2101653.

(39) Hußmann, M.; Weintrub, B.; Feicht, P.; Germer, G.; Kirchhof, J. N.; Bolotin, K. I.; Eigler, S. Controlled Assembly of Artificial 2D Materials Based on the Transfer of Oxo-Functionalized Graphene. *Nanoscale Adv.* **2020**, *2*, 176−181.

Supporting Information

Photoluminescence Modulation of Graphene/MoS$_2$ Heterostructures Separated by Laser-Induced Functionalization

*Qing Cao,[1] Mira Kreßler,[2] Marleen Hußmann,[1] Yalei Hu,[1] Patryk Kusch,[2] and Siegfried Eigler[1] ***

[1]Institute of Chemistry and Biochemistry, Freie Universität Berlin, Altensteinstraße 23a, 14195 Berlin, Germany

[2]Department of Physics, Freie Universität Berlin, Arnimallee 14, 14195 Berlin, Germany

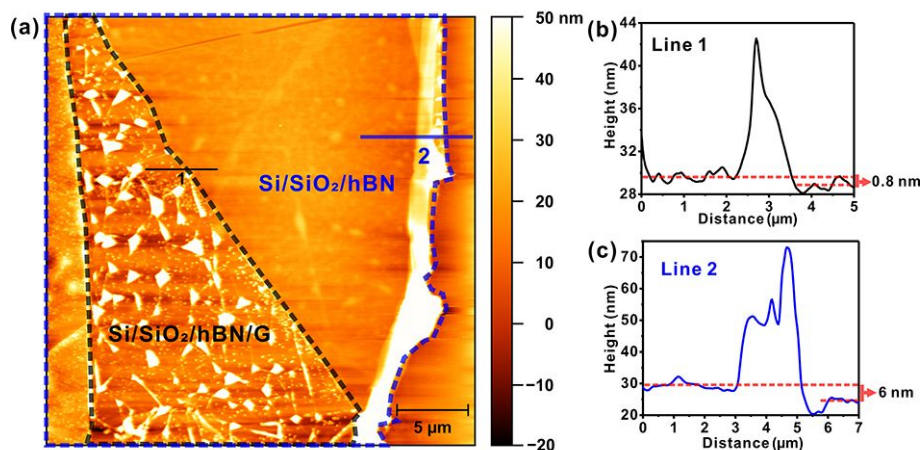*Corrsponding author: E-mail: siegfried.eigler@fu-berlin.de

1

Figure S1. AFM image of hBN/G heterostructure. Height profile of (b) the monolayer graphene along line 1 and (c) the few layer hBN flake along line 2 shown in (a).
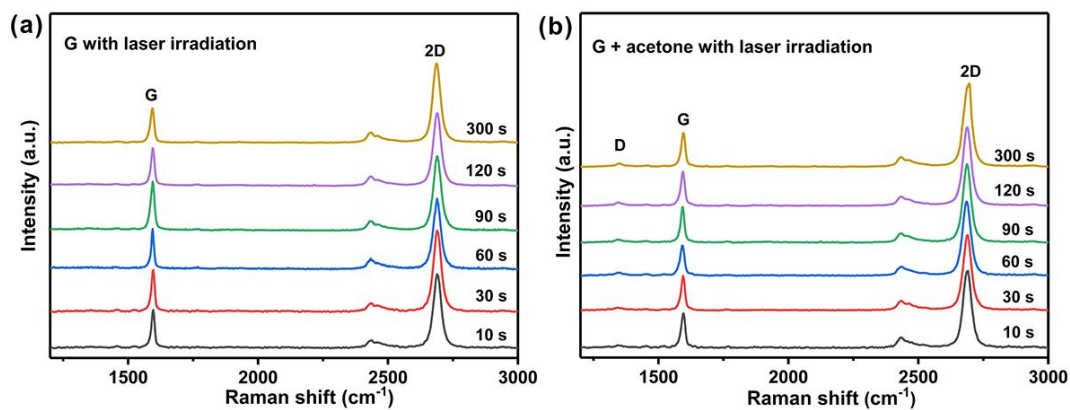

Figure S2. The read-out Raman spectra of laser irradiation test of pristine graphene and graphene with acetone after accumulated laser (532 nm, 1 mW) irradiation-time from 1 s to 300 s.
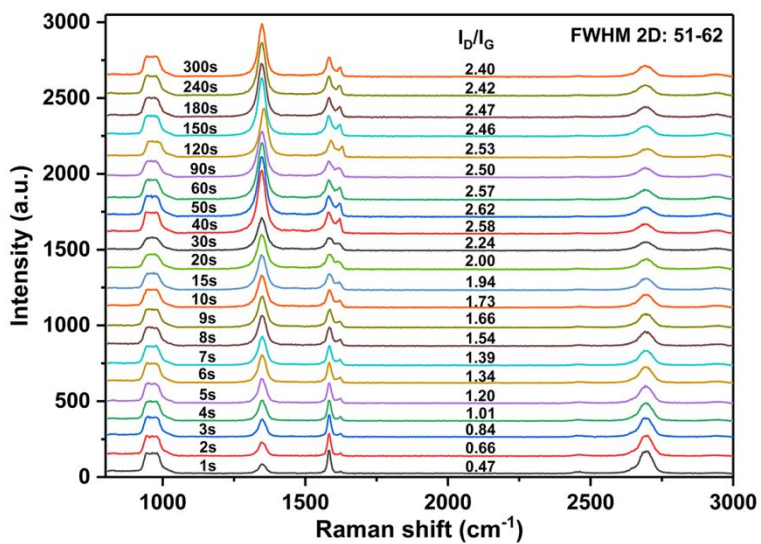
2

Figure S3. The read-out Raman spectra of functionalized G with benzoyl-peroxide (BPO) after

accumulated laser (532 nm, 1 mW) irradiation-time from 1 s to 300 s (FWHM: full-width at half-

maximum).
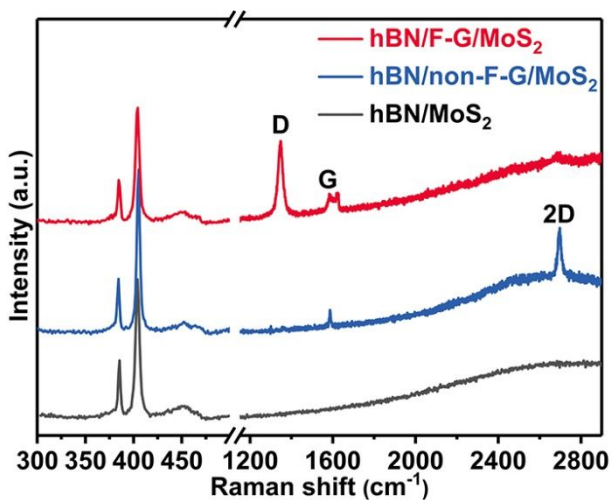
Figure S4. Raman spectra of hBN/(non-)F-G/MoS$_2$ heterostructure.
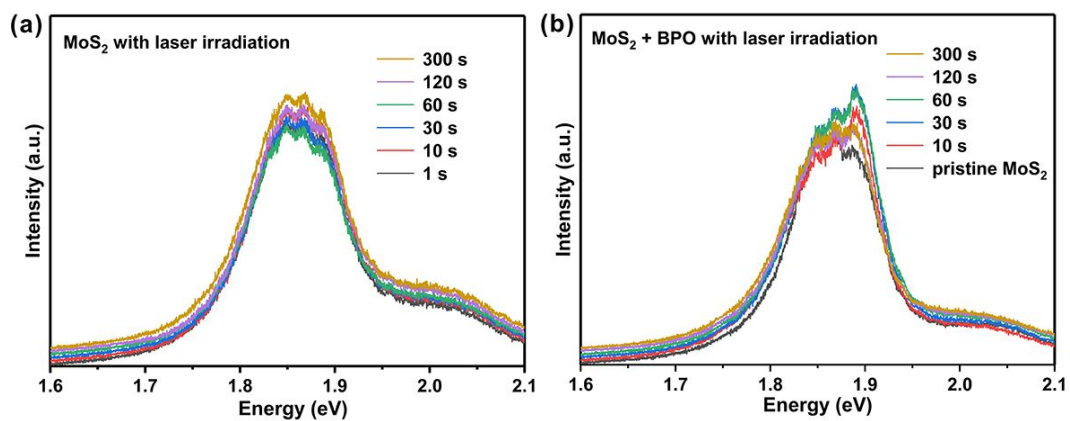
Figure S5. The read-out PL spectra (acquisition time 1s) of pristine MoS_2 and MoS_2 with BPO

after accumulated laser (532 nm, 1 mW) irradiation-time ranging from 1 s to 300 s.
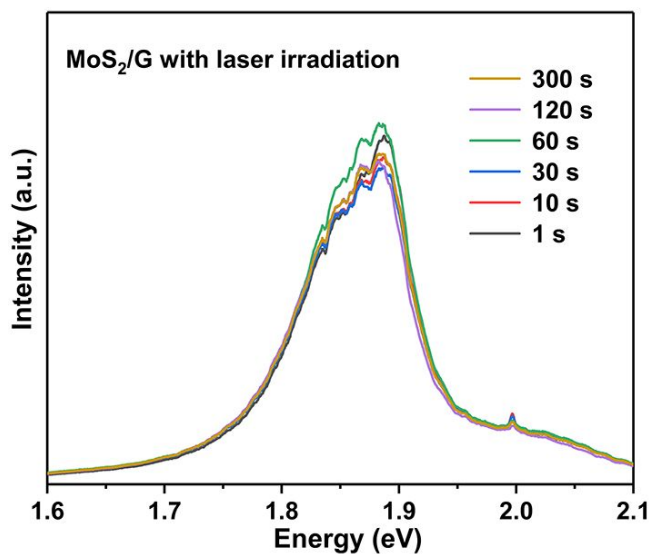
Figure S6. The read-out PL spectra (acquisition time 1s) of G/MoS_2 pristine heterostructure after

accumulated laser (532 nm, 1 mW) irradiation-time ranging from 1 s to 300 s.

4
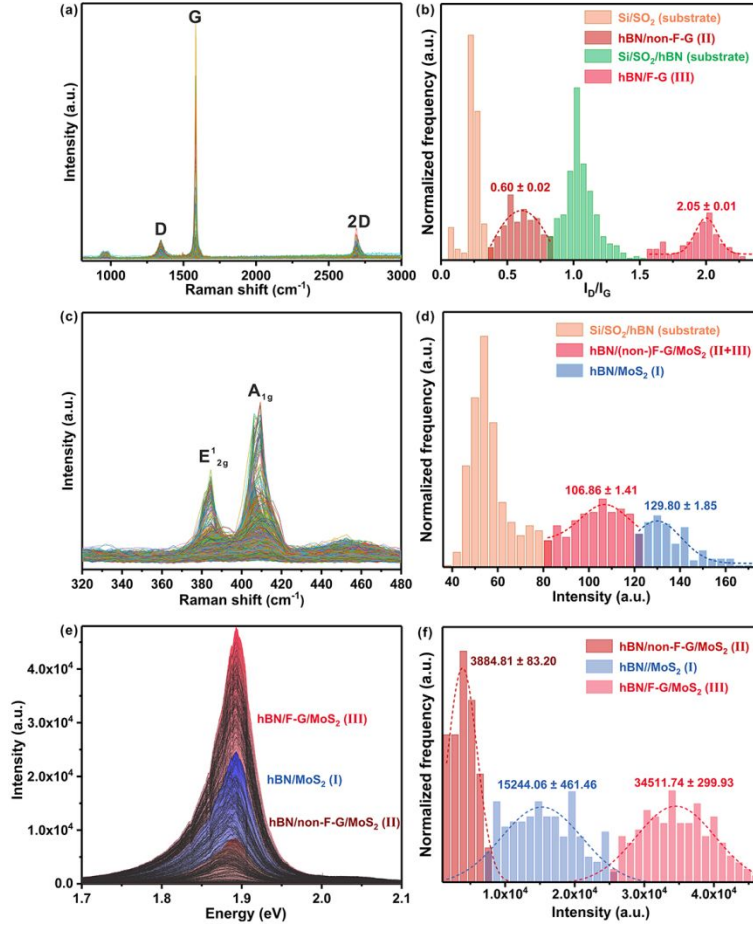
Figure S7. Raman, PL map profiles, and corresponding intensity frequency distribution over the entire hBN/(non-)F-G/MoS$_2$ heterostructures: (a-b) Raman statistics of hBN/(non-)F-G, (c-d) Raman statistics of MoS$_2$, and (e-f) PL statistics, which correspond to the mapping images shown in **Figure 1c**, **1f**, and **1g**, respectively.

5
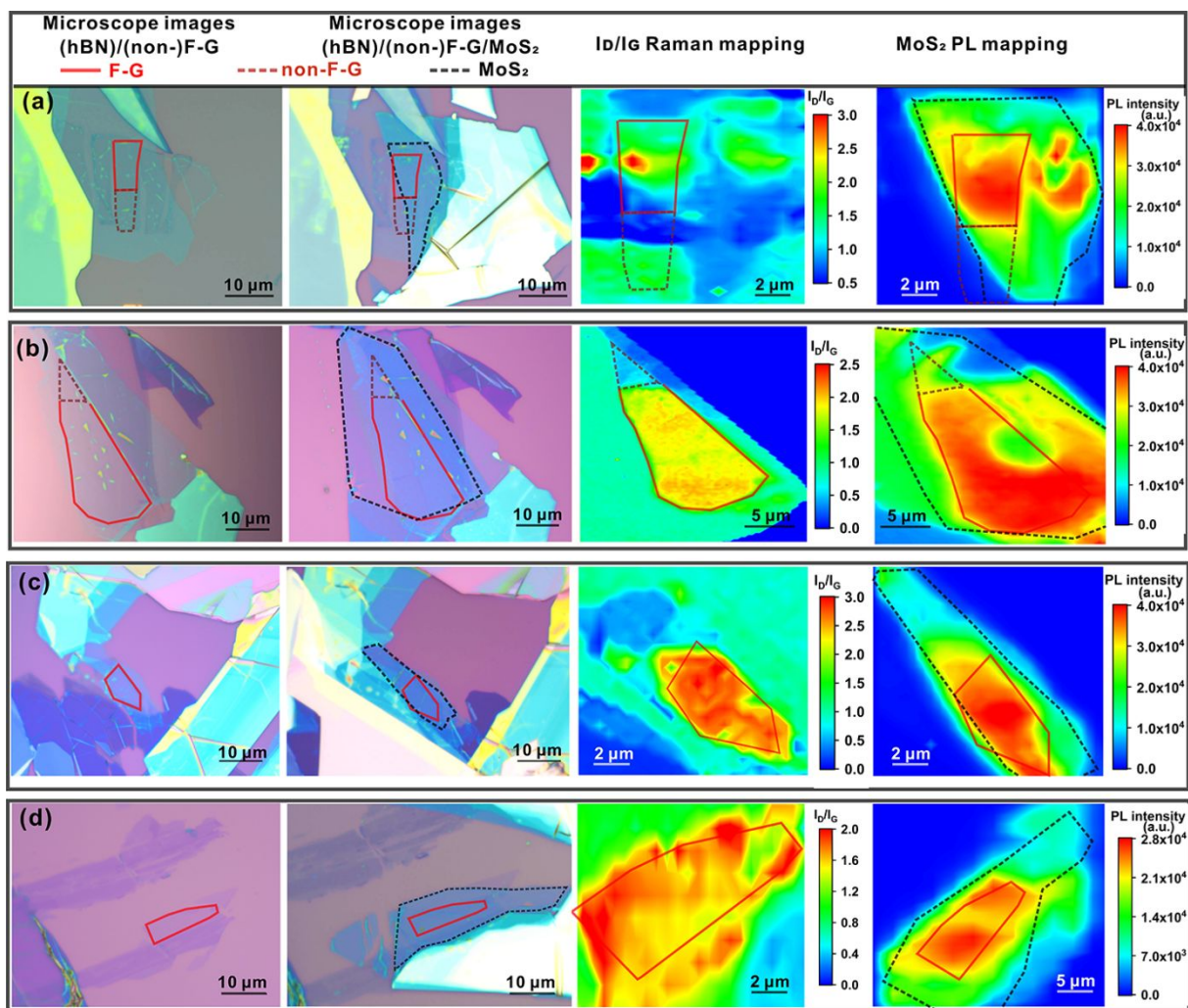
Figure S8. The microscope images, I_D/I_G Raman mapping, and MoS$_2$ PL intensity of four

different (hBN)/(non-)F-G/MoS$_2$ heterostructures.

6
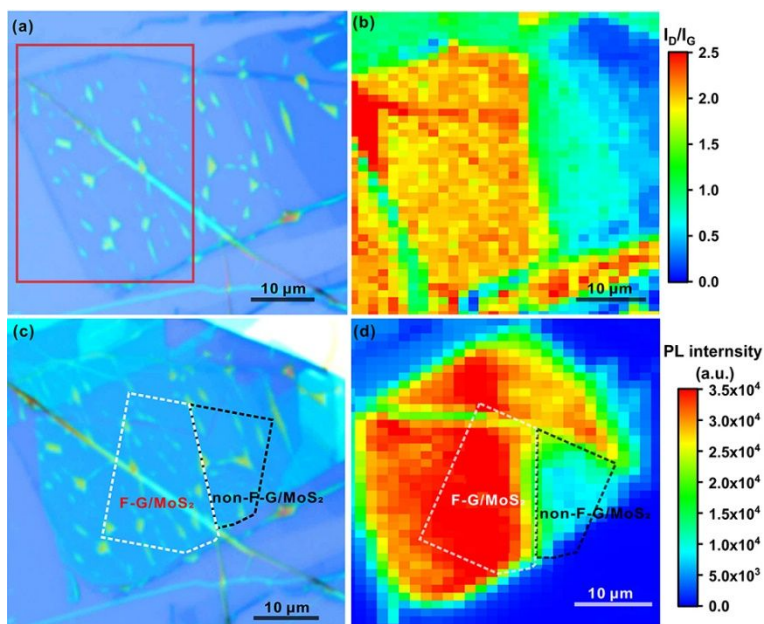
Figure S9. (a) Optical microscopy image of hBN/G heterostructure. Laser exposed area on

hBN/G as marked in the red box. (b) I_D/I_G Raman mapping of hBN/G after functionalization. (c)

Optical microscopy image and (d) MoS$_2$ Raman intensity mapping of hBN/(non-)F-G/MoS$_2$.

7
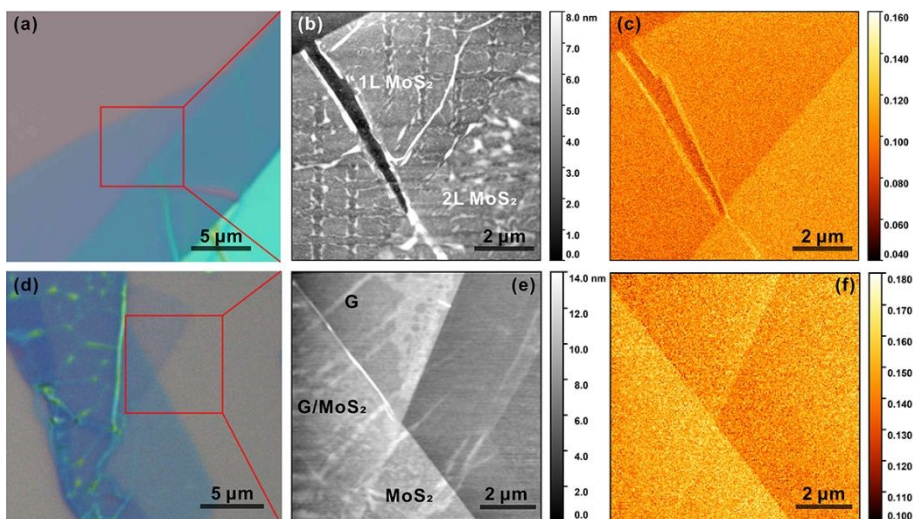
Figure S10. Optical microscopy images (a) and (d), AFM images (b) and (e), and s-SNOM

images (c) and (f) of Si/SiO$_2$/MoS$_2$ and G/MoS$_2$ heterostructures, respectively.
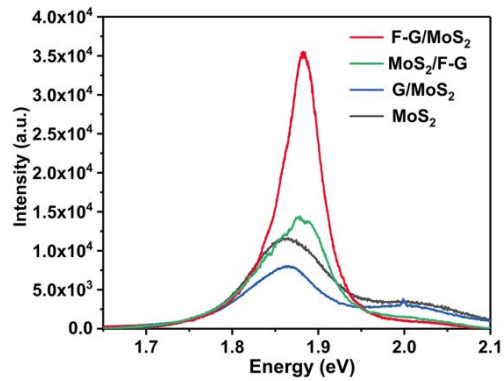
Figure S11. PL spectra of different structures on Si/SiO$_2$: F-G/MoS$_2$, MoS$_2$/F-G, G/MoS$_2$, and

MoS$_2$.
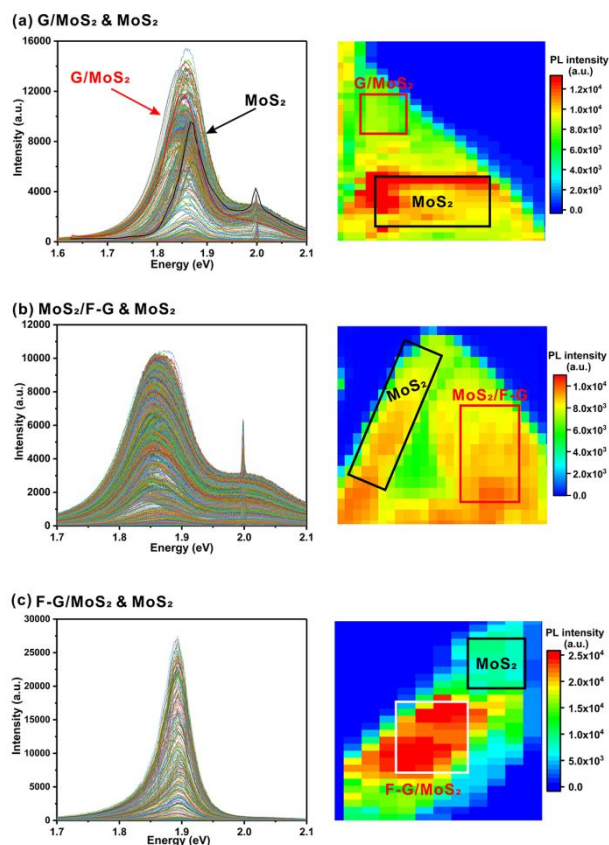
Figure S12. PL map profile and mapping of the four heterostructures on Si/SiO$_2$ wafers: (a-b) G/MoS$_2$ and MoS$_2$, (b) MoS$_2$/F-G, and (c) F-G/MoS$_2$. The normalized PL intensity shown in **Figure 4e** and **S11** are extracted from the relevant marked rectangles.

9
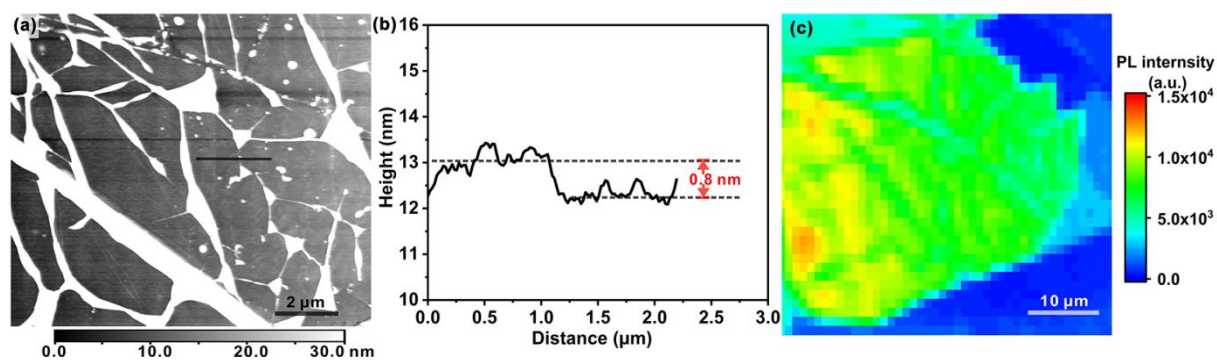
Figure S13. **(a)** AFM image, (b) height profile, and (c) MoS_2 PL intensity mapping of hBN/(non-)F-G/MoS_2 after annealing at 300 °C for 2 h (the characterizations of the sample before annealing are shown in **Figure 3** and **Figure S9**).
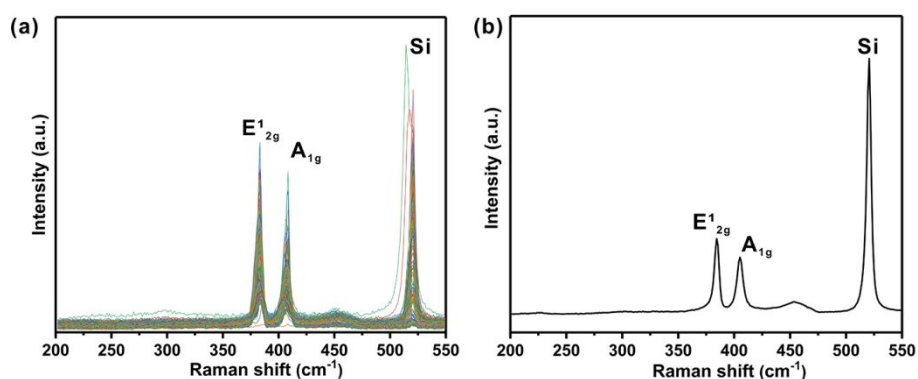
Figure S14. (a) Raman map and (b) average Raman map of MoS_2 over the de-F-G/MoS_2 heterostructure.

Table S1. Parameters about fitted PL peaks in **Figure 4e** by the Lorentz function.

	A^0		A$^-$		B		Area ratio of A^0/A$^-$
	Intensity	Area	Intensity	Area	Intensity	Area	
F-G/MoS$_2$	34406.4	2271.3	5629.7	511.5	424.4	70.3	4.4
MoS$_2$/F-G	12522.7	1198.1	4913.6	568.9	812.9	79.7	2.1
G/MoS$_2$	3122.6	359.3	8627.2	1198.8	2391.3	362.5	0.3
MoS$_2$	6321.6	794.1	7244.0	848.0	2224.2	302.7	0.9

5.3 Emerging Field of Few-layered Intercalated 2D Materials

Authors	Qing Cao, Fabian Grote, Marleen Hußmann, and Siegfried Eigler
Journal	*Nanoscale Adv.*, **2021**,*3*, 963-982
DOI	10.1039/D0NA00987C
Links	https://doi.org/10.1039/D0NA00987C
Detailed scientific contribution	The concept of this review was elaborated by all authors. All authors participated in writing this review, but primarily by Q. Cao and Prof. Dr. S. Eigler.
Estimated own contribution	~40%

ROYAL SOCIETY
OF CHEMISTRY

REVIEW

Check for updates

Emerging field of few-layered intercalated 2D materials†

Qing Cao, [ID] Fabian Grote, [ID] Marleen Hußmann [ID] and Siegfried Eigler [ID] *

The chemistry and physics of intercalated layered 2D materials (2DMs) are the focus of this review article. Special attention is given to intercalated bilayer and few-layer systems. Thereby, intercalated few-layers of graphene and transition metal dichalcogenides play the major role; however, also other intercalated 2DMs develop fascinating properties with thinning down. Here, we briefly introduce the historical background of intercalation and explain concepts, which become relevent with intercalating few-layers. Then, we describe various synthetic methods to yield intercalated 2DMs and focus next on current research directions, which are superconductivity, band gap tuning, magnetism, optical properties, energy storage and chemical reactions. We focus on major breakthroughs in all introduced sections and give an outlook to this emerging field of research.

1 Introduction

Our mobile and rechargeable world is based on intercalation chemistry. Thus, it is not surprising that the Nobel Prize in Chemistry 2019 was given to the pioneers of the Li-ion battery, Goodenough, Whittingham, and Yoshino.[1] The pioneering work of Whittingham was the report on the reversible intercalation of layered TiS_2 by Li-ions. The work of Goodenough led to the discovery of layered cobalt oxide as cathode material and the work of Yoshino explored graphite as anode material. Now, energy can be stored by collecting photons from the sun or collecting kinetic energy from wind or water and used at will.

With the discovery of graphene by Geim and Novoselov, which was awarded with a Nobel Prize in 2010 it was revealed that properties of materials change with thinning down to the single layer.[2] Thus, novel materials emerged and were studied by physicists. In addition, the chemistry of 2D materials (2DMs) came into the focus of research and new functionalization principles were developed, both of covalent and non-covalent nature.[3–5] Surface physics and surface chemistry, both accelerated in recent years and thus, researchers realized that 2DMs properties can be tailored by surface modification, such as the deposition of metal particles or organic donor and acceptor type molecules, respectively.[6,7] In general, countless investigations are being made into the chemistry and physics of 2DMs and a practically infinite variety is emerging. Thereby, transition metal dichalcogenides (TMDCs) or 2D allotropes of Si, Bi, P and others possess different band structures. Thus, 2DMs are insulators, topological insulators, semiconductors, conductors,

Institute of Chemistry and Biochemistry, Freie Universität Berlin, Takustraße 3, 14195 Berlin, Germany. E-mail: siegfried.eigler@fu-berlin.de

† Dedicated to Professor Andreas Hirsch on the occasion of his 60th birthday.

Qing Cao received her MSc from the Institute of Advanced Materials at Nanjing Tech University in 2019. She received her BSc in polymer materials from Shandong University of Science and Technology in 2016. She is currently a doctoral candidate in the research group of Prof. Siegfried Eigler at Freie Universität Berlin. Her research mainly focuses on intercalation and functionalization of 2D materials.

Fabian Grote is a doctoral candidate in the group of Prof. Siegfried Eigler at Freie Universität Berlin. He received his MSc in chemistry from the Julius-Maximilians-Universität Würzburg in 2019 and his BSc in chemistry from the Friedrich-Alexander-Universität Erlangen-Nürnberg in 2016. His research focuses on the chemistry and fundamental properties of oxo-functionalized graphene.

semimetals or semiconductors with direct or indirect bandgap.[8] In recent years, research on the fabrication of heterostructures is targeted by artificially assembling those 2DMs with combining and extending physical properties.[9]

Historically, the term intercalation and intercalation chemistry was coined by Rüdorff and Hoffmann in 1938,[10] although intercalation in the form of swelling was already observed in 1841 by Schafhaeutl.[11] Key-results of graphite intercalation compounds (GICs) are summarized and explained by M. S. Dresselhaus and G. Dresselhaus.[12] Thereby, intercalation is performed in bulk materials and various GICs are described, which are divided into acceptor and donor type GICs, respectively. Examples are graphite sulfate and potassium graphite, which are the best studied materials so far.[12]

However, in light of recent developments, it is more obvious than ever that the intercalation of stacks of 2DMs is of particular interest. While a single layer of a 2DM cannot be intercalated, bilayers (2Ls) and few-layers can already be intercalated, as summarized in this review. As known from the experience of graphene physics compared to graphite physics, the properties of single- and few-layered 2DMs differ from the bulk e.g. due to confinement of charge carriers.[13] Because of the ease of language, the expression "intercalation of 2DMs" is used in this article for the intercalation of any few-layered 2DMs. In addition, we propose to expand the terminology of intercalation, which should not be limited to the traditional process in which atoms or ions penetrate the galleries of layered compounds. In this review we use the term "intercalated" to describe the final product, which can be regarded as an intercalated layered system. Accordingly, a 2DM may be intercalated between molecular layers of e.g. organic molecules. In this example surface science and intercalation mix. A single layer of a 2DM may be intercalated between other 2DMs, such as graphene encapsulated between hBN layers, e.g. by artificial assembly, a structure which can also be termed as van der Waals (vdW) structure.[14] With this expanded view of intercalation, a huge research area can be identified and summarized.
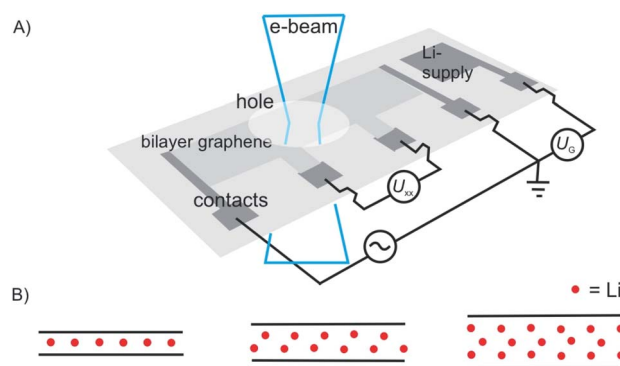

Fig. 1 Illustration of *in situ* transmission electron microscopy of the Li-intercalation process in suspended 2L graphene, triggered in a device. (A) Illustration of the device on a Si_3N_4-covered Si substrate. (B) from left to right: side-views of expected 'conventional' C_6LiC_6 configuration and of the experiment matching structures with 2L Li crystal and 3L Li crystal.[15]

As a motivating and fascinating recent example, we want to highlight the intercalation of 2L graphene by Li, a process which is related to the anode process of a Li-ion battery.[15] A 2L of graphene was mounted on a grid in the SALVE microscope (sub-Angstrom-low-voltage-electron microscope) and the intercalation was triggered by a 5 V potential (Fig. 1A). As depicted in Fig. 1, the process of intercalation can be followed microscopically with atomic resolution. The growth of the Li crystal between 2L graphene was conducted and filtering the structure of the 2L graphene led to the conclusion that the Li crystal differs from the expected packing for C_6LiC_6 (Fig. 1B), but can be explained by the formation of a 2L and a trilayer (3L) of Li. Thus, those results differ from bulk lithium graphite with the formular LiC_6, since more Li atoms can be intercalated between two layers compared to the bulk.

Other review articles and books are available, however summarizing primarily the intercalation of bulk materials. In particular the review by Stark *et al.* summarizes intercalation

Marleen Hußmann received her BSc as well as her MSc in chemistry from Freie Universität Berlin in 2016 and 2019, respectively. She is currently a doctoral candidate in the group of Prof. Siegfried Eigler with the research topic of photoluminescence analysis and construction of heterostructures including molecules.

Siegfried Eigler received his PhD in organic chemistry from the Friedrich-Alexander-Universität Erlangen-Nürnberg in 2006. Subsequently, he conducted basic research on electrically conductive polymers and graphene oxide as an industry chemist. In 2016 he accomplished habilitation at Friedrich-Alexander-Universität Erlangen-Nürnberg and became Associate Professor at the Chalmers University of Technology. Now, he is Professor at Freie Universität Berlin and his research focuses on the controlled chemistry of graphene, synthesis and evaluation of fluorophores and fabrication of devices.

114

processes not only on bulk, but also 2D level.[12,16–20] Thus, here we keep history and bulk information short, since it is covered in the above mentioned articles. Further, we introduce important principles relevant for few-layer, trilayer (3L), bilayer (2L) and monolayer (1L) intercalation. Moreover, we highlight the recent advances. More specifically, we will focus on concepts, the synthetic access to intercalated 2DMs and introduce common methods, such as vapor transport, solvent based or electrochemical methods and artificial assembly. Next, we highlight recent results and properties of intercalated 2DM systems.

2 Concept of staging

Here, we introduce concepts and definitions relevant for 2DMs intercalation, which are derived from definitions introduced for GICs. We note that the historical background and intercalation concepts for bulk materials are summarized in the excellent perspective article of Lerf.[20] In particular, staging and charge transfer are of importance to describe the structure and properties of intercalation compounds. With thinning down the bulk to the 1L additional considerations become important, which are bridging intercalation and surface science.

2.1 Staging in bulk materials

As depicted in Fig. 2A surface functionalization differs from intercalation. The most important concept for describing intercalated materials is staging, which is used to describe the structure of layered materials with guest atoms, ions or molecules. This concept is best studied for GICs. Accordingly, stage n was defined with n as number of layers. Thus, if we define A as materials layer and B as intercalant layer, stage 1 possesses an ABABAB sequence (Fig. 2B), stage 2 AABAABAAB sequence (Fig. 2C), stage 3 AAABAAAB sequence *etc.*

However, also mixed systems are possible with *e.g.* partially-filled layers, in particular occurring for natural systems, as a consequence of the kinetic control of intercalation (Fig. 2D). It is obvious that a small intercalant must enter the galleries of a layered bulk material from the side and intercalation starts from all rims at the same time. However, for the example of a stage 2 compound the hypothetical left rim intercalant does

Fig. 3 Concept of few-layer surface functionalization/intercalation. (A) Surface functionalized few-layer material, here the interior 2L differ from the outer layers; (B) as in (A), but with substrate influence leading to Janus-type properties; (C) few-layered material with intercalation only on the top; (D) and (E) illustration of stage 2 and stage 2′ intercalation for 3L materials.

not know at which layer the intercalant on the right rim starts. Such a mismatch cannot be corrected and will consequently lead to a mixed layer sequence. For a 2L material there is only one gallery to be intercalated. With the given examples, the difference between surface manipulation, by interacting molecules or atoms, and intercalation becomes clear, since with intercalation layers, the bulk can be influenced from inside. With thinning the layered materials, the surface becomes more important for manipulating materials properties and thus, interesting effects emerge as outlined in the next chapters.

2.2 From bulk to few-layers of intercalated 2D materials

Few-layered 2DMs are obtained at first sight with thinning down from bulk.[21] However, the concept of staging loses its validity with reaching 1L, instead surface science describes the systems. Here, we introduce some of the possible structures for few-layered systems, followed by three, two and one layers of 2DMs (Fig. 3 and 4).

As shown in Fig. 3A the four layers (4L) are an example of a few-layered material with the surface influenced by molecules or atoms. In that example with 4L the orange marked layers can be distinguished from the inner black marked layers and there is consequently a junction between orange and black layers. However, for more than roughly six layers surface functionalization does not play a crucial role for the interior layers, since the proportion of surface layers to the interior layers becomes minor.
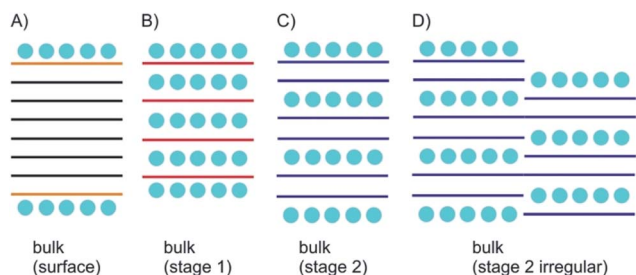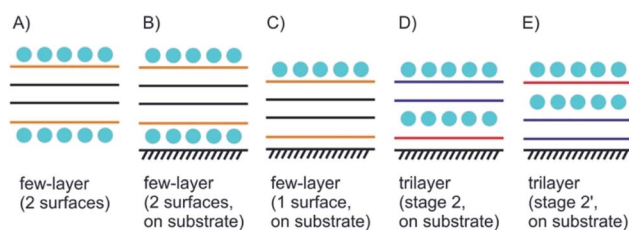

Fig. 2 Concept of bulk surface functionalization/intercalation. (A) Layered bulk material with surface functionalization; the interior is not influenced; (B) stage 1 intercalation compound; (C) stage 2 intercalation compound; (D) irregular, ill-defined stage 2 intercalation compound.

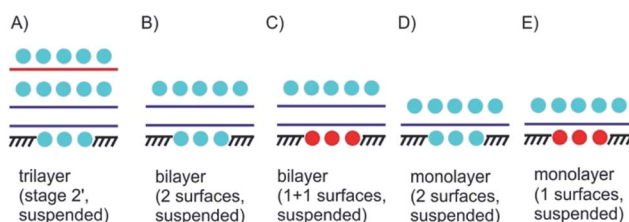Fig. 4 Suspended 3L, 2L and 1L materials with surface functionalization/intercalation. (A) 3L stage 2′ intercalated and bottom surface functionalization; (B) surface functionalized suspended 2L; (C) Janus-type surface functionalized 2L; (D) 1L material intercalated between molecular layers; (E) Janus-type suspended 1L material; (D) and (E) could be considered as 2D 1L intercalated between molecular layers.
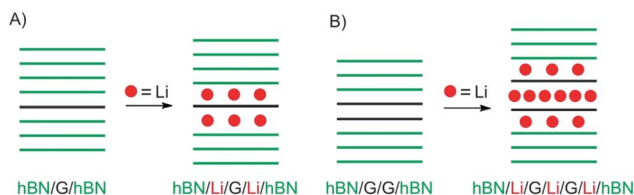
A) hBN/G/hBN → hBN/Li/G/Li/hBN ● = Li

B) hBN/G/G/hBN → hBN/Li/G/Li/G/Li/hBN ● = Li

Fig. 5 Study of device-based electrochemical intercalation of Li in heterostructures of (A) graphene (G) artificially intercalated in hBN and (B) 2L graphene artificially intercalated in hBN.

Even for the example of 4Ls the substrate plays an important role. As illustrated in Fig. 3B and C, with considering a substrate, Janus-type functionalization (different functionalities on two sides) is realized no matter whether atoms or molecules are placed between the substrate and the 2DM or not. For the 3L examples in Fig. 3D and E the concept of staging is adopted, here, with stage 2 as an example. Starting with a 3L on a substrate and an intercalant preferring stage 2 formation, two different configurations can be considered, and thus, either a 1L or 2L is on the substrate. Here, we introduce stage 2 and stage 2′, respectively, to differentiate between those two cases. The example in Fig. 3D starts from the top like a stage 2 compound. Thus, we assign stage 2′ to the example in Fig. 3E.

In Fig. 4A a stage 2′ structure is shown, however, in contrast to Fig. 3E the structure is suspended, which can be realized by placing the structure on top of a hole in the substrate. A similar structure is shown in Fig. 1A for a 2L of graphene. In general, with suspending few-layered 2DMs transmission is possible, however, also surface manipulation, such as doping becomes possible accounting for different surfaces. This is the point where surface science plays the decisive role in manipulating 2DMs. For a 2L both surfaces can be accessed by molecules or atoms, which are the same (Fig. 4B) or different ones (Fig. 4C); the latter leading to Janus-type functionalization. Taking the concept of staging into account a stage 2 configuration can be realized for a 2L, although no intercalation occurs. For a 1L similar surface functionalization is possible, as shown in Fig. 4D and E. In those examples, the 1L is however intercalated between molecular layers and thus, surface science and intercalation chemistry merge.

In a recent study, intercalation of vdW heterostructures of graphene and 2L graphene, respectively, was studied in an electrochemical device (as outlined in chapter 3).[22] The structures prepared are illustrated in Fig. 5A and B. As shown in Fig. 5A intercalation proceeds at the interface between hBN and graphene, on both sides. However, the properties differ from pure surface functionalization or a stage 1 bulk intercalation compound, due to the interaction of Li and hBN (about 30L on each side). The authors conclude that Li is randomly distributed, and the amount of Li atoms is significantly lower compared to the bulk with carrier densities of about 7×10^{13} cm^{-2}, corresponding to a stoichiometry of LiC$_{60}$.

In contrast, a 2L of graphene intercalated in hBN, as shown in Fig. 5B, behaves differently because intercalation of the 2L allows a much higher loading compared to the graphene/hBN

interface. Here, the carrier density was determined to 5.5×10^{14} cm^{-2}, with a contribution of 4.6×10^{14} cm^{-2} for the graphene/graphene interface.

2.3 Considerations on geometry and charge carrier densities

When approaching a 1L of a 2DM, or by stacking few-layers of 2DMs on top of each other or by intercalating materials, atomic-scale illustrations become important to imagine the dimensions. In this regard, structures are often evaluated by transport measurements in devices. As a result, the mobility of charge carriers is determined, either in field effect transistors or in magnetic fields by Hall-bar measurements. Finally, taking the dimensions of the device into account a charge carrier density is derived with the unit cm^{-2} for 2DMs. However, for an atomic imagination the unit cell dimensions are important to take into account. For graphene, the unit cell contains two carbon atoms, with two equal lattice vectors. The calculated area for one carbon atom is 0.026195 nm^2 or 0.026195×10^{-14} cm^2 (order of magnitude comparable to typical charge carrier densities), respectively.[23] This means that there are 38×10^{14} C-atoms per cm^2. For the example illustrated in Fig. 5, this consideration means that there is one charge on about 14 C-atoms, taking the 2L structure and interaction of all intercalated Li-atoms into account.

For MoS$_2$ the area of the unit cell is 0.088 nm^2 including one Mo and two S atoms, of which one points up and one down. Accordingly, there are 11×10^{14} Mo-atoms per cm^2 and 22×10^{14} S-atoms per cm^2. In another example the intercalated heterostructure MoS$_2$/Li/graphene was analyzed by density functional theory calculations,[24] with a charge carrier density of 3.6×10^{14} cm^{-2} for graphene and 6.0×10^{14} cm^{-2} for MoS$_2$. According to the considerations above those value relate to one charge carrier on about 10.6 C-atoms and 3.7 S-atoms, respectively.

A) T$_g$ Graphite ... T$_i$ Intercalant ... ● = K

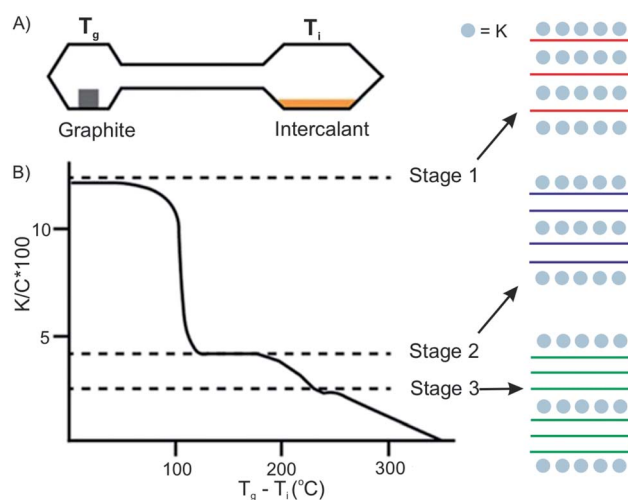B) K/C*100 ... Stage 1 ... Stage 2 ... Stage 3 ... T$_g$ - T$_i$ (°C)

Fig. 6 Two-zone thermal transport for potassium into graphite and stage control by temperature difference. Reproduced from ref. 16 with permission from Wiley-VCH Verlag GmbH & Co, Copyright 2019.

3 Synthetic access to intercalated 2D materials

3.1 Intercalation by vapor-transport

The vapor transport method usually proceeds under vacuum or an inert gas atmosphere in a sealed two-zone cell (Fig. 6A).[12] The intercalants and host materials are placed in separate zones, which are heated under different or same temperatures, respectively. The success of intercalation depends on controlling the temperature of the host zone and intercalant zone. Also, the stage of the intercalation compounds can be controlled by temperature adjustments. The temperature of the two zones can be different or isotherm, depending on the chemical and physical properties of the intercalant and the host material.[25] For example, the stage of the prototype intercalation compound K-GICs is controlled by the temperature difference $T_g - T_i$ (T_g: temperature of graphite; T_i: temperature of intercalant) as shown in Fig. 6B.[26] The higher stages are formed at a smaller $T_g - T_i$.

In the case of halogen intercalation, typical preparation temperatures are around 20 °C to 60 °C for T_g. Owing to the high threshold vapor pressure of the halogens, such as Br_2,[27] IBr and ICl, T_i is set from −30 °C to 60 °C to control the pressure in the reaction cell.[28] Other parameters, including heating time, the size of host materials, the amount of intercalant, and the volume and shape of ampoule also affect the homogeneity and in general the quality of the final compound.[12,29,30]

Vapor transport intercalation is the most widely applied method for the intercalation of bulk materials, because it works for most of the possible hosts, such as graphite,[12] fullerenes,[31] single-walled carbon nanotubes,[32] hBN[33] and TMDCs (MoS_2, TaS_2, WS_2 and WSe_2)[34–36] and a variety of intercalants, such as alkali metal (K, Rb and Cs)[26,37,38] or their alloys,[39,40] halogens (Br_2)[27] or interhalogens (IBr and ICl),[28,41] metal halides ($FeCl_3$, $AlCl_3$, $SbCl_5$ and AsF_5)[42–45] and organic molecules (pyridine, cyclopropylamine).[46] This method is already well developed for bulk intercalation. Thus, it can be easily and directly applied to 2D host materials using the same equipment (two-zone cell) and similar experimental conditions (temperature). The 2D host is normally deposited on a substrate or a manufactured device that can be directly inserted into the reaction cell, as depicted in Fig. 7A–D, illustrating $FeCl_3$ intercalation.[47] With reduced lateral dimensions, the intercalation rate of few-layered materials is much faster compared to the bulk. The synthesis of stage 1 alkali metal (K, Rb) GICs usually takes more than 12 h,[48] while only 5 min are needed for the intercalation of 1–15L of graphene.[49]

Over the past decade, progress has been made in few-layered 2DMs intercalation by the vapor transport method. The 2DM intercalation compounds were studied and some showed similarities to their bulk intercalation compound, such as the formed stage,[49,50] which offers good references for the investigation and characterization of few-layered 2DMs intercalation.
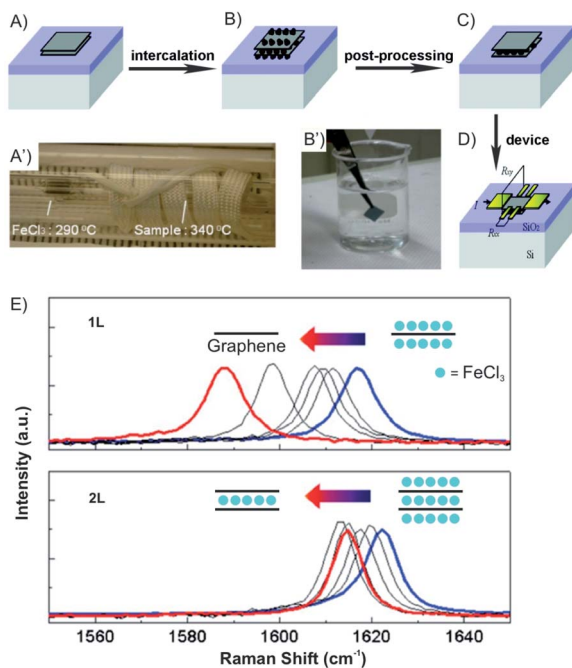
Fig. 7 Fabrication of an $FeCl_3$ intercalated 2L graphene device. (A) Pristine and (B) after $FeCl_3$ intercalation of 2L graphene deposited on Si/SiO$_2$ substrate. (A′) The sealed tube is placed in the furnace. (B′) Sufficient washing with acetone (C) removes the adsorbed molecules from the surface. (D) Deposition of electrodes using standard lithography fabrication techniques. (E) Gradual downshifts of the Raman G peaks is observed (after intercalation without air exposure; blue) and after washing in acetone for 0, 0.16, 0.5, 1 (black), and 12 h (red). Adapted from ref. 47 with permission from the American Chemical Society, Copyright 2011.
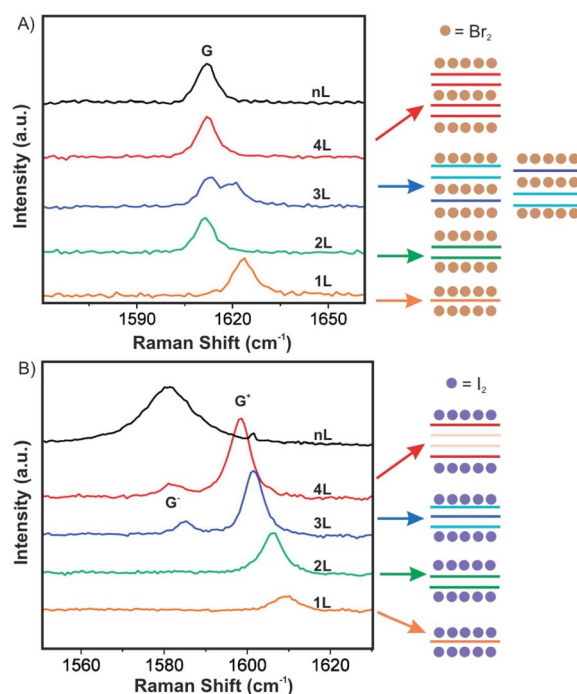
Fig. 8 Raman spectra of few layer graphene materials exposed to (A) Br_2 and (B) I_2 and the derived intercalation models. Adapted from ref. 50 with permission from the American Chemical Society, Copyright 2009.

For few-layered 2DMs the effect of surface adsorption of intercalants becomes non-negligible as discussed in chapter 2. For example, Br_2 and I_2 have been attempted to intercalate in mechanically exfoliated 1–4L of graphene on a p-type Si/SiO_2 wafer.[50,51] The wafer with host materials was placed in one zone of a glass cell, while liquid halogen was placed in another zone at a temperature of 10 °C to keep a constant vapor pressure in the cell. To avoid any impurities, the tube cell was initially evacuated to 2.7×10^{-5} mbar and the liquid halogen was frozen and thawed several times to remove dissolved gases. After 1 h of Br_2 exposure, Br_2 was successfully intercalated into 3L and 4L of graphene, respectively. In contrast, for 2L and 1L graphene, Br_2 was symmetrically adsorbed on the top and bottom surfaces. Those results are consistent with the observations made for the Br_2-GIC, with stage 2 as the lowest reported stage.[27] Accordingly, the model as shown in Fig. 8A is concluded from Raman spectra of the intercalation compounds. A single G peak near 1612 cm^{-1} is found for 2L and 4L graphene, which are symmetrically intercalated and doped, similar to the bulk Br_2-GIC reference. However, the 1L showed an upshift of the G peak to 1614 cm^{-1}, which relates to a higher charge carrier concentration for the single graphene layer. For intercalated 3L graphene, two G peaks are detected, which indicates two different types of inequivalent graphene layers as a result of asymmetric intercalation.

Few-layer graphene was also exposed to I_2. Raman spectra for 3L and more layers treated with I_2 showed two G peaks (Fig. 8B). This means I_2 adsorbs only on the top and the bottom of few-layer graphene without intercalation, possibly because the longer I_2 bond length does not allow an intercalation structure.[52] Similar to bulk intercalation, Br_2 is also the only diatomic nonpolar halogen molecule that can be easily intercalated into graphite. However, iodine in interhalogen compounds such as ICl and IBr can be intercalated.[53]

Compared to alkali metal intercalation compounds, it is reported that $FeCl_3$ intercalation compounds are relatively stable at ambient conditions.[54] Those materials can be safely removed

from their encapsulating ampoules for short periods of time, and therefore, provide prototype materials for the measurements to determine properties and further exploratory investigations. Due to that, $FeCl_3$ intercalation was investigated on the 2D level.[47,55–58] Accordingly, 1-4L graphene flakes were intercalated by $FeCl_3$ to a stage 1 intercalation compound ($FeCl_3$-few-layered graphene (FLGs), Fig. 9).[56] Owing to the highly hygroscopic property of $FeCl_3$, it was heated at 393 K for more than 90 min to remove any residual water. Next, $FeCl_3$ and the host were sealed in an ampoule and inserted in an oven at a reaction temperature of 613 K for 6 h. The Raman spectra for 1L, 2L and 3L graphene display an upshift of the G peak and a change of the 2D peak from a multi- to a single-peak structure. This is an indication of electronic decoupling of the layers by the intercalant for 2L and 3L graphene intercalated by $FeCl_3$. The single G peak also indicates uniform adsorption and intercalation of layers by $FeCl_3$ (Fig. 9A). For 1L graphene both surfaces adsorb $FeCl_3$ and the highest upshift of the G peak is observed at 1627 cm^{-1}, compared to 1623 cm^{-1} for $FeCl_3$ intercalated 2L and $FeCl_3$ intercalated 3L, respectively. However, multiple G peaks also have been reported in the Raman spectra of stage 1 $FeCl_3$-FLGs.[56–58] There are two explanations for this observation: (1) $FeCl_3$ molecules only intercalate between interlayers without adsorbing on the surface layers of graphene. The lower G_1 peak is a signature of a graphene sheet with only one adjacent $FeCl_3$ layer, whereas the higher shift G_2 peak characterizes a graphene sheet sandwiched between two $FeCl_3$ layers.[58] (2) The additional G peak is caused by nonuniform intercalation, due to desorption of $FeCl_3$ during cooling down in vacuum. To prove the hypotheses, $FeCl_3$-FLGs were exposed to air by two ways. In the first approach, $FeCl_3$-FLGs were immediately removed from the hot glass tube. In the second approach, the glass tube was first air-cooled to room temperature while still sealed and then the samples were removed. The samples obtained from the first method exhibited a single G peak and a higher doping level, which was stable up to one month in air.[56] Moreover, as shown
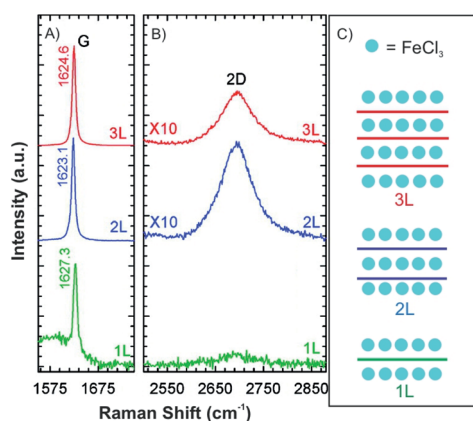
Fig. 9 (A) G peak, (B) 2D peak and (C) schematic illustrations of stage 1 for 1L, 2L and 3L graphene–$FeCl_3$ intercalation compounds. Adapted from ref. 56 with permission from the American Chemical Society, Copyright 2011.
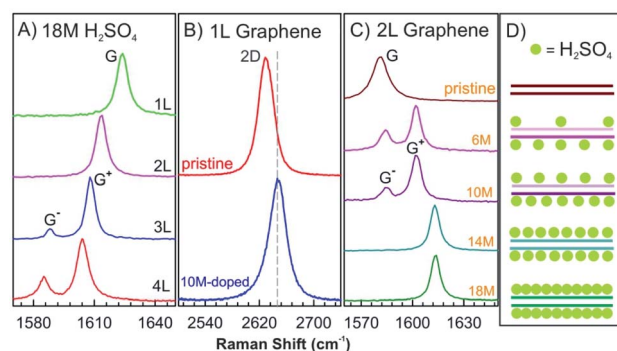
Fig. 10 (A) *In situ* Raman spectra of the G peak of 1–4L graphene samples dipped into 18 M sulfuric acid. (B) The 2D peak of pristine 1L graphene and that doped by 10 M sulfuric acids. (C) *In situ* Raman spectra of the G peak of the 2L graphene doped by different sulfuric acid concentrations of 18 M, 14 M, 10 M, and 6 M and a pristine BLG as a reference. (D) Structural model of 2L graphene structures doped with sulfuric acid derived from Raman spectra in (C). Adapted from ref. 62 with permission from the American Physical Society, Copyright 2010.
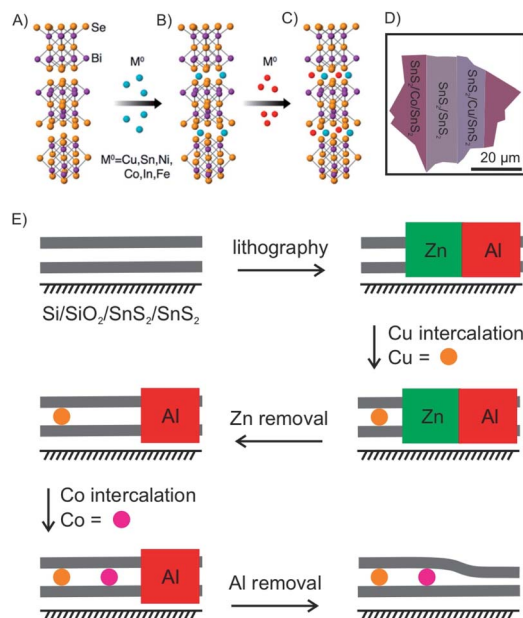
Fig. 11 Intercalation of (A and B) single and multiple (C) zero-valent metal atoms into Bi_2Se_3. Adapted from ref. 66 with permission from the American Chemical Society, Copyright 2015. (D) Schematic illustration of seamlessly integrated n-type SnS_2, p-type $Cu–SnS_2$ and metallic $Co–SnS_2$ within a single nanosheet. (E) Schematics of the spatially controlled intercalation process for 2L SnS_2.[67]

in Fig. 7B and C, adsorbed $FeCl_3$ on graphene surface can be simply removed by washing in acetone. According to the Raman spectrum, the G peak shifts down continuously with increased washing time. Finally, a 1L is recovered with a normal G peak position, which decreased to $\sim$1580 cm^{-1}, while the G peak of 2L graphene did not shift back to the undoped value (Fig. 7E). This difference indicates that the intercalated molecules are more stable owing to the protection between graphene layers, but would be eventually deintercalated by more extensive rinsing in acetone or other solvents such as hydrochloric acid.[47]

Through vapor transport intercalation, a lot of intercalant and host pairs have been fabricated on the bulk level (as mentioned above), but only few are reported for few-layered

2DMs. As the vapor transport method can directly be applied for few-layered 2DMs intercalation, more intercalants and host materials can be investigated in the future. However, the instability of the intercalation compounds hampers the real-time characterization and thus, also limits further investigations.

3.2 Solvent-based intercalation

Nonelectrochemical solvent-based intercalation is easy to apply, compared to other methods, since no special equipment or reaction conditions are necessary. Typically, the host material is soaked in a solution of the intercalant. The intercalation process is often accompanied by chemical reactions, enabling intercalation or post reactions. The most representative example is the synthesis of graphite oxide by Hummers method.[59] In the first step, graphite is dispersed in sulfuric acid with an oxidant to form graphite sulfate, an intercalation compound with the stoichiometry $[C_{24}^+HSO_4^- \cdot 2H_2SO_4]_n$.[10,60] During this process the oxidant p-dopes graphite enabling intercalation of hydrogensulfate counterions and sulfuric acid molecules.[61] With adding more oxidant, such as potassium permanganate further chemical modifications occur on both sides of the interlayers and finally covalent C–O bonds are formed. In this way, graphite oxide is formed, which can be delaminated to graphene oxide.[3]

Nevertheless, in the absence of oxidizing agents, this reaction works differently for 1–4L of graphene hosts, for which sulfuric acid molecules are found to be only physically adsorbed on the top and bottom layers without intercalation.[62] The G peaks of 1–4L of graphene in 18 M sulfuric acid show similar Raman spectra as observed for graphene few-layers with adsorbed I_2, although the chemical doping of I_2 vapours on graphene is quite different (Fig. 8B and 10A). The 2D peak of 1L graphene upshifts by about 10 cm^{-1} after dipping into 10 M sulfuric acid, as shown in Fig. 10B, which is a typical characteristic of hole doping in graphene layers.[63] As shown in Fig. 10C and D, the doping level of the top and bottom graphene layers can be asymmetric by adjusting the concentration of sulfuric acid to 6 M and 10 M, respectively. At a low concentration of sulfuric acid, the molecules are not completely adsorbed on the

Table 1 Summary of reactions to generate zerovalent species, and precursor chemistry. Adapted with permission from ref. 64 from the American Chemical Society, Copyright 2012^a

Intercalant	Precursor(s)	Reaction
Copper	Tetrakis (acetonitrile) copper(I) hexafluorophosphate	$2Cu_{(aq)}^+ \rightarrow Cu_{(aq)}^{2+} + Cu(0)$
Silver	Silver nitrate; 0.1 g 5,5,7,12,12,14-hexamethyl-1,4,8,11-tetraazocyclotetradecane	$2Ag^+ + L \rightarrow AgL^{2+} + Ag(0)$
Tin	Stannous chloride; 0.1 g tartaric acid	$2Sn^{2+} \rightarrow Sn^{4+} + Sn(0)$
Gold	Gold(I) chloride or chlorotristriphenylphosphine gold(I)	$3Au_{(aq)}^+ \rightarrow Au_{(aq)}^{3+} + 2Au(0)$
Indium	Indium(I) chloride	$3InCl \leftrightarrow InCl_3 + 2In(0)$
Cobalt	Dicobalt octacarbonyl	$Co_2(CO)_8 \rightarrow 8CO + 2Co(0)$
Iron	Iron pentacarbonyl	$Fe(CO)_5 \rightarrow 5CO + Fe(0)$
Nickel	Nickel(II) nitrate pentahydrate; hydrazine hydrate	$2Ni^{2+} + N_2H_4 + 4OH^- \rightarrow 2Ni(0) + N_2 + 4H_2O$

^{a} 1L = tetraazocyclic amine ligand.

two surface layers, which causes the splitting of the G peak, indicating two graphene layers of different doping degree.

Another advantage of the solvent-based intercalation is that zero-valent metal intercalation in 2D host materials can be realized, which is difficult to achieve with other intercalation methods. As illustrated in Fig. 11A a variety of zero-valent metal atoms, including Ag, Au, Co, Cu, Fe, In, Ni, and Sn, were intercalated into 2D layered Bi_2Se_3 nanoribbons (50 nm thick).[64] The zerovalent guest species were generated by a disproportionation redox reaction in solution or by carbonyl decomposition (Table 1) in a refluxing solution, and then intercalated into the layered Bi_2Se_3 structure. The atom% of intercalant is controlled by either the concentration or the reaction time. Among all the metal atoms, Cu showed the highest intercalation concentration up to 60 atom%, which is much larger than concentrations of compounds synthesized by heating or electrochemical insertion (below ∼3 atom%).[65] The Cu-intercalated nanoribbons appeared reddish, close to the colour of Cu metal, suggesting high concentrations of zero-valent copper. Additionally, 30 different ordered multiple pairs of zero-valent atomic species (Cu, Sn, Ni, Co, In and Fe) were also intercalated into Bi_2Se_3 nanoribbons by a stepwise combination of different solvent-based intercalation processes to form 2D alloys inside the host lattice (Fig. 11A and B). Depending on the type of intercalant and their intercalating order, the intercalant exhibits a variety of ordered and disordered structures (including superlattices and charge density waves). In most cases, the intercalant remains at zero valence.[66] Furthermore, chemical vapor deposition (CVD) grown n-type semiconducting 2L SnS_2, which was intercalated with Cu and Co atoms, is transformed into a p-type semiconductor and a highly conductive metal.[67] Combining this method with lithography, spatially controlled intercalation can be realized to seamlessly integrate n-type and p-type semiconductors and metals in 2DMs, which is difficult to achieve with mechanical transfer or other methods (Fig. 11D and E).[67] These methods have been further extended to intercalate various TMDCs (MoS_2, $MoSe_2$, $NbSe_2$, WS_2, Sb_2Te_3, In_2Se_3, GaSe)[68,69] and non-TMDs, such as MoO_3,[70] as well as incorporating dual metal elements into those materials. As apparent from the reported results it seems that the solvent-based method to intercalate zero-valent metals in 2DMs is universal, although more investigations are necessary.

Solution-phase intercalation has also been applied to MXenes,[71–73] a new family of 2D layered materials discovered in 2011.[74] Organic molecules[72,73] and alkali metal ions[71,75] have been investigated for the intercalation of solid MXene nanosheets. For example, hydrazine monohydrate, hydrazine monohydrate dissolved in N,N-dimethylformamide (DMF), urea and dimethyl sulfoxide (DMSO) were successfully intercalated into hydrofluoric acid (HF) modified 2D MXene f-Ti_3C_2 (Ti_3C_2(-OH)$_xO_yF_z$).[72] To prove the universality of this method rather than the exclusive property of f-Ti_3C_2, other MXenes Ti_3CN and TiNbC were also intercalated by hydrazine monohydrate. The intercalation process can be reversed by heating the intercalated material above the boiling point of the intercalated species leading to a recovery of the c-lattice parameter. DMSO-intercalated f-Ti_3C_2 can be exfoliated due to its hygroscopic

character by sonication in water affording a stable colloidal solution of separate sheets, from which a Ti_3C_2 film can be prepared on an Al membrane. Although there are many studies on bulk MXenes intercalation,[75–78] investigations conducted on few-layered MXenes remains a field of research which is in progress.

Solvent-based intercalation can be applied easily to few-layered 2DMs by immersing the substrate with the 2D host adsorbed on the surface into the solution of the intercalant.[62,79] Unlike electrochemical intercalation, solvent-based intercalation can intercalate insulating host materials, such as hBN.[80] The concentration of intercalants is adjustable by the concentration of solutions, however precise control is hard to achieve. It is reported that these intercalation compounds are more stable than those formed by the vapor-transport method, and can thus be easily characterized.[71,75] In addition, the intercalation may lead to exfoliation of the layered material or is reversible. These properties can be exploited either for preparing few-layered 2DMs, 2D intercalated materials or exploited in applications.

3.3 Electrochemical intercalation

Electrochemical intercalation allows to reversibly intercalate cations or anions into a layered host material driven by an external bias. For bulk intercalation, this is typically carried out in a three-electrode setup as depicted in Fig. 12. The host material serves as the working electrode (WE); therefore, it must be electrically conductive. The counter electrode (CE) is typically made of an inert metal plate or wire, e.g. Pt. A reference electrode (RE) provides a known potential (e.g. Ag/AgCl or calomel) that is used to reference the relative potentials of the WE and CE during the experiment. The electrodes are placed in an aqueous, non-aqueous or solid-state electrolyte containing a salt for ion conductivity and the intercalant.

A direct or alternating current between the WE and CE is applied by an external power supply. The applied voltage is measured versus the potential between the RE and the WE. The intercalant enters the galleries of the host either via the vdW gaps or through defects of the top layer.[82] The intercalation process can be followed in situ by the response of the current to the applied voltage. By further increasing the voltage, the
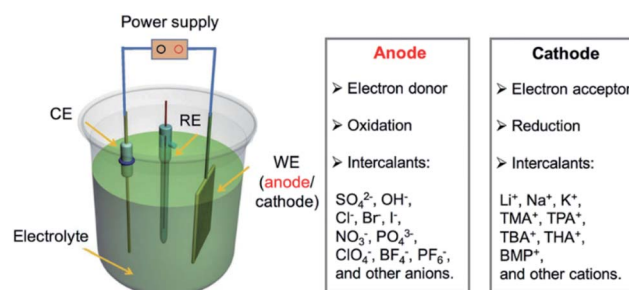

Fig. 12 Configuration of an electrochemical cell for bulk intercalation and typical reactions as well as typical intercalants. Reproduced from ref. 81 with permission from Wiley-VCH Verlag GmbH & Co, Copyright 2020.
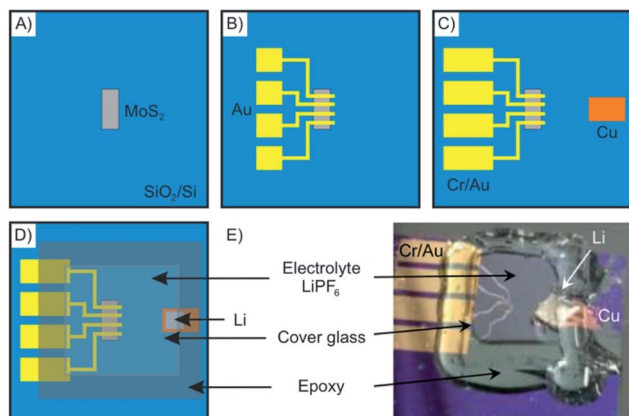
120

Fig. 13 Schematics showing the fabrication steps of an electrochemical device for *in situ* monitoring of Li intercalation into nanosheets of MoS_2. (A) Mechanically exfoliated MoS_2 flakes are deposited onto a Si/SiO_2-wafer. (B and C) Metal electrodes are deposited *via* e-beam lithography and shadow mask evaporation. (D) The electrolyte is applied on top of the electrodes and a cover glass is used to sandwich the device that is sealed by epoxy resin to avoid oxidation. (E) Photograph of the as-prepared electrochemical intercalation device. Adapted from ref. 84 with permission from the American Chemical Society, Copyright 2015.

electrochemical intercalation can be used to functionalize or exfoliate few-layered 2DMs from a bulk sample. In aqueous solutions, *e.g.* GICs can be further oxidized to graphite oxide, which is subsequently delaminated to yield graphene oxide.[83] This approach is not limited to graphite but can be applied to a wide variety of 2DMs such as black phosphorous, TMDCs and transition metal carbides, as recently reviewed elsewhere.[81]

Moving from the bulk to few-layered materials, the size of the experimental setup decreases accordingly. Microfabrication techniques are therefore required to fabricate electrochemical devices from few-layered 2DMs. The electrodes must be connected to a voltage source meter, either by placing on a conductive substrate or by contacting the flakes directly from the top by metal electrodes deposited onto the 2DM. In both cases the sample can lose electrical contact during the experiment due to swelling of the sample or deformation of the electrodes. The disadvantageous effect of swelling on the electrode contact may depend on the 2DMs thickness and should therefore be the smallest for a 2L device.

As an example, in Fig. 13 the fabrication of a microscopic electrochemical intercalation device is depicted. The device enabled investigating the process of intercalation of Li into 2–50 nm thin MoS_2. Such a typical device is fabricated starting by mechanical exfoliation of the 2DM. It is then dry-transferred onto a suitable substrate such as a Si/SiO_2 wafer (Fig. 13A). The 2DM can be subsequently etched into any desired shape to allow for example the *in situ* measurement of the Hall effect. The metal electrodes are then deposited by electron-beam lithography and physical vapor deposition (Fig. 13B and C). In the last fabrication step, the electrolyte solution containing the intercalant is applied onto the device (Fig. 13D and E). Measuring the small currents of the micrometer sized devices is challenging, however, possible.

In the case of few-layer intercalation of black phosphorous, the measured currents are in the range of tens of nanoampere.[85] Zhao *et al.* encapsulated single and few-layers of graphene between hBN layers for shielding from the environment and to avoid parasitic currents originating from reactions in the electrolyte.[22] The gold contacts used to contact the graphene layer were sealed using SU-8 resist to suppress any corrosion reactions at higher voltages.

The electrochemical intercalation between vdW heterostructures of different 2DMs is a huge new field of intercalation research. Zhao *et al.* not only used hBN to encapsule graphene layers and to avoid side reactions, but also studied the intercalation of Li ions at the interface of a single layer of graphene covered on both sides by hBN.[22] Other vdW heterostructures of graphene and MoS_2 were studied by Oakes *et al.* showing a large influence of strain at the interface of the two materials due to the lattice mismatch on the intercalation process.[86] In another study Bediako *et al.* investigated Li intercalation at the interface of heterostructures of hBN, graphene, MoS_2 and $MoSe_2$.[87] This growing new field of research is also reviewed elsewhere.[88]

Despite the possibility to electrochemical intercalation of a wide range of both anions, such as sulfates,[89] nitrates[90] and hexafluorophosphates[91] and cations into bulk materials, most of the recent reports on the intercalation of few-layered materials are focused on the intercalation by alkali metals, while examples of anion intercalation are scarce.[89] The intercalation of Li is by far the most studied process, which is motivated by the impact of its large-scale use in Li-ion battery technology. The intercalation of Li into few-layered 2DMs may help to better understand the underlying processes and guide further improvements of the technology.[84,92,93] As shown in the introductory example (Fig. 1), Kühne *et al.* showed superdense ordering of Li in 2L graphene.[15] They conclude that a 2L of graphene may spread more easily upon intercalation compared to its bulk counterpart, showcasing the differences between few-layer and bulk materials. In another study, they further showed very fast Li diffusion into 2L graphene with a diffusion coefficient as high as 7×10^{-5} cm^2 s^{-1}.[93] Aside from energy storage applications, electrochemical intercalation of charged organic
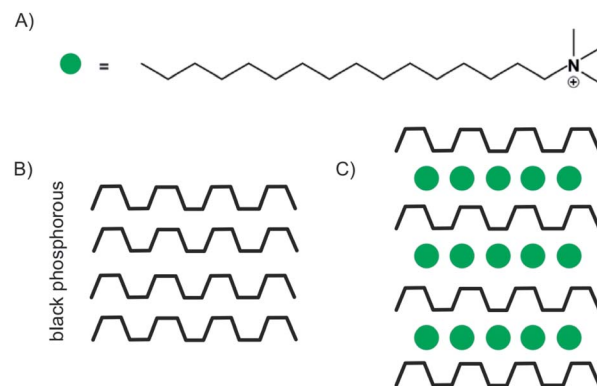

Fig. 14 (A) Illustration of the chemical structure of the cetyltrimethylammonium cation. (B) Schematic illustration of black phosphorous. (C) Schematic illustration of the stage 1 intercalation compound.[85]

molecules is used to fabricate well defined organic/vdW-hybrid heterostructures.[85,94] By applying a potential of −3 V, Wang *et al.* intercalated multi-layered black phosphorous nanosheets with cetyltrimethylammonium cations (Fig. 14A). The intercalation could be followed by the response of the electrochemical gate current measured *versus* the applied voltage. The interlayer distance increased from 5.24 Å to 11.21 Å as illustrated in Fig. 14B and C. Thereby, superlattices of alternating molecule and 2DM layers were formed in which the individual phosphorene layers are electronically decoupled from each other. The decoupling of the phosphorene layers leads to an increased optical bandgap, as observed by *in situ* photoluminescence measurements.[85]

Recently, He *et al.* performed the electrochemical intercalation of the neutral organic semiconductor molecule perylene-3,4,9,10-tetracarboxylic dianhydride (PTCDA) into few-layered MoS_2 demonstrating a powerful design scheme for the fabrication of well-defined organic devices.[95] This may bridge the gap from the research of 2DMs and vdW heterostructures and organic semiconductor research. Electrochemical intercalation of 2DMs enables a high control over the intercalation process by controlling the applied external bias. However, the 2DM must be conductive, excluding insulating materials such as hBN. Moreover, electrochemical intercalation requires the fabrication of microscale devices which increases the techniques complexity.

3.4 Artificial assembly

Artificial assembly, as sketched in the introduction, provides the opportunity to access distinct heterostructures to previously introduced conventional intercalation methods. The structures to be fabricated are not limited to certain ions or small molecules, which tend to intercalate specific hosts. Thus, the artificial assembly serves chances to integrate novel building blocks for the fabrication of few-layered intercalation compounds. However, the increasing freedom of parameters leads to complexity and thus a process, which is less controllable. For example, the integrity of the lattice of 1Ls may be harmed

during exfoliation and transfer. Thereby cracks or folds may be formed. Furthermore, each process may introduce contaminants. Moreover, controlling the respective orientations in stacked lattices, twisted layers can be formed in which however unique properties emerge from lattice mismatch.[96–98] Furthermore, the orientation of ions/molecules or the number of layers are other degrees of freedom to be considered. However, with overcoming those issues, extraordinary structures with outstanding properties are created, as outlined in chapter 4.

The mechanical transfer of 2DMs is based on overcoming vdW forces of stacked layers. It is a method to design structures of twisted layers,[97–99] containing molecules,[100,101] or of various 2DMs, such as graphene, hBN, TMDCs, black phosphorous or silicene. The yielded structures are also termed as heterostructures or vdW heterostructures.[102–104]

The most common transfer method for flakes is a dry stamp technique using polydimethylsiloxane (PDMS) as illustrated in Fig. 15. It is an easily handled, clean, fast and reliable technique compared to others, like vdW pick up, usage of a sacrificial layer or wedging method. Those methods have been extensively compared by Frisenda *et al.*[105]

With a PDMS stamp a 1L of bulk 2DMs can also be delaminated, a process, which is similar to the first invented scotch tape method (Fig. 15A). For the transfer, the flake is picked-up by the PDMS stamp, which is attached to a glass slide. The glass slide is fixed to a micromanipulator. Due to the transparency of PDMS, the alignment to an underlying flake or substrate can be traced under an optical microscope (Fig. 15B). After bringing PDMS and substrate in contact, PDMS can be slowly peeled off leaving the flake behind on the substrate (Fig. 15C–E).

The means of choice for large flake sizes, as can be produced by CVD, is a polymethylmethacrylate (PMMA)-supported etch transfer method (Fig. 16).[106] Therefore, PMMA is dropped on a large 1L, spin casted and dried to stabilize the intact lattice (Fig. 16B). In the case of CVDgrown graphene the underlying substrate is a Cu foil, which is *e.g.* etched by a $Fe(NO_3)_3$ solution and washed with water. For a Si/SiO_2 substrate the removal of
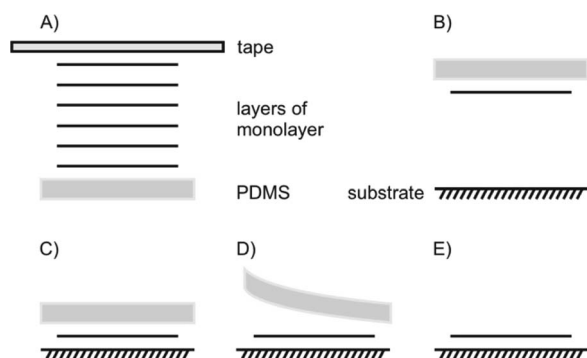
Fig. 15 Dry transfer with viscoelastic stamp of PDMS. (A) Tape exfoliation of bulk 2DM, (B) exfoliated 1L on PDMS, upside down attached to a glass slide, that PDMS and the target substrate can be aligned by a micromanipulator, (C) contacting PDMS/1L and substrate, (D) lift off of PDMS leaving the 1L on the substrate due to their stronger interaction, (E) transferred 1L on new substrate.
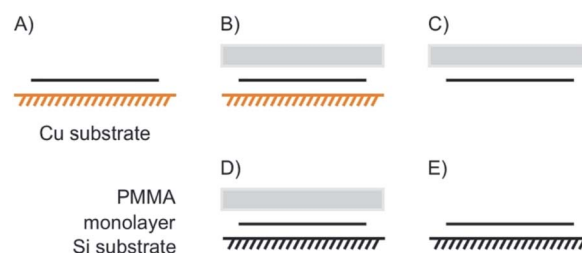
Fig. 16 PMMA supported etching transfer commonly used for large areas of CVD grown materials. (A) 1L on CVD supporting substrate (*e.g.* copper for CVD graphene). (B) Spin casting of PMMA on top of the 1L. (C) Removal of the substrate by etching. (D) Wet or dry transfer onto new substrate; wet transfer: after etching, PMMA/1L is washed in a water bath. By decreasing the water level, the 2DM can be transferred on a new substrate, which is placed at the bottom of the bath; dry transfer: an additional layer of PDMS is fixed on PMMA to handle PMMA/1L without the stabilizing interface of water. (E) PMMA is removed by acetone leaving the CVD 1L on new substrate.

122

the substrate can be achieved by intercalation of water between the hydrophobic polymer/flake and hydrophilic substrate (named wedging transfer method; Fig. 16C). In both cases a subsequent wet-transfer may be performed by decreasing the water level. However, also a dry transfer is possible (Fig. 16D).[107] Finally, PMMA is dissolved in acetone, rinsed and dried, leaving an intact lattice on the desired substrate (Fig. 16E).

Further methods are reported,[105,108–111] which are specific for materials, such as oxo-functionalized graphene,[112] TMDCs[113] or requirements due to the shape of the substrate.[114]

4 Directions of research of intercalated few-layer 2D materials

With thinning down the *z*-direction of layered 2DMs, properties changes, as introduced in the introduction. In this section, we highlight some research directions reported for intercalated few-layered 2DMs. In particular, we will focus on superconductivity, band-gap tuning, magnetic properties, optical properties, energy storage and chemical reactions.

4.1 Superconductivity

Superconductivity is a general research direction to find materials, which transport charge carriers at room temperature without resistance. The search for new superconductive materials is ongoing. In 1987 the Nobel prize in Physics was awarded to J. Georg Bednorz and K. Alex Müller "for their important break-through in the discovery of superconductivity in ceramic materials".[115] Thereby, the research is based on the preparation of oxo-cuprates. Currently, $Hg_{12}Tl_3Ba_{30}Ca_{30}Cu_{45}O_{127}$ holds the world record for superconductivity at ambient pressure at 138 K.[116] Superhydrides, which possess structures of solid atomic metallic hydrogen, such as LaH_{10} (ref. 117) show a transition temperature of astonishing 259 K, however, at 170 GPa.[118] The current world record holding superconductive materials are brittle and making km-long wires is not in reach. Thus, superconductivity in few-layered 2DMs would be the next superlative. Superconductivity is well-known for carbon materials, such as fullerenes,[119] carbon nanotubes[120] and diamond.[121] For graphene and doped graphene, superconductivity was predicted,[121] and for bulk CaC_6, synthesized from graphite and Li–Ca alloy, superconductivity was reported below 11.5 K.[122] A surprising discovery in this field was reported in 2018 for twisted 2L

graphene with a twisting angle of 1.1°. At this "magic-angle" superconductivity is occurring at 1.7 K.[97,123] In 2016 Ca intercalated 2L graphene (C_6CaC_6) was reported to be superconductive at 4 K.[124] The structure was prepared from epitaxial 2L graphene. First Li atoms were intercalated and then exchanged by Ca (Fig. 17). Although this temperature is lower compared to the bulk, the experiment demonstrates that superconductive properties remain in 2L. Also other intercalated 2DMs are predicted to be superconductive, such as 2L borophene (B_2MgB_2) below 23 K.[125]

4.2 Band gap tuning

In this section, we highlight the possibilities to tune the electronic properties of 2L and 3L graphene by intercalation. Since graphene lacks a band gap, conventional transistors with I_{on}/I_{off} ratios $>10^6$ are by far not possible.[12,126] Thus, opening a band gap is necessary to generate a transistor behaviour with reasonable I_{on}/I_{off} ratios. Breaking the inversion symmetry in 2L graphene is one way to induce a band gap.[127] It was reported that dual gating of 2L graphene can open a band gap, reaching even an insulating state.[128] With tuning the voltages of the top and bottom gate, tuning of the band gap of 2L graphene was demonstrated with values up to 250 eV.[129] Instead of dual-gating also intercalation/surface chemistry can induce a band gap.

Using density functional theory with vdW density functional, it was predicted that 2L graphene can be intercalated between K on the bottom and $FeCl_3$ on top to open a band gap in 2L graphene with application relevant 0.4 eV coming into reach.[132] Experimentally, a 2L of graphene was grown on Ru and
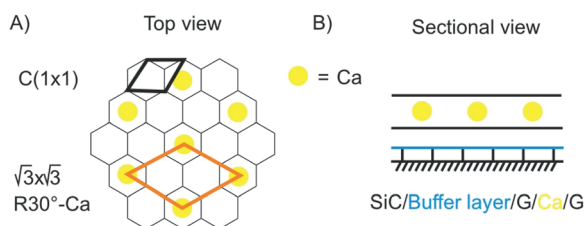
Fig. 17 Illustration of the structure of superconductive Ca-intercalated 2L graphene. (A) Top view with graphene lattice in grey and position of Ca atoms in yellow. (B) Sectional view illustrating the layered structure.[124]
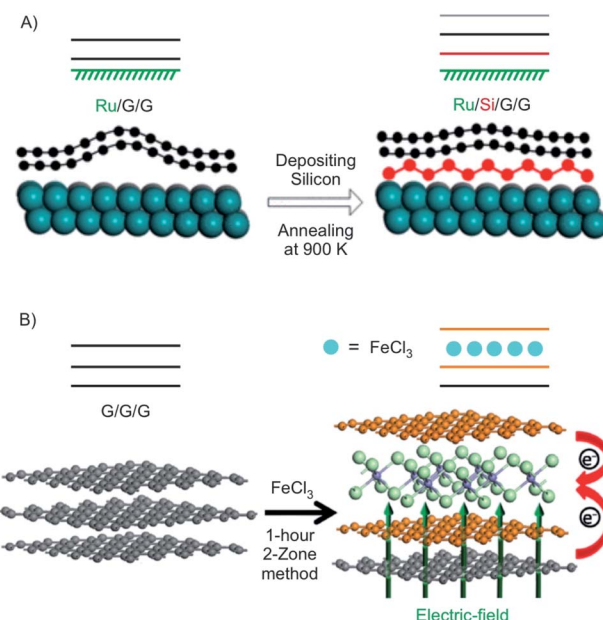
Fig. 18 (A) Illustration of the formation of the structure of Ru/Si/G/G with silicene intercalated between Ru and 2L graphene in which silicene induces a band gap. Adapted from ref. 130 with permission from the American Chemical Society, Copyright 2020. (B) Illustration of the intercalation of 3L graphene by $FeCl_3$. Reproduced with from ref. 131 with permission from Wiley-VCH Verlag GmbH & Co, Copyright 2020.

subsequently intercalated by silicene (Fig. 18A). It is reported that the layer of silicene, which is intercalated between Ru and the 2L of graphene induces a band gap of about 0.2 eV.[130] In another approach 3L graphene, prepared by mechanical cleavage, was intercalated by $FeCl_3$ by the two-zone method (Fig. 18B). Under the experimental conditions a stage 2 intercalation product is obtained, as evidenced by a splited G peak in the Raman spectrum. A band gap of 0.13 eV was calculated for the experimentally obtained structure. In addition, the authors report that the intercalation compound is stable in ambient conditions.[131] In general, the decomposition of $FeCl_3$ intercalated graphite is kinetically hindered, since water must diffuse into the interlayers. It is described that $[FeCl_2(OH_2)_4]^+$ and 4 Cl^- are initially formed by the reaction of 4 H_2O and $[FeCl_6]^{3-}$. Subsequently, $[FeCl_4]^-$ ions are formed, which are less densely packed.[133]

4.3 Magnetism

Among many important properties of 2DMs, the active magnetic response or magnetism has been studied for the development of various applications, including spill oil recovery, targeted drug delivery, and antibacterial interfaces.[134–137] Few-layered hosts with magnetic intercalants are unique systems to study magnetism in the 2D limit of materials.[47,57,138] $FeCl_3$ has been intercalated into macroscopic scale (1 cm²) epitaxial 3L graphene grown on 4H–SiC to a stage 1 compound (Fig. 19A).[57] The measured magnetoconductance shows a strong weak localization (WL) feature at cryogenic temperatures (<25 K, Fig. 19C). We note that similar WL in resistance have been reported in bulk magnetic-acceptor GICs ($FeCl_3$, $CoCl_2$),[139,140] where the abrupt change of resistance has been connected with its magnetic transition.[47]

As shown in Fig. 19B, a detailed study of the temperature dependence of the longitudinal magnetoresistance shows that the WL peak is heavily suppressed when the temperature increases. These findings demonstrate that the intercalation of $FeCl_3$ originates from single layer-like hole gases in the stacking with a phase coherence length ($L\phi$) as large as 1.17 ± 0.08 μm at 280 mK. The temperature dependence of $L\phi$ shows a steep decrease for temperatures higher than ~30 K (compatible with the 2D magnetic correlations in the plane of $FeCl_3$), while $L\phi$ tends to saturate at temperatures lower than ~4 K (compatible with 3D antiferromagnetic coupling between planes of $FeCl_3$).[57] For temperatures higher than 30 K, a sharper decrease of $L\phi$ is observed in $FeCl_3$-FLG, as compared to pristine graphene indicating that randomly oriented magnetic moments in the intercalated FLG are driving excessive dephasing (Fig. 19D). Ferromagnetism and superconductivity are two antagonistic phenomena since ferromagnetic exchange fields tend to destroy singlet Cooper pairs.

The coordination of these two competing phases has been achieved by alternative stacking of superconductor and ferromagnetic layers in vertical heterostructures.[142,143] However, an interlayer-space-confined chemical design (ICCD) is reported to integrate these two phases in one single-atom-doped TaS_2 layer, whereby ferromagnetism is observed in the superconducting
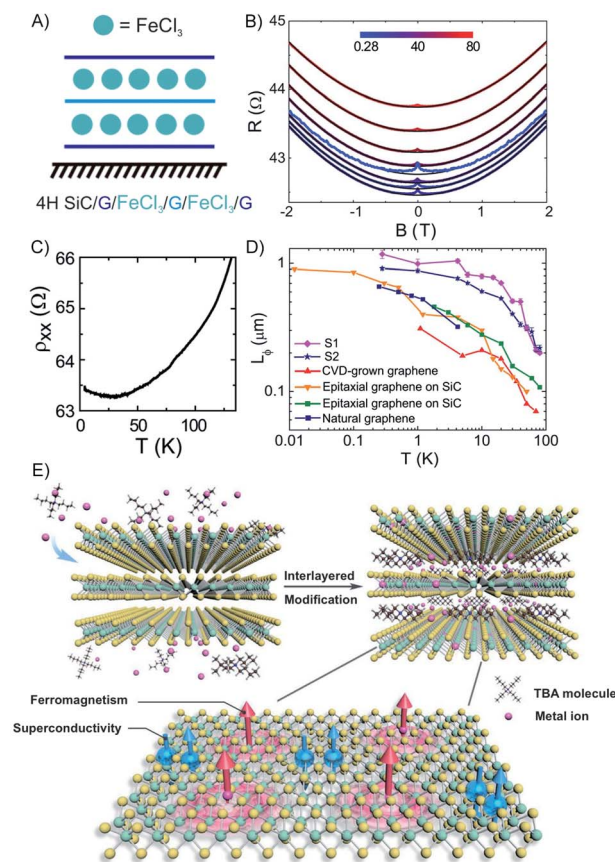
Fig. 19 (A) Scheme of $FeCl_3$ intercalated 3L graphene. (B) The temperature dependence of the longitudinal resistivity. (C) Magneto resistance at various temperatures (see color-coded legend). (D) The temperature dependence of $L\phi$ for pristine graphene prepared by different methods. The values are compared to other works (original works are referenced in the cited publication) to the estimated values of $FeCl_3$-3L graphene. Adapted from ref. 57 with permission from the American Chemical Society, Copyright 2014. (E) Illustration of the interlayer-space-confined chemical design toward the synthesis of TaS_2 inorganic/organic molecular superlattice with the superconducting regions and ferromagnetic regions in single atomic layers. Reproduced from ref. 141 with permission from Wiley-VCH Verlag GmbH & Co, Copyright 2020.

TaS_2 layers.[141] The intercalation of bulky 2H–TaS_2 crystal with tetrabutylammonium chloride molecules expands its gap between layers, now suitable for single-atom doping via co-intercalated Co ions, resulting in the formation of quasi-1L Co-doped TaS_2 superlattices (Fig. 19E). Furthermore, Co-doped TaS_2 is exfoliated into ultrathin flakes (20 nm) under ultrasonication and dispersed in DMF, by which their magnetic properties were investigated. Isolated Co atoms are decorated in the basal plane of the TaS_2 via replacing the Ta atom or anchoring at a hollow site, wherein the orbital-selected p–d hybridization between Co and adjacent Ta and S atoms induces local magnetic moments with strong ferromagnetic coupling. This ICCD approach can be applied to intercalate various metal ions, enabling the synthesis of a series of crystal-size TaS_2 molecular superlattices.

124

4.4 Optical properties

4.4.1 Transparency. The combination of transparency and electrical conductivity of materials is the basis for touchscreen applications or organic light emitting devices. Most touch panels use indium tin oxide and the surface resistance is between 5-100 Ω sq^{-1}. Thereby, the transmittance at 550 nm is about 85%. Reaching such values using 2DMs as single or multilayer is difficult. Graphene, as thinnest material absorbs 2.3% of light per layer and after chemical doping by *e.g.* TFSA (($CF_3SO_2)_2$NH) the resistance dropped to 129 Ω sq^{-1}.[144] With stacking four layers of graphene and doping by $AuCl_3$ the sheet resistance can be reduced to 34 Ω sq^{-1}.[145] However, intercalation of few-layer graphene, such as 4L or 5L was demonstrated to reduce the sheet resistance keeping the transparency high.[58] Thus, exfoliated few-layers, such as 5L graphene, were intercalated by $FeCl_3$ at 360 °C using the two-zone method. The realized sheet resistance for intercalated 5L graphene was determined to 8.8 Ω sq^{-1} at an optical transmittance of about 84%.[58] Large area graphene films (11 × 11 cm^2) were fabricated by artificial layer-by-layer transfer of $AuCl_3$ doped graphene. The sheet resistance of layer-by-layer $AuCl_3$ doped 4L graphene was 54 Ω sq^{-1} at 85% transmittance. This method offers not only an improvement of sheet resistance and uniformity but also better environmental stability compared to topmost layer doping.[146]

Metallization of graphite and few-layer graphene, respectively, is possible by intercalation with Li, K or Cs as intercalant.[38,49] With intercalation the Fermi level is shifted to higher energy. Accordingly, interband optical transitions are suppressed, which can be explained by Pauli blocking. Thus, the transmittance is increased and reaches the visible at high charge-carrier densities.[147] Since those optical transitions are no longer possible, as those states are filled by the heavy n-doping.

With n-doping of graphene the charge carrier density increases to about 6 × 10^{14} cm^{-2} and therefore the conductivity. The Fermi energy increases to about 1.5 eV.[149] This concept was studied *in situ* for few- and multilayer graphene.[148] As depicted in Fig. 20, a maximum in transmittance is reached at 500 nm for multi-layers of graphene, such as 19L with transmission of 91.7%. The results of *e.g.* few-layer graphene (8L) are also shown in Fig. 20.

4.4.2 Optoelectronic properties. Few-layered 2DMs and their heterostructures have shown great promise for new optoelectronic applications,[150,151] such as high-speed optical communications[152,153] and wide-optical-bandwidth photodetectors.[154,155] Graphene has attracted intense research due to its atomic layer thickness, ultrahigh strength and free carrier mobility. Nevertheless, the weak light absorption and zero bandgap of graphene largely limited its application in the optoelectronic field. Thus, graphene-based intercalated structures have been proposed to improve the low optical absorption and quantum efficiency of graphene. Fano-resonant Au plasmonic clusters have been sandwiched between 2L graphene producing a photodetector, where two graphene layers perform as two carrier channels. The photocurrent of the device was enhanced 8 times, which is owing to the hot electrons transfer generated in antenna structure and direct plasmon-enhanced excitation of intrinsic graphene electrons. The internal quantum efficiency for the device achieved up to 20% in the visible and near-infrared regions of the spectrum.[156] As a low-cost and easy-accessible alternative, rhodamine 6G (R6G) dye with only 1L thickness (0.85 nm) was deposited by a simple dip-
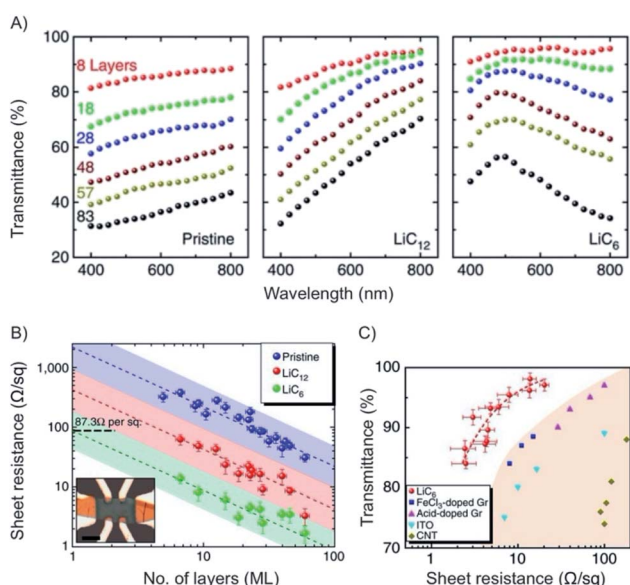
Fig. 20 (A) Plots of transmittance *vs.* wavelength for few- and multi-layers of graphene and intercalated materials. (B) Plot of the sheet resistance *vs.* number of layers of intercalated materials. (C) Plot of transmittance *vs.* sheet resistance for intercalated materials and other reference materials. Reprinted from ref. 148 with permission from Macmillan Publishers Ltd: Nature Communications, Copyright 2014.
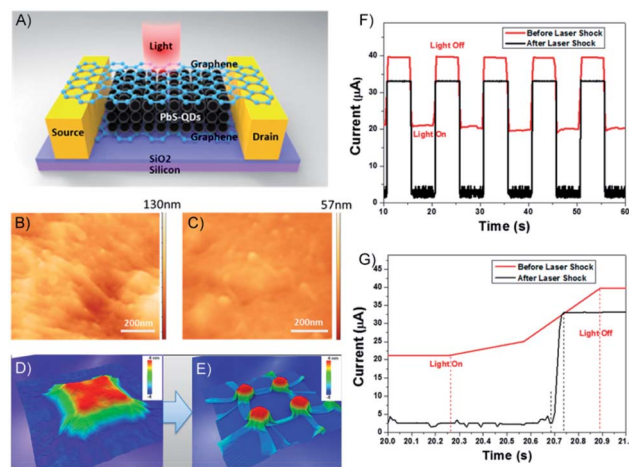
Fig. 21 (A) Structure of graphene/PbS/graphene hybrid structures. The channel length between source and drain is 50 μm. AFM image of graphene wrapped on PbS QDs (B) before and (C) after laser shock fabrication. Molecular dynamics simulation results demonstrate graphene wrapping on 3D feature surface (D) before and (E) after the laser shock process. (F) *I vs. t* curve of graphene/PbS/graphene hybrid photosensor before and after the laser shock process at the gate voltage of 20 V and (G) magnified image of (F). Adapted from ref. 158 with permission from the American Chemical Society, Copyright 2017.
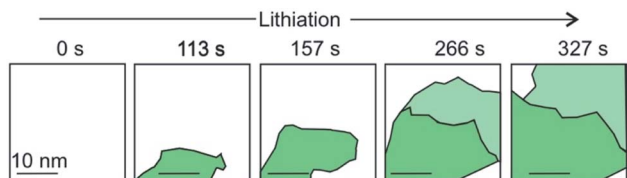
Fig. 22 A schematic and simplified illustration of the temporal evolution of lithium intercalation into 2L graphene as evaluated by transmission electron microscopy. Crystal grains are color-coded by their in-plane orientation in green and light green. More details can be found in the original figure.[15]

coating method to build a graphene–dye–graphene (G–R–G) sandwich photodetector.[157] The strong π–π interaction force in the G–R–G structure reduced the intermolecular distance, which accelerated the photoexcited charge transfer from the top and bottom graphene to the R6G 1L. The photocurrent and responsivity of the G–R–G device was found to be ∼40 times better than R6G-attached single-graphene device.[157] However, traditional transfer methods restrict the contact between the top layer of graphene and the underlying intercalant (especially for 0D and 3D intercalant) to grid-space contact, resulting in a weaker transmission in the structure and inevitable artificial scattering. To solve the problem, a graphene/PbS-quantum dots (PbS-QDs)/graphene sandwich structure with seamless 2D/0D contact was fabricated by laser shock imprinting, which opto-mechanically tunes the morphology of 2DMs to perfectly wrap on 0D materials and efficiently collect carriers from the PbS-QDs (Fig. 21A–E). This seamless integrated 2D/0D/2D structure significantly enhanced the carrier transmission, double increase of photoresponse, 20-fold response time and 13-fold photoresponse speed (Fig. 21F and G).[158]

The valley degree of freedom in 2D-crystals recently emerged as a novel information carrier in addition to spin and charge applications.[159] TMDC-1Ls feature a coupled spin-valley degree of freedom and have emerged as an exciting spin/valleytronic platform. However, the intralayer exciton spin/valley lifetime in 1L TMDCs is limited to tens of nanoseconds due to the unique spin-valley locking behaviour. Achieving long-lived population and polarization lifetimes in TMDC materials is of central importance for their optoelectronic, photonic, and spin/valleytronic applications.

Type II heterostructures, such as $WSe_2/MoSe_2$ have been fabricated to reach long valley polarization times, but precise control of the exciton transformation process (including intra-layer to interlayer exciton transition and recombination) and a valley polarization process *via* structural tuning is more challenging. An intermediate layer of hBN was transferred between a WSe_2/WS_2 heterostructure. The increased spatial separation with hBN intercalation weakens the electron–hole Coulomb interaction and significantly prolongs the interlayer exciton population and valley relaxation lifetime in vdW heterostructures.[160] Therefore, WSe_2/WS_2 heterostructures with 1L hBN intercalation exhibit a hole valley polarization lifetime of ∼60 ps at room temperature, which is approximately threefold

and 3 orders of magnitude longer than that in WSe_2/WS_2 hetero-2L without hBN and WSe_2-1L, respectively.[160]

4.5 Energy storage

The intercalation of Li ions into the galleries of a graphite anode is the key step of electrical energy storage in Li-ion batteries that are the major energy storage technology from electric cars to mobile devices. The ideal energy storage device must combine a high energy and power density with a long cycling lifetime. The energy density depends on the amount of charge that can be stored in the material. The power density depends on how fast the intercalant can diffuse into and out of the layered material. These two factors should be combined with a high cycling life time, that is a large number of intercalation/deintercalation cycles without significant performance loss. For the further development of this key technology a thorough understanding of the processes at the atomic level is highly desired. Studying the intercalation at the 2D level allows to follow the electrochemical intercalation process by various techniques *in situ* such as XRD,[161] Hall measurements[22,93] and also to follow the process by optical microscopy[89,162] and even transmission electron microscopy at atomic resolution.[15,93,163] TEM imaging not only allows to optically follow the intercalation and deintercalation of the ions into the few-layered 2DM, but also identifies areas of varying crystallinity and grain sizes (Fig. 22). As highlighted in chapter 1, Kühne *et al.* have demonstrated the Li intercalation of 2L and 3L graphene deviating from the expected C_6LiC_6 compound structure using TEM imaging at atomic resolution. The increased Li storage capacity by super dense ordering of Li in the vdW gap of 2L graphene compared to its bulk counterpart is attributed to the fact that
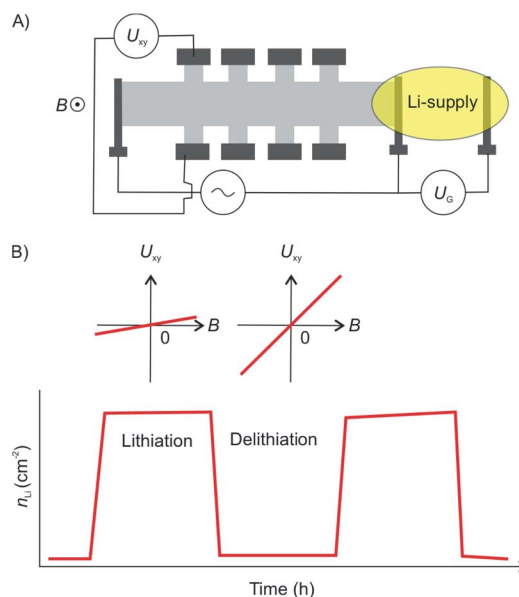

Fig. 23 (A) Illustration the 2L graphene device for measurement of Li-ion diffusion rates. The 2L device was shaped into a Hall bar configuration. (B) Lithiation/delithiation cycles visualized by charge carrier concentration extracted from Hall measurements showing full reversibility of the intercalation cycles.[93]

the 2L spread more easily when they are isolated from their bulk crystal. This finding indicates distinct Li storage arrangements with larger storage capacities in 2L compounds compared to their bulk counterparts.

The diffusion of the intercalant into the layered material is an important parameter as it defines the speed at which a device can be charged and discharged. The diffusion rate of Li ions into graphite is relatively low at 10^{-8} cm^2 s^{-1} resulting in a low power density of Li-ion batteries. By thinning down the electrode to 2L of graphene an exceptional diffusion rate of up to 7 $\times$ 10^{-5} cm^2 s^{-1} was reported.[93] The diffusion rate was determined by measuring the temporal evolution of the Li density at discrete positions in the device using Hall measurements (Fig. 23A and B). The increased diffusion rate is attributed to the widening of the vdW gap by the intercalated Li ions. Again, this effect can be attributed to the fact that the isolated layers may spread more easily compared to their bulk counterparts.

As a general scheme, tuning the interlayer distance in 2L materials can be used to engineer the energy storage properties. This can be achieved by stacking different 2DMs, creating vdW heterostructures. The intercalation of heterostructures of 2DMs with dissimilar properties may be a promising way to develop high-performance energy storage devices with increasing complexity. The combination of 2DMs allows to make use of the materials advantages by eliminating some of their shortcomings by creating new heterointerfaces and combining the materials electronic properties. For example, the expansion of an electrode upon intercalation is a crucial factor for the cycling lifetime of a battery device. A heterostructure of multi-layered VOPO$_4$ with multilayer graphene showed negligible expansion upon electrochemical intercalation and deintercalation with Na$^+$, K$^+$, Zn^{2+}, Al^{3+} cations that was attributed to the in-plane lattice mismatch and the resulting compressive strain on the VOPO$_4$ sheets.[164] As the number of 2DMs is still increasing they are covering a wide range of electronic properties from metallic materials such as Ti$_3$C$_2$, zero-band gap as in the case of graphene, semiconducting such as MoS$_2$ or black phosphorous to large band gap materials such as hBN. The combination of these materials creates a large library of new materials that allow to tune their electrode properties in energy storage devices.[165]

Mechanical strain induced by the lattice mismatch in vdW heterostructures has been demonstrated in multi-layered materials to control various materials properties.[166] Mechanical strain induced by the lattice mismatch of vertically stacked multi-layered MoS$_2$ and thin carbon layers was utilized to influence the pathways of electrochemical reactions upon Li intercalation. By engineering the strain in the system the chemical reaction could be influenced from intercalation in the pristine MoS$_2$ system to the chemical conversion to Lithium sulfide in the case of thin carbon layers stacked MoS$_2$ multi-layers.[86] On the 2L level, the Li intercalation in vdW heterostructures of graphene and molybdenum dichalcogenide (MoX$_2$, X = S, Se) encapsulated in hBN showed a 10-fold increase of accumulated charge compared to MoS$_2$/MoS$_2$ 2L devices as demonstrated by Bediako *et al.*[87] They fabricated five vdW heterostructures of graphene, TMDCs and hBN in which
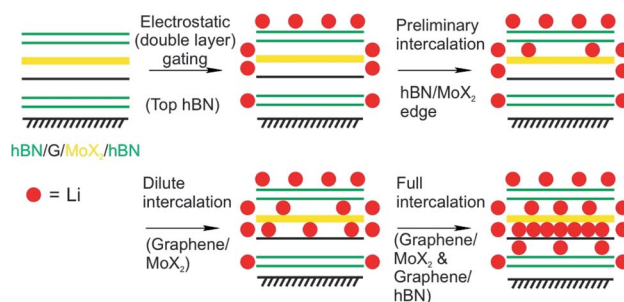

Fig. 24 Proposed four-step Li intercalation mechanism for a hBN (green)/MoX$_2$ (yellow)/graphene (black)/hBN heterostructure, evidenced by *in situ* HRTEM imaging.[87]

graphene and MoX$_2$ layers are encapsulated by hBN and employed as the working electrode of an electrochemical cell. By using the Hall potentiometry method they followed the Li intercalation upon sweeping the potential in various heterostructures. They elucidated the mechanisms of the Li intercalation at the various heterointerfaces. By combining the results of transmission electron microscopy, *in situ* magnetoresistance, optical spectroscopy techniques, *ab initio* calculations and low-temperature quantum magneto-oscillation measurements they derived an intercalation mechanism that describes the intercalation into a graphene/MoX$_2$ 2L encapsulated by hBN (Fig. 24). The proposed mechanism showcases the varying intercalation processes at the heterointerfaces of the 2DMs that can be understood by the Li binding energies calculated for the various heterointerfaces. Their study revealed that the capacity of the graphene/MoX$_2$ heterointerface is more than 10-times larger than the capacity of the other heterointerfaces (graphene/hBN, MoX$_2$/hBN). Furthermore, they observed a decreased onset intercalation voltage of graphene/MoX$_2$ that is about 0.5 V larger than that of a graphene/hBN heterostructure shown in a previous study.[22] MoS$_2$ undergoes a phase transition from the initial semiconducting H-phase to the metallic T'-MoS$_2$ phase after charge transfer from Li. This phase transition lowers the activation barrier for further Li intercalation.

4.6 Chemical reactions

The process of chemical reactions takes basically place on the surface of a bulk material. By thinning down the material, properties change such as the reactivity or absorption and emission properties for example in QDs, as outlined below. Not only by increasing the surface, but also by intercalation, layers become more accessible to the reactant or are activated by the intercalant. In principle, chemical reactions can be accelerated or observed for the first time in intercalated structures.

One of the first heterostructures with mixed dimensional materials (2D/0D/2D) consists of a graphene-coated TEM grid with thermally evaporated fullerenes and transferred graphene as top-layer (Fig. 25A and B).[101] Due to the low fullerene moving barrier of 5 meV, the self-assembly of the 0D component leads to big areas of single-layered, hexagonally closed packaging in between graphene. It turned out that the lattice spacing is 4–5%
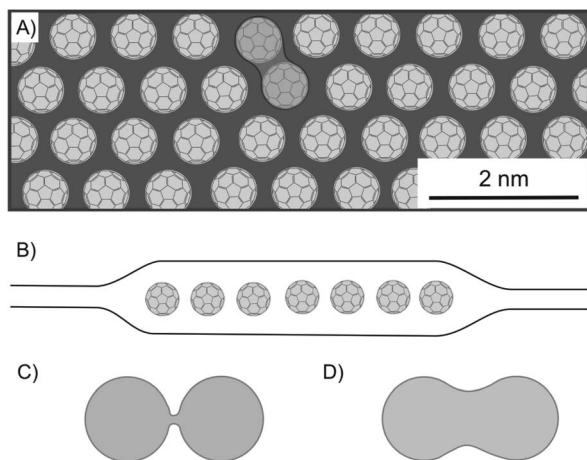
Fig. 25 Fullerenes encapsulated between graphene layers and investigated by STEM analysis. (A) Illustration of a 1L of hexagonally ordered fullerenes, showing a bonded couple. (B) Schematic illustration of the heterostructure of graphene/C_{60}/graphene. (C) Illustration of a loosely bound fullerene dimer and (D) of a fullerene peanut dimer.[101]

Fig. 26 Enhanced electron transfer in covalent bonded CdSe QDs/reduced graphene oxide (GR) heterostructure obtaining enhanced photoredox conversion. (A) Schematic and chemical structure of ethylenediamine functionalized graphene. (B) Schematic and chemical structure of sulfanylacetic acid functionalized CdSe QDs. (C) Schematic illustration of CdSe QDs/reduced graphene oxide heterostructure. (D) Comparison of conversion efficiency of the heterostructure and the sole QD for the oxidation of benzyl alcohol to the aldehyde. (E) Comparison of the conversion efficiency of the heterostructure and the sole QD for the reduction of nitrobenzene to aniline. Adapted from ref. 168 with permission from the American Chemical Society, Copyright 2019.

smaller than in equivalent 3D crystallites, while the fullerenes remain rotationally active. Although graphene acts as a protecting layer during STEM, the e-beam irradiation activates the molecules and causes bond formation between fullerenes forming a peanut-like dimer, as shown in Fig. 25A and D, a process which is supported by calculations starting from a loosely bound dimer of fullerenes (Fig. 25C). Due to the regular structure of the graphene lattices, those lattices can be filtered out in TEM images, enabling the unhindered observation and study of the intercalant. The encapsulation within graphene can also be applied to other 2DM, as demonstrated for MoS_2.[167] With this approach, molecular structures and their dynamics can be analyzed.

The factor for improving reactivity using the concept of heterostructures is significant for QDs.[168] QDs gained attention in photocatalysis for their high quantum yields and specific quantum confinement, but lacked in photostability, long lifetime and fast electron transfer. However, Huang *et al.* fabricated a heterostructure that did overcome those drawbacks (Fig. 26C).[168] The heterostructure is fabricated layer-by-layer, by electrostatic self-assembly in aqueous solution, with positively charged graphene oxide, which was functionalized by ethylenediamine (Fig. 26A), and negatively charged CdSe QDs, modified by sulfanylacetic acid (Fig. 26B) connecting graphene oxide layers and QDs by peptide bonds. Subsequently, reduction generates reduced graphene oxide, which is further termed as graphene. It was shown that graphene improves the photostability, adsorption of reactants and the separation of excitons of QDs due to fast electron transport.

The oxidation of aromatic alcohols to aldehydes (Fig. 26D), such as benzyl alcohol to benzaldehyde, and the reduction of nitroaromatics to amino aromatics, here to aniline (Fig. 26E), are enhanced compared to mere QDs, because the reactivity is ascribed to holes and electrons as well as hydroxyl radicals. The

heterostructure in this example possesses enhanced photoredox activity due to the artificial intercalation of QD between graphene.

5 Perspectives

We presented the emerging field of research of the intercalation of 2DMs with a special focus on intercalated 2L and 3L systems. As described in the last Section 4.6, a heterostructure assembled of a 2DM and a photosensitizer is promising for developing photocatalysts. However, the self-assembly strategy used in that example does not stop at the thinnest intercalated counterpart to the bulk but leads to 3D structures. Although not investigated yet, intercalated 2L systems bear a larger area for the interaction with substrate molecules and will possibly lead to higher quantum yields and thus, more efficiency. With thinning intercalated 2DMs the ultimate surface access is possible, in particular once intercalated few-layered 2DMs are placed on a membrane support, giving access to both sides. Furthermore, manipulating the intercalant can be highly effective in such systems, since only one layer of a 2DM is shielding the intercalant. Therefore, we speculate that novel concepts for sensing devices will emerge and unforeseen properties will be found, as already described for 1L or 2L graphene and the 2DMs family in general. Another benefit of thinning materials to the limit is the ability to observe elemental processes by spectroscopy probing the complete system compared to the surface as only a minor

128

part of the bulk, *e.g.* by Raman spectroscopy. Moreover, microscopes improve and can monitor intercalation processes on the atomic scale, leading to a better understanding of even application relevant charge storage systems. Assembly techniques are already established to fabricate complex layered systems, which are based on 2DMs as well as molecules, respectively. At the same time, different scientific fields come together and envision novel applications.

In this review, we focused on the fields of superconductivity, band gap tuning, magnetic ordering, optical properties, energy storage and chemical reactions. However, with advancing the field of intercalated few-layered 2DMs more functional systems with a defined focus on specific applications will emerge. Possible highlights in sensing applications can be imagined since it is already a highly active field of research relevant for all kinds of science, *e.g.* for sensing of small environmental molecules, monitoring biologically relevant species in cells, light sensors or mechanical force sensors, to mention only some. Finally, with increasing the understanding of intercalated 2DMs, it will be possible to gain more control over the chemistry, which can be induced close to the surface. Thus, there is a good chance to develop more energy-efficient chemical reactions with even accelerated kinetics and specificity.

Conflicts of interest

There are no conflicts to declare.

Acknowledgements

Notes and references

1 *Angew. Chem., Int. Ed.*, 2019, **58**, 16723, https://onlinelibrary.wiley.com/doi/epdf/10.1002/anie.201912886.

2 A. K. Geim, *Angew. Chem., Int. Ed.*, 2011, **50**, 6966–6985.

3 S. Eigler and A. Hirsch, *Angew. Chem., Int. Ed.*, 2014, **53**, 7720–7738.

4 A. Hirsch and F. Hauke, *Angew. Chem., Int. Ed.*, 2018, **57**, 4338–4354.

5 J. Sturala, Z. Sofer and M. Pumera, *Angew. Chem., Int. Ed.*, 2019, **58**, 7551–7557.

6 K. S. Subrahmanyam, A. K. Manna, S. K. Pati and C. N. R. Rao, *Chem. Phys. Lett.*, 2010, **497**, 70–75.

7 B. Cai, S. Zhang, Z. Yan and H. Zeng, *ChemNanoMat*, 2015, **1**, 542–557.

8 P. Miró, M. Audiffred and T. Heine, *Chem. Soc. Rev.*, 2014, **43**, 6537–6554.

9 K. S. Novoselov, A. Mishchenko, A. Carvalho and A. H. Castro Neto, *Science*, 2016, **353**, aac9439.

10 W. Rüdorff and U. Hofmann, *Z. Anorg. Allg. Chem.*, 1938, **238**, 1–50.

11 C. Schafhaeutl, *London, Edinburgh Dublin Philos. Mag. J. Sci.*, 2009, **16**, 570–590.

12 M. S. Dresselhaus and G. Dresselhaus, *Adv. Phys.*, 1980, **30**, 139–326.

13 A. T. S. Wee, *ACS Nano*, 2012, **6**, 5739–5741.

14 J. Wang, F. Ma and M. Sun, *RSC Adv.*, 2017, **7**, 16801–16822.

15 M. Kühne, F. Börrnert, S. Fecher, M. Ghorbani-Asl, J. Biskupek, D. Samuelis, A. V. Krasheninnikov, U. Kaiser and J. H. Smet, *Nature*, 2018, **564**, 234–239.

16 M. S. Stark, K. L. Kuntz, S. J. Martens and S. C. Warren, *Adv. Mater.*, 2019, **31**, 1808213.

17 J. Wan, S. D. Lacey, J. Dai, W. Bao, M. S. Fuhrer and L. Hu, *Chem. Soc. Rev.*, 2016, **45**, 6742–6765.

18 L. Daukiya, M. N. Nair, M. Cranney, F. Vonau, S. Hajjar-Garreau, D. Aubel and L. Simon, *Prog. Surf. Sci.*, 2019, **94**, 1–20.

19 Y. Li, Y. Lu, P. Adelhelm, M.-M. Titirici and Y.-S. Hu, *Chem. Soc. Rev.*, 2019, **48**, 4655–4687.

20 A. Lerf, *Dalton Trans.*, 2014, **43**, 10276–10291.

21 A. Jain, P. Bharadwaj, S. Heeg, M. Parzefall, T. Taniguchi, K. Watanabe and L. Novotny, *Nanotechnology*, 2018, **29**, 265203.

22 S. Y. F. Zhao, G. A. Elbaz, D. K. Bediako, C. Yu, D. K. Efetov, Y. Guo, J. Ravichandran, K.-A. Min, S. Hong, T. Taniguchi, K. Watanabe, L. E. Brus, X. Roy and P. Kim, *Nano Lett.*, 2018, **18**, 460–466.

23 S. Eigler, *Chem.–Eur. J.*, 2016, **22**, 7012–7027.

24 D. T. Larson, I. Fampiou, G. Kim and E. Kaxiras, *J. Phys. Chem. C*, 2018, **122**, 24535–24541.

25 L. B. Ebert, *Annu. Rev. Mater. Sci.*, 1976, **6**, 181–211.

26 D. E. Nixon and G. S. Parry, *J. Phys. D: Appl. Phys.*, 1968, **1**, 291–298.

27 T. Sasa, Y. Takahashi and T. Mukaibo, *Carbon*, 1971, **9**, 407–416.

28 D. E. Wessbecher, W. C. Forsman and J. R. Gaier, *Synth. Met.*, 1988, **26**, 185–194.

29 J. G. Hooley, W. P. Garby and J. Valentin, *Carbon*, 1965, **3**, 7–16.

30 J. G. Hooley, *Materials Science and Engineering*, 1977, **31**, 17–24.

31 M. J. Rosseinsky, *J. Mater. Chem.*, 1995, **5**, 1497–1513.

32 Y. Iwai, M. Hirose, R. Kano, S. Kawasaki, Y. Hattori and K. Takahashi, *J. Phys. Chem. Solids*, 2008, **69**, 1199–1202.

33 A. Sumiyoshi, H. Hyodo and K. Kimura, *J. Phys. Chem. Solids*, 2010, **71**, 569–571.

34 R. B. Somoano, V. Hadek and A. Rembaum, *J. Chem. Phys.*, 1973, **58**, 697–701.

35 F. J. Di Salvo, G. W. Hull Jr, L. H. Schwartz, J. M. Voorhoeve and J. V. Waszczak, *J. Chem. Phys.*, 1973, **59**, 1922–1929.

36 D. Dumchenko, C. Gherman, L. Kulyuk, E. Fortin and E. Bucher, *Thin Solid Films*, 2006, **495**, 82–85.

37 M. G. Alexander, D. P. Goshorn and D. G. Onn, *Phys. Rev. B: Condens. Matter Mater. Phys.*, 1980, **22**, 4535–4542.

38 M. H. Whangbo, W. Liang, J. Ren, S. N. Magonov and A. Wawkuschewski, *J. Phys. Chem. C*, 1994, **98**, 7602–7607.

39 S. A. Solin and H. Zabel, *Adv. Phys.*, 1988, **37**, 87–254.

40 N. Emery, C. Hérold, J.-F. Marêché and P. Lagrange, *Sci. Technol. Adv. Mater.*, 2008, **9**, 044102.

41 W. Krone, G. Wortmann and G. Kaindl, *Synth. Met.*, 1989, **29**, 247–252.

42 J. G. Hooley and M. Bartlett, *Carbon*, 1967, **5**, 417–422.

43 J. G. Hooley, *Carbon*, 1973, **11**, 225–236.

44 L. Salamanca-Riba, G. Roth, J. M. Gibson, A. R. Kortan, G. Dresselhaus and R. J. Birgeneau, *Phys. Rev. B: Condens. Matter Mater. Phys.*, 1986, **33**, 2738–2748.

45 C. Zeller, L. A. Pendrys and F. L. Vogel, *J. Mater. Sci.*, 1979, **14**, 2241–2248.

46 A. R. Beal and W. Y. Liang, *Philos. Mag.*, 2006, **27**, 1397–1416.

47 N. Kim, K. S. Kim, N. Jung, L. Brus and P. Kim, *Nano Lett.*, 2011, **11**, 860–865.

48 M. E. Huster, P. A. Heiney, V. B. Cajipe and J. E. Fischer, *Phys. Rev. B: Condens. Matter Mater. Phys.*, 1987, **35**, 3311–3326.

49 N. Jung, B. Kim, A. C. Crowther, N. Kim, C. Nuckolls and L. Brus, *ACS Nano*, 2011, **5**, 5708–5716.

50 N. Jung, N. Kim, S. Jockusch, N. J. Turro, P. Kim and L. Brus, *Nano Lett.*, 2009, **9**, 4133–4137.

51 N. Jung, A. C. Crowther, N. Kim, P. Kim and L. Brus, *ACS Nano*, 2010, **4**, 7005–7013.

52 J. G. Hooley, *Carbon*, 1972, **10**, 155–163.

53 C.-J. Shih, A. Vijayaraghavan, R. Krishnan, R. Sharma, J.-H. Han, M.-H. Ham, Z. Jin, S. Lin, G. L. C. Paulus, N. F. Reuel, Q. H. Wang, D. Blankschtein and M. S. Strano, *Nat. Nanotechnol.*, 2011, **6**, 439–445.

54 D. J. Wehenkel, T. H. Bointon, T. Booth, P. Bøggild, M. F. Craciun and S. Russo, *Sci. Rep.*, 2015, **5**, 7609.

55 D. Zhan, L. Sun, Z. H. Ni, L. Liu, X. F. Fan, Y. Wang, T. Yu, Y. M. Lam, W. Huang and Z. X. Shen, *Adv. Funct. Mater.*, 2010, **20**, 3504–3509.

56 W. Zhao, P. H. Tan, J. Liu and A. C. Ferrari, *J. Am. Chem. Soc.*, 2011, **133**, 5941–5946.

57 T. H. Bointon, I. Khrapach, R. Yakimova, A. V. Shytov, M. F. Craciun and S. Russo, *Nano Lett.*, 2014, **14**, 1751–1755.

58 I. Khrapach, F. Withers, T. H. Bointon, D. K. Polyushkin, W. L. Barnes, S. Russo and M. F. Craciun, *Adv. Mater.*, 2012, **24**, 2844–2849.

59 W. S. Hummers Jr and R. E. Offeman, *J. Am. Chem. Soc.*, 1958, **80**, 1339.

60 S. Eigler, *Commun. Chem.*, 2015, **51**, 3162–3165.

61 S. Seiler, C. E. Halbig, F. Grote, P. Rietsch, F. Börrnert, U. Kaiser, B. Meyer and S. Eigler, *Nat. Commun.*, 2018, **9**, 836.

62 W. J. Zhao, P. H. Tan, J. Zhang and J. Liu, *Phys. Rev. B: Condens. Matter Mater. Phys.*, 2010, **82**, 245423.

63 A. Das, B. Chakraborty, S. Piscanec, S. Pisana, A. K. Sood and A. C. Ferrari, *Phys. Rev. B: Condens. Matter Mater. Phys.*, 2009, **79**, 155417.

64 K. J. Koski, C. D. Wessells, B. W. Reed, J. J. Cha, D. Kong and Y. Cui, *J. Am. Chem. Soc.*, 2012, **134**, 13773–13779.

65 K. J. Koski, J. J. Cha, B. W. Reed, C. D. Wessells, D. Kong and Y. Cui, *J. Am. Chem. Soc.*, 2012, **134**, 7584–7587.

66 K. P. Chen, F. R. Chung, M. Wang and K. J. Koski, *J. Am. Chem. Soc.*, 2015, **137**, 5431–5437.

67 Y. Gong, H. Yuan, C.-L. Wu, P. Tang, S.-Z. Yang, A. Yang, G. Li, B. Liu, J. van de Groep, M. L. Brongersma, M. F. Chisholm, S.-C. Zhang, W. Zhou and Y. Cui, *Nat. Nanotechnol.*, 2018, **13**, 294–299.

68 M. Wang, I. Al-Dhahir, J. Appiah and K. J. Koski, *Chem. Mater.*, 2017, **29**, 1650–1655.

69 J. P. Motter, K. J. Koski and Y. Cui, *Chem. Mater.*, 2014, **26**, 2313–2317.

70 M. Wang and K. J. Koski, *ACS Nano*, 2015, **9**, 3226–3233.

71 N. C. Osti, M. Naguib, A. Ostadhossein, Y. Xie, P. R. Kent, B. Dyatkin, G. Rother, W. T. Heller, A. C. van Duin, Y. Gogotsi and E. Mamontov, *ACS Appl. Mater. Interfaces*, 2016, **8**, 8859–8863.

72 O. Mashtalir, M. Naguib, V. N. Mochalin, Y. Dall'Agnese, M. Heon, M. W. Barsoum and Y. Gogotsi, *Nat. Commun.*, 2013, **4**, 1716.

73 O. Mashtalir, M. R. Lukatskaya, M.-Q. Zhao, M. W. Barsoum and Y. Gogotsi, *Adv. Mater.*, 2015, **27**, 3501–3506.

74 M. Naguib, M. Kurtoglu, V. Presser, J. Lu, J. Niu, M. Heon, L. Hultman, Y. Gogotsi and M. W. Barsoum, *Adv. Mater.*, 2011, **23**, 4248–4253.

75 J. Li, X. Yuan, C. Lin, Y. Yang, L. Xu, X. Du, J. Xie, J. Lin and J. Sun, *Adv. Energy Mater.*, 2017, **7**, 1602725.

76 J. L. Hart, K. Hantanasirisakul, A. C. Lang, B. Anasori, D. Pinto, Y. Pivak, J. T. van Omme, S. J. May, Y. Gogotsi and M. L. Taheri, *Nat. Commun.*, 2019, **10**, 522.

77 M. Boota, M. Pasini, F. Galeotti, W. Porzio, M.-Q. Zhao, J. Halim and Y. Gogotsi, *Chem. Mater.*, 2017, **29**, 2731–2738.

78 M. Okubo, A. Sugahara, S. Kajiyama and A. Yamada, *Acc. Chem. Res.*, 2018, **51**, 591–599.

79 L. Zhao, R. Zhang, C. Deng, Y. Peng and T. Jiang, *Nanomaterials*, 2019, **9**, 1096.

80 N. I. Kovtyukhova, Y. Wang, R. Lv, M. Terrones, V. H. Crespi and T. E. Mallouk, *J. Am. Chem. Soc.*, 2013, **135**, 8372–8381.

81 S. Yang, P. Zhang, A. S. Nia and X. Feng, *Adv. Mater.*, 2020, **32**, 1907857.

82 J. Zhang, A. Yang, X. Wu, J. van de Groep, P. Tang, S. Li, B. Liu, F. Shi, J. Wan, Q. Li, Y. Sun, Z. Lu, X. Zheng, G. Zhou, C.-L. Wu, S.-C. Zhang, M. L. Brongersma, J. Li and Y. Cui, *Nat. Commun.*, 2018, **9**, 5289.

83 J. Cao, P. He, M. A. Mohammed, X. Zhao, R. J. Young, B. Derby, I. A. Kinloch and R. A. W. Dryfe, *J. Am. Chem. Soc.*, 2017, **139**, 17446–17456.

84 F. Xiong, H. Wang, X. Liu, J. Sun, M. Brongersma, E. Pop and Y. Cui, *Nano Lett.*, 2015, **15**, 6777–6784.

85 C. Wang, Q. He, U. Halim, Y. Liu, E. Zhu, Z. Lin, H. Xiao, X. Duan, Z. Feng, R. Cheng, N. O. Weiss, G. Ye, Y.-C. Huang, H. Wu, H.-C. Cheng, I. Shakir, L. Liao, X. Chen, W. A. Goddard III, Y. Huang and X. Duan, *Nature*, 2018, **555**, 231–236.

86 L. Oakes, R. Carter, T. Hanken, A. P. Cohn, K. Share, B. Schmidt and C. L. Pint, *Nat. Commun.*, 2016, **7**, 11796.

87 D. K. Bediako, M. Rezaee, H. Yoo, D. T. Larson, S. Y. F. Zhao, T. Taniguchi, K. Watanabe, T. L. Brower-Thomas, E. Kaxiras and P. Kim, *Nature*, 2018, **558**, 425–429.

88 Y. Li, H. Yan, B. Xu, L. Zhen and C.-Y. Xu, *Adv. Mater.*, 2020, 2000581.

130

89 E. R. White, J. J. Lodico and B. C. Regan, *Nat. Commun.*, 2017, **8**, 1969.

90 V. V. Avdeev, O. A. Tverezovskaya, N. E. Sorokina, I. V. Nikol'skaya and A. I. Finaenov, *Inorg. Mater.*, 2000, **36**, 214–218.

91 J. A. Seel and J. R. Dahn, *J. Electrochem. Soc.*, 2000, **147**, 892–898.

92 K. Ji, J. Han, A. Hirata, T. Fujita, Y. Shen, S. Ning, P. Liu, H. Kashani, Y. Tian, Y. Ito, J.-I. Fujita and Y. Oyama, *Nat. Commun.*, 2019, **10**, 275.

93 M. Kühne, F. Paolucci, J. Popovic, P. M. Ostrovsky, J. Maier and J. H. Smet, *Nat. Nanotechnol.*, 2017, **12**, 895–900.

94 Q. He, Z. Lin, M. Ding, A. Yin, U. Halim, C. Wang, Y. Liu, H.-C. Cheng, Y. Huang and X. Duan, *Nano Lett.*, 2019, **19**, 6819–6826.

95 W. He, H. Zang, S. Cai, Z. Mu, C. Liu, M. Ding, P. Wang and X. Wang, *Nano Res.*, 2020, **13**, 2917–2924.

96 D. Wang, L.-M. Liu, S.-J. Zhao, Z.-Y. Hu and H. Liu, *J. Phys. Chem. C*, 2016, **120**, 4779–4788.

97 Y. Cao, V. Fatemi, A. Demir, S. Fang, S. L. Tomarken, J. Y. Luo, J. D. Sanchez-Yamagishi, K. Watanabe, T. Taniguchi, E. Kaxiras, R. C. Ashoori and P. Jarillo-Herrero, *Nature*, 2018, **556**, 80–84.

98 A. Kerelsky, L. J. McGilly, D. M. Kennes, L. Xian, M. Yankowitz, S. Chen, K. Watanabe, T. Taniguchi, J. Hone, C. Dean, A. Rubio and A. N. Pasupathy, *Nature*, 2019, **572**, 95–100.

99 J. W. Jeon, H. Kim, H. Kim, S. Choi and B. H. Kim, *AIP Adv.*, 2018, **8**, 075228.

100 A. Black, J. Roberts, M. Acebrón, R. Bernardo-Gavito, G. Alsharif, F. J. Urbanos, B. H. Juárez, O. V. Kolosov, B. J. Robinson, R. Miranda, A. L. Vázquez de Parga, D. Granados and R. J. Young, *ACS Appl. Mater. Interfaces*, 2018, **10**, 6805–6809.

101 R. Mirzayev, K. Mustonen, M. R. A. Monazam, A. Mittelberger, T. J. Pennycook, C. Mangler, T. Susi, J. Kotakoski and J. C. Meyer, *Sci. Adv.*, 2017, **3**, e1700176.

102 D. Deng, K. S. Novoselov, Q. Fu, N. Zheng, Z. Tian and X. Bao, *Nat. Nanotechnol.*, 2016, **11**, 218–230.

103 W. Zhang, Q. Wang, Y. Chen, Z. Wang and A. T. S. Wee, *2D Mater.*, 2016, **3**, 022001.

104 X. Zhou, X. Hu, J. Yu, S. Liu, Z. Shu, Q. Zhang, H. Li, Y. Ma, H. Xu and T. Zhai, *Adv. Funct. Mater.*, 2018, **28**, 1706587.

105 R. Frisenda, E. Navarro-Moratalla, P. Gant, D. Pérez de Lara, P. Jarillo-Herrero, R. V. Gorbachev and A. Castellanos-Gomez, *Chem. Soc. Rev.*, 2018, **47**, 53–68.

106 X. Yang and M. Yan, *Nano Res.*, 2020, **13**, 599–610.

107 J. W. Suk, A. Kitt, C. W. Magnuson, Y. Hao, S. Ahmed, J. An, A. K. Swan, B. B. Goldberg and R. S. Ruoff, *ACS Nano*, 2011, **5**, 6916–6924.

108 Z. Hu, Z.-B. Liu and J.-G. Tian, *Chin. J. Org. Chem.*, 2020, **38**, 981–995.

109 X. Ma, Q. Liu, D. Xu, Y. Zhu, S. Kim, Y. Cui, L. Zhong and M. Liu, *Nano Lett.*, 2017, **17**, 6961–6967.

110 Y. Hou, X. Ren, J. Fan, G. Wang, Z. Dai, C. Jin, W. Wang, Y. Zhu, S. Zhang, L. Liu and Z. Zhang, *ACS Appl. Mater. Interfaces*, 2020, **12**, 40958–40967.

111 Y. Huang, Y.-H. Pan, R. Yang, L.-H. Bao, L. Meng, H.-L. Luo, Y.-Q. Cai, G.-D. Liu, W.-J. Zhao, Z. Zhou, L.-M. Wu, Z.-L. Zhu, M. Huang, L.-W. Liu, L. Liu, P. Cheng, K.-H. Wu, S.-B. Tian, C.-Z. Gu, Y.-G. Shi, Y.-F. Guo, Z.-G. Cheng, J. P. Hu, L. Zhao, G.-H. Yang, E. Sutter, P. Sutter, Y.-L. Wang, W. Ji, X.-J. Zhou and H.-J. Gao, *Nat. Commun.*, 2020, **11**, 2453.

112 M. Hußmann, B. Weintrub, P. Feicht, G. Germer, J. N. Kirchhof, K. I. Bolotin and S. Eigler, *Nanoscale Adv.*, 2020, **2**, 176–181.

113 M. Velický, G. E. Donnelly, W. R. Hendren, S. McFarland, D. Scullion, W. J. I. DeBenedetti, G. C. Correa, Y. Han, A. J. Wain, M. A. Hines, D. A. Muller, K. S. Novoselov, H. D. Abruña, R. M. Bowman, E. J. G. Santos and F. Huang, *ACS Nano*, 2018, **12**, 10463–10472.

114 G. F. Schneider, V. E. Calado, H. Zandbergen, L. M. K. Vandersypen and C. Dekker, *Nano Lett.*, 2010, **10**, 1912–1916.

115 J. G. Bednorz and K. A. Müller, *Angew. Chem., Int. Ed.*, 1988, **27**, 735–748.

116 G. F. Sun, K. W. Wong, B. R. Xu, Y. Xin and D. F. Lu, *Phys. Lett. A*, 1994, **192**, 122–124.

117 Z. M. Geballe, H. Liu, A. K. Mishra, M. Ahart, M. Somayazulu, Y. Meng, M. Baldini and R. J. Hemley, *Angew. Chem., Int. Ed.*, 2018, **130**, 696–700.

118 I. A. Kruglov, D. V. Semenok, H. Song, R. Szczęśniak, I. A. Wrona, R. Akashi, E. M. M. Davari, D. Duan, T. Cui, A. G. Kvashnin and A. R. Oganov, *Phys. Rev. B*, 2020, **101**, 024508.

119 A. F. Hebard, M. J. Rosseinsky, R. C. Haddon, D. W. Murphy, S. H. Glarum, T. T. M. Palstra, A. P. Ramirez and A. R. Kortan, *Nature*, 1991, **350**, 600–601.

120 Z. K. Tang, L. Zhang, N. Wang, X. X. Zhang, G. H. Wen, G. D. Li, J. N. Wang, C. T. Chan and P. Sheng, *Science*, 2001, **292**, 2462–2465.

121 E. A. Ekimov, V. A. Sidorov, E. D. Bauer, N. N. Mel'nik, N. J. Curro, J. D. Thompson and S. M. Stishov, *Nature*, 2004, **428**, 542–545.

122 B. Uchoa and A. H. C. Neto, *Phys. Rev. Lett.*, 2007, **98**, 146801.

123 Y. Cao, V. Fatemi, S. Fang, K. Watanabe, T. Taniguchi, E. Kaxiras and P. Jarillo-Herrero, *Nature*, 2018, **556**, 43–50.

124 S. Ichinokura, K. Sugawara, A. Takayama, T. Takahashi and S. Hasegawa, *ACS Nano*, 2016, **10**, 2761–2765.

125 J.-H. Liao, Y.-C. Zhao, Y.-J. Zhao, H. Xu and X.-B. Yang, *Phys. Chem. Chem. Phys.*, 2017, **19**, 29237–29243.

126 K. S. Novoselov, A. K. Geim, S. V. Morozov, D. Jiang, Y. Zhang, S. V. Dubonos, I. V. Grigorieva and A. A. Firsov, *Science*, 2004, **306**, 666–669.

127 W. Zhang, C.-T. Lin, K.-K. Liu, T. Tite, C.-Y. Su, C.-H. Chang, Y.-H. Lee, C.-W. Chu, K.-H. Wei, J.-L. Kuo and L.-J. Li, *ACS Nano*, 2011, **5**, 7517–7524.

128 J. B. Oostinga, H. B. Heersche, X. Liu, A. F. Morpurgo and L. M. K. Vandersypen, *Nat. Mater.*, 2008, **7**, 151–157.

129 Y. Zhang, T.-T. Tang, C. Girit, Z. Hao, M. C. Martin, A. Zettl, M. F. Crommie, Y. R. Shen and F. Wang, *Nature*, 2009, **459**, 820–823.

131

130 H. Guo, R. Zhang, H. Li, X. Wang, H. Lu, K. Qian, G. Li, L. Huang, X. Lin, Y.-Y. Zhang, H. Ding, S. Du, S. T. Pantelides and H.-J. Gao, *Nano Lett.*, 2020, **20**, 2674–2680.

131 D. Zhan, J. X. Yan, Z. H. Ni, L. Sun, L. F. Lai, L. Liu, X. Y. Liu and Z. X. Shen, *Small*, 2015, **11**, 1177–1182.

132 J. W. Yang, G. Lee, J. S. Kim and K. S. Kim, *J. Phys. Chem. Lett.*, 2011, **2**, 2577–2581.

133 R. Schlögl, W. Jones and H.-P. Boehm, *Synth. Met.*, 1983, **7**, 133–140.

134 K. Li, T. H. Chang, Q. Xie, Y. Cheng, H. Yang, J. Chen and P. Y. Chen, *Adv. Electron. Mater.*, 2019, **5**, 1900040.

135 S. Yang, L. Chen, L. Mu and P.-C. Ma, *J. Colloid Interface Sci.*, 2014, **430**, 337–344.

136 K. Yang, L. Feng and Z. Liu, *Adv. Drug Delivery Rev.*, 2016, **105**, 228–241.

137 X. Lu, X. Feng, J. R. Werber, C. Chu, I. Zucker, J.-H. Kim, C. O. Osuji and M. Elimelech, *Proc. Natl. Acad. Sci. U. S. A.*, 2017, **114**, E9793–E9801.

138 X. Zhang, X. Zhao and Y. Liu, *J. Phys. Chem. C*, 2016, **120**, 22710–22717.

139 M. Kinany-Alaoui, L. Piraux, V. Bayot, J.-P. Issi, P. Pernot and R. Vangélisti, *Synth. Met.*, 1989, **34**, 537–542.

140 K. Sugihara, N.-C. Yeh, M. S. Dresselhaus and G. Dresselhaus, *Phys. Rev. B: Condens. Matter Mater. Phys.*, 1989, **39**, 4577–4587.

141 Z. Li, X. Zhang, X. Zhao, J. Li, T. S. Herng, H. Xu, F. Lin, P. Lyu, X. Peng, W. Yu, X. Hai, C. Chen, H. Yang, J. Martin, J. Lu, X. Luo, A. H. Castro Neto, S. J. Pennycook, J. Ding, Y. Feng and J. Lu, *Adv. Mater.*, 2020, **32**, 1907645.

142 E. Coronado, C. Martí-Gastaldo, E. Navarro-Moratalla, A. Ribera, S. J. Blundell and P. J. Baker, *Nat. Chem.*, 2010, **2**, 1031–1036.

143 B. Baek, W. H. Rippard, S. P. Benz, S. E. Russek and P. D. Dresselhaus, *Nat. Commun.*, 2014, **5**, 3888.

144 S. Tongay, K. Berke, M. Lemaitre, Z. Nasrollahi, D. B. Tanner, A. F. Hebard and B. R. Appleton, *Nanotechnology*, 2011, **22**, 425701.

145 T.-H. Han, Y. Lee, M.-R. Choi, S.-H. Woo, S.-H. Bae, B. H. Hong, J.-H. Ahn and T.-W. Lee, *Nat. Photonics*, 2012, **6**, 105–110.

146 F. Güneş, H.-J. Shin, C. Biswas, G. H. Han, E. S. Kim, S. J. Chae, J.-Y. Choi and Y. H. Lee, *ACS Nano*, 2010, **4**, 4595–4600.

147 G. R. Hennig, *J. Chem. Phys.*, 1965, **43**, 1201–1206.

148 W. Bao, J. Wan, X. Han, X. Cai, H. Zhu, D. Kim, D. Ma, Y. Xu, J. N. Munday, H. D. Drew, M. S. Fuhrer and L. Hu, *Nat. Commun.*, 2014, **5**, 4224.

149 N. A. W. Holzwarth, S. G. Louie and S. Rabii, *Phys. Rev. B: Condens. Matter Mater. Phys.*, 1983, **28**, 1013–1025.

150 T. Mueller, F. Xia and P. Avouris, *Nat. Photonics*, 2010, **4**, 297–301.

151 H. Zhang, *ACS Nano*, 2015, **9**, 9451–9469.

152 F. Bonaccorso, Z. Sun, T. Hasan and A. C. Ferrari, *Nat. Photonics*, 2010, **4**, 611–622.

153 M. Freitag, T. Low, F. Xia and P. Avouris, *Nat. Photonics*, 2012, **7**, 53–59.

154 R. R. Nair, P. Blake, A. N. Grigorenko, K. S. Novoselov, T. J. Booth, T. Stauber, N. M. Peres and A. K. Geim, *Science*, 2008, **320**, 1308.

155 M. Liu, X. Yin, E. Ulin-Avila, B. Geng, T. Zentgraf, L. Ju, F. Wang and X. Zhang, *Nature*, 2011, **474**, 64–67.

156 Z. Fang, Z. Liu, Y. Wang, P. M. Ajayan, P. Nordlander and N. J. Halas, *Nano Lett.*, 2012, **12**, 3808–3813.

157 Y. Lee, H. Kim, S. Kim, D. Whang and J. H. Cho, *ACS Appl. Mater. Interfaces*, 2019, **11**, 23474–23481.

158 Q. Nian, L. Gao, Y. Hu, B. Deng, J. Tang and G. J. Cheng, *ACS Appl. Mater. Interfaces*, 2017, **9**, 44715–44723.

159 J. Kim, C. Jin, B. Chen, H. Cai, T. Zhao, P. Lee, S. Kahn, K. Watanabe, T. Taniguchi, S. Tongay, M. F. Crommie and F. Wang, *Sci. Adv.*, 2017, **3**, e1700518.

160 H. Zhou, Y. Zhao, W. Tao, Y. Li, Q. Zhou and H. Zhu, *ACS Nano*, 2020, **14**, 4618–4625.

161 P. Zielinski, M. Kühne, D. Kärcher, F. Paolucci, P. Wochner, S. Fecher, J. Drnec, R. Felici and J. H. Smet, *Nano Lett.*, 2019, **19**, 3634–3640.

162 F. Li, J. Zou, L. Cao, Z. Li, S. Gu, Y. Liu, J. Zhang, H. Liu and Z. Lu, *J. Phys. Chem. C*, 2019, **123**, 5067–5072.

163 J. P. Bonacum, A. O'Hara, D.-L. Bao, O. S. Ovchinnikov, Y.-F. Zhang, G. Gordeev, S. Arora, S. Reich, J.-C. Idrobo, R. F. Haglund, S. T. Pantelides and K. I. Bolotin, *Phys. Rev. Mater.*, 2019, **3**, 064004.

164 P. Xiong, F. Zhang, X. Zhang, S. Wang, H. Liu, B. Sun, J. Zhang, Y. Sun, R. Ma, Y. Bando, C. Zhou, Z. Liu, T. Sasaki and G. Wang, *Nat. Commun.*, 2020, **11**, 3297.

165 E. Pomerantseva and Y. Gogotsi, *Nat. Energy*, 2017, **2**, 17089.

166 P. A. Vermeulen, J. Mulder, J. Momand and B. J. Kooi, *Nanoscale*, 2018, **10**, 1474–1480.

167 G. Algara-Siller, S. Kurasch, M. Sedighi, O. Lehtinen and U. Kaiser, *Appl. Phys. Lett.*, 2013, **103**, 203107.

168 M.-H. Huang, X.-C. Dai, T. Li, Y.-B. Li, Y. He, G. Xiao and F.-X. Xiao, *J. Phys. Chem. C*, 2019, **123**, 9721–9734.

132

6 Publications - Minor Contributions

6.1 Synthesis of Wet-chemically Prepared Porous-graphene Single Layers on Si/SiO₂ Substrate Increasing the Photoluminescence of MoS₂ in Heterostructures

Authors	Yiqing Wang, Christof Neumann, Marleen Hußmann, Qing Cao, Yalei Hu, Oisín Garrity, Patryk Kusch, Andrey Turchanin, and Siegfried Eigler
Journal	*Adv. Mater. Interfaces* **2021**, *8*, 2100783
DOI	10.1002/admi.202100783
Links	https://doi.org/10.1002/admi.202100783
Detailed scientific contribution	The concept of this manuscript was elaborated by Y. Wang and Prof. Dr. S. Eigler. Oxo-G and oxo-G with pores were fabricated and characterized with optical microscopy and atomic force microscopy by Y. Wang. X-ray photoelectron spectroscopy was measured by C. Neumann. The MoS₂ heterostructures shown in the manuscript were prepared by M. Hußmann, Q. Cao, Y. Wang and Y. Hu. The Raman and PL measurements of MoS₂ heterostructures were done by Q. Cao and Y. Wang. PL intensity maps were done by O.Garrity and P. Kusch. The manuscript was written by Y. Wang and Prof. Dr. S. Eigler. The revision of the manuscript was assisted by Prof. Dr. S. Eigler, Dr. C. Neumann, Prof. Dr. A. Turchanin and Q. Cao.
Estimated own contribution	~15%

Synthesis of Wet-Chemically Prepared Porous-Graphene Single Layers on Si/SiO₂ Substrate Increasing the Photoluminescence of MoS₂ in Heterostructures

Yiqing Wang, Christof Neumann, Marleen Hußmann, Qing Cao, Yalei Hu, Oisín Garrity, Patryk Kusch, Andrey Turchanin, and Siegfried Eigler*

Wet-chemical generation of pores in graphene is a challenging synthetic task. Although graphene oxide is available in large quantities and chemically diverse, extended lattice defects already present from synthesis hamper the controlled growth of pores. However, membrane, energy, or nanoelectronic applications essentially require uniform pores in applications. Here, oxo-functionalized graphene (oxoG), a type of graphene oxide with a controlled density of vacancy defects, is used as starting material. Pores in graphene are generated from potassium permanganate treated oxoG and heating from room temperature to 400 °C. With etching time, the size of pores increases and pore-diameters of, for example, 100–200 nm in majority become accessible. The experiments are conducted on the single-layer level on Si/SiO₂ wafers. Flakes remain stable on the µm scale and do not fold. The process leads to rims of pores, which are functionalized by carbonyl groups in addition to hydroxyl and carboxyl groups. In addition, it is found that heterostructures with intrinsically n-doped MoS₂ can be fabricated and photoluminescence (PL) measurements reveal a 10-fold increased PL. Thus, graphene with pores is a novel highly temperature-stable electron-accepting 2D material to be integrated into van der Waals heterostructures.

Y. Wang, M. Hußmann, Q. Cao, Y. Hu, Prof. S. Eigler
Institute of Chemistry and Biochemistry
Freie Universität Berlin
Takustraße 3, 14195 Berlin, Germany
E-mail: siegfried.eigler@fu-berlin.de
Dr. C. Neumann, Prof. A. Turchanin
Institute of Physical Chemistry
Center for Energy and Environmental Chemistry (CEEC) Jena
Friedrich Schiller University Jena
Lessingstraße 10, 07743 Jena, Germany
O. Garrity, Dr. P. Kusch
Department of Physics
Freie Universität Berlin
Arnimallee 14, 14195 Berlin, Germany

The ORCID identification number(s) for the author(s) of this article can be found under https://doi.org/10.1002/admi.202100783.

1. Introduction

Graphene with defects, such as pores in the lattice of graphene[1–3] finds emerging applications for water separation, gas separation and purification, or sensing.[4–10] The chemical functionalization of graphene can either be accomplished with graphene dispersed in solvents,[11] or with graphene deposited on surfaces.[12] Applications based on bulk functionalization target, for example, composite formation, exploiting the mechanical properties of graphene, or electronic properties for energy applications and energy conversion or storage.[13–19] In particular sensing applications are targeted using graphene, which is deposited on surfaces. Thereby, functionalization of deposited graphene can in principle occur on the surface or at the rim of flakes. However, since investigated sensing devices typically have µm dimensions, functionalization at rims of flakes is supposed to have only little influence on the device performance. With drilling pores into the graphene lattice, the proportion of rims can be increased. In principle, pores can be etched using focused ion beam and the approach allows for regular patterning, shape, and size control.[16,20–22] Thereby, the successful patterning is a technological challenge. Since the focused ion beam also interacts with the substrate the dielectric layer, such as SiO₂ may become damaged. Thus, although that approach is appealing, it bears some drawbacks, since high-end technology is required.[16,23]

The growth of pores in graphene on the single-layer level is described by numerous methods in the literature in particular etching methods.[24] Nanometer-sized pores were created in graphene by oxygen plasma or other plasmas.[25,26] Moreover, pores on the nanoscale were created in few-layered graphene using oxygen, ozone, or liquid phase etching using HNO₃ solution as etching reagents.[26–28] In addition, it is reported that a single Ni atom can be used to cut graphene to a nanomesh with a pore size of about 10–50 nm.[29] Sub-nanometer diameter pores in single-layer graphene membranes were also fabricated, accordingly, defects were introduced into the graphene lattice through ion bombardment and oxidative etching enlarged defects into pores with sizes of 0.40 ± 0.24 nm.[30,31] Moreover, also graphene oxide

2100783 (1 of 8)

**ADVANCED
SCIENCE NEWS**
www.advancedsciencenews.com

**ADVANCED
MATERIALS
INTERFACES**
www.advmatinterfaces.de

Figure 1. Scheme describing the fabrication of pores starting from oxoG. Flakes of oxoG are deposited on a Si/SiO₂ substrate. Pr-oxoG₁₂ₕ is fabricated from oxoG, immersed in KMnO₄ solution, followed by washing, drying, and annealing in argon atmosphere at 400 °C for 12 h. The white scale bar relates to 10 μm in optical microscopy images.

was used as precursor for etching pores, however, no uniform size was reported and the size of pores is limited to few nm, assumedly due to too many lattice defect sites already present in common graphene oxide, which act as origins for etching. Thus, the formation of larger pores is not possible, since flakes start to disintegrate.[28,32–35] Accordingly, graphene oxide with extended lattice defects conceptionally can't be considered as a precursor for generating graphene with pores of reasonable lateral dimensions, of tens to hundreds of nm (Table S1, Supporting Information). Here we describe the formation of pores of circular shape by a Mn-species assisted etching procedure at 400 °C in argon atmosphere. The approach starts from oxo-functionalized graphene (oxoG) with a low density of init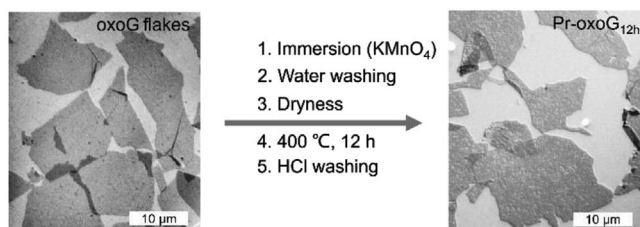ial vacancy defects (0.8%, as determined by Raman spectroscopy), which is a subclass of the graphene oxide family. By controlling the reaction conditions, it is possible to gain a certain control over the formation of pores with diameters between 100–200 nm in majority. Those pore-graphene materials are highly temperature stable since they are synthesized at 400 °C. Moreover, integration into heterostructures is possible. We report that the amplitude of the photoluminescence (PL) signal of MoS₂ enhances 10-times.

2. Results and Discussion

The formation of pores in monolayers of oxoG was elaborated in a five-step procedure (**Figure 1**). Accordingly, oxoG flakes are deposited on Si/300 nm SiO₂ wafer by Langmuir–Blodgett technique.[36–38] The lateral dimensions of monolayer oxoG flakes are roughly 20 μm (Figure 1 left and Figure S2A–C, Supporting Information). Figure S1A,B, Supporting Information, show the results of the statistical Raman analysis of flakes of reduced oxoG revealing an I_D/I_G ratio of the defect induced D band and the G band of 2.7 ± 0.14 and a full-width at half-maximum (Γ) of the 2D band $\Gamma_{2D} = 93 \pm 9$ cm⁻¹. Thus, the average distance of defects L_D is about 2 nm, following the relation introduced by Lucchese and Cançado.[39,40] The distance of defects can be related to a density of defects of about 0.8%.

Then the wafer was immersed into a solution of potassium permanganate (KMnO₄) overnight (for details see experimental part). Metal ions are bound to the surface of the single-layers of oxoG on Si/SiO₂ substrates. A study based on the roughness analysis performed by atomic force microscopy (AFM) was conducted focusing on one specific flake of oxoG before and after KMnO₄ immersion (step 1 in Figure 1) and finally after washing the surface with water (step 2 in Figure 1, see also Figure S2,

Supporting Information). Line height scans indicate that the root mean square roughness of the surface increases from about 0.14 nm to about 0.39 and 0.32 nm, respectively. As we showed before, organosulfate groups with hydronium counter ions explain the thickness of flakes of oxoG.[41] Here, we propose that hydronium ions are exchanged by Mn-species. Although we realized that step 2, washing the wafer with water to remove possible excess or loosely bound Mn-species is essential for the controlled growth of pores, the AFM height profile remains similar (Figure S2F, Supporting Information) with a roughness of 0.32 nm. After drying the sample at room temperature, the annealing process was carried out in a tube furnace in argon at 400 °C for 12 h. Afterward, the annealed material on the wafer was washed with 1 M hydrochloric acid (HCl) to remove metal or metal oxide particles.[33] The annealing process induces the disproportionation reaction of oxoG, and we identified in an earlier study that pores can grow by the release of CO₂, while intact graphene patches with diameters of around 3 nm in diameter are generated, as a consequence of mobile oxo-groups on the lattice of graphene.[42] However, by the here described procedure, graphene with pores (Pr-oxoG₁₂ₕ; index indicated the annealing time) is generated with much larger pores.

By varying the annealing time, graphene materials with pores of different sizes are generated. The formed pores can be visualized by AFM and optical microscopy, respectively. Here, through comparative experiments, we can confirm that manganese plays a very important role in the formation process of pores. For single layers, we suggest that there are small nanoparticles at the edges of pores. Because of the little amount, the content is below the detection limit of, for example, X-ray photoelectron spectroscopy (XPS) or Raman (Mn−O vibrations, Figure S6A, Supporting Information). We further assume that the metal particles move along the edge of the pore to continuously catalyze the pore formation leading to increased diameters of pores. Accordingly, based on this assumption it can be explained why round pores are formed, and thus, the size of the pores can be controlled by etching-time. Figure S3A, Supporting Information, shows an AFM image of single-layer oxoG with no visible pores in the zoomed area depicted in Figure S3B, Supporting Information. As we visualized before by transmission electron microscopy at atomic resolution, oxoG bears only one or few atom vacancies.[42,43] Figure S3C,D, Supporting Information, show AFM images of Pr-oxoG₆ₕ. The presence of small pores is visible in Figure S3D, Supporting Information. To make the comparison reliable, we analyzed the same flake and same area of the flake before and after annealing. Therefore, we conclude that there are small pores of 45 ± 24 nm formed in Pr-oxoG₆ₕ, as can be observed from Figure S3D and Table S2, Supporting Information.[30]

Extending the annealing time from 6 to 12 h results in the formation of larger pores (Pr-oxoG₁₂ₕ). Pores in Pr-oxoG₁₂ₕ on Si/SiO₂ substrates are visible under the optical microscope (**Figure 2**A). As shown in the AFM image of Figure 2B, (the stacked square is visible in the center with higher resolution) there are many pores distributed over the entire flake. An AFM image with a further enlarged area of the flake of Pr-oxoG₁₂ₕ is depicted in Figure 2C. The circular shape of pores with an apparently uniform size of 147 ± 73 nm is clearly visible (Table S2, Supporting Information). The height of Pr-oxoG₁₂ₕ is about 1.4 nm, as measured by the AFM tip hitting the underneath surface
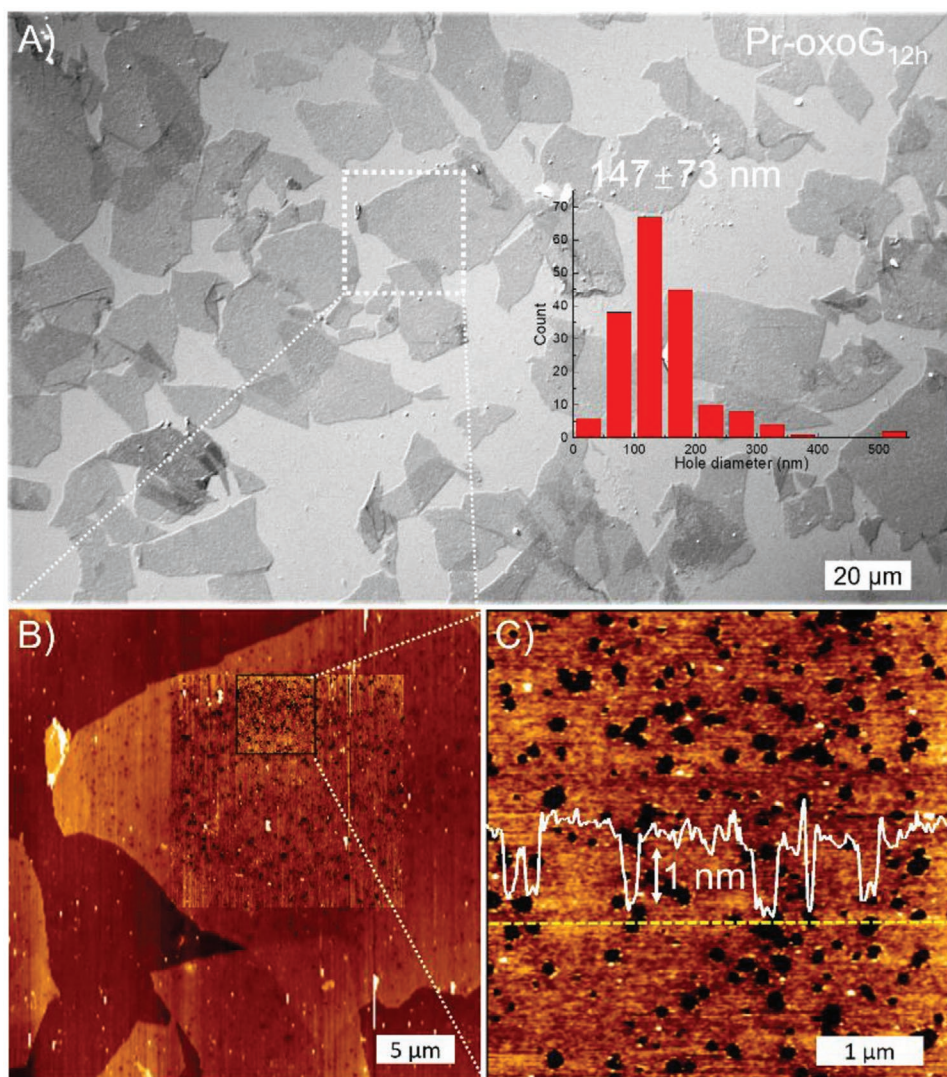
**ADVANCED
SCIENCE NEWS**
www.advancedsciencenews.com

**ADVANCED
MATERIALS
INTERFACES**
www.advmatinterfaces.de

Figure 2. A) Optical microscopy image (differential interference contrast, DIC) of flakes of Pr-oxoG$_{12h}$ on Si/SiO$_2$ substrates. Inset: histogram shows the size distribution of pores shown in B and C, smaller than 50 nm are not counted. B) AFM topography image of Pr-oxoG$_{12h}$ with overlay of detailed scanned area; C) zoomed AFM topography image of (B) showing pores. White line: height profile, arrow indicates 1 nm.

through the pores. The results of the quantitative analysis of the lateral dimensions of pores in graphene are illustrated in the histogram shown in the inset of Figure 2A. The analysis reveals that the pores diameters are roughly 150 ± 70 nm.

Skipping the final step of HCl washing results in an increased height when measuring through a hole from the SiO$_2$ surface to the surface of graphene (**Figure 3**). We assume that a uniform hydration layer may be present between the substrate and graphene. We note that Mn-species, such as nanoparticles, supposed to be located at the rims of pores are not detected by AFM.[29,33] An analysis of the pore size before and after HCl washing indicates a little increase from 129 ± 75 to 147 ± 72 nm in Figure 3D. Those data are also listed in Table S2, Supporting Information. Next, a reference experiment was performed to eliminate the possibility that similar pores are formed using oxoG without the influence of Mn-species. Thus, flakes of oxoG were annealed for 12 h. As shown in Figure S4, Supporting Information, by optical microscopy and AFM, no

obvious large pores are observed. Therefore, we conclude that annealing alone is not leading to the formation of large pores, starting from oxoG.

To further investigate the effect of annealing time on the pore diameter, we further extended the processing time to 16 h. As shown in Figure S5, Supporting Information, large and merged pores are visible for Pr-oxoG$_{16h}$, both in the optical microscopy image of Figure S5A, Supporting Information, and AFM images of Figure S5B,C, Supporting Information. As shown in Figure S5B, Supporting Information, there are many pores in the flakes (enlargement in Figure S5C, Supporting Information) and the mean diameter is 168 ± 94 nm. To gain more insights into the mechanism of pore formation process was conducted on few-layers of oxo-G. The AFM images in Figure S6, Supporting Information, reveal some dots in the center of the pore. The thickness of the dots is basically the same as the material height. We suggest that those dots are either trapped etched carbon dots or manganese nanoparticles.
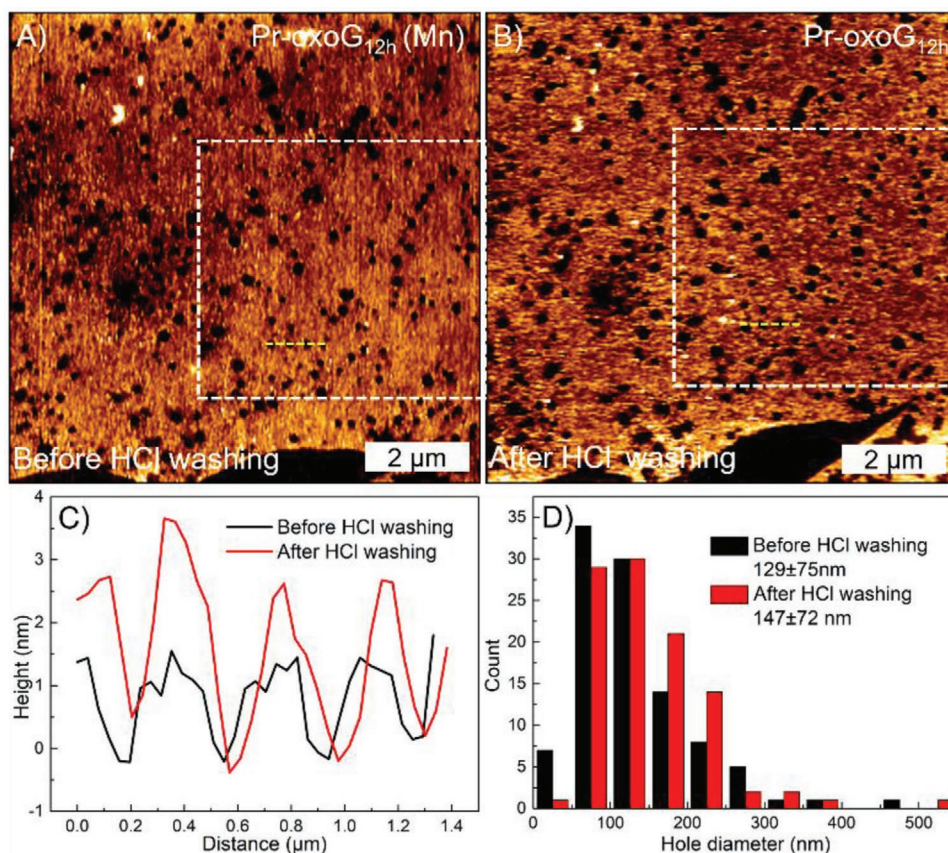
ADVANCED
SCIENCE NEWS
www.advancedsciencenews.com

ADVANCED
MATERIALS
INTERFACES
www.advmatinterfaces.de

Figure 3. AFM topography images in (A); before (Pr-oxoG$_{12h}$ (Mn)), and B) after (Pr-oxoG$_{12h}$) HCl washing. C) Height profiles of AFM images along yellow dashed lines. The black and red lines represent the pores height profiles of Pr-oxoG$_{12h}$ (Mn) and Pr-oxoG$_{12h}$, respectively. D) Distribution of pores in the white box. The black and red bars represent the pores quantity profiles of Pr-oxoG$_{12h}$ (Mn) and Pr-oxoG$_{12h}$.

Although, evidence is found supporting the hypothesis of the catalytical role of Mn-species such as Mn-atoms or nanoparticles, the final proof is a matter of further research.

A comparison between the different mean diameters and mean pore areas after different annealing time are shown in Figure S7, Supporting Information (data listed in the Table S2, Supporting Information). As the pyrolysis time increases, the average diameter and area of the pores increase according. In the process of growing pores, as shown in Figure 1, we pointed out that skipping washing step 2 with water results in a highly uncontrolled etching process. Compared with Figure 2A, the same annealing time of 12 h was chosen and the AFM image in Figure S8, Supporting Information, shows small pores, very large and also merged pores distributed all over the flakes. We suggest that Mn-species are unevenly distributed on the surface of oxoG if the water washing step is skipped. We note that we observed also partly destroyed and crumpled/folded layers. Therefore, we conclude that washing step 2 is essential to control the generation of pores, and to get some control over the uniformity of grown pores.

Next, an XPS study was conducted to analyze changes in the chemical composition of oxoG and Pr-oxoG$_{12h}$ (**Figure 4**). All XPS data are listed in Table S3. The high-resolution C 1s spectrum of oxoG in Figure 4A displays a typical saddle-like pattern, which stems from significant oxidation in oxoG.

The content of sp^2-C is about 47.8% (due to oxo-groups) and the content of C—O/C—OH/C=O is up to 46.3%. It can be seen from the high-resolution Mn 2p that there is no obvious peak in Figure 4E. Thus, few-layer oxoG contains less than 0.1 at% Mn. Before HCl washing, the high-resolution Mn 2p of Pr-oxoG$_{12h}$ (Mn) reveals also less than 0.1 at% Mn, as shown in Figure 4F. This finding further support that little quantities of Mn-species are catalytically active in the etching process. After annealing, the oxygen content of Pr-oxoG$_{12h}$ is significantly reduced compared to oxoG. As expected, the content of sp^2-C increased, here to 50.8%. The high-resolution O 1s spectrum of Pr-oxoG$_{12h}$ displays the peaks of C—O, C=O, O—C=O (Figure 4D). We note that the O 1s peak in Figure 4B is only for reference, since Pr-oxoG$_{12h}$ is not completely covering the Si/SiO$_2$ substrate and since large pores exist in Pr-oxoG$_{12h}$. Thus, the influence of the surface O-signal from SiO$_2$ is affecting the quantitative analysis. The oxygen content is significantly reduced in comparison to oxoG and close to zero if we consider its influence on SiO$_2$.[2,44,45] We note, for analyzing the C—O species the C 1s analysis is representative. The analyses of C 1s peaks reveal the formation of C=O and C—O/C—OH groups as a consequence of annealing and the accompanied growth of pores (Figure 4B). Thus, we conclude that the rims of pores are functionalized by carbonyl groups in addition to hydroxyl and carboxyl groups.
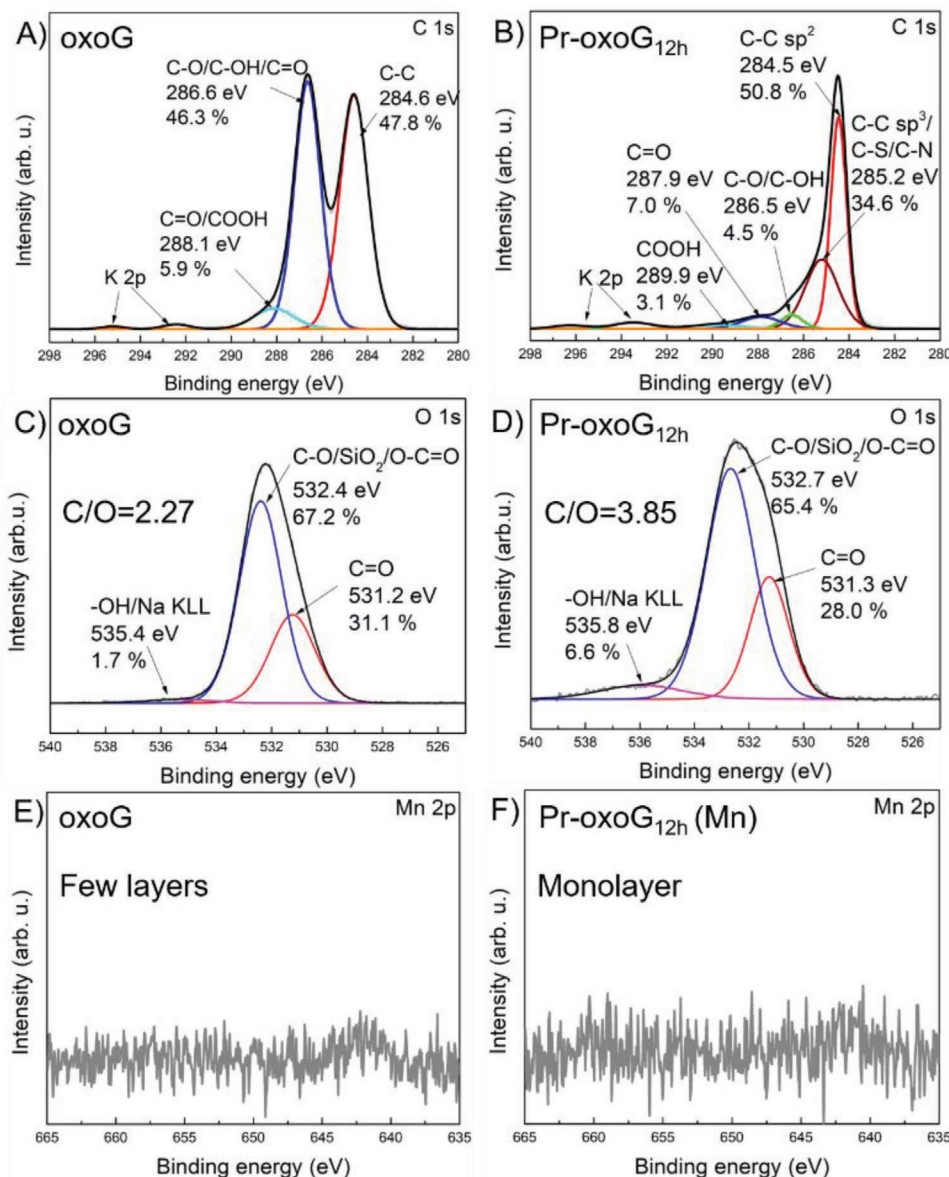
**ADVANCED
SCIENCE NEWS**

www.advancedsciencenews.com

**ADVANCED
MATERIALS
INTERFACES**

www.advmatinterfaces.de

Figure 4. High-resolution C 1s (top) and O 1s (middle) spectra of (A), C) oxo-G, and B,D) Pr-oxoG$_{12h}$. High-resolution Mn 2p spectra (bottom) of E) oxo-G and F) Pr-oxoG$_{12h}$ (Mn).

Moreover, with growing pores into graphene the sp^2-patches become smaller and consequently, the Raman spectra in Figure S9, Supporting Information, shows, as expected, a broadened D peak with $\Gamma_D = 106$ cm^{-1} for Pr-oxoG$_{12h}$, compared to $\Gamma_D = 84$ cm^{-1} for oxoG.

In the following, oxoG and Pr-oxoG$_{12h}$, respectively, are used to fabricate van-der-Waals heterostructures with a single-layer flake of MoS$_2$ deposited on top (illustrated in **Figure 5**). Raman spectra (Figure S10, Supporting Information) confirm that the transferred flake of MoS$_2$ is a monolayer by the measured difference between the out-of-plane A$_{1g}$ mode and the E$_{2g}$ mode of about 19.0 cm^{-1}, as typical for a monolayer.[46] For the fabrication of the heterostructures, we used a previously described procedure.[47] Figures 5B,D show optical microscopy images of the realized oxoG/MoS$_2$ and Pr-oxoG$_{12h}$/MoS$_2$ heterostructures,

respectively. The AFM images of the Pr-oxoG$_{12h}$/MoS$_2$ heterostructure is depicted in Figure S11A,B, Supporting Information, and proved the expected morphology.

The PL of MoS$_2$ on SiO$_2$, on oxoG, on Pr-oxoG$_{6h}$, and on Pr-oxoG$_{12h}$ are studied next. Figure 5E shows the respective PL of heterostructures. Obviously, the amplitude of the PL is increased for oxoG/MoS$_2$ and Pr-oxoG$_{12h}$/MoS$_2$, using pure MoS$_2$ on Si/SiO$_2$ substrate as internal reference, respectively, compared to the PL of the MoS$_2$ monolayer. The most intense PL is detected for Pr-oxoG$_{12h}$/MoS$_2$ with a 10-times increased amplitude. In contrast, the PL of Pr-oxoG$_{6h}$/MoS$_2$ is increased 3-times (Figure S12, Supporting Information) and for oxoG/MoS$_2$ a fourfold increased PL. As depicted in **Figure 6** there is a constant PL intensity over the complete flake, without any modulation. A related investigation demonstrated that
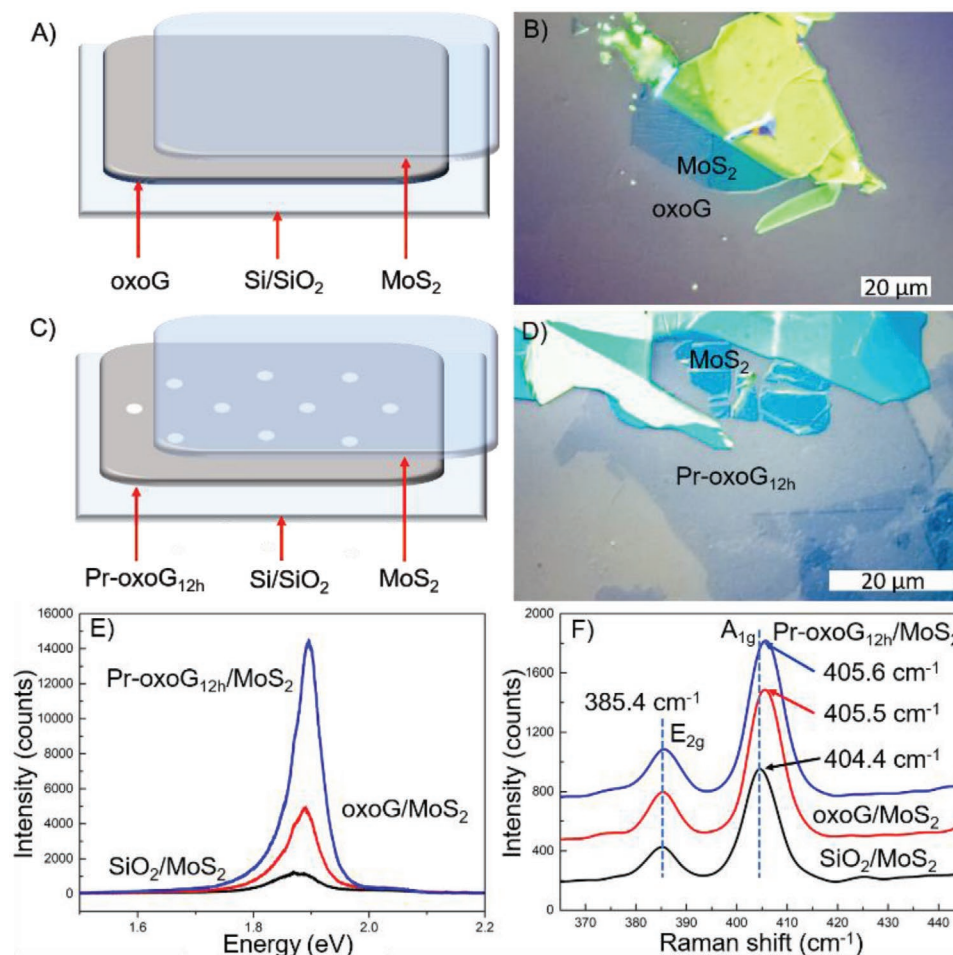
ADVANCED
SCIENCE NEWS
www.advancedsciencenews.com

ADVANCED
MATERIALS
INTERFACES
www.advmatinterfaces.de

Figure 5. A) Illustration of the heterostructure of oxoG/MoS$_2$ and B) optical microscopy image of the realized oxoG/MoS$_2$ heterostructure. C) Illustration of the heterostructure of Pr-oxoG$_{12h}$/MoS$_2$ and D) optical microscopy image of the realized Pr-oxoG$_{12h}$/MoS$_2$ heterostructure. E) PL spectra of monolayer MoS$_2$ on SiO$_2$ (black), oxoG/MoS$_2$ (red), and Pr-oxoG$_{12h}$/MoS$_2$ (blue). F) Raman spectra of the same samples as in (E).

graphene oxide forms a p-type contact with monolayer MoS$_2$ and this is plausible due to electron-accepting groups detected by XPS, such as carbonyl groups.[48] Overall, the highest PL enhancement is achieved by using Pr-oxoG$_{12h}$. Figure 5F shows the Raman spectra of heterostructures detecting the A$_{1g}$ mode of MoS$_2$ in the heterostructures at around 404.4 cm^{-1}, which is blue-shifted to 405.5 and 405.6 cm^{-1} for MoS$_2$ on oxoG and Pr-oxoG$_{12h}$, respectively, while the position of E_{2g} mode is not shifted. Those observations indicate the p-doping of MoS$_2$ in the heterostructures by oxoG and Pr-oxoG$_{12h}$, respectively.[49,50] Moreover, Pr-oxoG$_{12h}$ reflects a p-doped graphene type material, as indicated by the analysis of the shifts of the G and 2D peak, respectively (Figure S15, Supporting Information). The p-doping effect of Pr-oxoG$_{12h}$ was further investigated by fabricating a heterostructure with a trilayer of MoS$_2$. Consistent with the expectations, the PL investigation (Figure S13, Supporting Information) indicates less enhancement (trilayer MoS$_2$ possesses an indirect band-gap), however, a fourfold increased PL is measured, compared to that of a monolayer MoS$_2$ with a direct band-gap on SiO$_2$. Thus, the highest, here 10-times increased PL is detected for assembled heterostructure of monolayer Pr-oxoG$_{12h}$/MoS$_2$.

In order to exclude the influence of remaining Mn-species on the PL, the PL enhancement of Pr-oxoG$_{12h}$ (Mn) (without HCl washing) was studied by forming the heterostructure of Pr-oxoG$_{12h}$ (Mn)/MoS$_2$. As shown in Figure S14, Supporting Information, the PL increases, however, only twice, indicating that full enhancement of PL is only achieved after HCl washing and the accompanied removal of particles. Thus, we speculate that Mn-species may form complexes with, for example, carbonyl groups at the rims of pores inhibiting the dramatic PL enhancement, although Raman spectra show the E_{2g} shift to 405.6 cm^{-1} for Pr-oxoG$_{12h}$ (Mn)/MoS$_2$. We note that the experimental observations give evidence for a p-doping effect by pore-graphene.

3. Conclusion

Here, we demonstrated the fabrication of graphene with circular pores on the 100 nm scale deposited on Si/SiO$_2$ surface by annealing of oxo-functionalized and potassium permanganate treated graphene flakes at 400 °C. While excess of Mn-species leads to heterogeneously formed pores and
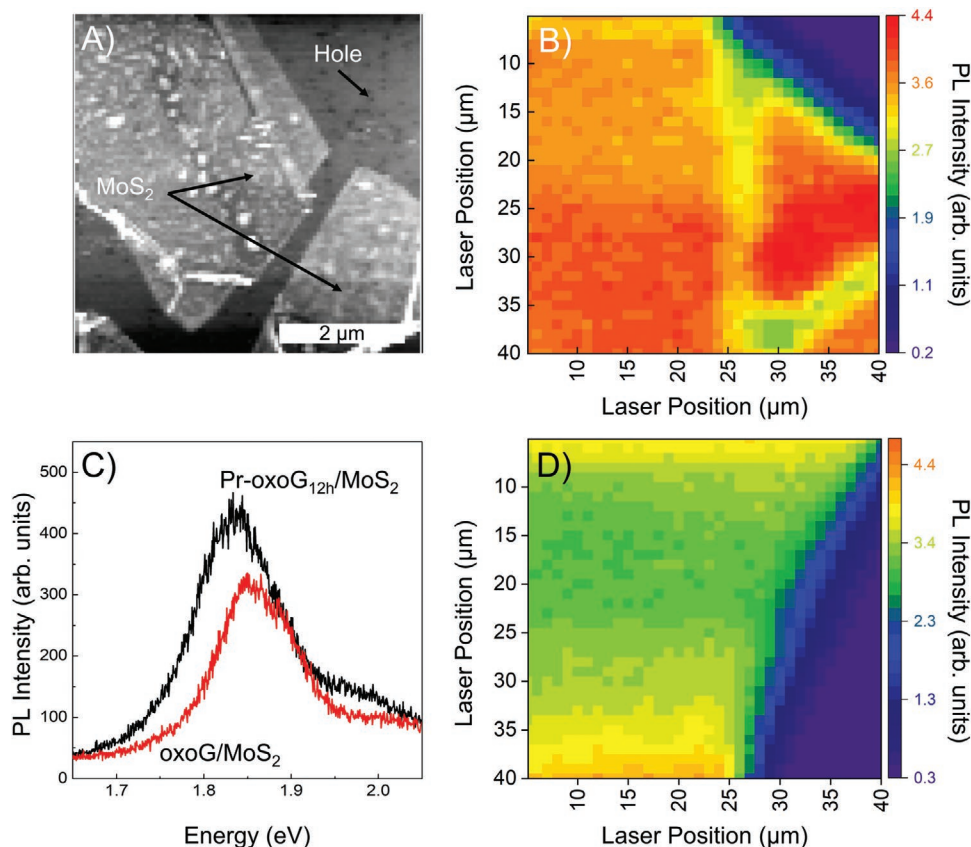
**ADVANCED
SCIENCE NEWS**

www.advancedsciencenews.com

**ADVANCED
MATERIALS
INTERFACES**

www.advmatinterfaces.de

Figure 6. A) Features an AFM map of MoS_2 on top of Pr-oxoG$_{12h}$. Holes of sizes ranging from 50 nm to 200 nm are visible in the top right of the image and are well separated from one another. The Pr-oxoG$_{12h}$/MoS$_2$ PL intensity map (B) shows a constant PL intensity over the MoS_2 flake, exhibiting no sign of a spatial PL modulation that may arise from free-standing MoS_2. C) shows PL spectra from oxo-G/MoS$_2$ (red) and Pr-oxoG$_{12h}$/MoS$_2$ (black), the PL on the Pr-oxoG$_{12h}$ sample exhibiting higher intensity than that seen in the oxo-G/MoS$_2$ sample. A PL Intensity map of oxo-G/MoS$_2$ (D) taken with the same parameters as (B) shows a similar constant PL intensity in addition to having slightly lower intensity to that of Pr-oxoG$_{12h}$/MoS$_2$.

destroyed flakes, removal of excess potassium permanganate leads to the growth of circular pores with diameters of 50 to 250 nm, depending on the annealing time. Thereby, for example, uniform pores have mean diameters of 147 ± 73 nm after annealing for 12 h. From XPS analysis we conclude that carbonyl, hydroxyl, and carboxyl groups decorate the rims of pores. Since carbonyl groups have electron-accepting properties, it is plausible that the 2D material pore-graphene, can p-dope other 2D materials, such as MoS_2. However, further research, such as correlating field-effect measurements with PL mapping is necessary to further elucidate the mechanism behind PL enhancement by 10-times. Moreover, we showed that Mn-impurities limit the increase of the PL of MoS_2 in the heterostructure with pore-graphene and thus, we propose that the interaction of Mn-species with carbonyl groups may be responsible. Moreover, we conclude that not all defects detected by Raman spectroscopy lead to the growth of pores, taking into account that the initial distance of defects is 2 nm and the final pore-size increased to several hundreds of nm. Finally, we propose that pore-graphene is a 2D material with functional groups at the rims of pores and thus an attractive novel material for sensing applications in the future.

Supporting Information

Supporting Information is available from the Wiley Online Library or from the author.

Conflict of Interest

The authors declare no conflict of interest.

Data Availability Statement

The data that support the findings of this study are available from the corresponding author upon reasonable request.

[1] C. Neumann, D. Kaiser, M. J. Mohn, M. Füser, N.-E. Weber, O. Reimer, A. Gölzhäuser, T. Weimann, A. Terfort, U. Kaiser, A. Turchanin, *ACS Nano* **2019**, *13*, 7310.

[2] Z. Wang, Q. Yao, C. Neumann, F. Borrnert, J. Renner, U. Kaiser, A. Turchanin, H. J. W. Zandvliet, S. Eigler, *Angew. Chem., Int. Ed.* **2020**, *59*, 13657.

[3] F. Hao, D. Fang, Z. Xu, *Appl. Phys. Lett.* **2011**, *99*, 041901.

[4] B. Zhan, C. Li, J. Yang, G. Jenkins, W. Huang, X. Dong, *Small* **2014**, *10*, 399.

[5] D. Akinwande, C. J. Brennan, J. S. Bunch, P. Egberts, J. R. Felts, H. Gao, R. Huang, J.-S. Kim, T. Li, Y. Li, K. M. Liechti, N. Lu, H. S. Park, E. J. Reed, P. Wang, B. I. Yakobson, T. Zhang, Y.-W. Zhang, Y. Zhou, Y. Zhu, *Extreme Mech. Lett.* **2017**, *13*, 42.

[6] J. Xie, Q. Chen, H. Shen, G. Li, *J. Electrochem. Soc.* **2020**, *167*, 037541.

[7] K. G. Zhou, K. S. Vasu, C. T. Cherian, M. Neek-Amal, J. C. Zhang, H. Ghorbanfekr-Kalashami, K. Huang, O. P. Marshall, V. G. Kravets, J. Abraham, Y. Su, A. N. Grigorenko, A. Pratt, A. K. Geim, F. M. Peeters, K. S. Novoselov, R. R. Nair, *Nature* **2018**, *559*, 236.

[8] W. Wu, Y. Shi, G. Liu, X. Fan, Y. Yu, *Desalination* **2020**, *491*, 114452.

[9] H. Liu, H. Wang, X. Zhang, *Adv. Mater.* **2015**, *27*, 249.

[10] Q. Xu, H. Xu, J. Chen, Y. Lv, C. Dong, T. S. Sreeprasad, *Inorg. Chem. Front.* **2015**, *2*, 417.

[11] C. E. Halbig, R. Lasch, J. Krull, A. S. Pirzer, Z. Wang, J. N. Kirchhof, K. I. Bolotin, M. R. Heinrich, S. Eigler, *Angew. Chem., Int. Ed.* **2019**, *58*, 3599.

[12] A. Criado, M. Melchionna, S. Marchesan, M. Prato, *Angew. Chem., Int. Ed.* **2015**, *54*, 10734.

[13] S. Chen, J. Duan, M. Jaroniec, S. Z. Qiao, *J. Mater. Chem. A* **2013**, *1*, 9409.

[14] A. C. Lokhande, I. A. Qattan, C. D. Lokhande, S. P. Patole, *J. Mater. Chem. A* **2020**, *8*, 918.

[15] Y. Zhang, Q. Wan, N. Yang, *Small* **2019**, *15*, 1903780.

[16] A. Guirguis, J. W. Maina, L. Kong, L. C. Henderson, A. Rana, L. H. Li, M. Majumder, L. F. Dumée, *Carbon* **2019**, *155*, 660.

[17] X. Yang, C. Cheng, Y. Wang, L. Qiu, D. Li, *Science* **2013**, *341*, 534.

[18] S. Han, D. Wu, S. Li, F. Zhang, X. Feng, *Adv. Mater.* **2014**, *26*, 849.

[19] H. Yang, Q. He, Y. Liu, H. Li, H. Zhang, T. Zhai, *Chem. Soc. Rev.* **2020**, *49*, 2916.

[20] C. J. Russo, J. A. Golovchenko, *Proc. Natl. Acad. Sci. USA* **2012**, *109*, 5953.

[21] S. Standop, O. Lehtinen, C. Herbig, G. Lewes-Malandrakis, F. Craes, J. Kotakoski, T. Michely, A. V. Krasheninnikov, C. Busse, *Nano Lett.* **2013**, *13*, 1948.

[22] A. Guirguis, J. W. Maina, X. Zhang, L. C. Henderson, L. Kong, H. Shon, L. F. Dumée, *Mater. Horiz.* **2020**, *7*, 1218.

[23] N. I. Kato, *J. Electron Microsc.* **2004**, *53*, 451.

[24] Y. Lin, Y. Liao, Z. Chen, J. W. Connell, *Mater. Res. Lett.* **2017**, *5*, 209.

[25] S. P. Surwade, S. N. Smirnov, I. V. Vlassiouk, R. R. Unocic, G. M. Veith, S. Dai, S. M. Mahurin, *Nat. Nanotechnol.* **2015**, *10*, 459.

[26] T. He, Z. Wang, F. Zhong, H. Fang, P. Wang, W. Hu, *Adv. Mater. Technol.* **2019**, *4*, 1900064.

[27] A. Kaplan, Z. Yuan, J. D. Benck, A. Govind Rajan, X. S. Chu, Q. H. Wang, M. S. Strano, *Chem. Soc. Rev.* **2017**, *46*, 4530.

[28] X. Wang, L. Jiao, K. Sheng, C. Li, L. Dai, G. Shi, *Sci. Rep.* **2013**, *3*, 1996.

[29] H. Zhang, W. Liu, Z. Zhang, M. Li, B. Xu, J. Guo, *Phys. Chem. Chem. Phys.* **2018**, *20*, 26814.

[30] S. C. O'Hern, M. S. Boutilier, J. C. Idrobo, Y. Song, J. Kong, T. Laoui, M. Atieh, R. Karnik, *Nano Lett.* **2014**, *14*, 1234.

[31] L. Huang, M. Zhang, C. Li, G. Shi, *J. Phys. Chem. Lett.* **2015**, *6*, 2806.

[32] H.-K. Kim, S.-M. Bak, S. W. Lee, M.-S. Kim, B. Park, S. C. Lee, Y. J. Choi, S. C. Jun, J. T. Han, K.-W. Nam, K. Y. Chung, J. Wang, J. Zhou, X.-Q. Yang, K. C. Roh, K.-B. Kim, *Energy Environ. Sci.* **2016**, *9*, 1270.

[33] D. Zhou, Y. Cui, P. W. Xiao, M. Y. Jiang, B. H. Han, *Nat. Commun.* **2014**, *5*, 4716.

[34] Z. Fan, Q. Zhao, T. Li, J. Yan, Y. Ren, J. Feng, T. Wei, *Carbon* **2012**, *50*, 1699.

[35] Y. Xu, C.-Y. Chen, Z. Zhao, Z. Lin, C. Lee, X. Xu, C. Wang, Y. Huang, M. I. Shakir, X. Duan, *Nano Lett.* **2015**, *15*, 4605.

[36] S. Eigler, *Phys. Chem. Chem. Phys.* **2014**, *16*, 19832.

[37] S. Eigler, M. Enzelberger-Heim, S. Grimm, P. Hofmann, W. Kroener, A. Geworski, C. Dotzer, M. Rockert, J. Xiao, C. Papp, O. Lytken, H. P. Steinruck, P. Müller, A. Hirsch, *Adv. Mater.* **2013**, *25*, 3583.

[38] S. Eigler, F. Hof, M. Enzelberger-Heim, S. Grimm, P. Müller, A. Hirsch, *J. Phys. Chem. C* **2014**, *118*, 7698.

[39] M. M. Lucchese, F. Stavale, E. H. M. Ferreira, C. Vilani, M. V. O. Moutinho, R. B. Capaz, C. A. Achete, A. Jorio, *Carbon* **2010**, *48*, 1592.

[40] L. G. Cancado, A. Jorio, E. H. Ferreira, F. Stavale, C. A. Achete, R. B. Capaz, M. V. Moutinho, A. Lombardo, T. S. Kulmala, A. C. Ferrari, *Nano Lett.* **2011**, *11*, 3190.

[41] S. Eigler, C. Dotzer, F. Hof, W. Bauer, A. Hirsch, *Chem. - Eur. J.* **2013**, *19*, 9490.

[42] F. Grote, C. Gruber, F. Börrnert, U. Kaiser, S. Eigler, *Angew. Chem., Int. Ed.* **2017**, *56*, 9222.

[43] P. Feicht, J. Biskupek, T. E. Gorelik, J. Renner, C. E. Halbig, M. Maranska, F. Puchtler, U. Kaiser, S. Eigler, *Chem. - Eur. J.* **2019**, *25*, 8955.

[44] M. González, J. Baselga, J. Pozuelo, *J. Mater. Chem. C* **2016**, *4*, 8575.

[45] K. Garg, R. Shanmugam, P. C. Ramamurthy, *Opt. Mater.* **2018**, *76*, 42.

[46] C. Lee, H. Yan, L. E. Brus, T. F. Heinz, J. Hone, S. Ryu, *ACS Nano* **2010**, *4*, 2695.

[47] Z. Wang, Q. Yao, Y. Hu, C. Li, M. Hußmann, B. Weintrub, J. N. Kirchhof, K. Bolotin, T. Taniguchi, K. Watanabe, S. Eigler, *RSC Adv.* **2019**, *9*, 38011.

[48] T. Musso, P. V. Kumar, A. S. Foster, J. C. Grossman, *ACS Nano* **2014**, *8*, 11432.

[49] X. Wei, Z. Yu, F. Hu, Y. Cheng, L. Yu, X. Wang, M. Xiao, J. Wang, X. Wang, Y. Shi, *AIP Adv.* **2014**, *4*, 123004.

[50] W. Zhang, J.-K. Huang, C.-H. Chen, Y.-H. Chang, Y.-J. Cheng, L.-J. Li, *Adv. Mater.* **2013**, *25*, 3456.

**ADVANCED
MATERIALS
INTERFACES**

Supporting Information

Synthesis of Wet-Chemically Prepared Porous-Graphene Single Layers on Si/SiO$_2$ Substrate Increasing the Photoluminescence of MoS$_2$ in Heterostructures

Yiqing Wang, Christof Neumann, Marleen Hußmann, Qing Cao, Yalei Hu, Oisín Garrity, Patryk Kusch, Andrey Turchanin, and Siegfried Eigler*

Supporting Information

Synthesis of p-doped porous-graphene single layers on Si/SiO₂ substrate increasing the photoluminescence of MoS₂ in heterostructures

Yiqing Wang, Christof Neumann Marleen Hußmann, Qing Cao, Yalei Hu, Oisín Garrity, Patryk Kusch, Andrey Turchanin, Siegfried Eigler

Experimental Section

Materials and Methods

Double-distilled water from Carl Roth GmbH. Graphite (3061) was obtained from Asbury Carbon. Si wafers with a 300 nm thick SiO_2 layer were purchased from Fraunhofer Institut für Integrierte Systeme und Bauelementetechnologie IISB in Erlangen. Chemicals were purchased from Sigma-Aldrich. A Nikon Eclipse LV150-NL with differential interference contrast was used to visualize materials. Statistical Raman spectroscopy (SRS) was recorded using a Horiba Explora spectrometer with a 532 nm laser for excitation combined with 100x magnification objective. Increment of Raman spectra measurements is 0.7 μm. PL map parameters for Figure 6: The steps between two recorded spectra was 250 nm, with a laser spot size of around 400 nm. As excitation we use a 532 nm laser and kept the laser power below 0.5 mW to avoid sample heating. As a reference, we record a PL map with the same experimental parameters for a sample without holes.

For preparation of Langmuir-Blodgett films, we used a Kibron μThroug system with water as subphase. The surface tension of water = 72.8 mN m^{-1} was set to zero. The films were formed at a surface tension value of 3 mN m^{-1}. AFM images were recorded on an JPK Nanowizard 4 equipped with NSG10/Au probes and intermittent contact mode was chosen. Using Tap300-G AFM Probe. X-ray photoelectron spectroscopy (XPS) was performed using a multiprobe system (Scienta Omicron) with a monochromatic X-ray source (Al K$_\alpha$) and an electron analyzer (Argus CU) with 0.6 eV spectral energy resolution. The spectra were fitted using Voigt functions (30:70) after Shirley background subtraction. The Si 2p peak (SiO_2, 103.5 eV) was used for binding energy calibration. Putting the entire substrate with monolayer flakes in the XPS instrument.

Synthesis of Oxo-Functionalized Graphene (oxoG)

OxoG was prepared by low-temperature oxidation of graphite according to our previously developed method[1, 2]. Accordingly, 2 g of graphite (type 3061, Asbury Carbon Mills) were mixed with 50 mL of sulfuric acid (97.5%) in a Teflon reactor under mechanical stirring at a temperature below 10 °C. After that, 4 g of $KMnO_4$ were slowly added within 4 h and further stirred for 16 h. Then, 40 mL of cold diluted sulfuric acid (20 wt%) and followed by 100 mL of cold double distilled water were slowly continuously added through a programmed pump within 4 h and 16 h, respectively. Then, 40 mL of H_2O_2 (5 wt%) were added into the reaction mixture to solubilize manganese species. Then, the dispersion was washed with cold double

1

distilled water by repeated centrifugation and redispersion in double distilled water for six times.

Formation of films of flakes of oxoG on Si/SiO$_2$ wafer:
Flakes of oxoG were deposited on a Si/300 nm SiO$_2$ wafer by Langmuir Blodgett technique. First, an light yellowish oxoG dispersion was prepared by dilution of water/methanol, 1/2 by volume (the exact concentration was found to have only little influence on the quality of the formed film of flakes). The dispersion was dropped on the water-interface of the Langmuir-Blodgett trough and the barriers were compressed until a surface tension of 3 mN/m was reached.

Reduction of flakes of oxoG on Si/SiO$_2$ wafer (Preparation of red-oxoG).
Wafers with deposited flakes of oxoG were placed in a 20 mL glass vial filled with glass wool and were reduced by the vapor of HI and TFA for 10 min at 80 °C. Subsequently, the wafers were extensively washed with pure water and dried.

Preparation of Pr-oxoG.
Pr-oxoG was prepared by using potassium permanganate (KMnO$_4$) as the etching agents. Flakes of oxoG on a Si/SiO$_2$ wafer were immersed in aqueous KMnO$_4$ solution (0.2 mmol). The oxoG flakes on Si/SiO$_2$ the wafer was washed with water and dried in the air. Then, the wafer was heated in argon atmosphere at a rate of 10 °C min^{-1} to 400 °C for 6 h, 12 h and 16 h, respectively and cooled down to room temperature.

Preparation of tp-oxoG.
The oxoG flakes on Si/SiO$_2$ mixture were dried in the air and then heated at a rate of 10 °C min^{-1} to 400 °C for 12 h in an atmosphere of Argon and cooled down to room temperature.

Removal of metal containing species.
Annealed wafers were immersed in aqueous HCl solution (1 M) for two days to remove the metal-containing species. Then, wafers were shaked gently in double distilled water to wash off acids. Finally, Pr-oxoG on Si/300 nm SiO$_2$ wafers is obtained. As reference tp-oxoG was obtained the same way, however without KMnO$_4$ treatment.

Pore diameter and area analysis
Pore diameters were estimated manually by using the straight line tool in ImageJ. After counting the pores, export the results of the pore diameter and area.[3]

2

Table S1. Survey of perforation techniques, with indicated starting material, layer thickness, etching process, realized pore size and targeted application.

Raw material	Thickness	Perforation technique	Pore size (nm)	application	Ref.
Graphene	Few layers	Oxygen plasma, ozone	<5	permeance membranes	[4]
Graphene	Few layers	Focused ions beam (SEM)	<50	-	[5]
Graphene	Monolayer	Bottom-up synthesis	0-250	Charge Carrier Transport	[6]
GO	-	Chemical-oxidative etching (KMnO$_4$), microwave irradiation.	2-4	supercapacitor	[7]
GO	-	Chemical-oxidative etching (HNO$_3$)	60-90	Catalyst （Bulk）	[8]
GO	-	Chemical-oxidative etching (H$_2$O$_2$)	2-70	supercapacitor	[9]
Graphene	Few layers	Liquid arc discharge, Ni atoms	10–50	-	[10]
Graphene	Monolayer	Strain-assisted annealing treatment, Pt nanoparticles etching	<50	Charge Carrier Transport	[11]
RGO	Few layers	Annealing treatment, Pt nanoparticles etching	<50	-	[11]
GO	Bulk	Annealing treatment, Fe$_2$O$_3$ etching	-	electrocatalyst	[12]
RGO	Bulk	Carbothermal reaction by using the metal oxide nanoparticles （Oxometalates）	5-10, 20-50	-	[13]
Oxo-functionalized graphene	Monolayer	Disproportionation , functionalization of 4%	1-3	-	[2]
Oxo-functionalized graphene	Monolayer	Disproportionation, functionalization of 60%	5	Charge Carrier Transport	[14]

3
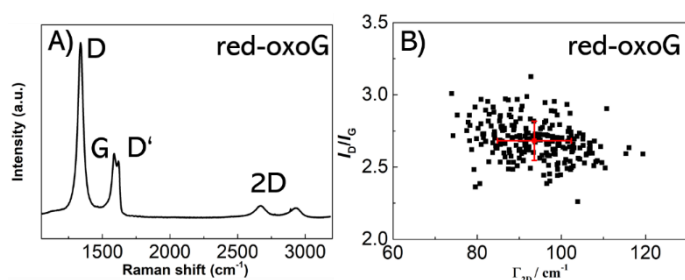
Figure S1. Statistical Raman analysis of chemically reduced oxoG (Statistical Raman microscopy measured at 532 nm laser excitation wavelength. The laser power is below 0.1 mW to avoid heating induced by laser). A) Average spectrum of reduced oxoG with I_D/I_G ratio of 2.7±0.14 and Γ_{2D}=93±9 cm^{-1}. B) Scatter plot of ID/IG vs FWHM of the 2D peak.
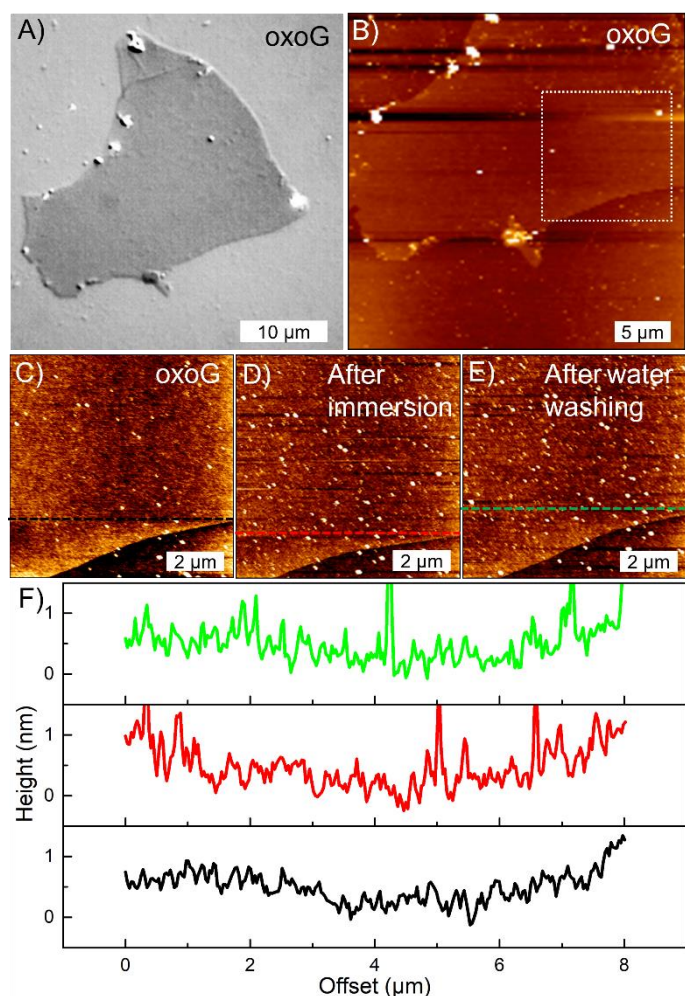
Figure S2. A) Optical microscope images of flakes of oxoG on Si/300 nm SiO$_2$ wafer and AFM topography images in B and C; before, D) after immersion in KMnO$_4$ solution and E) after washing in water. F) Height profiles of AFM images along black, red and green lines. The black, red and green line represent the height profiles of oxoG, oxoG after immersion and oxoG after washing with water, respectively.
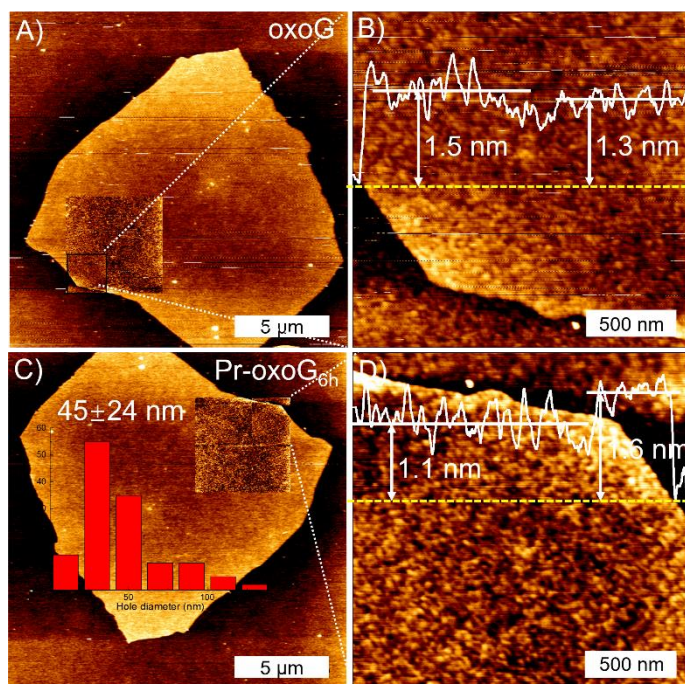
Figure S3. A and B) AFM topography images of single layer oxoG, showing no big pores. C and D) AFM images of Pr-oxoG$_{6h}$. The yellow lines represent the height profiles of oxoG and Pr-oxoG$_{6h}$, respectively.
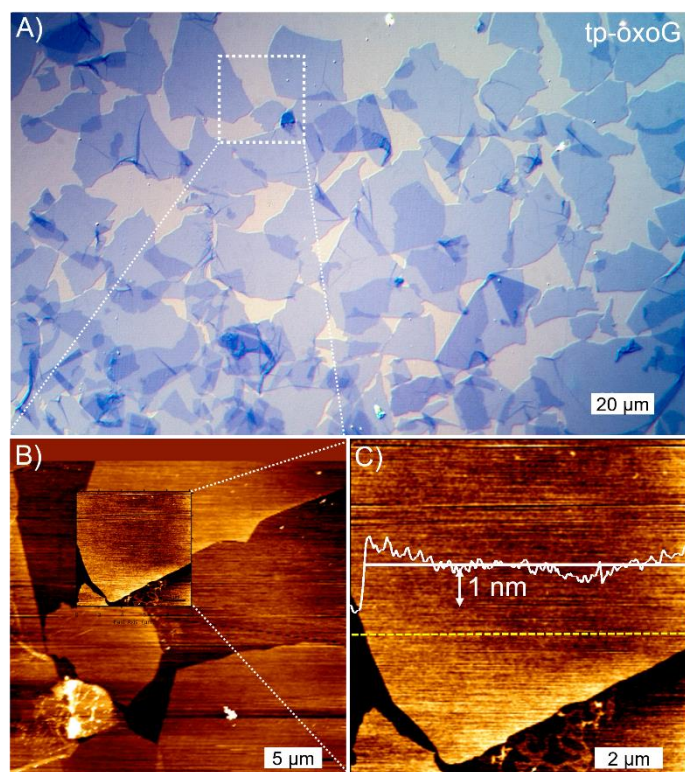
Figure S4. A) Optical microscope image of flakes of tp-oxoG on Si/300 nm SiO$_2$ substrate. B) AFM topography image of tp-oxoG (12 h annealing time). C) Figure S3B shows no big pores after annealing single layer oxoG for 12 h without Mn-species. The yellow line represents the height profile of tp-oxoG.

5
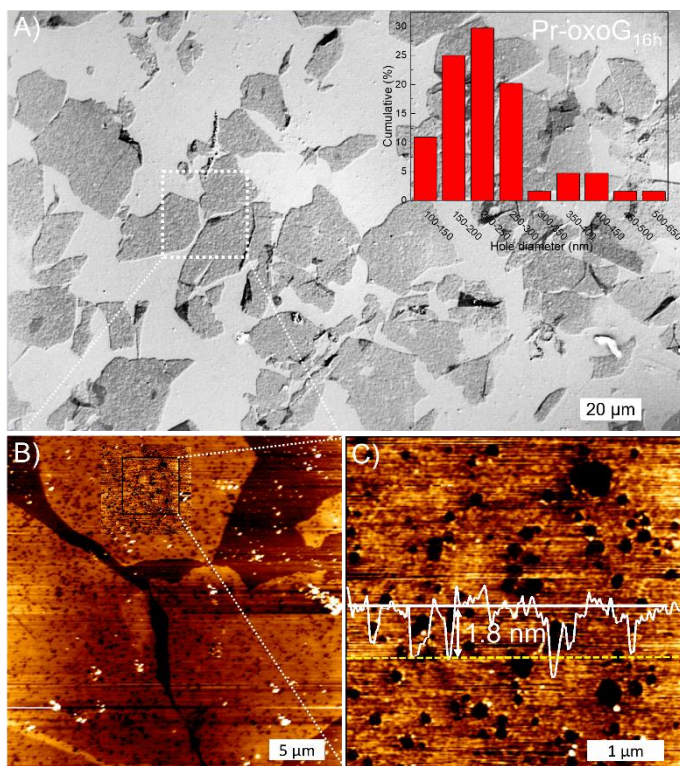
Figure S5. A) Optical microscope image of flakes of Pr-oxoG$_{16h}$ on Si/300 nm SiO$_2$ substrate; B) AFM topography image of Pr-oxoG$_{16h}$. C) AFM image showing pores. The yellow line represents the height profile of Pr-oxoG$_{16h}$.
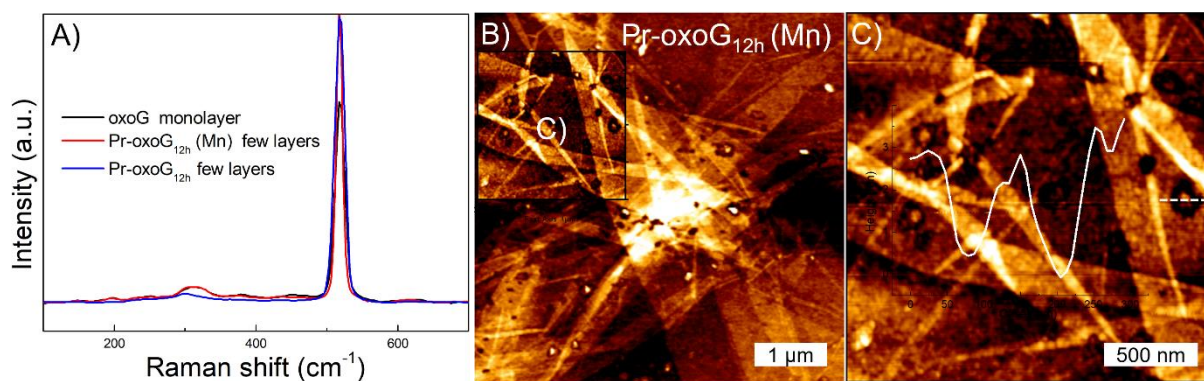
Figure S6. A) Raman spectrum of monolayer oxoG, few-layer Pr-oxoG12h (Mn) and few-layer Pr-oxoG12h on Si/300 nm SiO$_2$ substrate; B, C) AFM topography image of few-layer Pr-oxoG12h (Mn). The white line represents the height profile of few-layer Pr-oxoG12h (Mn).

Table S2. Number total of pores, mean (average), standard deviation, minimum, Median and maximum of diameter of pores.

	Number total	Mean (diameter)	Standard Deviation	Sum	Minimum	Median	Maximum
Pr-oxoG$_{6h}$	126	45.45256	24.35966	5727.022	9.298	37.749	127.104
Pr-oxoG$_{12h}$	181	146.74168	73.25105	26560.244	37.771	133.539	503.704
Pr-oxoG$_{16h}$	104	167.95725	93.74814	17635.511	40.323	153.438	620.968
Pr-oxoG$_{12h}$ (Mn)*	101	128.59717	74.66974	12988.314	26.845	108.216	457.154
Pr-oxoG$_{12h}$*	101	146.98062	72.06714	14845.043	48.65	138.462	523.981
	Number total	Mean **(Area)**	Standard Deviation	Sum	Minimum	Median	Maximum
Pr-oxoG$_{6h}$	126	149.94286	75.35488	18892.8	38.42	124.863	403.405
Pr-oxoG$_{12h}$	181	1138.8772	542.72571	206136.774	329.218	1042.524	3786.008
Pr-oxoG$_{16h}$	105	3680.27461	1830.97899	386428.834	1144.409	3433.228	12588.501
Pr-oxoG$_{12h}$ (Mn)*	101	1903.31623	1003.89167	192234.939	540.492	1621.476	6305.738
Pr-oxoG$_{12h}$*	101	2502.78283	1099.68609	252781.066	1183.432	2366.864	8284.024

* same analyzed area
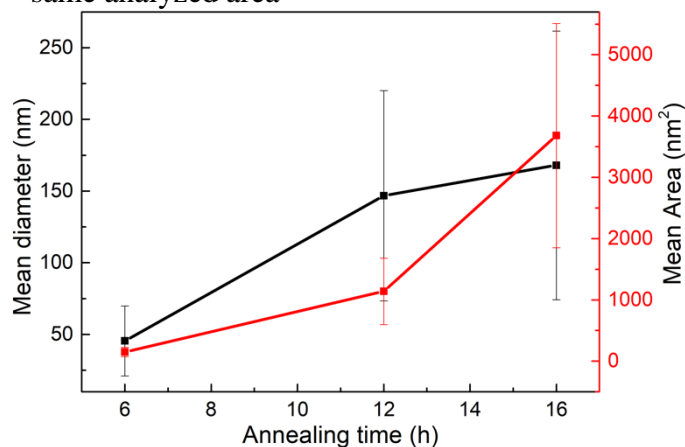
Figure S7. A comparison between the different mean diameters and mean pores areas after different annealing time.

7
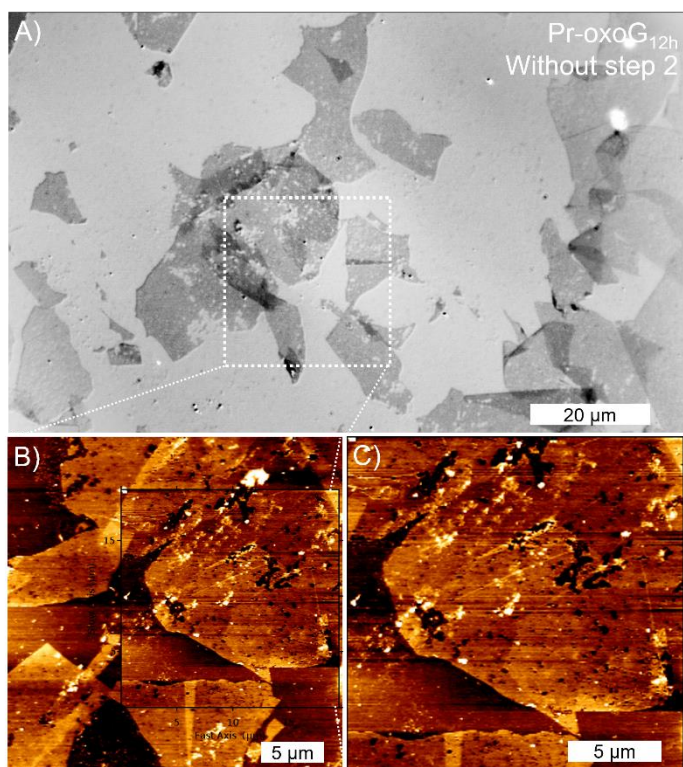
Figure S8. A) Optical microscope image of flakes of Pr-oxoG$_{12h}$ on Si/SiO$_2$ substrate without water washing step 2; B) AFM topography image of flakes of Pr-oxoG$_{12h}$ on Si/SiO$_2$ substrate without water washing step 2.

Table S3. Quantitative analysis of the high resolution XP C 1s and O 1s spectra presented in Figure 3A and B of the main text including peak assignment, binding energies and areas obtained from the spectra deconvolution.

sample		Peak assignment	Binding energy, eV	Area, %
oxoG	C 1s	C-C /C-H	284.6	47.8
		C-O/C-OH/C=O	286.6	46.3
		C=O/COOH	288.1	5.9
	O 1s	C=O	531.2	31.1
		C-O/SiO$_2$/O-C=O	532.4	67.2
		-OH/Na KLL	535.4	1.7
Pr-oxoG$_{12h}$	C 1s	C-C sp^2	284.5	50.8
		C-C sp^3 / C-S/C-N	285.2	34.6
		C-O/C-OH	286.5	4.5
		C=O	287.9	7.0
		COOH	289.9	3.1
	O 1s	C=O	531.3	28.0
		C-O/SiO$_2$/O-C=O	532.7	65.4
		-OH/Na KLL	535.8	6.6
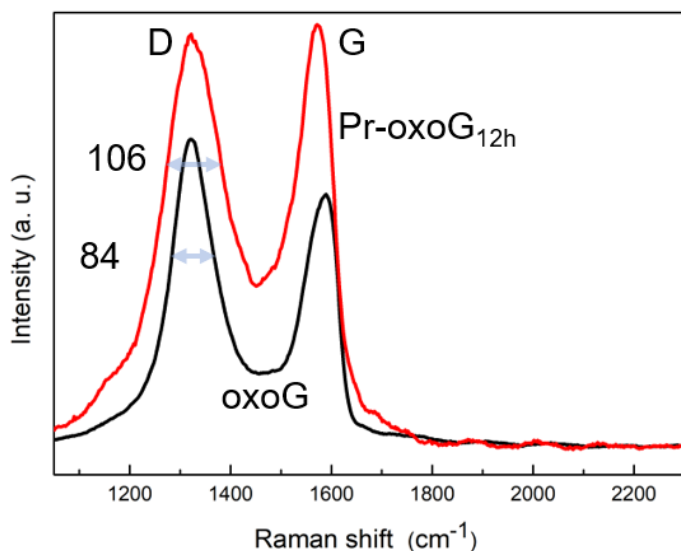
Figure S9. Raman spectrum of oxoG, and Pr-oxoG$_{12h}$. Numbers indicate the full-width at half-maximum of the D band.

9
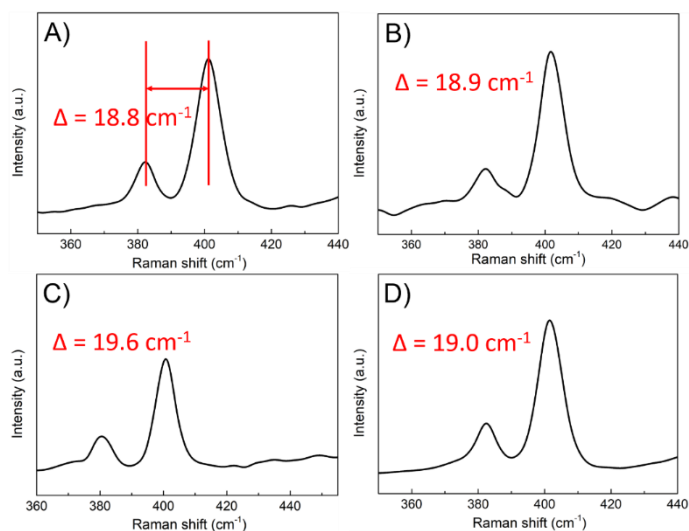
Figure S10. Raman spectrum of monolayer MoS_2 for A) MoS_2 on SiO_2, B）Pr-oxoG$_{6h}$/MoS$_2$, C）Pr-oxoG$_{12h}$/MoS$_2$ and D）Pr-oxoG$_{12h}$/MoS$_2$ (Mn) heterostructure.
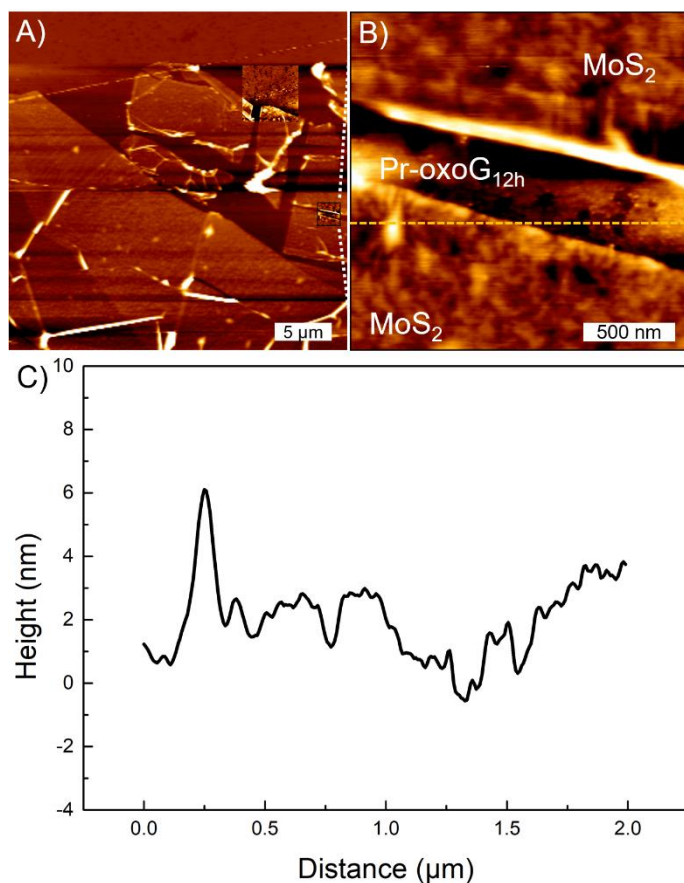
Figure S11. A and B）AFM topography images of monolayer Pr-oxoG$_{12h}$/MoS$_2$ heterostructure. C)The white line represents the height of Pr-oxoG$_{12h}$/MoS$_2$ heterostructure. MoS$_2$ and Pr-oxoG$_{12h}$ almost have same thickness.
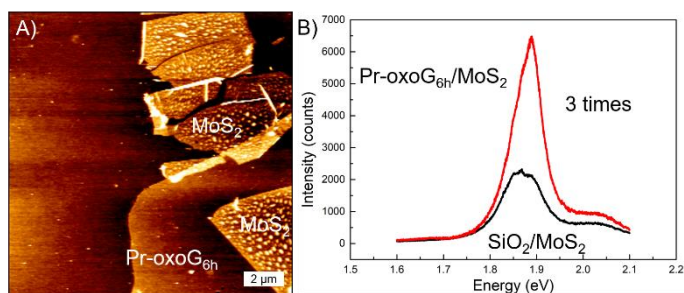
Figure S12. A) AFM topography images of monolayer Pr-oxoG$_{6h}$/MoS$_2$ heterostructure; B) PL spectra of monolayer MoS$_2$ on SiO$_2$ (black) and monolayer Pr-oxoG$_{6h}$/MoS$_2$ heterostructure (red), respectively.
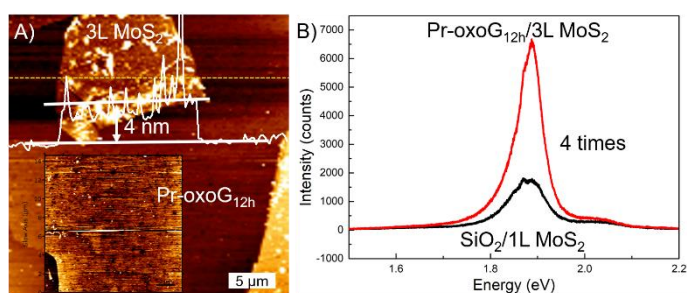
Figure S13. A) AFM topography images of trilayer Pr-oxoG$_{12h}$/MoS$_2$ heterostructure. The height of 3L MoS$_2$ is almost 4 nm. B) PL spectra of monolayer MoS$_2$ on SiO$_2$ and trilayer Pr-oxoG$_{12h}$/MoS$_2$ heterostructure.
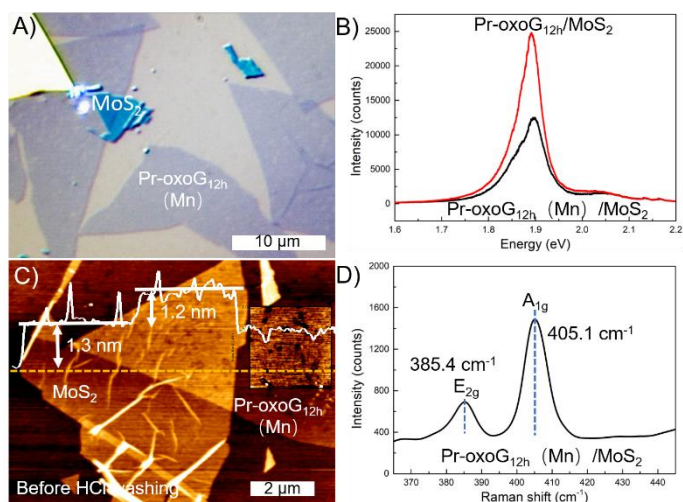
Figure S14. A) Optical microscope image of a monolayer Pr-oxoG$_{12h}$ (Mn)/MoS$_2$ heterostructure; B) PL spectra of a monolayer Pr-oxoG$_{12h}$/MoS$_2$ heterostructure and a monolayer Pr-oxoG$_{12h}$ (Mn)/MoS$_2$ heterostructure. C) AFM topography image of Pr-oxoG$_{12h}$ (Mn)/MoS$_2$ heterostructure. The white line represents the height profile along yellow line. D) Raman spectra of Pr-oxoG$_{12h}$ (Mn)/MoS$_2$.
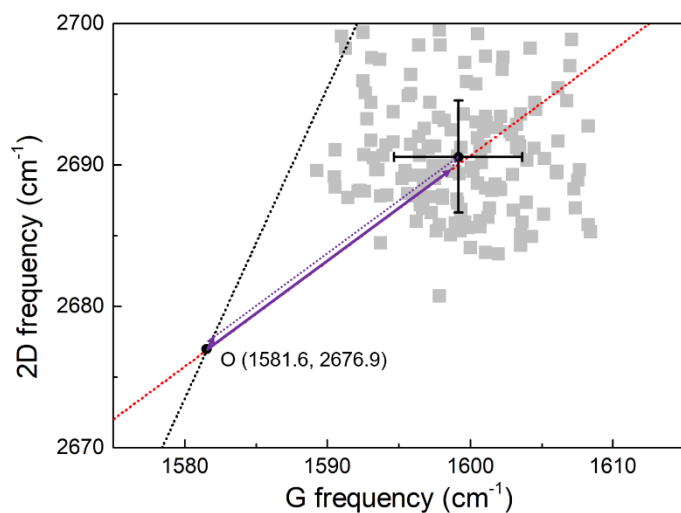
Figure S15. The grey dots were obtained from Raman mapping of Pr-oxoG$_{12h}$. The black dot (1581.6, 2676.9 cm^{-1}) stems from reference [15] and the position relates to graphene, which is not affected by charge or strain doping. The red dashed line represent doped graphene with varying density of holes with a slope is 0.75. The black dashed line represents charge-neutral graphene under randomly oriented uniaxial stress with a slope of 2.20. The purple solid line is the effects corresponding to the hole doping and strain decomposed by the vector model.

12

References

[1]   S. Eigler, M. Enzelberger-Heim, S. Grimm, P. Hofmann, W. Kroener, A. Geworski, C. Dotzer, M. Rockert, J. Xiao, C. Papp, O. Lytken, H. P. Steinruck, P. Müller, A. Hirsch, *Adv. Mater.* **2013**, 25, 3583.

[2]   F. Grote, C. Gruber, F. Börrnert, U. Kaiser, S. Eigler, *Angew. Chem. Int. Ed.* **2017**, 56, 9222.

[3]   S. C. O'Hern, M. S. Boutilier, J. C. Idrobo, Y. Song, J. Kong, T. Laoui, M. Atieh, R. Karnik, *Nano Lett.* **2014**, 14, 1234.

[4]   G. He, S. Huang, L. F. Villalobos, J. Zhao, M. Mensi, E. Oveisi, M. Rezaei, K. V. Agrawal, *Energy Environ. Sci.* **2019**, 12, 3305.

[5]   S. Standop, O. Lehtinen, C. Herbig, G. Lewes-Malandrakis, F. Craes, J. Kotakoski, T. Michely, A. V. Krasheninnikov, C. Busse, *Nano Lett.* **2013**, 13, 1948.

[6]   C. Neumann, D. Kaiser, M. J. Mohn, M. Füser, N.-E. Weber, O. Reimer, A. Gölzhäuser, T. Weimann, A. Terfort, U. Kaiser, A. Turchanin, *ACS Nano* **2019**, 13, 7310.

[7]   Z. Fan, Q. Zhao, T. Li, J. Yan, Y. Ren, J. Feng, T. Wei, *Carbon* **2012**, 50, 1699.

[8]   X. Wang, L. Jiao, K. Sheng, C. Li, L. Dai, G. Shi, *Sci. Rep.* **2013**, 3, 1996.

[9]   Y. Xu, C.-Y. Chen, Z. Zhao, Z. Lin, C. Lee, X. Xu, C. Wang, Y. Huang, M. I. Shakir, X. Duan, *Nano Lett.* **2015**, 15, 4605.

[10]   H. Zhang, W. Liu, Z. Zhang, M. Li, B. Xu, J. Guo, *Phys. Chem. Chem. Phys.* **2018**, 20, 26814.

[11]   X. Liao, B. Zhang, T. Furutani, Y. Chen, H. Xiao, Y. Ni, A. Yonezu, X. Chen, *Small* **2019**, 15, e1903213.

[12]   T. Palaniselvam, H. B. Aiyappa, S. Kurungot, *J. Mater. Chem.* **2012**, 22, 23799.

[13]   D. Zhou, Y. Cui, P. W. Xiao, M. Y. Jiang, B. H. Han, *Nat. Commun.* **2014**, 5, 4716.

[14]   Z. Wang, Q. Yao, C. Neumann, F. Börrnert, J. Renner, U. Kaiser, A. Turchanin, H. J. W. Zandvliet, S. Eigler, *Angew. Chem. Int. Ed.* **2020**, 59, 13657.

[15]   J. E. Lee, G. Ahn, J. Shim, Y. S. Lee, S. Ryu, *Nat. Commun.* **2012**, 3, 1024.

13

6.2 Wet-chemical Synthesis of Solution-processible Porous Graphene via Defect-driven Etching

Authors	Yalei Hu, Qing Cao, Christof Neumann, Tibor Lehnert, Felix Börrnert, Yiqing Wang, Ute Kaiser, Andrey Turchanin, and Siegfried Eigler
Journal	*Carbon* **2021**, *185*, 568-577
DOI	10.1016/j.carbon.2021.09.027
Links	https://doi.org/10.1016/j.carbon.2021.09.027
Detailed scientific contribution	The concept of this manuscript was elaborated by Y. Hu and Prof. Dr. S. Eigler. Y. Hu conducted etching experiments, prepared samples for analyses. Q. Cao participated the design of Scheme and Raman measurement. T. Lehnert made in deep HRTEM measurements. F. Börrnert scanned samples for quality for HRTEM. Y. Wang conducted AFM experiments. U. Kaiser interpreted HRTEM measurements. A. Turchanin analyzed and interpreted XPS spectra. Y. Hu and Prof. Dr. S. Eigler wrote manuscript. The revision of the manuscript was assisted by Q. Cao.
Estimated own contribution	~20%

6.3 Regiochemically Oxo-functionalized Graphene, Guided by Defect Sites, as Catalyst for Oxygen Reduction to Hydrogen Peroxide

Authors	Yiqing Wang, Fabian Grote, Qing Cao, and Siegfried Eigler
Journal	*J. Phys. Chem. Lett.* **2021**, *12,* 10009−10014.
DOI	10.1021/acs.jpclett.1c02957
Links	https://doi.org/10.1021/acs.jpclett.1c02957
Detailed scientific contribution	The concept of this manuscript was elaborated by Y. Wang and Prof. Dr. S. Eigler.
	Oxo-G and related materials were prepared and characterized with optical microscopy and atomic force microscopy by Y. Wang. Y. Wang did electrochemical measurements, including electrochemical reduction and oxidation of oxoG, catalyst performance testing. OxoG* was synthesised by F. Grote. Y. Wang did the electrochemical test of oxoG* and related materials. Q. Cao did Raman measurement. X-ray photoelectron spectroscopy was measured by R.T. Qie from Technical University of Denmark. Y. Wang analyzed the data of Raman and X-ray photoelectron spectroscopy.
	Y. Wang wrote the manuscript. The revision of the manuscript was assisted by Prof. Dr. S. Eigler, F. Grote and Q. Cao.
Estimated own contribution	~15%

6.4 Managing Excess Lead Iodide with Functionalized Oxo-graphene Nanosheets for Stable Perovskite Solar Cells

Authors	Guixiang Li, Dr. Yalei Hu, Meng Li, Ying Tang, Zuhong Zhang, Artem Musiienko, Qing Cao, Fatima Akhundova, Jinzhao Li, Karunanantharajah Prashanthan, Fengjiu Yang, Patryk Janasik, Augustine N. S. Appiah, Sergei Trofimov, Nikolaos Livakas, Shengnan Zuo, Luyan Wu, Luyao Wang, Yuqian Yang, Benjamin Agyei-Tuffour, Rowan W. MacQueen, Boris Naydenov, Thomas Unold, Eva Unger, Ece Aktas, Siegfried Eigler, and Antonio Abate
Journal	*Angew. Chem. Int. Ed.*, **2023**, *135(39)*, e202307395.
DOI	10.1002/anie.202307395
Links	https://doi.org/10.1002/anie.202307395
Detailed scientific contribution	The concept of this manuscript was elaborated by G. Li, Y. Hu, Prof. Dr. S. Eigler, and Prof. Dr. A. Abate Q. Cao performed some of the Raman and FTIR measurement.
Estimated own contribution	~5%

6.5 Evidence for Trans-oligoene Chains in Iodinated Graphene

Authors	Fabian Grote, Benjamin I. Weintrub, Mira Kreßler, Qing Cao, Christian E. Halbig, Patryk Kusch, Kirill I. Bolotin, and Siegfried Eigler
Journal	*Small*
DOI	10.1002/smll.202311987
Links	https://doi.org/10.1002/smll.202311987
Detailed scientific contribution	The concept of this manuscript was elaborated by F. Grote and Prof. Dr. S. Eigler. F. Grote prepared the iodinated graphene samples and measured Raman. B. I. Weintrub did the transport measurement. M. Kreßler and P. Kusch did the KPFM measurement. Q. Cao prepared some of the graphene samples. C. E. Halbig did the XPS measurement. F. Grote and Prof. Dr. S. Eigler wrote manuscript. The revision of the manuscript was assisted by all authors.
Estimated own contribution	~15%

Evidence for *Trans*-Oligoene Chain Formation in Graphene Induced by Iodine

Fabian Grote, Benjamin I. Weintrub, Mira Kreßler, Qing Cao, Christian E. Halbig, Patryk Kusch, Kirill I. Bolotin, and Siegfried Eigler

Functionalization of pristine graphene by hydrogen and fluorine is well studied, resulting in graphane and fluorographene structures. In contrast, functionalization of pristine graphene with iodine has not been reported. Here, the functionalization of graphene with iodine using photochemical activation is presented, which is thermally reversible at 400 °C. Additional dispersive dominant Raman modes that are probed by resonance Raman spectroscopy are observed. Additionally, iodinated graphene is probed by Kelvin probe force microscopy and by transport measurements showing p-doping surpassing non-covalent iodine doping by charge transfer-complex formation. The emergent Raman modes combined with strong p-doping indicate that iodine functionalization is distinct from simple iodine doping. A reaction mechanism based on these findings is proposed, identifying the large size of iodine atoms as the probable cause governing regiochemically controlled addition due to steric hinderance of reactive sites. The modification of the electronic structure is explained by the confinement of 1D *trans*-oligoene chains between sp^3-defects. These results demonstrate the uniqueness of iodine reactivity toward graphene and the modification of the electronic structure of iodinated graphene, highlighting its dependence on the spatial arrangement of substituents.

1. Introduction

Pristine graphene is highly inert and requires harsh reaction conditions to form additional out-of-plane chemical bonds for developing advanced post-functionalization strategies.[1] Efficient methods have been developed to achieve the controlled functionalization of pristine graphene,[2] such as strong n-doping by alkali metals enabling the reaction with electrophiles, for example, diazonium ions or alkylhalides.[3] Another approach relies on cycloaddition reactions, for example with azido compounds.[4] Radical addition reactions have been widely used in graphene functionalization with hydrogen, oxygen,[5] halogens, alkyl, nitrenes, and phenyl groups.[2,6] However, they often require activated graphene, for example by defects. Therefore, reduced graphene oxide is often used as a defect-activated graphene starting material. In earlier studies, we demonstrated that organic and hydroxyl radicals preferentially react close to defect sites and thus, defects guide the regiochemical addition of addends.[7] Among the functionalization reactions of pristine graphene hydrogenation and fluorination have been widely studied. The syntheses of those materials typically require either preactivation by n-doping,[8] or high temperatures and highly reactive reactants such as fluorine or xenon difluoride making reaction control challenging.[9]

In contrast to the extensive reports of halogenation reactions including chlorine and bromine,[10] there is, to the best of our knowledge, no example of iodination of high-quality graphene. Previous studies have reported the iodination of graphene but using reduced graphene oxide as starting material, where the reactivity is dominated by defects.[11] Li et al. investigated the electrochemical iodination of graphene and found no reaction of iodine radicals with graphene but reported deposition of molecular iodine instead. This was explained by the lower reactivity of iodine radicals compared to other halogen radicals.[12] In addition to the bare halogenation reaction of graphene, the substantial van der Waals radius of iodine radicals (198 pm[13]) should result in distinctive regiochemical control of addition patterns on graphene[14], besides the most stable 1,2-addition.[15] However, thus far, only a few Raman studies have hinted at the existence of such reactivity, with minor Raman bands being reported for arylated graphene[16] and a few more accounts of similar modes can be found, which were assigned to *trans*-polyacetylene chain formation.[17] Similar signals in chlorinated graphene have been assigned to doping-activated Raman modes, making the

F. Grote, Q. Cao, C. E. Halbig, S. Eigler
Institut für Chemie und Biochemie
Freie Universität Berlin
Altensteinstraße 23a, 14195 Berlin, Germany
E-mail: siegfried.eigler@fu-berlin.de
B. I. Weintrub, M. Kreßler, P. Kusch, K. I. Bolotin
Institut für Physik
Freie Universität Berlin
Arnimallee 14, 14195 Berlin, Germany

**ADVANCED
SCIENCE NEWS**

www.advancedsciencenews.com
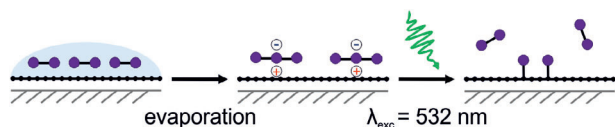
NANO · MICRO

small

www.small-journal.com

Figure 1. Schematic illustration of the iodination process. A solution of iodine in methanol is deposited on graphene supported on SiO_2/Si substrate. Upon evaporation of methanol, polyiodides I_3^- and I_5^- form by charge-transfer complex formation. Irradiation of this complex with $\lambda_{exc} = 532$ nm forms iodine radicals (Equation 1) that react with the graphene and excess iodine evaporates.

origin of these signals disputed.[18] Scanning tunneling microscopy (STM) experiments of hydrogen radicals on graphene allowed direct observation of effects of addition patterns on graphene properties.[19] Additionally, DFT calculations suggest considerable influence of the addition patterns on electronic and magnetic properties (e.g., bandgap opening).[20] To date, a lack of insight into possible reaction mechanisms prohibits the rational design of regular addition patterns on 2D materials.

Here, we present a novel approach to photochemically iodinate defect-free graphene after doping with polyiodides (**Figure 1**). We observe new dispersive Raman signals with unprecedented intensity and a strong p-doping effect measured by transport measurements, X-ray photoelectron spectroscopy (XPS), and Kelvin probe force microscopy (KPFM), that exceeds iodine doping. A reaction mechanism is proposed to explain the observed properties, in which steric hinderance of reactive sites due to the large iodine atom size forms well-defined addition patterns of *trans*-oligoene chains between sp^3-defects.

2. Results and Discussion

In this study, we used single-layer graphene obtained either by tape exfoliation or by chemical vapor deposition (CVD). With those approaches we ensure high quality of graphene to exclude dominant effects of pre-existing defects or residues from the fabrication process on the iodination reaction (Figure 1). To mitigate the influence of the substrate, we deposited monolayers of graphene on SiO_2, Au, and h-BN, respectively (Figure S1, Supporting Information). The graphene structures were thermally annealed ($T = 200$ °C, $p = 1 \times 10^{-3}$ mbar, 2 h) to ensure stable adhesion of graphene to the substrate and to remove volatile impurities. Before inducing the iodination reaction, the density of defects was quantified by Raman spectroscopy.

First, we deposited iodine onto graphene from a methanol solution (20 mM), leading to p-doping of graphene and polyiodide formation.[11a,21] After evaporation of methanol at room temperature, the doped graphene was iteratively irradiated using the laser of the Raman microscope ($\lambda_{exc} = 532$ nm, 3.03 mW, 30 accumulations). The Raman spectrum (**Figure 2**, purple spectrum) of iodinated graphene features two new dominant Raman modes at 1115 and 1498 cm^{-1}, while no new signals are observed on the substrate. This excludes reactions with the substrate or adsorbates as the cause of these signals. The observed signals were persistent after evaporation of iodine in a vacuum ($T = $ rt, $p = 1 \times 10^{-3}$ mbar, 16 h) and washing with water or alcohols that should remove any non-covalently bound iodine. To gain further

insights into the proceeding reaction, we elucidated the reaction mechanism, focusing our attention on the iodine species.

Polyiodides I_3^- and I_5^-, detected by Raman spectroscopy at 107 and 162 cm^{-1} (Figure S2, Supporting Information) are observed exclusively on graphene while no polyiodide signals are detected on the substrate. The doping effect is apparent by the shift of the G-peak by up to 15 cm^{-1} (Figure S2, Supporting Information) and partial 2D-peak suppression.[22] When iodine-doped graphene is irradiated with $\lambda_{exc} = 532$ nm, iodine radicals $I^\bullet$ and $I_2^{-\bullet}$ are generated through the photodissociation of I_3^- and I_5^- anions, as shown by Gardner et al. (Equation 1).[23]

$$I_3^- \xrightarrow{h\nu} [I_3^-]^* \rightarrow I_2^{-\bullet} + I^\bullet \tag{1}$$

The $I_2^{-\bullet}$ radical can further dissociate into an $I^\bullet$ radical and iodine anion.[13] While the photoredox chemistry of polyhalides is widely studied in metal halide complexes, examples on the photochemistry of halides at the surface of 2D materials are rare.[18a,24] The nascent radicals near the graphene surface subsequently react with sp^2-carbon atoms to form carbon-iodine bonds. Throughout this manuscript we will refer to the product of this reaction as "iodinated graphene" without distinction between tape-exfoliated and CVD graphene since we did not find a difference for the reactivity of the starting materials. Although only triiodide and pentaiodide are directly observed in the Raman spectra, higher polyiodides could form a network on the graphene surface.[25] To the best of our knowledge this is the first time that a photochemical reaction of a polyhalide and graphene is described. In contrast to the common evolution of Raman spectra of functionalized graphene,[26] the G/2D-ratio increases from 0.52 to 0.92 indicating increased disorder in the graphene lattice (Figure 2), however, no D-peak at ≈ 1340 cm^{-1} is observed.

Signals with smaller intensity evolve (v_2, $2v_1$, and v_1+v_3, Figure 2), of which a detailed description can be found in the SI (Figure S3A, Supporting Information). The lack of a D-peak

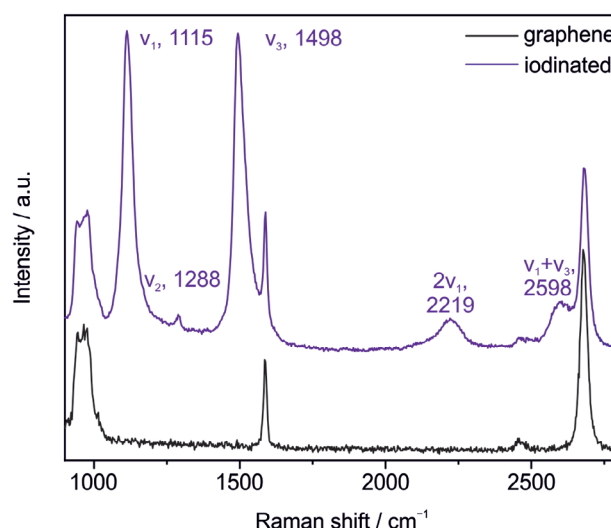**Figure 2.** Raman spectrum ($\lambda_{exc} = 532$ nm) of tape-exfoliated graphene on SiO_2/Si before (black) and after iodination (purple). Two strong new modes (v_1, v_3) and three smaller modes (v_2, $2v_1$, and v_1+v_3) are observed in the same range.

ADVANCED
SCIENCE NEWS
www.advancedsciencenews.com

NANO · MICRO
small
www.small-journal.com

either indicates absence of functionalization or formation of Raman silent defects, as reported, for example, for zigzag edges, charged impurities, and intercalants.[27]. Raman probing iodinated samples with λ_{exc} = 638 nm (1.94 eV) shows dispersion of the new Raman modes and a strong change in the intensity relative to the graphene signals (**Figure** 3A). At higher excitation energies (λ_{exc} = 405 nm, 3.06 eV) no Raman modes were observed, while the signal intensities measured at longer wavelengths were shifted after irradiation due to defunctionalization (Figure S5A, Supporting Information). Surprisingly, in some areas of the sample, using the same reaction conditions, the G- and 2D-peaks typical for graphene completely vanish, indicating the formation of a new material (Figure 3B). A strong increase of the photoluminescence background is observed and formation of two strong new signals at 1121 and 1504 cm^{-1} that show a striking similarity to *trans*-polyacetylene (Table S1, Supporting Information). *Trans*-polyacetylene has two strong modes at 1125 and 1512 cm^{-1} (upon irradiation with λ_{exc} = 532 nm[28]) and a similar pattern of signals and overtones.[29] It also shows resonance Raman effects due to the chainlength-dependent bandgap and a large Raman cross section leads to high intensities of the Raman modes (Figure S4A, Supporting Information).[30] The Raman results therefore suggest a structure like *trans*-polyacetylene polymer (Figure S3B, Supporting Information). Those localized conjugated double bonds may result from a regioselective addition reaction of large and sterically demanding iodine atoms to graphene. To distinguish the structures in iodinated graphene from *trans*-polyacetylene, where each carbon atom is bonded to a hydrogen atom, we refer to the chains we propose in iodinated graphene as *trans*-oligoene chains. These 1D carbon chains are bonded to carbon atoms within the graphene structure, have varying finite lengths and are spread randomly across the iodinated graphene area with an unknown distribution. While we expect different Raman signal positions between *trans*-polyacetylene and graphene-embedded *trans*-oligoenes, we expect to observe similar trends depending on the chain length due to bandgap opening.[31]

The reversibility of iodination reactions is of special interest for patterning applications, for example, for writing, reading, and erasing information.[18b] Thus, we investigated the thermal defunctionalization of iodinated graphene, which we find to occur between 150 and 400 °C. Interestingly, a thermal iodination of graphene occurs without irradiation, as identified by the appearance of similar but less intense Raman modes at 150 °C under ambient conditions (Figure S6, Supporting Information). After extended times of vacuum annealing at 200 °C, an increase of the new modes is observed that remain stable up to 300 °C. This may be due to iodine intercalated between graphene and the SiO$_2$ substrate that is unable to evaporate, and thus, the iodine can react with graphene.[21b] Heating of iodinated graphene to 400 °C removes the new modes and a broad D-peak at 1349 cm^{-1} (FWHM = 171 cm^{-1}) forms. Additionally, the base of the G-peak broadens, while the top remains sharp (Figure 3C). The broad D-peak is reminiscent of disordered carbon[32] and may originate from amorphous carbon on the graphene surface formed by graphitization of organic adsorbates from the environment.[33] Defunctionalization was also observed when high laser intensities were used, probably due to local heating or assisted photochemical bond dissociation, shifting the distribution of *trans*-
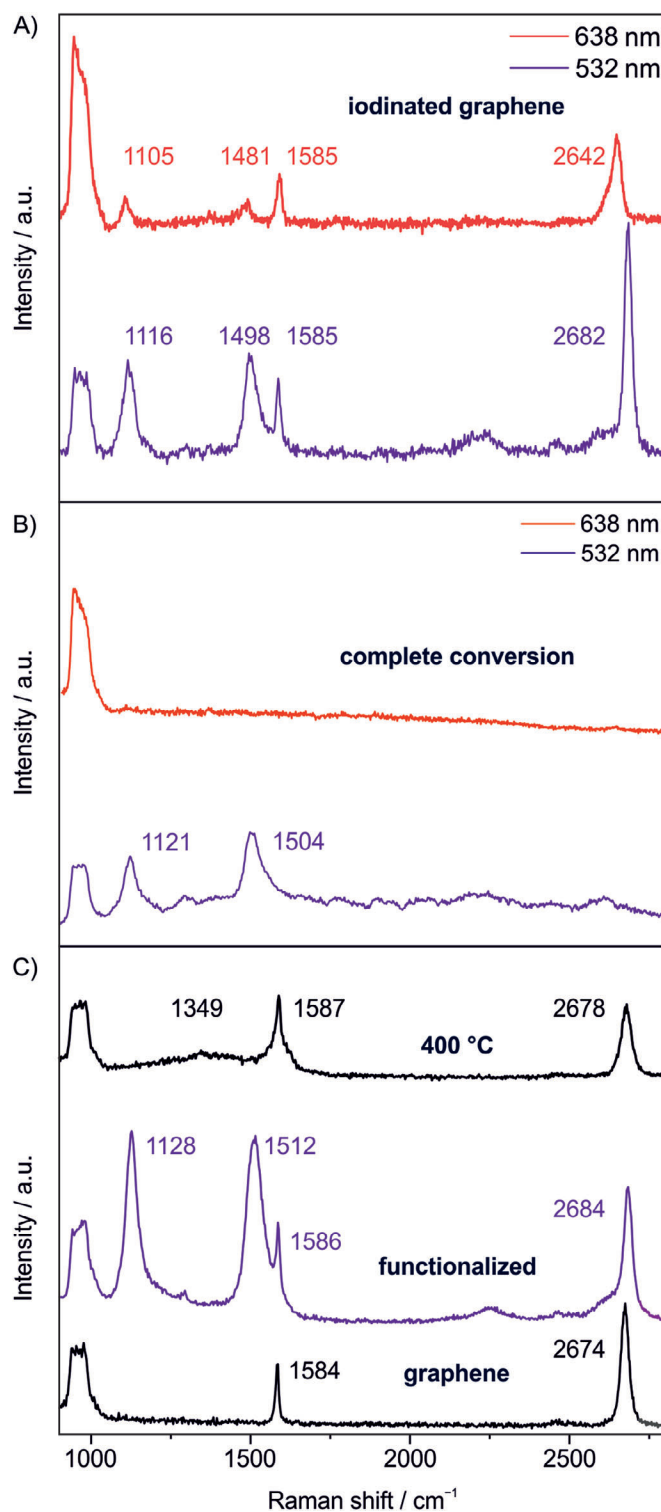
Figure 3. A) Raman spectra of tape-exfoliated graphene on hBN/SiO$_2$/Si after iodination measured at 532 nm (purple) and 638 nm (red), showing signal dispersion and a strong decrease of intensity relative to the graphene signals. B) Example spectra of vanished graphene Raman modes. No Raman signals are observed at 638 nm indicating the complete conversion of graphene. C) Raman spectra of pristine tape-exfoliated graphene, iodinated graphene, and graphene annealed at 400 °C. The graphene rests on a SiO$_2$/Si substrate.

ADVANCED
SCIENCE NEWS
www.advancedsciencenews.com

NANO · MICRO
small
www.small-journal.com

oligoene chains (Figure S5B, Supporting Information). The high thermal stability indicates a thermodynamically stable structure.

With XPS the halogen content was determined and covalent bond formation of halogens to graphene was confirmed.[34] We functionalized CVD graphene on a large area (Figure S7A, Supporting Information) and thoroughly washed it (water, isopropanol, acetone) to remove all residues on the material before measurements. The survey spectrum (Figure S7B, Supporting Information) shows the characteristic I $3d_{5/2}$ and I $3d_{3/2}$ peaks at 619.5 and 630.5 eV respectively, but with very low signal intensities (Figure S7C, Supporting Information). The deconvolution of the C 1s signal shows no significant change of the carbon composition (Figure S7D, Supporting Information), as expected due to the small amount of iodine present. With respect to the intensity of the C 1s peak at ≈284.4 eV, we estimated the atomic ratio of iodine to carbon to be ≈1–300. Thus, deconvolution of the high-resolution C 1s and I 3d core spectra cannot provide further meaningful information due to the small signal-to-noise ratio in the present spectra. Hence C 1s core spectra of graphene before and after functionalization are practically similar (Figure S7D–F, Supporting Information).

Similar Raman signals emerge when graphene is irradiated under similar conditions with bromine instead of iodine (Figure S8D, Supporting Information). The larger difference of electronegativity between carbon and bromine should cause a stronger separation of XPS signals. We thermally brominated CVD graphene (Figure S9A, Supporting Information) to ensure homogenous functionalization across a large sample. The survey spectrum shows the characteristic Br 3d peak at 70 eV albeit with a low intensity (Figure S9B,C, Supporting Information) but the broadness of the bromine high resolution Br 3d core spectrum indicates the presence of C—Br bonds.[35] Deconvolution of the C 1s signal showed no significant change of the carbon composition, as expected from the low intensity of the bromine signals (Figure S9D, Supporting Information).

The introduction of semiconductive *trans*-oligoene chains and difference in electronegativity between carbon and iodine should cause p-doping of the iodinated graphene. To test this, we performed electrical transport measurements on graphene transistors before and after iodination. In contrast to Raman spectroscopy where we can only observe a small portion of the *trans*-oligoene chain distribution the entire system is probed in transport measurements. The carrier density of graphene for the transport measurements can be calculated using Equation 2, where n = carrier density, C = total areal capacitance, V_g = gate voltage, V_{CNP} = charge neutrality point, and e = elementary charge.

$$n = C \frac{(V_g - V_{CNP})}{e} \quad (2)$$

We find that pristine graphene has a carrier density of 0.9×10^{12} holes cm^{-2} (V_{CNP} = 11.5 V), probably due to the SiO$_2$ substrate as well as water and impurities trapped between graphene and the substrate.[36] Graphene exposed to gaseous iodine is also p-doped due to charge-transfer complex formation.[37] Measurements of iodine-doped graphene prepared by our process under ambient conditions showed decreasing doping levels during the measurement (≈30 min) due to its con-
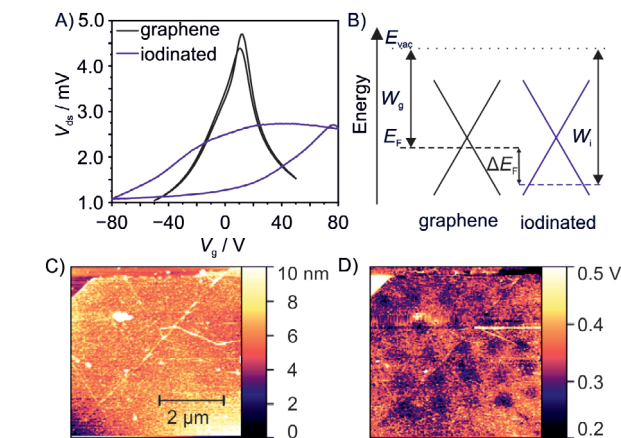

Figure 4. A) Drain-source voltage versus gate voltage of graphene field-effect transistor before (black) and after (purple) iodination. B) Energy level diagram of graphene and iodinated graphene. The Fermi energy (E$_F$) is significantly decreased upon iodination as evidenced by KPFM and transport data. C) Topography image of iodinated CVD graphene showing no signs of patterning. D) KPFM image of the same area. A 4×4 μm pattern was made by irradiation with λ_{exc} = 532 nm and 1 μm step size, visualized by black dots wihich indicate a lower work function relative to unfunctionalized areas.

siderable vapor pressure and did not exceed 3.2×10^{12} holes cm^{-2} (V_{CNP} = 43 V), consistent with literature values (Figure S10C, Supporting Information). To minimize iodine doping effects in our device, we stored the samples under high vacuum conditions (≈10^{-5} mbar) for several hours to evaporate any leftover iodine from the functionalization process. Iodination strongly increased the hole density to 5.8×10^{12} holes cm^{-2} (V_{CNP} = 77 V, **Figure 4A**), corresponding to a Fermi energy difference of ΔE_F = 173 meV, exceeding doping levels from charge-transfer into polyiodide molecules. A significant hysteresis is observed for iodinated graphene that is distinct from the pristine or iodine-doped graphene. This may be explained by capacitive charging of trap states that are formed by the *trans*-oligoene chains.[38] In contrast to iodine-doped graphene, the carrier density was stable under vacuum conditions and over several gate voltage sweeps, since the covalently attached iodine is not removed in low pressure conditions (Figure S10D, Supporting Information). It is interesting to note that iodine functionalization induces a free carrier concentration in graphene close to the limit of conventional SiO$_2$ gating. Other halogenated graphene devices showed strong p-doping as well, however in these examples no V_{CNP} of the functionalized graphene were reported, due to the limited measurement window.[24,39] Calculating carrier densities is limited, since it relies on accurately extracting V_{CNP} from the transport curves, which is in some cases beyond the range of V_g values which could be applied without destroying the sample.

Thus, we used KPFM as a complementary experimental method to measure local carrier density differences. The work function difference of pristine (W_g) and iodinated areas (W_i) directly corresponds to the difference of the Fermi level ($\Delta E_F = W_i - W_g$) of the two areas (Figure 4B). We measured KPFM on a graphene flake with both pristine and iodinated areas and compared the work functions between these areas to calculate a local work function difference. The topographic scan shows

ADVANCED
SCIENCE NEWS

www.advancedsciencenews.com

NANO · MICRO

small

www.small-journal.com

no significant variation of sample height between pristine and iodinated areas (Figure 4C), but the overall height of the monolayer reveals the presence of adsorbates despite extensive washing (water, isopropanol, acetone) and evaporation in vacuum. If the material properties would result from adsorbates on the surface of graphene, differences in the intensity of the Raman and KPFM signals must be detectable between cleaned and uncleaned domains. To investigate this we measured Raman spectra and KPFM of the CVD graphene sample before (Figure 4C,D) and after (Figure S11D,E, Supporting Information) removal of adsorbates by mechanical cleaning with an AFM tip.[40] After cleaning of the graphene surface, the v_1 and v_3 mode remain unchanged in the cleaned areas while no change of Raman signal was observed for the piled adsorbates (Figure S11B,C, Supporting Information). Also, the work function patterns remain in the KPFM image (Figure S11E–I, Supporting Information), while the contrast between functionalized and unfunctionalized areas is improved due to the removal of adsorbates with a higher work function (Figure S11G,I, Supporting Information). No change of the Raman signals of brominated graphene (Figure S8C,D, Supporting Information) was observed after mechanical cleaning. The adsorbates therefore have no significant influence on the material properties and consequently, the new Raman modes must stem from the carbon lattice.

To extract a reliable work function difference, we prepared a tape-exfoliated graphene sample contacted with a gold electrode to ensure proper grounding (Figure S12A, Supporting Information). The sample was patterned, and the functionalization was followed by Raman spectroscopy (Figure S12B, Supporting Information). The average difference of the work function between pristine and iodinated areas measured by KPFM was 141.5 meV (Figure S12C–E and Table S2, Supporting Information). This is in good agreement with ΔE_F extracted from transport measurements (173 meV) considering that these two values are measured on different samples and by different techniques. The observed shift of E_F suggests that the carrier density changes by iodination exceed iodine doping and are stable against decay by iodine evaporation.

In an earlier report by Englert et al. small Raman modes at 1139 and 1512 cm^{-1} (λ_{exc} = 532 nm) were observed in the covalent functionalization of graphene with aryl radicals, similar to the v_1 and v_3 modes of iodinated graphene.[16] They assigned the modes to *trans*-oligoene chains formed within areas defined by sp^3-defects based on their similarity to Raman modes observed in nano-crystalline diamond samples.[30] Similar modes were observed upon photochlorination of graphene with chlorine gas; again with relatively low intensities.[18] They assigned the signals to effects of strong doping by chlorine addition leading to symmetry lowering and zone folding that activate new Raman modes by comparison to potassium-doped graphene (n-doped).[41] The modes observed in that system however are observed at 1134 and 1267 cm^{-1} while no signal ≈1500 cm^{-1} was observed that would account for the v_3-modes. Instead, a Fano-shaped G-peak is observed and such a mode is also not predicted by calculations of the Raman modes of KC$_8$.[42] If the observed Raman modes would arise from a doping effect, then they should evolve without irradiation of the sample and should be sensitive toward removal of the dopant by washing or evaporation. Interestingly, in other reports of chlorination of graphene,

these spectral features were not reported.[12,24,43] We find that the spectral modes of the polyiodides vanish, while two strong new modes appear (Figure 2), which we would not expect for a non-covalent polyiodide network. The Raman modes of iodinated graphene are also persistent under ambient and high vacuum conditions or washing with water and organic solvents in contrast to the polyiodide signals. The complete disappearance of graphene Raman signals in some areas and the dispersive nature of the Raman modes indicate the direct interaction with the carbon lattice. Their unprecedented intensity allowed us to observe the v_2 mode and additional overtone modes that have not been reported for any functionalized graphene before and further indicate an origin from a *trans*-polyacetylene like structure. Their strong p-doping effect exceeds doping by non-covalently adsorbed polyiodides as shown by transport and KPFM measurements, and the weak doping effect of iodine makes doping-activated Raman modes appear unlikely.

We explain these experimental results by the formation of *trans*-oligoene chains formed with regiochemical control due to the large iodine size. Their formation depends on the reactivity of the iodine radical on the graphene sheet,[44] since the reaction of an iodine radical with graphene forms a π-radical that initially resides in a non-bonding orbital adjacent to the iodine addition site (**Figure 5A**). The delocalization of the π-radical was directly observed for hydrogenated graphene by STM causing a long-range modification of the local spin density of states and showing a threefold symmetry,[45] reaching as far as 6 nm or 20–25 lattice constants.[45] It corresponds to the delocalization of the π-radical on the B sublattice and can be interpreted as delocalization along the *trans*-oligoene paths shown in red in Figure 5B. The highest spin density, and therefore highest reactivity, is located on the three carbon atoms in 1,2-position adjacent to the addition site and at the 3 *cis*-1,4-positions (grey, Figure 5B) across six-membered rings[46] and the second hydrogen radical addition thus occurs at these positions, as observed experimentally.[15] The high reactivity of radicals may enable other addition patterns to form under kinetic control,[14] but here the low reactivity of iodine radicals is expected to lead to thermodynamic rather than kinetic reactivity. Equally important, addition in the 1,2-position is sterically blocked by iodine due to the large van der Waals radii of the iodine atoms (198 pm) and the resulting electrostatic repulsion.[13] The *cis*-1,4-addition motif (A, Figure 5C) leads to a separation of the iodine pair of 284 pm (assuming C—C bond distance of 142 pm), which is only slightly longer than the covalent bond length of diiodine (267 pm), making it also unlikely. By addition in the *trans*-1,4-position (B, Figure 5C) the defect distance is 376 pm, making a stable addition possible, explaining the observed regioselectivity. Since in our experiment the whole surface is covered with iodine, the second reaction step may be very fast and could potentially even extend beyond the irradiated area due to the delocalization of the π-radical on the graphene sheet. The confinement of localized double bonds between sp^3-defects induces bond length alternation through Peierls distortion, causing chain-length dependent local bandgap opening and hence resonance Raman effect.[47] A distribution of various chain lengths is formed that explains the varying intensities and dispersion of the Raman modes (Figures S4B and S5B, Supporting Information).

Up to three *trans*-oligoene chains may form from a single sp^3-defect, following the symmetry observed for the spin
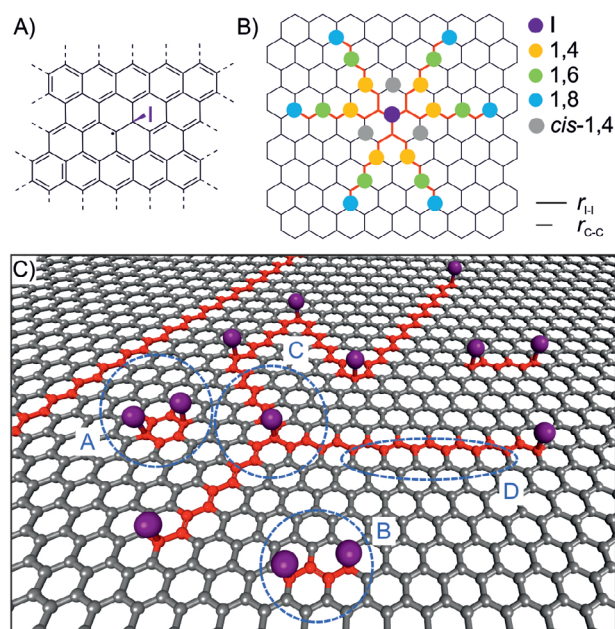
Figure 5. A) Addition of an iodine radical to graphene. The π-radical is located adjacent to the sp^3-defect and can be delocalized on the sublattice. B) Scheme showing potential sites for secondary iodine addition on graphene forming all-*trans*-oligoene chains. The 1,2-, and *cis*-1,4 positions are precluded due to iodine atom size and I-I bond length (bottom right). C) Schematic illustration of the proposed iodinated graphene structure, explaining the observed Raman signals and doping properties. *Trans*-oligoene chains (red) with varying lengths and localized double bonds are embedded in graphene domains (grey) with a delocalized π-system. A The *cis*-1,4-addition is unlikely given the small I-I distance, despite the high spin density in this position. B Addition along a *trans*-1,4-oligoene chain ensures sufficient distance between iodine atoms. C Up to three *trans*-oligoene chains can extend from a single sp^3-defect, connecting to adjacent sp^3-defects across the graphene sheet. D Perfect zigzag edges separate the chains from graphene domains along the length of the chains. The delocalized double bonds have been omitted for clarity.

density (C, Figure 5C). The absence of a D-peak in the Raman spectra can be attributed to the perfect zigzag edges to the neighboring graphene domains (D, Figure 5C), rendering them Raman silent.[27,48] The polydisperse nature of iodinated graphene makes it impossible to give a definite structure since the patterns formed will be randomly distributed across the illuminated area and only a small part of the distribution is probed at a given laser wavelength matching the bandgap of the chains. As more and more radicals are added to the graphene sheet more conjugated double bonds become confined between defects and the uninterrupted graphene domains become smaller. The distribution of *trans*-oligoene chains will shift due to the decreasing defect distance, making long chains less likely.

3. Conclusion

In summary, defect-free graphene was functionalized by a photochemical iodination reaction for the first time and strong new Raman modes were observed. Thermal reversibility of the reaction, dispersion of Raman modes and complete disappearance of graphene Raman modes in some areas indicate the interaction of iodine with the graphene lattice carbon atoms. KPFM and transport measurements demonstrate the strong p-doping effect of iodinated graphene, exceeding non-covalent iodine doping. Due to the size of iodine atoms the usually observed 1,2- and *cis*-1,4-position addition patterns are sterically hindered, leading to regioselective functionalization of graphene, and generating *trans*-oligoene substructures. Those *trans*-oligoene structures generate new Raman modes by the isolation of conjugated double bonds between sp^3-defects. The proposed structure and reaction mechanism will serve as a starting point for further experimental and theoretical inquiries toward the rational design of regioselective patterning of graphene. The iodination-based functionalization approach paths a way to patterning applications accompanied with a strong p-doping effect and the ability of readout due to the strong Raman modes.

Supporting Information

Supporting Information is available from the Wiley Online Library or from the author.

Conflict of Interest

The authors declare no conflict of interest.

Data Availability Statement

The data that support the findings of this study are available in the supplementary material of this article.

[1] a) T. Wei, X. Liu, M. Kohring, S. Al-Fogra, M. Moritz, D. Hemmeter, U. Paap, C. Papp, H. P. Steinrück, J. Bachmann, H. B. Weber, F. Hauke, A. Hirsch, *Angew. Chem., Int. Ed.* **2022**, *61*, e202201169; b) M. Z. Hossain, M. B. A. Razak, H. Noritake, Y. Shiozawa, S. Yoshimoto, K. Mukai, T. Koitaya, J. Yoshinobu, S. Hosaka, *J. Phys. Chem. C* **2014**, *118*, 22096.

[2] C. Wetzl, A. Silvestri, M. Garrido, H. L. Hou, A. Criado, M. Prato, *Angew. Chem., Int. Ed.* **2023**, *62*, e202212857.

[3] G. Abellan, M. Schirowski, K. F. Edelthalhammer, M. Fickert, K. Werbach, H. Peterlik, F. Hauke, A. Hirsch, *J. Am. Chem. Soc.* **2017**, *139*, 5175.

[4] H. Qin, T. Hwang, C. Ahn, J. A. Kim, Y. Jin, Y. Cho, C. Shin, T. Kim, *J. Nanosci. Nanotechnol.* **2016**, *16*, 5034.

[5] M. Z. Hossain, J. E. Johns, K. H. Bevan, H. J. Karmel, Y. T. Liang, S. Yoshimoto, K. Mukai, T. Koitaya, J. Yoshinobu, M. Kawai, A. M. Lear, L. L. Kesmodel, S. L. Tait, M. C. Hersam, *Nat. Chem.* **2012**, *4*, 305.

[6] A. Criado, M. Melchionna, S. Marchesan, M. Prato, *Angew. Chem., Int. Ed.* **2015**, *54*, 10734.

[7] a) C. E. Halbig, R. Lasch, J. Krüll, A. S. Pirzer, Z. Wang, J. N. Kirchhof, K. I. Bolotin, M. R. Heinrich, S. Eigler, *Angew. Chem., Int. Ed.* **2019**, *58*, 3599; b) Y. Wang, F. Grote, Q. Cao, S. Eigler, *J. Phys. Chem. Lett.* **2021**, *12*, 10009.

[8] R. A. Schäfer, D. Dasler, U. Mundloch, F. Hauke, A. Hirsch, *J. Am. Chem. Soc.* **2016**, *138*, 1647.

[9] R. A. Borse, M. B. Kale, S. H. Sonawane, Y. Wang, *Adv. Funct. Mater.* **2022**, *32*, 2202570.

[10] F. Karlicky, K. Kumara Ramanatha Datta, M. Otyepka, R. Zboril, *ACS Nano* **2013**, *7*, 6434.

[11] a) P. Šimek, K. Klímová, D. Sedmidubský, O. Jankovský, M. Pumera, Z. Sofer, *Nanoscale* **2015**, *7*, 261; b) M. S. Mirshekarloo, M. C. D. Cooray, P. Jovanović, C. D. Easton, F. Wu, T. D. Gamot, M. J. Abedin, M. R. Yuce, M. Shaibani, M. Majumder, *Batter. Supercaps* **2021**, *4*, 1175; c) A. Wang, S. Bok, C. J. Mathai, K. Gangopadhyay, J. McFarland, M. R. Maschmann, S. Gangopadhyay, *Nano Futures* **2020**, *4*, 045002; d) X. Zhang, G. Lu, *Carbon* **2016**, *108*, 215.

[12] W. Li, Y. Li, K. Xu, *Nano Lett.* **2021**, *21*, 1150.

[13] L. Troian-Gautier, M. D. Turlington, S. A. M. Wehlin, A. B. Maurer, M. D. Brady, W. B. Swords, G. J. Meyer, *Chem. Rev.* **2019**, *119*, 4628.

[14] S. Niyogi, E. Bekyarova, J. Hong, S. Khizroev, C. Berger, W. de Heer, R. C. Haddon, *J. Phys. Chem. Lett.* **2011**, *2*, 2487.

[15] R. Balog, B. Jorgensen, J. Wells, E. Laegsgaard, P. Hofmann, F. Besenbacher, L. Hornekaer, *J. Am. Chem. Soc.* **2009**, *131*, 8744.

[16] J. M. Englert, C. Dotzer, G. Yang, M. Schmid, C. Papp, J. M. Gottfried, H. P. Steinrück, E. Spiecker, F. Hauke, A. Hirsch, *Nat. Chem.* **2011**, *3*, 279.

[17] a) V. Nagyte, D. J. Kelly, A. Felten, G. Picardi, Y. Shin, A. Alieva, R. E. Worsley, K. Parvez, S. Dehm, R. Krupke, S. J. Haigh, A. Oikonomou, A. J. Pollard, C. Casiraghi, *Nano Lett.* **2020**, *20*, 3411; b) Z. Wang, Q. Yao, C. Neumann, F. Börrnert, J. Renner, U. Kaiser, A. Turchanin, H. J. W. Zandvliet, S. Eigler, *Angew. Chem., Int. Ed.* **2020**, *59*, 13657.

[18] a) G. Copetti, E. H. Nunes, G. K. Rolim, G. V. Soares, S. A. Correa, D. E. Weibel, C. Radtke, *J. Phys. Chem. C* **2018**, *122*, 16333; b) Y. Rho, K. Lee, L. Wang, C. Ko, Y. Chen, P. Ci, J. Pei, A. Zettl, J. Wu, C. P. Grigoropoulos, *Nat. Electron.* **2022**, *5*, 505.

[19] H. González-Herrero, J. M. Gómez-Rodríguez, P. Mallet, M. Moaied, J. J. Palacios, C. Salgado, M. M. Ugeda, J. Y. Veuillen, F. Ynduráin, I. Brihuega, *Science* **2016**, *352*, 437.

[20] a) I. A. Popov, Y. Li, Z. Chen, A. I. Boldyrev, *Phys. Chem. Chem. Phys.* **2013**, *15*, 6842; b) F. Marsusi, N. D. Drummond, M. J. Verstraete, *Carbon* **2019**, *144*, 615; c) P. A. Denis, *ChemPhysChem* **2013**, *14*, 3271.

[21] a) Z. Yao, H. Nie, Z. Yang, X. Zhou, Z. Liu, S. Huang, *Chem. Commun.* **2012**, *48*, 1027; b) N. Jung, A. C. Crowther, N. Kim, P. Kim, L. Brus, *ACS Nano* **2010**, *4*, 7005.

[22] N. Jung, N. Kim, S. Jockusch, N. J. Turro, P. Kim, L. Brus, *Nano Lett.* **2009**, *9*, 4133.

[23] J. M. Gardner, M. Abrahamsson, B. H. Farnum, G. J. Meyer, *J. Am. Chem. Soc.* **2009**, *131*, 16206.

[24] B. Li, L. Zhou, D. Wu, H. Peng, K. Yan, Y. Zhou, Z. Liu, *ACS Nano* **2011**, *5*, 5957.

[25] P. H. Svensson, L. Kloo, *Chem. Rev.* **2003**, *103*, 1649.

[26] J. M. Englert, P. Vecera, K. C. Knirsch, R. A. Schäfer, F. Hauke, A. Hirsch, *ACS Nano* **2013**, *7*, 5472.

[27] A. C. Ferrari, D. M. Basko, *Nat. Nanotechnol.* **2013**, *8*, 235.

[28] M. Tasumi, H. Yoshida, M. Fujiwara, H. Hamaguchi, H. Shirakawa, *Synth. Met.* **1987**, *17*, 319.

[29] V. Rives-Arnau, N. Sheppard, *J. Chem. Soc., Faraday Trans.* **1980**, *76*, 394.

[30] A. C. Ferrari, J. Robertson, *Phys. Rev. B* **2001**, *63*, 075414.

[31] a) H. E. Schaffer, R. R. Chance, R. J. Silbey, K. Knoll, R. R. Schrock, *J. Chem. Phys.* **1991**, *94*, 4161; b) K. Furuya, A. Sakamoto, M. Tasumi, *J. Phys. Chem. A* **2023**, *127*, 5344.

[32] A. C. Ferrari, J. Robertson, *Phys. Rev. B* **2000**, *61*, 14095.

[33] J. Hong, M. K. Park, E. J. Lee, D. Lee, D. S. Hwang, S. Ryu, *Sci. Rep.* **2013**, *3*, 2700.

[34] X. Tang, T. Fan, C. Wang, H. Zhang, *Small* **2021**, *17*, e2005640.

[35] O. Jankovsky, P. Simek, D. Klimova, D. Sedmidubsky, S. Matejkova, M. Pumera, Z. Sofer, *Nanoscale* **2014**, *6*, 6065.

[36] Z. Wang, Q. Yao, Y. Hu, C. Li, M. Hussmann, B. Weintrub, J. N. Kirchhof, K. Bolotin, T. Taniguchi, K. Watanabe, S. Eigler, *RSC Adv.* **2019**, *9*, 38011.

[37] S. W. Chu, S. J. Baek, D. C. Kim, S. Seo, J. S. Kim, Y. W. Park, *Synth. Met.* **2012**, *162*, 1689.

[38] a) H. Wang, Y. Wu, C. Cong, J. Shang, T. Yu, *ACS Nano* **2010**, *4*, 7221; b) T. S. Sreeprasad, V. Berry, *Small* **2013**, *9*, 341.

[39] a) X. Zhang, A. Hsu, H. Wang, Y. Song, J. Kong, M. S. Dresselhaus, T. Palacios, *ACS Nano* **2013**, *7*, 7262; b) L. Zhou, L. Zhou, M. Yang, D. Wu, L. Liao, K. Yan, Q. Xie, Z. Liu, H. Peng, Z. Liu, *Small* **2013**, *9*, 1388.

[40] A. M. Goossens, V. E. Calado, A. Barreiro, K. Watanabe, T. Taniguchi, L. M. K. Vandersypen, *Appl. Phys. Lett.* **2012**, *100*, 073110 .

[41] N. Jung, B. Kim, A. C. Crowther, N. Kim, C. Nuckolls, L. Brus, *ACS Nano* **2011**, *5*, 5708.

[42] C. Horie, M. Maeda, Y. Kuramoto, *Physica B+C* **1980**, *99*, 430.

[43] a) L. Bao, B. Zhao, B. Yang, M. Halik, F. Hauke, A. Hirsch, *Adv. Mater.* **2021**, *33*, 2101653; b) T. Wei, M. Kohring, H. B. Weber, F. Hauke, A. Hirsch, *Nat. Commun.* **2021**, *12*, 552; c) M. Yang, L. Zhou, J. Wang, Z. Liu, Z. Liu, *J. Phys. Chem. C* **2011**, *116*, 844.

[44] D. E. Jiang, B. G. Sumpter, S. Dai, *J. Phys. Chem. B* **2006**, *110*, 23628.

[45] P. Ruffieux, O. Groning, P. Schwaller, L. Schlapbach, P. Groning, *Phys. Rev. Lett.* **2000**, *84*, 4910.

[46] O. V. Yazyev, L. Helm, *Phys. Rev. B* **2007**, *75*, 125408.

[47] C. Castiglioni, M. Tommasini, G. Zerbi, *Philos. Trans. R. Soc. A* **2004**, *362*, 2425.

[48] C. Casiraghi, A. Hartschuh, H. Qian, S. Piscanec, C. Georgi, A. Fasoli, K. S. Novoselov, D. M. Basko, A. C. Ferrari, *Nano Lett.* **2009**, *9*, 1433.

Evidence for *Trans*-Oligoene Chain Formation in Graphene Induced by Iodine

Fabian Grote, Benjamin I. Weintrub, Mira Kreßler, Qing Cao, Christian E. Halbig, Patryk Kusch, Kirill I. Bolotin and Siegfried Eigler*

Evidence for *trans*-Oligoene Chain Formation in Graphene Induced by Iodine

Fabian Grote,[a] Benjamin I. Weintrub,[b] Mira Kreßler,[c] Qing Cao,[a] Christian E. Halbig,[a] Patryk Kusch,[c] Kirill I. Bolotin[b] and Siegfried Eigler*[a]

[a]   M.Sc. F. Grote, M.Sc. Q. Cao, Dr. C.E. Halbig, Prof. Dr. S. Eigler
        Institut für Chemie und Biochemie
        Freie Universität Berlin
        Altensteinstraße 23a, D-14195 Berlin, Germany
        E-mail: siegfried.eigler@fu-berlin.de
[b]   M.A. B.I. Weintrub, Prof. Dr. K.I. Bolotin
        Institut für Physik
        Freie Universität Berlin
        Arnimallee 14, D-14195 Berlin, Germany
[c]   B.Sc. M. Kreßler, Dr. P. Kusch
        Institut für Physik
        Freie Universität Berlin
        Arnimallee 14, D-14195 Berlin, Germany

Abstract: Functionalization of pristine graphene by hydrogen and fluorine is well studied, resulting in graphane and fluorographene structures. In contrast, functionalization of pristine graphene with iodine has not been reported. Here, the functionalization of graphene with iodine using photochemical activation is presented, which is thermally reversible at 400 °C. Additional dispersive dominant Raman modes that are probed by resonance Raman spectroscopy are observed. Additionally, iodinated graphene is probed by Kelvin probe force microscopy and by transport measurements showing p-doping surpassing non-covalent iodine doping by charge transfer-complex formation. The emergent Raman modes combined with strong p-doping indicate that iodine functionalization is distinct from simple iodine doping. A reaction mechanism based on these findings is proposed, identifying the large size of iodine atoms as the probable cause governing regiochemically controlled addition due to steric hindrance of reactive sites. The modification of the electronic structure is explained by the confinement of 1D *trans*-oligoene chains between sp^3-defects. These results demonstrate the uniqueness of iodine reactivity toward graphene and the modification of the electronic structure of iodinated graphene, highlighting its dependence on the spatial arrangement of substituents.

Experimental Procedures

Materials and chemicals: Methanol used for sample preparation was distilled in a solvent circulation apparatus to remove any impurities before use. Iodine was purchased from TCI and was used as-received. For tape-exfoliation of graphene Kish graphite (Grade 200) from Graphene Supermarket was used. Si wafers with a 300 nm thick SiO$_2$ layer were purchased from Fraunhofer Institut für Integrierte Systeme und Bauelementetechnologie IISB in Erlangen.

Raman spectroscopy: Raman spectra were measured on a Horiba Jobin Yvon XploRA™ PLUS spectrometer equipped with a confocal microscope and an automated XYZ table at 532 nm (2.33 eV) combined with a 100x objective (NA = 0.9). The Raman shift was calibrated to the Si peak before measurement. Experiments using 638 nm (1.94 eV) laser light were performed on a Horiba Jobin Yvon XploRA™ spectrometer equipped with a 532 nm and 638 nm laser source and 100x objective (NA = 0.9). Experiments using 633 nm (1.96 eV) and 405 nm (3.06 eV) laser light were performed on a Horiba Jobin Yvon LabRAM Evolution spectrometer equipped with a 405 nm, 532 nm, and 633 nm laser source and 100x objective (NA = 0.9).

SUPPORTING INFORMATION

Atomic Force Microscopy (AFM) and Kelvin Probe Force Microscopy (KPFM): KPFM experiments were conducted under ambient conditions using the neaSNOM that is a scattering type scanning near-field optical microscope with a KPFM extension (neaSPEC). We used Pt-Ir coated Si tips (ACCESS-EFM probes, AppNano, k = 2.7 N m^{-1}). The setup operates in non-contact mode. AM-KPFM was used, which is sensitive to electrostatic forces and the surface potential measured. The work function of the samples (Φ_{sample}) is defined by the following formula, $\Phi_{sample} = q\,V_{CPD} + \Phi_{tip}$, where V_{CPD} is the contact potential difference measured by the KPFM, Φ_{tip} is the work function of the tip, and q is the elementary charge. The potential profile is measured by oscillating the tip at 100 kHz and with a tapping amplitude of 30 nm while maintaining a minimum distance of 1 nm between the tip and the sample surface.

Removal of adsorbates: Removal of non-covalently bound adsorbates from the surface of functionalized graphene was achieved by mechanical cleaning using a JPK Nanowizard AFM instrument in contact mode. We used ContAl-G tips (k = 0.2 N m^{-1}) with 4 nN force as setpoint for imaging. To remove adsorbed species, the setpoint was increased up to 60 nN and the sample area was repeatedly scanned until no further change was observed. To avoid damaging graphene, the scans were carried out parallel to graphene edges.

Transport measurements: Transport measurements were performed at low pressure (~10^{-5} mbar) and room temperature inside a Lakeshore TTPX probe station. Both a gate voltage ($|V_g| \leq 80$ V) and drain-source current (I_{ds} = 1 µA) were supplied by individual Keithley 2450 source measure units. The leakage current was negligible for all measurements. The carrier density of graphene at V_g = 0 V is calculated using the gate voltage corresponding to the charge neutrality point in the transport curves. The system is modeled by considering the areal capacitance of the system: $C_{tot} = en/(V_g - V_{CNP})$, where e is the fundamental charge, n is the carrier density, V_g is the gate voltage, V_{CNP} is the charge-neutrality point voltage, and $C_{tot} = (1/C_{geo} + 1/C_{quant})^{-1}$ is the series connection of geometric and quantum areal capacitances. The geometric and quantum areal capacitances are given respectively as $C_{geo} = \varepsilon_0\varepsilon_r/d$ and $C_{quant} = (2e^2)(\hbar v_F)^{-1}(n/\pi)^{1/2}$, where ε_0 is the vacuum permittivity, ε_r = 3.9 is the dielectric constant of SiO$_2$, d = 300 nm is the thickness of the SiO$_2$, $\hbar$ is the reduced Planck's constant, and $v_F \approx 10^6$ m/s is the Fermi velocity of graphene near the K/K' point. Fermi level shifts were calculated using areal density of states of graphene using the following formula: $DoS \equiv dn/dE = 2(\hbar v_F)^{-1}(n/\pi)^{1/2}$.

Gold electrodes for transport and KPFM measurements were patterned by electron beam lithography using a Raith Pioneer II or by optical lithography using a Heidelberg Instruments µMLA for direct maskless writing. A thermal evaporator was used to evaporate 3 nm Cr and ~70 nm Au.

X-ray Photoelectron Spectroscopy (XPS): XPS spectra of graphene samples were recorded on SiO$_2$/Si substrates using a SPECS EnviroESCA (Al Kα,1486.7 eV) under high-vacuum conditions (< 5 x 10^{-5} mbar). Survey spectra (50-700 eV) were measured using an analyzer pass energy of 100 eV, while high resolution spectra (e.g. C 1s, I 3d and Br 3d) were recorded using 15 eV pass energy in a suitable binding energy range.

All XPS spectra were processed with the UNIFIT software. A Shirley background was subtracted from the high resolution spectra and pseudo-Vogt peak shape model (Gaussian:Lorentzian; 50:50) was used to fit the individual components. An asymmetric pseudo-Vogt line shape (0.14) was used to fit the sp² carbon component (C=C) in the C 1s high-resolution spectrum, according to the literature.[1] The XPS spectra were referenced to the C 1s signal at 284.4 eV.

Preparation of CVD graphene: Graphene was prepared by chemical vapor deposition on copper foil using the envelope method. After annealing of the copper envelope for 1 h (1035 °C, 10 sccm H$_2$, 5 sccm Ar) a flow of methane (5 sccm) was added to the mixture for 10 min growth time. Then, the sample was rapidly cooled down to rt. Arbitrary pieces of graphene were transferred onto substrates by a wet-transfer method.

Preparation of monolayer tape-exfoliated graphene: High quality samples of graphene were prepared by tape exfoliation using the Scotch tape method and directly transferred onto SiO$_2$/Si substrates. After transfer, the sample was mildly annealed in vacuum (T = 150 °C, p = 1 x 10^{-3} mbar, t = 2 h) to remove water and residuals stemming from the transfer process.

Preparation of h-BN/G heterostructure: Few-layer h-BN was mechanically exfoliated from bulk h-BN via PDMS and transferred onto a SiO$_2$/Si wafer. Monolayer graphene was mechanically exfoliated from HOPG via PDMS and transferred onto few-layer h-BN flake. According to the transfer method reported previously, the transfer process was carried out under a microscope equipped with a self-built transfer stage.[2] The thicknesses of the exfoliated h-BN and graphene were determined by optical contrast and Raman spectroscopy. After every transfer step, the sample was mildly annealed in vacuum (T = 150 °C, p = 1 x 10^{-3} mbar, t = 2 h) to remove water and residuals stemming from the transfer process.

Preparation of iodine-doped graphene: Graphene deposited on SiO$_2$(300 nm)/Si wafers (0.5 x 0.5 cm) was covered with 10 µL of a 20 mM solution of I$_2$ in methanol. Methanol was evaporated under ambient conditions.

Functionalization experiments: Measurements of Raman spectra and the patterning experiments were performed at 3.03 mW laser power. Initial spectra were measured with an acquisition time of 0.1 s. The light dosage was controlled by the exposure time and the number of accumulations per patterning spot. Typically, between 10 and 30 accumulations of 0.1 s exposure times were used at each spot of the patterned area. Improved results were obtained this way compared to direct exposure for similar times.

For large-area functionalization used for XPS measurements 6.7 mW laser power combined with a 10x objective (NA = 0.25) was used. The sample was scanned in SWIFT mode (0.1 s exposure time, 80 µm step size) to ensure sufficient irradiation of a large sample area.

Results and Discussion

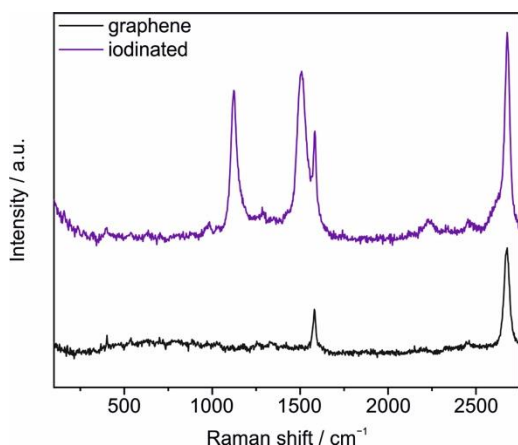**Supplementary Note 1: Functionalization on different substrates**

Figure S1. Raman spectra of graphene (black) and iodinated CVD graphene (purple) on a gold-coated (3 nm Cr/ 70 nm Au) SiO$_2$/Si substrate, demonstrating that the functionalization reaction does not depend on the substrate.

Figure S1 shows Raman spectra of CVD graphene and iodinated graphene on Au substrate with similar characteristics as on SiO$_2$/Si (e.g. **Figure 2**) and on h-BN on SiO$_2$/Si (**Figure 3**). In all cases no new signals were observed upon irradiation of the substrate excluding the possibility of iodine-substrate or iodine-adsorbate reactions as the cause of the new Raman modes. Due to the etching effect of iodine on gold small amounts of iodine solution (typically 5 µL were used), however repeated deposition of iodine solution led to the visible degradation of the gold substrate.

Supplementary Note 2: Polyiodide-doped graphene
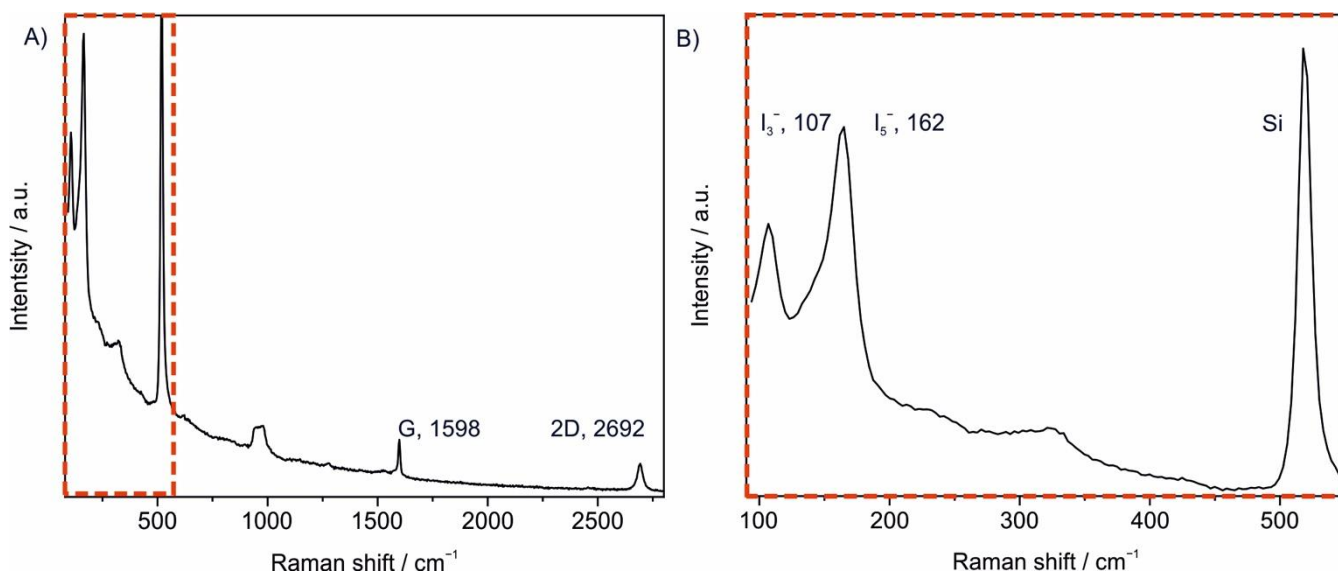
Figure S2. A) Raman spectrum of iodine-doped tape-exfoliated graphene with strong polyiodide signals. B) Zoom of the polyiodide signals. Two distinct peaks are observed corresponding to I$_3^-$ and I$_5^-$ respectively.

Figure S2A shows the spectrum of iodine-doped tape-exfoliated graphene. Polyiodide signals are observed at 107 cm^{-1} and 162 cm^{-1} (**Figure S2B**) consistent with literature values.[3] The G-peak shifts up to 1598 cm^{-1} and a decrease of the G/2D ratio becomes larger than 1 (FWHM(2D) = 27 cm^{-1}). The 2D-peak intensity is partially restored in iodinated graphene and the G-peak shifts back to lower Raman shifts (**Figure S3**). After extended irradiation the polyiodide signals disappear, indicating the evaporation of the adsorbed iodine species.

Supplementary Note 3: Discussion of Raman modes and overtones
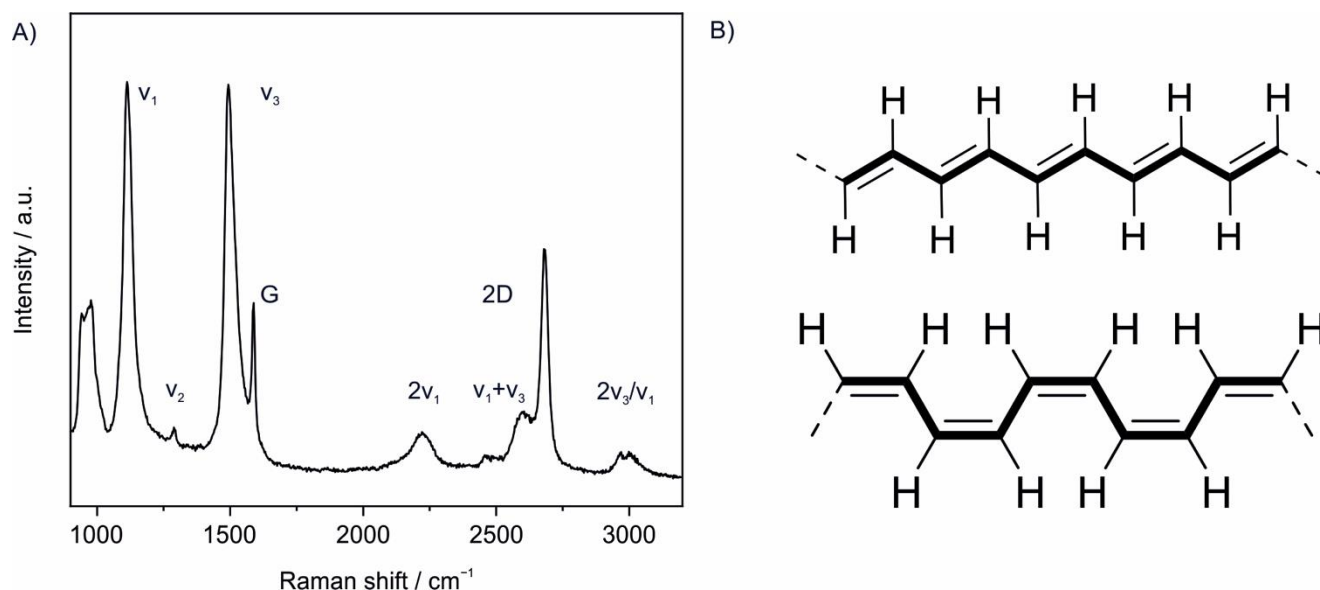
Figure S3. A) Full Raman spectrum of iodinated tape-exfoliated graphene. Three new modes (v_1- v_3) and four overtones are observed. The Raman shifts are given in **Table S1**. B) Chemical structures of thermodynamically more stable *trans*- and less stable *cis*-polyacetylene polymer.

Figure S3a shows the full Raman spectrum of iodinated tape-exfoliated graphene. Two strong new peaks evolve after irradiation at 532 nm at 1115 cm^{-1} (v_1) and 1498 cm^{-1} (v_3), that are stronger than the G- and 2D-peak. A relatively small mode is observed at 1289 cm^{-1} termed v_2. Four overtones are observed: The second harmonic $2v_1$ at 2219 cm^{-1}, the combination mode v_1+v_3 at 2598 cm^{-1} and two broad signals are observed at 2964 cm^{-1} and 3004 cm^{-1} that were assigned to a Fermi resonance between the mode $2v_3/v_1$ in *trans*-polyacetylene.[4] The small v_2 mode was described for *trans*-polyacetylene and appears in varying intensities depending on the chain length.[5] Experimental data of t-butyl group-capped *trans*-oligoenes[6] and DFT calculations[7] show trends in the peak positions of resonant Raman spectra; with increasing chain length, the v_1 and v_3 peaks shifts to smaller Raman shifts and a small v_2 signal is primarily observed at shorter chain lengths. The similarity of these signals and their positions compared to known *trans*-polyacetylene spectra give further evidence for structural similarity of the iodinated graphene (**Table S1**).

Table S1. Characteristic Raman modes of graphene, iodinated graphene and *trans*-polyacetylene (taken from ref.[4]) showing strong similarity to between the observed new modes and *trans*-polyacetylene.

Sample	v_1 / cm^{-1}	v_2 / cm^{-1}	v_3 / cm^{-1}	G / cm^{-1}	$2v_1$ / cm^{-1}	v_1+v_3 / cm^{-1}	2D / cm^{-1}	$2v_3/v_1$[b] / cm^{-1}	
Graphene	-	-	-	1587	-	-	2680	-	-
Iodinated grpahene	1115	1288	1498	1587	2219	2598	2682	2964	3004
trans-polyacetylene[a]	1108	1255	1486	-	2187	2577	-	2954	2994

[a] Measured at 520.8 nm, taken from ref.[4] [b] Fermi resonance

Figure S4A illustrates the difference between Raman and resonance Raman. While virtual states are excited in Raman scattering leading to a relatively low scattering probability (typically in the range of 10^{-6} to 10^{-8}) real states are excited in resonance Raman scattering strongly increasing scattering probability and phonon formation due to the greater perturbation efficiency (typically in the range of 10^{-4} to 10^{-2}). Since graphene has metallic character, excitation with light in a broad range resonantly excites graphene.[8] *Trans*-polyacetylene polymer in contrast is a semiconductor due to the Peierls distortion of the 1D-conjugated double bonds with a chain length-dependent bandgap, varying between 3.1 eV for a *tbu*-capped trans-polyene[6] with 6 double bonds to 1.7 eV measured in the polymer.[5] As mentioned in the main text, while exact energy values may differ in our system where the *trans*-oligoene chains are bonded to carbon atoms of the surrounding graphene instead of hydrogen atoms, similar trends can be expected.
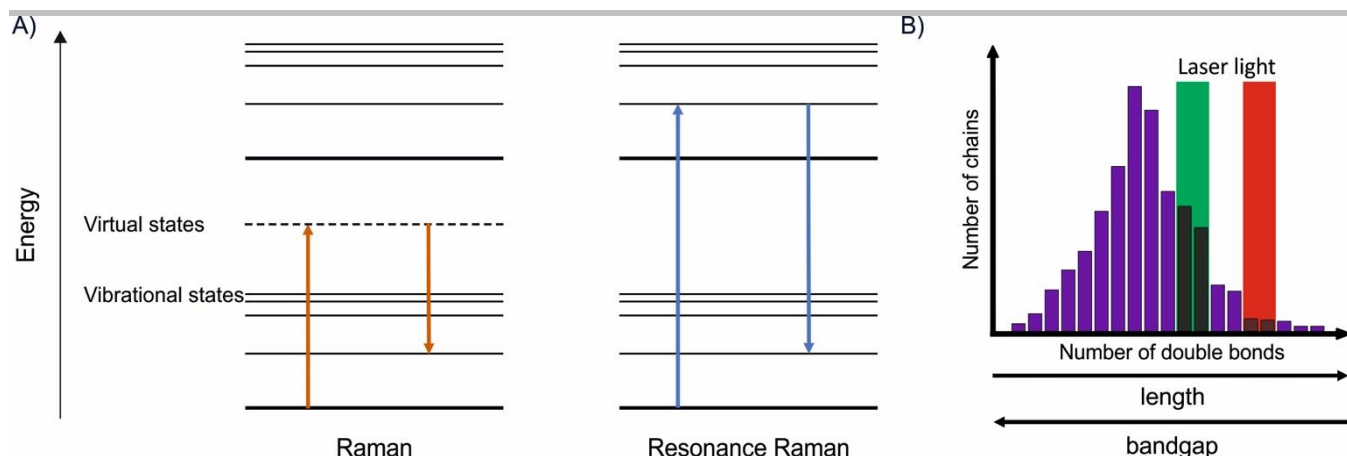
Figure S4. A) Schematic illustration of Raman and resonance Raman scattering. Electrons are excited into virtual states and loses energy to phonons emitting light with lower energy. If an electron is excited into a real excited state, the process is similar, but the signal intensity is strongly increased. B) Schematic illustration showing the influence of resonance Raman excitation on the unknown distribution of *trans*-oligoene chains of the functionalized system. Only a small portion of those exhibits a bandgap close to the probed excitation energy and is therefore probed.

The spectral modes arise from resonant Raman scattering, that is observed when the sample is excited near its electronic resonance energy, leading to a strong increase of the Raman signal. Since the *trans*-oligoene chains in iodinated graphene are of a finite length and can be categorized by their discrete length (given by the number of double bonds) we can visualize the system as an unknown distribution from which the contribution to the Raman signals will originate from *trans*-oligoene chains with a bandgap that is close to the laser energy (**Figure S4B**). By varying the excitation energy, the resonance energy and thereby the chain length that is excited, changes. By decreasing the excitation energy longer *trans*-oligoene chains are resonantly excited, but still only a portion of the complete distribution is observed.[9] Therefore, it is not possible to characterize the complete distribution by measurement at a single wavelength. The resulting Raman modes are a sum of the resonantly excited trans-oligoene chains at the given laser wavelength, explaining the varying peak intensities and positions observed for various samples and after either heat treatment or irradiation with 405 nm laser light (**Figure S5A**).

Supplementary Note 4: Defunctionalization after irradiation at 405 nm and evidence for shift of unknown *trans*-oligoene chain distribution
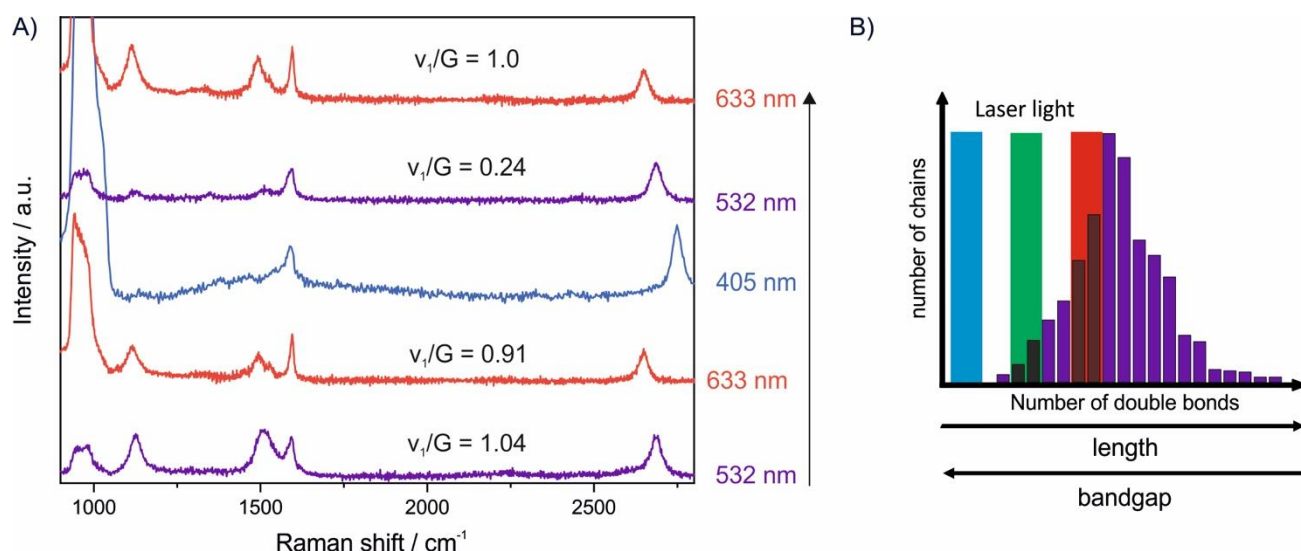
Figure S5. A) Raman spectrum of iodinated tape-exfoliated graphene (purple) and the same spot measured at 633 nm (red), before and after irradiation with 405 nm laser light (blue, 5 s irradiation time). No *trans*-oligoene signals are observed at 405 nm but the intensity of *trans*-oligoene signals at 532 nm is significantly decreased after irradiation. Signals at 633 nm increase, indicating a shift of distribution by high energy laser light. B) Schematic illustration of the shifted distribution after irradiation at 405 nm. Irradiation causes defunctionalisation shifting the distribution to longer chain lengths.

Figure S5A shows a series of Raman spectra of tape-exfoliated graphene taken before and after excitation with 405 nm (3.06 eV) laser light. Before irradiation the v_1 and v_3 modes at 532 nm (v_1/G = 1.04) are larger relative to the G-peak compared to the modes at 633 nm (v_1/G = 0.91). At 405 nm only graphene signals are observed, indicating no *trans*-oligoene chains with a matching bandgap. After irradiation with 405 nm the signal intensities at 532 nm decrease (v_1/G = 0.24) and increase at 633 nm (v_1/G = 1.0), consistent with a change of chain distribution due to partial removal of sp^3-defects leading to longer *trans*-oligoene chains with smaller bandgaps between the remaining defects, as shown schematically in **Figure S5B**. While the hypothetical chain distribution shown only shifts to longer

chain lengths in comparison to **Figure S4B**, in a real system the partial removal functionalization will also decrease the total number of chains.

Supplementary Note 5: Thermal iodination of graphene
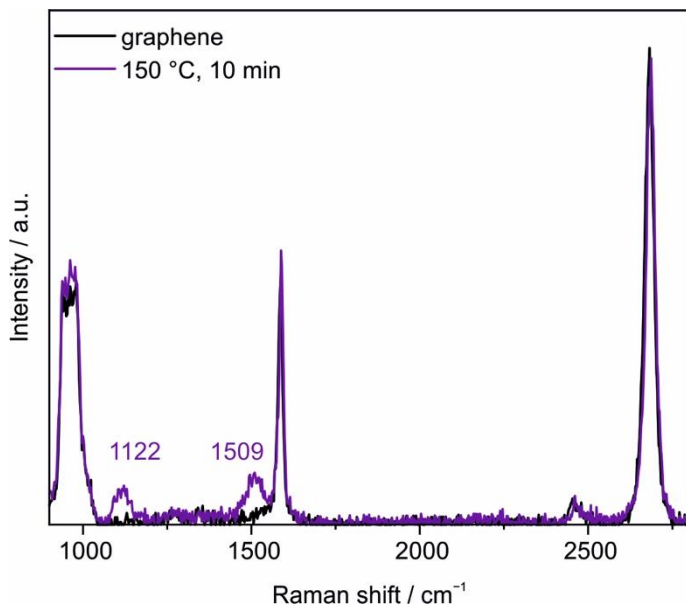
Figure S6. Raman spectra of CVD graphene before (black) and after (purple) thermal iodination in ambient conditions (150 °C, 10 min). Small v_1 and v_3 modes are observed indicating successful reaction, however at a low intensity compared to photochemical reaction.

Figure S6 shows Raman spectra of iodine-doped CVD graphene before and after thermal treatment (150 °C, 10 min). Iodine in methanol solution was deposited on graphene on SiO_2/Si wafer. After complete evaporation of the solution the sample was placed on a hot plate at ambient conditions. Despite the considerable vapor pressure of iodine new Raman signals were found while no D-peak was introduced in the process and the G- and 2D-peak remain almost unchanged. Due to the weak iodine-iodine bond homolytic dissociation can already occur at relatively low energies. While this approach only yields small *trans*-oligoene modes compared to the photochemical functionalization it may be interesting for wafer-scale functionalization of large graphene films.

Supplementary Note 6: XPS characterization of iodinated graphene

Figure S7. XPS characterization of iodinated CVD graphene on SiO$_2$/Si substrate. A) Example spectrum of iodinated CVD graphene used for XPS measurements. B) XPS survey spectrum of iodinated graphene. C) High-resolution spectrum of the I 3d signals at 619.5 eV (I 3d$_{5/2}$) and 630.5 eV (I 3d$_{3/2}$) respectively. The characteristic signals can be clearly distinguished from the noise. D) High-resolution C 1s spectrum of iodinated graphene. The inset shows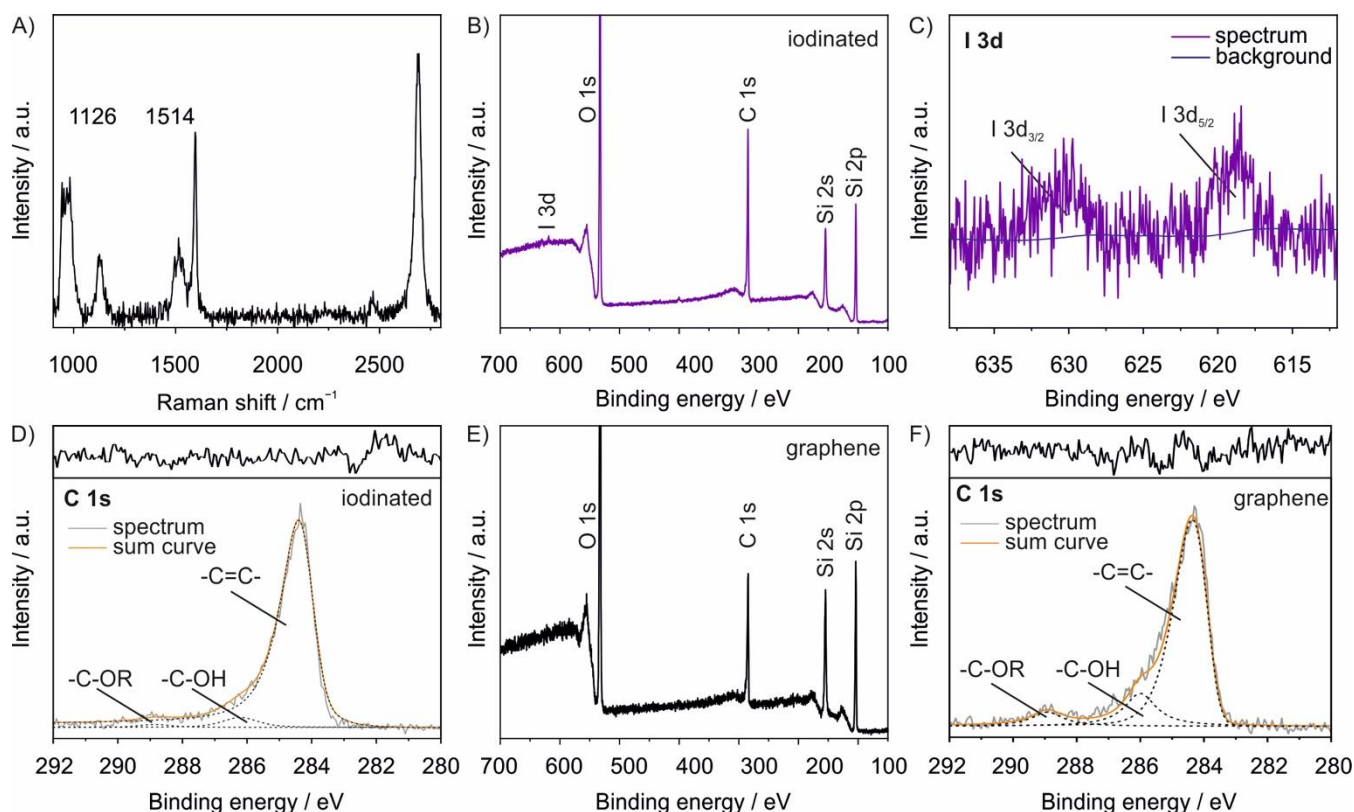 the residual of the fits. E) Survey spectrum of pristine CVD graphene. F) High-resolution C 1s spectrum of pristine CVD graphene. The inset shows the residual of the fits.

Figure S7A shows a representative Raman spectrum of CVD graphene after functionalization with iodine. Since the tape-exfoliated graphene layers are too small for XPS measurements (spot size ~300 µm), large-area CVD graphene was functionalized photochemically on a large scale using modified conditions (10x, 6.7 mW, SWIFT mode, 0.1 s, 20 µm step size). Prior to the measurements the samples were thoroughly cleaned by complete evaporation of the reaction mixture followed by washing with water, isopropanol and acetone.

The survey XPS spectrum of iodinated graphene (**Figure S7B**) shows two small signals at 619.5 eV (I 3d$_{5/2}$) and at 630.5 eV (I 3d$_{3/2}$) for iodine.[3] The intensity of these signals is at the resolution limit (**Figure S9C**) but can be clearly distinguished from the noise of the background.

The deconvolution of the C 1s peak (**Figure S9D**) does not show a new component for C-I bonds due to the low concentration if Iodine bound to the graphene and the low difference in electronegativity, responsible for a weak chemical shift. For carbon-iodine bonds a signal at 286.3 eV or less would be expected – the same position as carbon-oxygen single bonds.[3]

Supplementary Note 7: *Trans*-Oligoene chain formation induced by bromine and characterization by Raman and XPS
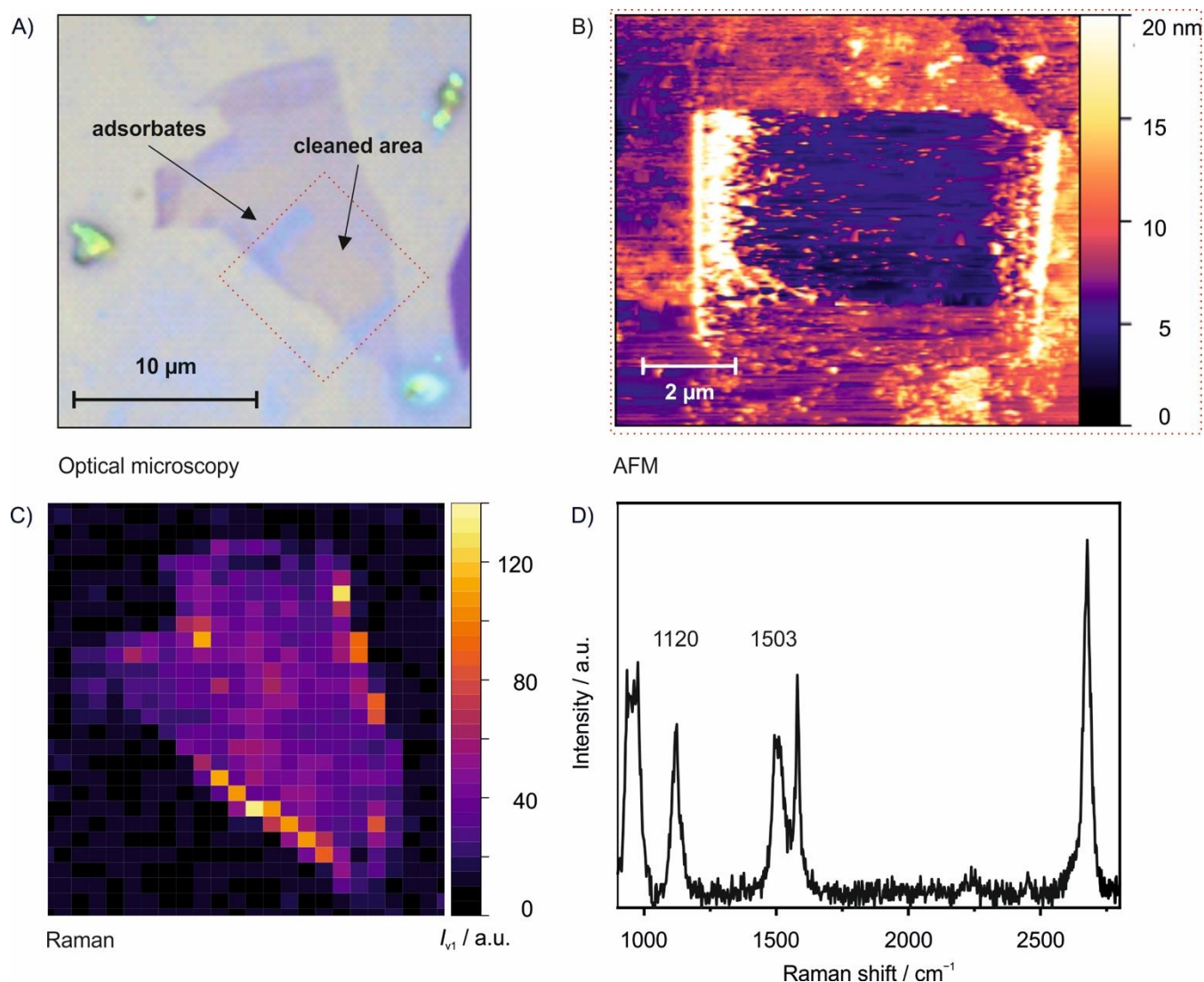
Figure S8. Photochemical bromination of tape-exfoliated graphene. A) Optical microscopy image showing graphene flake after mechanical cleaning of 7x7 µm area. The cleaned area is bordered by the piled adsorbates moved to the sides. B) AFM image of the area marked by the red square in A showing the mechanically cleaned area. C) Raman map showing the intensity of the v_1 peak. No difference is observed in the cleaned and uncleaned areas. The piled adsorbates do not give a measurable Raman signal. Each pixel has an area of 0.7x0.7 µm. A preferred reactivity of bromine at the edges of the graphene flake can be observed. D) Raman spectrum of the strongest signal observed in the cleaned area at the edge of the graphene flake.

Figure S8A shows a microscopy image of tape-exfoliated graphene after photochemical functionalization with bromine and subsequent mechanical cleaning of a 7x7 µm area with an AFM tip (**Figure S8B**). The sample was brought in contact with bromine vapor for 30 s followed by laser irradiation (3.03 mW, 0.1 s, 10 accumulations). The v_1 and v_3 mode emerge, similar to iodinated graphene (**Figure S8D)** however at lower intensities. To the best of our knowledge this is the first report of such Raman signals in brominated graphene. Notably, a strong difference between the edges and the plane is observed, as apparent from the Raman map (**Figure S8C**) that could be due to the increased reactivity of graphene at the edges.
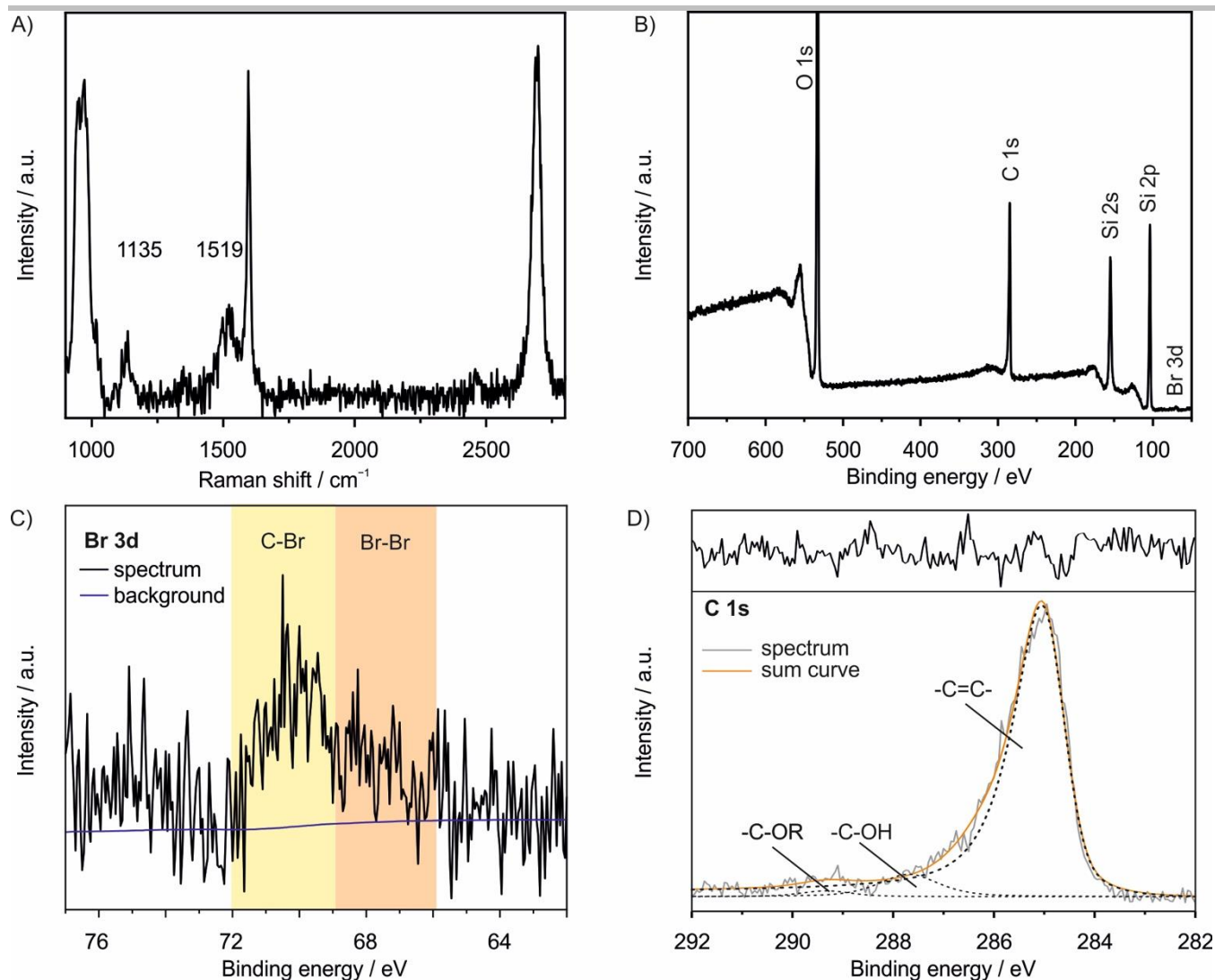
Figure S9. XPS characterization of thermally brominated CVD graphene on SiO₂/Si substrate. A) Raman spectrum of CVD graphene after thermal bromination (150 °C, 10 min). B) Survey spectrum of brominated graphene revealing a small Br 3d signal around 70 eV binding energy. C) High-resolution spectrum of the Br 3d signal showing a broad signal around 70 eV. The shaded area in brown indicates the location of adsorbed Br-Br species, while the yellow shaded area indicates the expected location of covalent C-Br signal.[10] D) High-resolution spectrum of the C 1s signal. No significant change compared to the pristine graphene (**Figure S7F**) can be observed. The inset shows the residual of the fits.

Figure S9A shows a Raman spectrum of CVD graphene after thermal functionalization with bromine (150 °C, 10 min) used for XPS measurements. The v_1 and v_3 signals indicate the successful functionalization of the sample. The XPS survey spectrum of thermally brominated graphene (**Figure S9B**) shows a small signal around 70 eV from Br 3d electrons that is persistent after thorough washing and extended times under the high-vacuum conditions inside the XPS instrument, while other characteristic bromine signals with lower relative sensitivity factors, e.g. Br 3p at ~185 eV cannot be observed.[10] The intensity of the signal is at the limit of detectability, but high-resolution measurement of the Br 3d signal reveals two distinguishable components (**Figure S9C**) that have been assigned to Br-Br adsorbed to graphene (68.5 eV) and carbon-bromine (70.2 eV).[10]

The deconvolution of the C 1s peak (**Figure S9D**) does not show a measurable alteration of the material compared to the starting material (**Figure S7F**). For carbon-bromine bonds a signal at 286.5 eV together with C-O signals would be expected.[10]

A reliable quantification of the signal areas cannot be made due to the low signal intensity, but the bromine content must be below 1 %.

Supplementary Note 8: Transport measurements of pristine and iodinated graphene
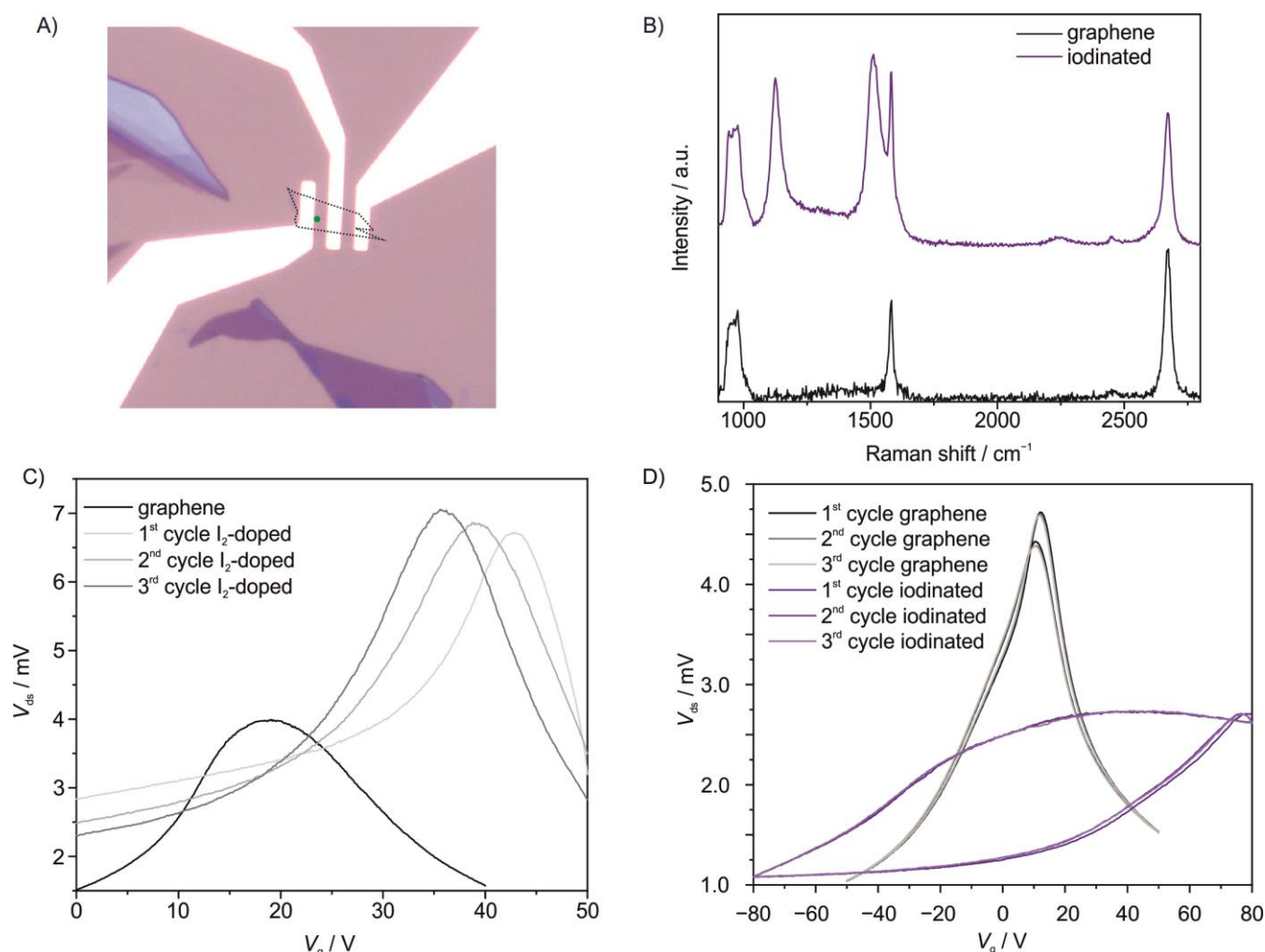
Figure S10. A) Optical image (100x) of the transistor with the tape-exfoliated flake area outlined. The green dot shows where Raman measurements were performed. B) Raman spectra from the flake before (black) and after (purple) iodination C) Drain-source voltage vs. gate voltage of pristine graphene (black) and polyiodide-doped graphene (colour gradient). Iodine causes hole doping in graphene by charge-transfer complex formation forming polyiodides. As we sweep the gate 3 times consecutively (~30 min total), the iodine evaporates over time, causing the initial doping of the graphene to tend toward its pristine value. D) Reproduction of **Figure 4A** from the main text showing all forward and backward sweeps of the data taken showing reproducibility of the data over time.

Figure S10A shows a microscopy image of the transistor device where the tape-exfoliated graphene flake area is outlined by the dotted lines. The green dot marks where the spectra in **Figure S10B** were taken before and after iodination. After fabrication and measurement of the pristine device iodine in methanol solution was deposited on the wafer (10 µL, 20 mM) and after complete evaporation of the solvent the sample was irradiated several times to ensure complete functionalization of the device area. V_{CNP} of graphene doped with iodine did not exceed 50 V and significant decrease of doping was already observed within the measurement time of around 30 min at ambient conditions (**Figure S10C**). Three cycles were measured of graphene before and after iodination to verify the reproducibility of the observed curves. **Figure S10D** shows all three cycles of the measurements shown in **Figure 4A** highlighting the reproducibility of the observed features.

Supplementary Note 9: Mechanical cleaning of patterned CVD graphene
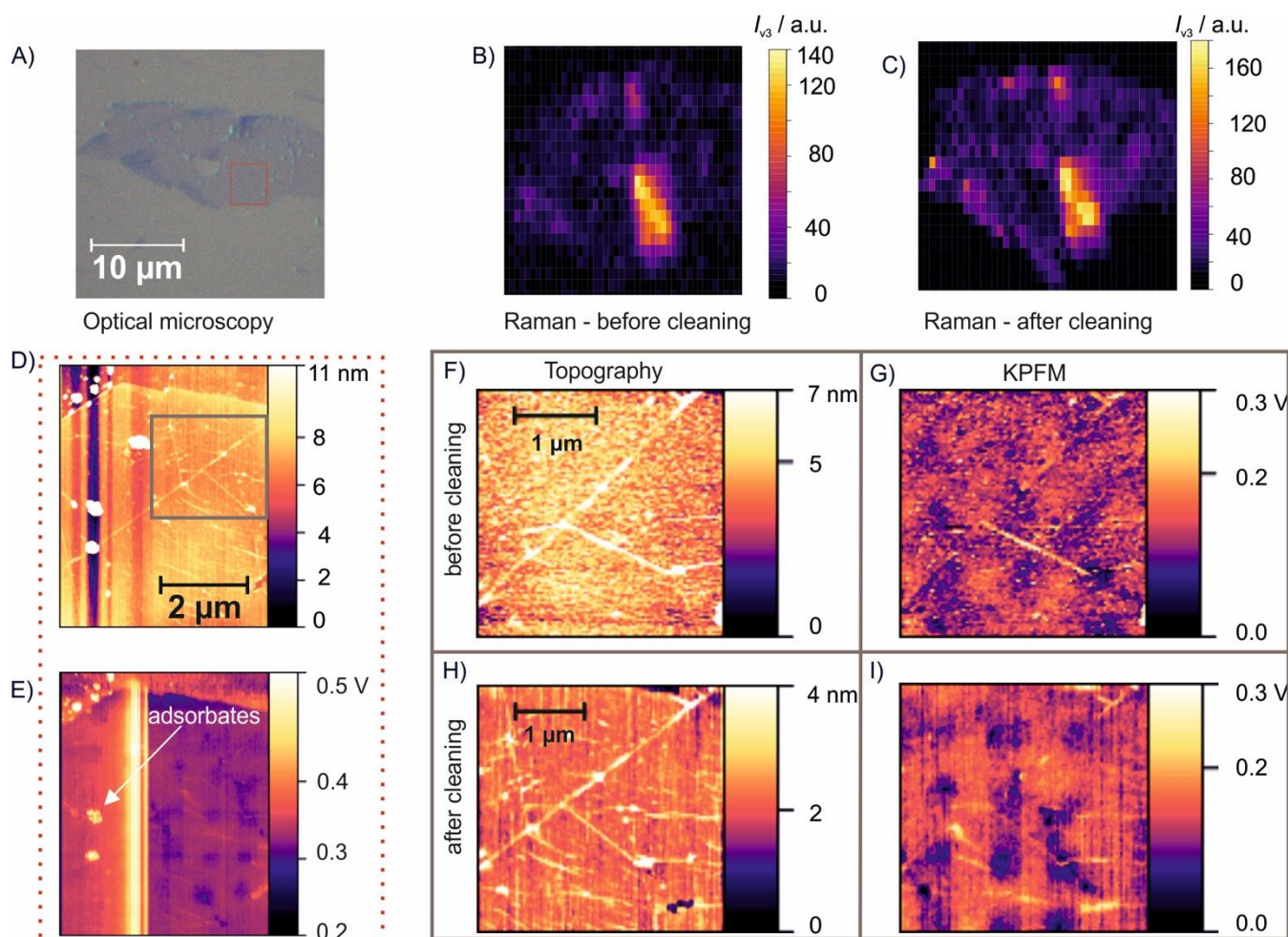
Figure S11. Mechanical cleaning of iodinated CVD graphene. A) Microscopy image showing graphene flake. The cleaned area is marked in red. B) Raman map of patterned area showing the v_3 mode before and C) after mechanical cleaning. The range was chosen so that a small portion of the G peak is included so that the outline of the graphene flake is visible and one pixel has a dimension of 0.7 x 0.7 µm. D) AFM image of mechanically cleaned area. The inset shows the area shown in F-I. E) KPFM image of the patterned area after mechanical cleaning. The highlighted adsorbates show a larger work function compared to graphene, contrary to the patterned areas. F) AFM image before mechanical cleaning. G) KPFM image before mechanical cleaning. H) AFM image after mechanical cleaning showing increased contrast due to removal of adsorbates. I) KPFM image after mechanical cleaning showing increased contrast between graphene and patterned areas due to removal

Figure S11A shows a microscopy image of the CVD graphene sample shown in **Figure 4C and D**. The Raman maps of the v_3 mode show no change of the signal intensity or location after mechanical cleaning (**Figure S11B and C**). The patterned area topography image (**Figure S11D and H**) reveals new features such as folds of the graphene sheet but no patterns that are visible in the KPFM image (**Figure S11E**). No change of the KPFM signal position can be observed in the patterned regions. The removed adsorbates show a large work function contrary to the patterns observed (**Figure S11E**). The contrast between the functionalized pattern and the surrounding graphene is increased by the removal of the adsorbates (**Figure S11G and I**).

SUPPORTING INFORMATION

Supplementary Note 10: KPFM measurements of contacted sample to ensure grounding for reliable data extraction
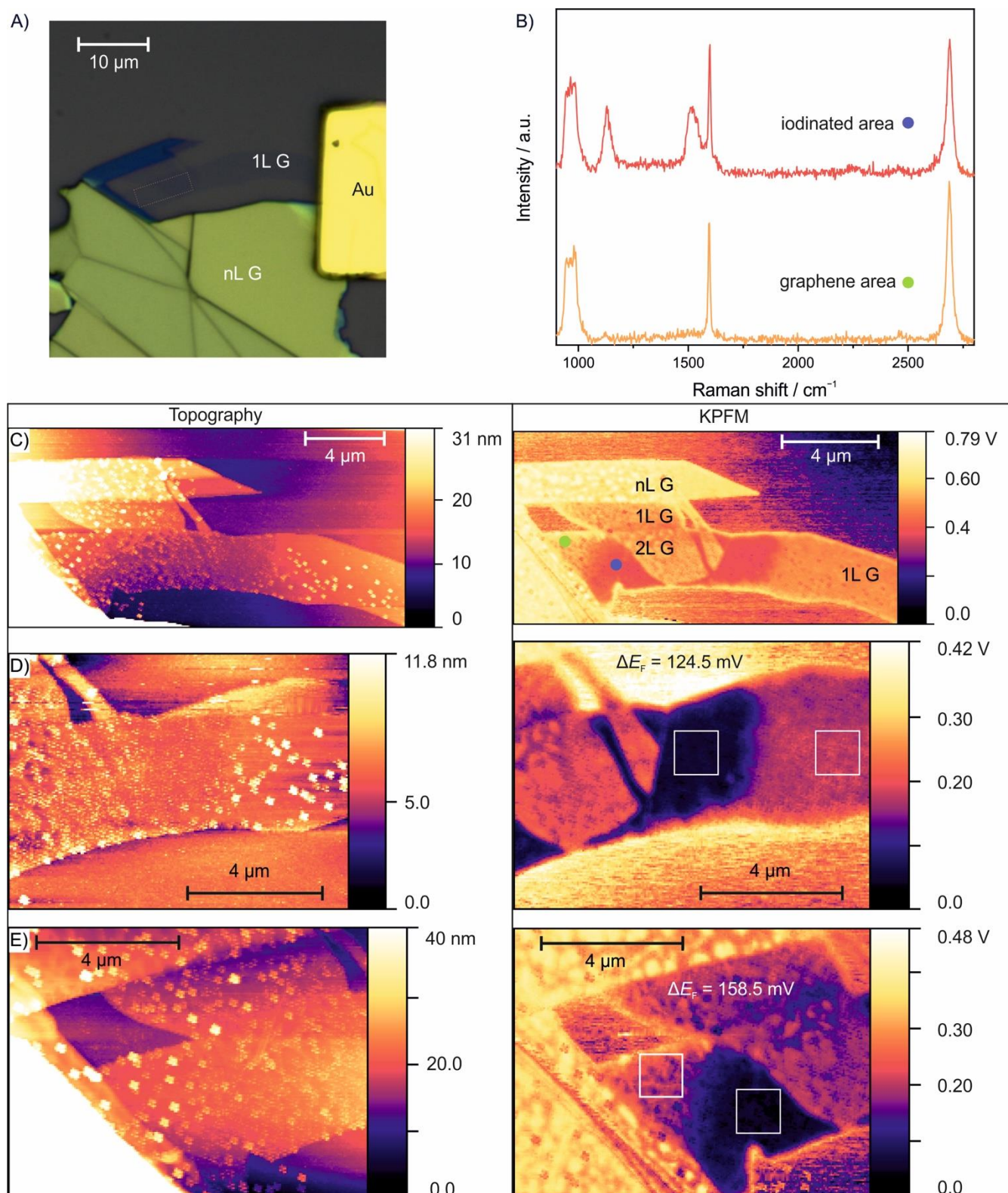
Figure S12. Experiments with a contacted tape-exfoliated graphene layer to ensure proper grounding of the sample during KPFM measurements. A) Microscopy image (100x) showing the monolayer graphene strip contacted by a gold electrode. The marked area corresponds to the irradiated area. B) Raman spectra of the areas indicated by the coloured dots (green and blue) in the KPFM image of **Figure S7C**. C) Overview image of the iodinated area. C) Overview topography (left) and KPFM (right) image of the iodinated area. D) Zoom on the iodinated area right of the bilayer. The white boxes mark areas from which ΔE_F was calculated given in black. E) Zoom on the iodinated area left of the bilayer. The white boxes mark areas from which ΔE_F was calculated given in white.

To quantify the work function measured by KPFM proper grounding of the sample must be ensured. Therefore, a tape-exfoliated graphene flake was contacted with a gold electrode to ensure electrical grounding (**Figure S12A**). An area of 8x3 µm was repeatedly

irradiated (step size = 0.5 µm, λ_{exc} = 532 nm, 0.1 s, 30 accumulations, 8 times, 3.03 mW, **Figure S12B**) and remaining iodine was evaporated (T = rt, p = 1 x 10^{-3} mbar, t = 2 h). The sample was contacted by applying conductive silver paint to the gold electrode. The measurements were performed under ambient conditions. Regular, flower-like structures can be observed on the surface of graphene that may be iodine/polyiodide crystals that have not completely evaporated. These structures show a reduction of the work function, however smaller compared to the iodinated areas, which is in line with the transport measurements showing stronger p-doping for the iodinated graphene compared to iodine-doped graphene (**Figure S2**). The height of the flake compared to the substrate is 4 nm indicating the coverage of graphene with adsorbates, e.g. remaining iodine. Less structures are observed in the iodinated areas, maybe due to the increased evaporation by laser irradiation, giving a contrast in the topography image. Nevertheless, the measured work function is lower in irradiated areas consistent with the increased doping level of iodinated graphene compared to iodine-doped graphene in transport measurements.

Table S2. Extracted contact potential difference values from contacted KPFM measurement each from a 25x25 pixel square.

Sample	iodinated / mV	pristine / mV	ΔE_F / mV
Right of bilayer (**Figure S8D**)	50.56 ±4.62	175.1 ±6.45	124.5
Left of bilayer (**Figure S8E**)	46.56 ±8.35	205.1 ±24.4	158.5
Average	48.56 ±6.48	190.1 ±15.4	141.5

To extract the work function differences an average of 25x25 pixels in the pristine areas were compared to the same number of pixels in the iodinated area (white squares, **Figure S12D** and **E**) in two different areas of the sample and averaged, giving a value of 141.5 mV (**Table S2**).

References

[1]   A. Kovtun, D. Jones, S. Dell'Elce, E. Treossi, A. Liscio, V. Palermo, *Carbon* **2019**, *143*, 268.
[2]   M. Hussmann, B. Weintrub, P. Feicht, G. Germer, J. N. Kirchhof, K. I. Bolotin, S. Eigler, *Nanoscale Adv.* **2020**, *2*, 176.
[3]   P. Šimek, K. Klímová, D. Sedmidubský, O. Jankovský, M. Pumera, Z. Sofer, *Nanoscale* **2015**, *7*, 261.
[4]   V. Rives-Arnau, N. Sheppard, *J. Chem. Soc., Faraday Trans. 1* **1980**, *76*.
[5]   E. Ehrenfreund, Z. Vardeny, O. Brafman, B. Horovitz, *Phys. Rev. B* **1987**, *36*, 1535.
[6]   H. E. Schaffer, R. R. Chance, R. J. Silbey, K. Knoll, R. R. Schrock, *J. Chem. Phys.* **1991**, *94*, 4161.
[7]   K. Furuya, A. Sakamoto, M. Tasumi, *J. Phys. Chem. A* **2023**, *127*, 5344.
[8]   P. Klar, E. Lidorikis, A. Eckmann, I. A. Verzhbitskiy, A. C. Ferrari, C. Casiraghi, *Phys. Rev. B* **2013**, *87*.
[9]   H. Kuzmany, *Macromol. Symp.* **1990**, *37*, 81.
[10]   O. Jankovsky, P. Simek, K. Klimova, D. Sedmidubsky, S. Matejkova, M. Pumera, Z. Sofer, *Nanoscale* **2014**, *6*, 6065.

Author Contributions

Fabian Grote: Conceptualization, data curation, investigation, visualization, writing – original draft. **Benjamin I. Weintrub:** Investigation, transport measurements, writing – review and editing. **Mira Kreßler:** Investigation, KPFM measurements. **Qing Cao:** Sample preparation. **Christian E. Halbig:** Investigation, XPS measurements. **Patryk Kusch:** Supervision, validation, funding acquisition. **Kiril I. Bolotin:** Supervision, validation, funding acquisition. **Siegfried Eigler:** Supervision, validation, funding acquisition, methodology, project administration, resources, writing – review and editing.

List of Abbreviations

2D	two-dimensional
AFM	atomic force microscopy
Bi_2Se_3	bismuth selenide
BP	black phosphorus
BPO	benzoyl peroxide
CH_4	methane
COFs	covalent-organic frameworks
CVD	chemical vapor deposition
DFT	density functional theory
DSM	dynamic structure model
F_4TCNQ	2,3,5,6-tetrafluoro-7,7,8,8-tetracyanoquinodimethane
FWHM	the full width at half maximum
G/MoS_2	graphene/MoS_2 heterostructures
GaS_2	gallium sulfide
GO	graphene oxides
H_2SO_4	sulfuric acid
h-BN	hexagonal boron nitride
In_2Se_3	indium(III) selenide
$KMnO_4$	potassium permanganate
KPFM	Kelvin probe force microscopy
LB	Langmuir-Blodgett
L_D	the distance between two nearest point defects
LDHs	layered double hydroxides
MOFs	metal-organic frameworks
MoS_2	molybdenum disulfide
$MoSe_2$	molybdenum diselenide

NADH	nicotinamide adenine dinucleotide
$NaNO_3$	sodium nitrate
$NbSe_2$	niobium diselenide
Ni	nickel
oxo-G	oxo-functionalized graphene
PDMS	polydimethylsiloxane
PL	photoluminescence
ReS_2	rhenium disulfide
r-oxo-G	reduced oxo-functionalized graphene
Ru	ruthenium
Si	silicon
SiO_2	silicon dioxide
SNOM	scanning near-field optical microscopy
TCNQ	7,7,8,8-tetracyanoquinodimethane
TMDCs	transition metal dichalcogenides
WF	work function
WS_2	tungsten disulfide
WSe_2	tungsten diselenide
θ	density of defects
Φ	surface potential
Γ	the center of the Brillouin zone

List of Publications

1) Z. Wang,[1] **Q. Cao**,[1] K. Sotthewes, Y. Hu, H. S. Shin, and S. Eigler
   Interlayer electron modulation in van der Waals heterostructures assembled by stacking monolayer MoS$_2$ onto monolayer graphene with different electron transfer ability
   Nanoscale **2021**, *13*, 15464-15470
   [1]These authors contribute equally to the work.

2) **Q. Cao**, F. Grote, M. Hußmann, and S. Eigler
   Emerging field of few-layered intercalated 2D materials
   Nanoscale Adv. **2021**,*3*, 963-982

3) Y. Hu, **Q. Cao**, C. Neumann, T. Lehnert, F. Börrnert, Y. Wang, U. Kaiser, A. Turchanin, and S. Eigler
   Wet-chemical synthesis of solution-processible porous graphene via defect-driven etching
   Carbon **2021**, *185*, 568-577

4) Y. Wang, F. Grote, **Q. Cao**, and S. Eigler
   Regiochemically oxo-functionalized graphene, guided by defect sites, as catalyst for oxygen reduction to hydrogen peroxide
   J. Phys. Chem. Lett. **2021**, *12,* 10009-10014

5) Y. Wang, C. Neumann, M. Hußmann, **Q. Cao**, Y. Hu, O. Garrity, P. Kusch, A. Turchanin, and S. Eigler
   Synthesis of Wet-Chemically Prepared Porous-Graphene Single Layers on Si/SiO$_2$ Substrate Increasing the Photoluminescence of MoS$_2$ in Heterostructures
   Adv. Mater. Interfaces **2021**, *8*, 2100783

6) G. Li, Dr. Y. Hu, M. Li, Y. Tang, Z. Zhang, A. Musiienko, **Q. Cao**, F. Akhundova, J. Li, K. Prashanthan, F. Yang, P. Janasik, A. N. S. Appiah, S. Trofimov, N. Livakas, S. Zuo, L. Wu, L. Wang, Y. Yang, B. Agyei-Tuffour, R. W. MacQueen, B. Naydenov, T. Unold, E. Unger, E. Aktas, S. Eigler, and A. Abate

*Managing excess lead iodide with functionalized oxo-graphene nanosheets
for stable perovskite solar cells*
Angew. Chem. Int. Ed. **2023**, *135(39)*, e202307395

7) **Q. Cao**, M. Kreßler, M. Hußmann, Y. Hu, P. Kusch, and S. Eigler
*Photoluminescence modulation of graphene/MoS$_2$ heterostructures
separated by laser-induced functionalization*
Chem. Mat. **2024**, *36*, 3267-3276. (featured as front cover)

8) F. Grote, B. I. Weintrub, M. Kreßler, **Q. Cao**, P. Kusch, C. E. Halbig, K. I. Bolotin and S. Eigler
Evidence for trans-oligoene chains in iodinated graphene
Small (DOI: 10.1002/smll.202311987)

9) **Q. Cao**, J. Dai, Z. Hao, B. Paulus, and S. Eigler
*Z-direction interface design of graphene/MoS$_2$ heterostructures: Towards
photoluminescence modulation of MoS$_2$*
To be submitted

Attended Conferences

1) 6th Erlangen Symposium on Synthetic Carbon Allotropes, Erlangen, Germany - **Poster** *(Oct. 2023)*

2) Horizons Symposium: Electronic & Energy Materials, Berlin, Germany - **Poster** *(Step. 2023)*

3) Chem2Dmat2023, Bologna, Italy - **Oral Presentation** *(May 2023)*

4) Innovation Forum 2D-Mat-Net, Jena, Germany *(Sept. 2022)*

5) 5th Erlangen Symposium on Synthetic Carbon Allotropes, Erlangen, Germany *(Sept. 2019)*

Reference

[1]   K. S. Novoselov, A. K. Geim, S. V. Morozov, D. Jiang, Y. Zhang, S. V. Dubonos, I. V. Grigorieva, A. A. Firsov, *Science* **2004**, *306*, 666-669.

[2]   a) Y. Cao, V. Fatemi, S. Fang, K. Watanabe, T. Taniguchi, E. Kaxiras, P. Jarillo-Herrero, *Nature* **2018**, *556*, 43-50; b) C. Lee, X. Wei, J. W. Kysar, J. Hone, *Science* **2008**, *321*, 385-388; c) P. Sun, K. Wang, H. Zhu, *Adv. Mater.* **2016**, *28*, 2287-2310; d) Y. Wei, R. Yang, *Natl. Sci. Rev.* **2019**, *6*, 324-348.

[3]   H. Liu, A. T. Neal, Z. Zhu, Z. Luo, X. Xu, D. Tomanek, P. D. Ye, *ACS Nano* **2014**, *8*, 4033-4041.

[4]   Y. Lin, T. V. Williams, J. W. Connell, *J. Phys. Chem. Lett.* **2009**, *1*, 277-283.

[5]   a) S. Susarla, A. Kutana, J. A. Hachtel, V. Kochat, A. Apte, R. Vajtai, J. C. Idrobo, B. I. Yakobson, C. S. Tiwary, P. M. Ajayan, *Adv. Mater.* **2017**, *29*, 1702457; b) M. Chhowalla, H. S. Shin, G. Eda, L. J. Li, K. P. Loh, H. Zhang, *Nat. Chem.* **2013**, *5*, 263-275; c) X. Huang, Z. Zeng, H. Zhang, *Chem. Soc. Rev.* **2013**, *42*, 1934-1946; d) H. J. Conley, B. Wang, J. I. Ziegler, R. F. Haglund, Jr., S. T. Pantelides, K. I. Bolotin, *Nano Lett.* **2013**, *13*, 3626-3630.

[6]   T. Rodenas, I. Luz, G. Prieto, B. Seoane, H. Miro, A. Corma, F. Kapteijn, I. X. F. X. Llabres, J. Gascon, *Nat. Mater.* **2015**, *14*, 48-55.

[7]   J. W. Colson, A. R. Woll, A. Mukherjee, M. P. Levendorf, E. L. Spitler, V. B. Shields, M. G. Spencer, J. Park, W. R. Dichtel, *Science* **2011**, *332*, 228-231.

[8]   M. Naguib, V. N. Mochalin, M. W. Barsoum, Y. Gogotsi, *Adv. Mater.* **2014**, *26*, 992-1005.

[9]   R. Uppuluri, A. Sen Gupta, A. S. Rosas, T. E. Mallouk, *Chem. Soc. Rev.* **2018**, *47*, 2401-2430.

[10]   Q. Wang, D. O'Hare, *Chem. Rev.* **2012**, *112*, 4124-4155.

[11]   a) H. Zhang, *ACS Nano* **2015**, *9*, 9451-9469; b) S. Z. Butler, S. M. Hollen, L. Cao, Y. Cui, J. A. Gupta, H. R. Gutierrez, T. F. Heinz, S. S. Hong, J. Huang, A. F. Ismach, E. Johnston-Halperin, M. Kuno, V. V. Plashnitsa, R. D. Robinson, R. S. Ruoff, S. Salahuddin, J. Shan, L. Shi, M. G. Spencer, M. Terrones, W. Windl, J. E. Goldberger, *ACS Nano* **2013**, *7*, 2898-2926; c) R. Mas-Balleste, C. Gomez-Navarro, J. Gomez-Herrero, F. Zamora, *Nanoscale* **2011**, *3*, 20-30.

[12]   Z. Xiong, L. Zhong, H. Wang, X. Li, *Materials* **2021**, *14*, 1192.

[13]   a) J. Di, C. Yan, A. D. Handoko, Z. W. Seh, H. Li, Z. Liu, *Mater. Today* **2018**, *21*, 749-770; b) X. Liu, M. C. Hersam, *Adv. Mater.* **2018**, *30*, 1801586.

[14]   B. Hunt, J. D. Sanchez-Yamagishi, A. F. Young, M. Yankowitz, B. J. LeRoy, K. Watanabe, T. Taniguchi, P. Moon, M. Koshino, P. Jarillo-Herrero, R. C. Ashoori, *Science* **2013**, *340*, 1427-1430.

[15]   a) K. S. Novoselov, A. Mishchenko, A. Carvalho, A. H. Castro Neto, *Science* **2016**, *353*, aac9439; b) D. Won, J. Bang, S. H. Choi, K. R. Pyun, S. Jeong, Y. Lee, S. H. Ko, *Chem. Rev.* **2023**, *123*, 9982-10078; c) T. Georgiou, R. Jalil, B. D. Belle, L. Britnell, R. V. Gorbachev, S. V. Morozov, Y. J. Kim, A. Gholinia, S.

J. Haigh, O. Makarovsky, L. Eaves, L. A. Ponomarenko, A. K. Geim, K. S. Novoselov, A. Mishchenko, *Nat. Nanotechnol.* **2013**, *8*, 100-103.

[16]   G. S. Lee, J. G. Kim, J. T. Kim, C. W. Lee, S. Cha, G. B. Choi, J. Lim, S. Padmajan Sasikala, S. O. Kim, *Adv. Mater.* **2024**, *36*, e2307689.

[17]   Y. Liu, S. Zhang, J. He, Z. M. Wang, Z. Liu, *Nano-Micro Lett.* **2019**, *11*, 13.

[18]   A. K. Geim, I. V. Grigorieva, *Nature* **2013**, *499*, 419-425.

[19]   N. R. Glavin, S. Nam, *Matter* **2023**, *6*, 4-6.

[20]   C. R. Dean, A. F. Young, I. Meric, C. Lee, L. Wang, S. Sorgenfrei, K. Watanabe, T. Taniguchi, P. Kim, K. L. Shepard, J. Hone, *Nat. Nanotechnol.* **2010**, *5*, 722-726.

[21]   a) A. S. Mayorov, R. V. Gorbachev, S. V. Morozov, L. Britnell, R. Jalil, L. A. Ponomarenko, P. Blake, K. S. Novoselov, K. Watanabe, T. Taniguchi, A. K. Geim, *Nano Lett.* **2011**, *11*, 2396-2399; b) P. Alonso-Gonzalez, A. Y. Nikitin, Y. Gao, A. Woessner, M. B. Lundeberg, A. Principi, N. Forcellini, W. Yan, S. Velez, A. J. Huber, K. Watanabe, T. Taniguchi, F. Casanova, L. E. Hueso, M. Polini, J. Hone, F. H. Koppens, R. Hillenbrand, *Nat. Nanotechnol.* **2017**, *12*, 31-35; c) R. V. Gorbachev, A. K. Geim, M. I. Katsnelson, K. S. Novoselov, T. Tudorovskiy, I. V. Grigorieva, A. H. MacDonald, S. V. Morozov, K. Watanabe, T. Taniguchi, L. A. Ponomarenko, *Nat. Phys.* **2012**, *8*, 896-901.

[22]   L. Wang, I. Meric, P. Y. Huang, Q. Gao, Y. Gao, H. Tran, T. Taniguchi, K. Watanabe, L. M. Campos, D. A. Muller, J. Guo, P. Kim, J. Hone, K. L. Shepard, C. R. Dean, *Science* **2013**, *342*, 614-617.

[23]   G. X. Ni, H. Wang, J. S. Wu, Z. Fei, M. D. Goldflam, F. Keilmann, B. Ozyilmaz, A. H. Castro Neto, X. M. Xie, M. M. Fogler, D. N. Basov, *Nat. Mater.* **2015**, *14*, 1217-1222.

[24]   C. H. Lee, G. H. Lee, A. M. van der Zande, W. Chen, Y. Li, M. Han, X. Cui, G. Arefe, C. Nuckolls, T. F. Heinz, J. Guo, J. Hone, P. Kim, *Nat. Nanotechnol.* **2014**, *9*, 676-681.

[25]   a) W. J. Yu, Y. Liu, H. Zhou, A. Yin, Z. Li, Y. Huang, X. Duan, *Nat. Nanotechnol.* **2013**, *8*, 952-958; b) L. Britnell, R. M. Ribeiro, A. Eckmann, R. Jalil, B. D. Belle, A. Mishchenko, Y. J. Kim, R. V. Gorbachev, T. Georgiou, S. V. Morozov, A. N. Grigorenko, A. K. Geim, C. Casiraghi, A. H. Castro Neto, K. S. Novoselov, *Science* **2013**, *340*, 1311-1314.

[26]   F. Withers, O. Del Pozo-Zamudio, A. Mishchenko, A. P. Rooney, A. Gholinia, K. Watanabe, T. Taniguchi, S. J. Haigh, A. K. Geim, A. I. Tartakovskii, K. S. Novoselov, *Nat. Mater.* **2015**, *14*, 301-306.

[27]   J. Mannhar, *Nat. Mater.* **2012**, *11*, 91.

[28]   H. Hong, C. Liu, T. Cao, C. Jin, S. Wang, F. Wang, K. Liu, *Adv. Mater. Interfaces* **2017**, *4*, 1601054.

[29]   H. W. Guo, Z. Hu, Z. B. Liu, J. G. Tian, *Adv. Func. Mater.* **2020**, *31*, 2007810.

[30]   a) J. M. Park, Y. Cao, K. Watanabe, T. Taniguchi, P. Jarillo-Herrero, *Nature* **2021**, *590*, 249-255; b) Y. Cao, V. Fatemi, A. Demir, S. Fang, S. L. Tomarken, J. Y.

Luo, J. D. Sanchez-Yamagishi, K. Watanabe, T. Taniguchi, E. Kaxiras, R. C. Ashoori, P. Jarillo-Herrero, *Nature* **2018**, *556*, 80-84.

[31] E. Suárez Morell, J. D. Correa, P. Vargas, M. Pacheco, Z. Barticevic, *Phys. Rev. B* **2010**, *82*, 121407.

[32] W. Chen, Z. Sun, Z. Wang, L. Gu, X. Xu, S. Wu, C. Gao, *Science* **2019**, *366*, 983-987.

[33] a) L. Zhang, Z. Zhang, F. Wu, D. Wang, R. Gogna, S. Hou, K. Watanabe, T. Taniguchi, K. Kulkarni, T. Kuo, S. R. Forrest, H. Deng, *Nat. Commun.* **2020**, *11*, 5888; b) C. Jin, E. C. Regan, A. Yan, M. Iqbal Bakti Utama, D. Wang, S. Zhao, Y. Qin, S. Yang, Z. Zheng, S. Shi, K. Watanabe, T. Taniguchi, S. Tongay, A. Zettl, F. Wang, *Nature* **2019**, *567*, 76-80.

[34] G. Hu, Q. Ou, G. Si, Y. Wu, J. Wu, Z. Dai, A. Krasnok, Y. Mazor, Q. Zhang, Q. Bao, C. W. Qiu, A. Alu, *Nature* **2020**, *582*, 209-213.

[35] G. X. Ni, H. Wang, B. Y. Jiang, L. X. Chen, Y. Du, Z. Y. Sun, M. D. Goldflam, A. J. Frenzel, X. M. Xie, M. M. Fogler, D. N. Basov, *Nat. Commun.* **2019**, *10*, 4360.

[36] T. H. Bointon, I. Khrapach, R. Yakimova, A. V. Shytov, M. F. Craciun, S. Russo, *Nano Lett.* **2014**, *14*, 1751-1755.

[37] H. Fang, C. Battaglia, C. Carraro, S. Nemsak, B. Ozdol, J. S. Kang, H. A. Bechtel, S. B. Desai, F. Kronast, A. A. Unal, G. Conti, C. Conlon, G. K. Palsson, M. C. Martin, A. M. Minor, C. S. Fadley, E. Yablonovitch, R. Maboudian, A. Javey, *Proc. Natl. Acad. Sci. U.S.A.* **2014**, *111*, 6198-6202.

[38] P. V. Pham, S. C. Bodepudi, K. Shehzad, Y. Liu, Y. Xu, B. Yu, X. Duan, *Chem. Rev.* **2022**, *122*, 6514-6613.

[39] S. K. Chakraborty, B. Kundu, B. Nayak, S. P. Dash, P. K. Sahoo, *iScience* **2022**, *25*, 103942.

[40] J. F. Sierra, J. Fabian, R. K. Kawakami, S. Roche, S. O. Valenzuela, *Nat. Nanotechnol.* **2021**, *16*, 856-868.

[41] Y. Li, J. Zhang, Q. Chen, X. Xia, M. Chen, *Adv. Mater.* **2021**, *33*, e2100855.

[42] X. Liu, M. C. Hersam, *Nat. Rev. Mater.* **2019**, *4*, 669-684.

[43] H. Huang, W. Feng, Y. Chen, *Chem. Soc. Rev.* **2021**, *50*, 11381-11485.

[44] M. Dulal, M. R. Islam, S. Maiti, M. H. Islam, I. Ali, A. M. Abdelkader, K. S. Novoselov, S. Afroj, N. Karim, *Adv. Func. Mater.* **2023**, *33*, 2305901.

[45] L. Jing, K. Li, H. Yang, P.-Y. Chen, *Mater. Horizons* **2020**, *7*, 54-70.

[46] V. K. Sangwan, M. C. Hersam, *Nat. Nanotechnol.* **2020**, *15*, 517-528.

[47] F. Lyu, S. Zeng, Z. Jia, F. X. Ma, L. Sun, L. Cheng, J. Pan, Y. Bao, Z. Mao, Y. Bu, Y. Y. Li, J. Lu, *Nat. Commun.* **2022**, *13*, 6249.

[48] D. S. L. Abergel, V. Apalkov, J. Berashevich, K. Ziegler, T. Chakraborty, *Adv. Phys.* **2010**, *59*, 261-482.

[49] B. Partoens, F. M. Peeters, *Phys. Rev. B* **2006**, *74*, 075404

[50] a) D. R. Cooper, B. D'Anjou, N. Ghattamaneni, B. Harack, M. Hilke, A. Horth, N. Majlis, M. Massicotte, L. Vandsburger, E. Whiteway, V. Yu, *ISRN Condens. Matter Phys.* **2012**, *2012*, 1-56; b) M. Ishigami, J. H. Chen, W. G. Cullen, M. S.

Fuhrer, E. D. Williams, *Nano Lett.* **2007**, *7*, 1643-1648.

[51] N. Tombros, C. Jozsa, M. Popinciuc, H. T. Jonkman, B. J. van Wees, *Nature* **2007**, *448*, 571-574.

[52] P. Avouris, *Nano Lett.* **2010**, *10*, 4285-4294.

[53] Y. Nishina, S. Eigler, *Nanoscale* **2020**, *12*, 12731-12740.

[54] S. Eigler, M. Enzelberger-Heim, S. Grimm, P. Hofmann, W. Kroener, A. Geworski, C. Dotzer, M. Röckert, J. Xiao, C. Papp, O. Lytken, H. P. Steinrück, P. Müller, A. Hirsch, *Adv. Mater.* **2013**, *25*, 3583-3587.

[55] A. M. Dimiev, L. B. Alemany, J. M. Tour, *ACS Nano* **2013**, *7*, 576-588.

[56] A. M. Dimiev, S. Eigler, *Graphene oxide: fundamentals and applications*, John Wiley & Sons, **2016**.

[57] P. Feicht, S. Eigler, *ChemNanoMat* **2018**, *4*, 244-252.

[58] S. Eigler, *Chem. Eur. J.* **2016**, *22*, 7012-7027.

[59] S. Eigler, A. Hirsch, *Angew. Chem. Int. Ed.* **2014**, *53*, 7720-7738.

[60] Z. Wang, Q. Yao, C. Neumann, F. Borrnert, J. Renner, U. Kaiser, A. Turchanin, H. J. W. Zandvliet, S. Eigler, *Angew. Chem. Int. Ed.* **2020**, *59*, 13657-13662.

[61] a) Z. Wang, Q. Yao, S. Eigler, *Chem. Eur. J.* **2020**, *26*, 6484-6489; b) Z. Wang, Q. Yao, Y. Hu, C. Li, M. Hussmann, B. Weintrub, J. N. Kirchhof, K. Bolotin, T. Taniguchi, K. Watanabe, S. Eigler, *RSC Adv.* **2019**, *9*, 38011-38016.

[62] A. J. Mannix, B. Kiraly, M. C. Hersam, N. P. Guisinger, *Nat. Rev. Chem.* **2017**, *1*, 0014.

[63] M. Yi, Z. Shen, *J. Mater. Chem. A* **2015**, *3*, 11700-11715.

[64] a) K. S. Novoselov, D. Jiang, F. Schedin, T. J. Booth, V. V. Khotkevich, S. V. Morozov, A. K. Geim, *Proc. Natl. Acad. Sci. U.S.A.* **2005**, *102*, 10451-10453; b) H. Li, J. Wu, Z. Yin, H. Zhang, *Acc. Chem. Res.* **2014**, *47*, 1067-1075; c) A. Castellanos-Gomez, L. Vicarelli, E. Prada, J. O. Island, K. L. Narasimha-Acharya, S. I. Blanter, D. J. Groenendijk, M. Buscema, G. A. Steele, J. V. Alvarez, H. W. Zandbergen, J. J. Palacios, H. S. J. van der Zant, *2D Mater.* **2014**, *1*, 025001; d) H. Li, G. Lu, Y. Wang, Z. Yin, C. Cong, Q. He, L. Wang, F. Ding, T. Yu, H. Zhang, *Small* **2013**, *9*, 1974-1981.

[65] A. S. Efimova, P. V. Alekseevskiy, M. V. Timofeeva, Y. A. Kenzhebayeva, A. O. Kuleshova, I. G. Koryakina, D. I. Pavlov, T. S. Sukhikh, A. S. Potapov, S. A. Shipilovskikh, N. Li, V. A. Milichko, *Small Methods* **2023**, *7*, 2300752.

[66] J. Y. Moon, M. Kim, S. I. Kim, S. Xu, J. H. Choi, D. Whang, K. Watanabe, T. Taniguchi, D. S. Park, J. Seo, S. H. Cho, S. K. Son, J. H. Lee, *Sci. Adv.* **2020**, *6*, eabc6601.

[67] K. R. Paton, E. Varrla, C. Backes, R. J. Smith, U. Khan, A. O'Neill, C. Boland, M. Lotya, O. M. Istrate, P. King, T. Higgins, S. Barwich, P. May, P. Puczkarski, I. Ahmed, M. Moebius, H. Pettersson, E. Long, J. Coelho, S. E. O'Brien, E. K. McGuire, B. M. Sanchez, G. S. Duesberg, N. McEvoy, T. J. Pennycook, C. Downing, A. Crossley, V. Nicolosi, J. N. Coleman, *Nat. Mater.* **2014**, *13*, 624-630.

[68]   L. Tang, J. Tan, H. Nong, B. Liu, H.-M. Cheng, *Acc. Mater. Res.* **2020**, *2*, 36-47.

[69]   X. Li, W. Cai, L. Colombo, R. S. Ruoff, *Nano Lett.* **2009**, *9*, 4268-4272.

[70]   R. Lv, M. C. dos Santos, C. Antonelli, S. Feng, K. Fujisawa, A. Berkdemir, R. Cruz-Silva, A. L. Elias, N. Perea-Lopez, F. Lopez-Urias, H. Terrones, M. Terrones, *Adv. Mater.* **2014**, *26*, 7593-7599.

[71]   a) S. Bae, H. Kim, Y. Lee, X. Xu, J. S. Park, Y. Zheng, J. Balakrishnan, T. Lei, H. R. Kim, Y. I. Song, Y. J. Kim, K. S. Kim, B. Ozyilmaz, J. H. Ahn, B. H. Hong, S. Iijima, *Nat. Nanotechnol.* **2010**, *5*, 574-578; b) Y. Zhang, L. Zhang, C. Zhou, *Acc. Chem. Res.* **2013**, *46*, 2329-2339.

[72]   a) R. Shi, P. He, X. Cai, Z. Zhang, W. Wang, J. Wang, X. Feng, Z. Wu, A. Amini, N. Wang, C. Cheng, *ACS Nano* **2020**, *14*, 7593-7601; b) L. Tang, T. Li, Y. Luo, S. Feng, Z. Cai, H. Zhang, B. Liu, H. M. Cheng, *ACS Nano* **2020**, *14*, 4646-4653.

[73]   a) L. Song, L. Ci, H. Lu, P. B. Sorokin, C. Jin, J. Ni, A. G. Kvashnin, D. G. Kvashnin, J. Lou, B. I. Yakobson, P. M. Ajayan, *Nano Lett.* **2010**, *10*, 3209-3215; b) F. Mahvash, E. Paradis, D. Drouin, T. Szkopek, M. Siaj, *Nano Lett.* **2015**, *15*, 2263-2268.

[74]   a) S. Zhou, X. Tao, Y. Gu, *J. Phys. Chem. C* **2016**, *120*, 4753-4758; b) M. Liu, F. Y. Liu, B. Y. Man, D. Bi, X. Y. Xu, *Appl. Surf. Sci.* **2014**, *317*, 257-261.

[75]   C. Young, J. Wang, J. Kim, Y. Sugahara, J. Henzie, Y. Yamauchi, *Chem. Mater.* **2018**, *30*, 3379-3386.

[76]   X. Li, W. Cai, J. An, S. Kim, J. Nah, D. Yang, R. Piner, A. Velamakanni, I. Jung, E. Tutuc, S. K. Banerjee, L. Colombo, R. S. Ruoff, *Science* **2009**, *324*, 1312-1314.

[77]   H. Xin, W. Li, *Appl. Phys. Rev.* **2018**, *5*, 031105.

[78]   Q. Yu, L. A. Jauregui, W. Wu, R. Colby, J. Tian, Z. Su, H. Cao, Z. Liu, D. Pandey, D. Wei, T. F. Chung, P. Peng, N. P. Guisinger, E. A. Stach, J. Bao, S. S. Pei, Y. P. Chen, *Nat. Mater.* **2011**, *10*, 443-449.

[79]   a) Y. Hao, M. S. Bharathi, L. Wang, Y. Liu, H. Chen, S. Nie, X. Wang, H. Chou, C. Tan, B. Fallahazad, H. Ramanarayan, C. W. Magnuson, E. Tutuc, B. I. Yakobson, K. F. McCarty, Y. W. Zhang, P. Kim, J. Hone, L. Colombo, R. S. Ruoff, *Science* **2013**, *342*, 720-723; b) T. Wu, X. Zhang, Q. Yuan, J. Xue, G. Lu, Z. Liu, H. Wang, H. Wang, F. Ding, Q. Yu, X. Xie, M. Jiang, *Nat. Mater.* **2016**, *15*, 43-47; c) X. Xu, Z. Zhang, J. Dong, D. Yi, J. Niu, M. Wu, L. Lin, R. Yin, M. Li, J. Zhou, S. Wang, J. Sun, X. Duan, P. Gao, Y. Jiang, X. Wu, H. Peng, R. S. Ruoff, Z. Liu, D. Yu, E. Wang, F. Ding, K. Liu, *Sci. Bull.* **2017**, *62*, 1074-1080; d) J. H. Lee, E. K. Lee, W. J. Joo, Y. Jang, B. S. Kim, J. Y. Lim, S. H. Choi, S. J. Ahn, J. R. Ahn, M. H. Park, C. W. Yang, B. L. Choi, S. W. Hwang, D. Whang, *Science* **2014**, *344*, 286-289.

[80]   a) S. Tang, H. Wang, H. S. Wang, Q. Sun, X. Zhang, C. Cong, H. Xie, X. Liu, X. Zhou, F. Huang, X. Chen, T. Yu, F. Ding, X. Xie, M. Jiang, *Nat. Commun.* **2015**, *6*, 6499; b) J. Sun, Z. Chen, L. Yuan, Y. Chen, J. Ning, S. Liu, D. Ma, X.

Song, M. K. Priydarshi, A. Bachmatiuk, M. H. Rummeli, T. Ma, L. Zhi, L. Huang, Y. Zhang, Z. Liu, *ACS Nano* **2016**, *10*, 11136-11144; c) J. Li, M. Chen, A. Samad, H. Dong, A. Ray, J. Zhang, X. Jiang, U. Schwingenschlogl, J. Domke, C. Chen, Y. Han, T. Fritz, R. S. Ruoff, B. Tian, X. Zhang, *Nat. Mater.* **2022**, *21*, 740-747.

[81]   F. Liu, P. Li, H. An, P. Peng, B. McLean, F. Ding, *Adv. Func. Mater.* **2022**, *32*, 2203191.

[82]   B. C. Brodie, *Phil. Trans. R. Soc.* **1997**, *149*, 249-259.

[83]   a) L. Staudenmaier, *Chem. Ber.* **2006**, *31*, 1481-1487; b) L. Staudenmaier, *Chem. Ber.* **2006**, *32*, 1394-1399; c) L. Staudenmaier, *Chem. Ber.* **2006**, *32*, 2824-2834.

[84]   W. S. Hummers, R. E. Offeman, *J. Am. Chem. Soc.* **2002**, *80*, 1339-1339.

[85]   G. Charpy, *Compt. rend.* **1909**, *148*, 920.

[86]   C. K. Chua, M. Pumera, *Chem. Soc. Rev.* **2014**, *43*, 291-312.

[87]   S. Eigler, S. Grimm, M. Enzelberger-Heim, P. Muller, A. Hirsch, *Commun. Chem.* **2013**, *49*, 7391-7393.

[88]   D. C. Elias, R. R. Nair, T. M. Mohiuddin, S. V. Morozov, P. Blake, M. P. Halsall, A. C. Ferrari, D. W. Boukhvalov, M. I. Katsnelson, A. K. Geim, K. S. Novoselov, *Science* **2009**, *323*, 610-613.

[89]   A. Sinitskii, A. Dimiev, D. A. Corley, A. A. Fursina, D. V. Kosynkin, J. M. Tour, *ACS Nano* **2010**, *4*, 1949-1954.

[90]   K. R. Nandanapalli, D. Mudusu, S. Lee, *Carbon* **2019**, *152*, 954-985.

[91]   a) V. Georgakilas, M. Otyepka, A. B. Bourlinos, V. Chandra, N. Kim, K. C. Kemp, P. Hobza, R. Zboril, K. S. Kim, *Chem. Rev.* **2012**, *112*, 6156-6214; b) A. Savchenko, *Science* **2009**, *323*, 589-590; c) J. T. Robinson, J. S. Burgess, C. E. Junkermeier, S. C. Badescu, T. L. Reinecke, F. K. Perkins, M. K. Zalalutdniov, J. W. Baldwin, J. C. Culbertson, P. E. Sheehan, E. S. Snow, *Nano Lett.* **2010**, *10*, 3001-3005; d) S. Vadukumpully, J. Gupta, Y. Zhang, G. Q. Xu, S. Valiyaveettil, *Nanoscale* **2011**, *3*, 303-308.

[92]   E. Bekyarova, M. E. Itkis, P. Ramesh, C. Berger, M. Sprinkle, W. A. de Heer, R. C. Haddon, *J. Am. Chem. Soc.* **2009**, *131*, 1336-1337.

[93]   Z. Qiu, J. Yu, P. Yan, Z. Wang, Q. Wan, N. Yang, *ACS Appl. Mater. Interfaces* **2016**, *8*, 28291-28298.

[94]   a) J. M. Englert, C. Dotzer, G. Yang, M. Schmid, C. Papp, J. M. Gottfried, H. P. Steinruck, E. Spiecker, F. Hauke, A. Hirsch, *Nat. Chem.* **2011**, *3*, 279-286; b) G. Abellan, M. Schirowski, K. F. Edelthalhammer, M. Fickert, K. Werbach, H. Peterlik, F. Hauke, A. Hirsch, *J. Am. Chem. Soc.* **2017**, *139*, 5175-5182.

[95]   T. Wei, F. Hauke, A. Hirsch, *Adv. Mater.* **2021**, *33*, 2104060.

[96]   a) J. Shen, M. Shi, H. Ma, B. Yan, N. Li, Y. Hu, M. Ye, *J. Colloid Interface Sci.* **2010**, *352*, 366-370; b) C. Xu, X. Wang, J. Wang, H. Hu, L. Wan, *Chem. Phys. Lett.* **2010**, *498*, 162-167.

[97]   J. Velasco, Jr., L. Jing, W. Bao, Y. Lee, P. Kratz, V. Aji, M. Bockrath, C. N. Lau, C. Varma, R. Stillwell, D. Smirnov, F. Zhang, J. Jung, A. H. MacDonald, *Nat.*

Nanotechnol. **2012**, *7*, 156-160.

[98] H. Liu, S. Ryu, Z. Chen, M. L. Steigerwald, C. Nuckolls, L. E. Brus, *J. Am. Chem. Soc.* **2009**, *131*, 17099-17101.

[99] K. F. Edelthalhammer, D. Dasler, L. Jurkiewicz, T. Nagel, S. Al-Fogra, F. Hauke, A. Hirsch, *Angew. Chem. Int. Ed.* **2020**, *59*, 23329-23334.

[100] L. Bao, B. Zhao, B. Yang, M. Halik, F. Hauke, A. Hirsch, *Adv. Mater.* **2021**, *33*, 2101653.

[101] T. Wei, S. Al-Fogra, F. Hauke, A. Hirsch, *J. Am. Chem. Soc.* **2020**, *142*, 21926-21931.

[102] a) T. Wei, X. Liu, S. Al-Fogra, J. Bachmann, F. Hauke, A. Hirsch, *Commun. Chem.* **2021**, *57*, 4654-4657; b) S. Al-Fogra, S. Rohde, M. Speck, F. Hauke, A. Hirsch, T. Wei, *Commun. Chem.* **2024**, *60*, 734-737.

[103] L. Bao, B. Zhao, M. Assebban, M. Halik, F. Hauke, A. Hirsch, *Chem. Eur. J.* **2021**, *27*, 8709-8713.

[104] A. Kuc, T. Heine, *Chem. Soc. Rev.* **2015**, *44*, 2603-2614.

[105] Q. H. Wang, K. Kalantar-Zadeh, A. Kis, J. N. Coleman, M. S. Strano, *Nat. Nanotechnol.* **2012**, *7*, 699-712.

[106] B. Radisavljevic, A. Radenovic, J. Brivio, V. Giacometti, A. Kis, *Nat. Nanotechnol.* **2011**, *6*, 147-150.

[107] R. J. Toh, Z. Sofer, J. Luxa, D. Sedmidubsky, M. Pumera, *Commun. Chem.* **2017**, *53*, 3054-3057.

[108] W. Choi, N. Choudhary, G. H. Han, J. Park, D. Akinwande, Y. H. Lee, *Mater. Today* **2017**, *20*, 116-130.

[109] A. Splendiani, L. Sun, Y. Zhang, T. Li, J. Kim, C. Y. Chim, G. Galli, F. Wang, *Nano Lett.* **2010**, *10*, 1271-1275.

[110] K. F. Mak, C. Lee, J. Hone, J. Shan, T. F. Heinz, *Phys. Rev. Lett.* **2010**, *105*, 136805.

[111] T. Böker, R. Severin, A. Müller, C. Janowitz, R. Manzke, D. Voß, P. Krüger, A. Mazur, J. Pollmann, *Phys. Rev. B* **2001**, *64*, 235305.

[112] S. Mouri, Y. Miyauchi, K. Matsuda, *Nano Lett.* **2013**, *13*, 5944-5948.

[113] K. F. Mak, K. He, C. Lee, G. H. Lee, J. Hone, T. F. Heinz, J. Shan, *Nat. Mater.* **2013**, *12*, 207-211.

[114] W. Su, H. Dou, D. Huo, N. Dai, L. Yang, *Chem. Phys. Lett.* **2015**, *635*, 40-44.

[115] a) K. C. Lee, Y. H. Chen, H. Y. Lin, C. C. Cheng, P. Y. Chen, T. Y. Wu, M. H. Shih, K. H. Wei, L. J. Li, C. W. Chang, *Sci. Rep.* **2015**, *5*, 16374; b) W. Gao, Y. H. Lee, R. Jiang, J. Wang, T. Liu, X. Y. Ling, *Adv. Mater.* **2016**, *28*, 701-706.

[116] A. Castellanos-Gomez, R. Roldan, E. Cappelluti, M. Buscema, F. Guinea, H. S. van der Zant, G. A. Steele, *Nano Lett.* **2013**, *13*, 5361-5366.

[117] H. Nan, Z. Wang, W. Wang, Z. Liang, Y. Lu, Q. Chen, D. He, P. Tan, F. Miao, X. Wang, J. Wang, Z. Ni, *ACS Nano* **2014**, *8*, 5738-5745.

[118] A. A. Balandin, *Nat. Mater.* **2011**, *10*, 569-581.

[119] J. S. Bunch, S. S. Verbridge, J. S. Alden, A. M. van der Zande, J. M. Parpia, H.

G. Craighead, P. L. McEuen, *Nano Lett.* **2008**, *8*, 2458-2462.

[120] J. Moser, A. Barreiro, A. Bachtold, *Appl. Phys. Lett.* **2007**, *91*, 163513.

[121] R. R. Nair, P. Blake, A. N. Grigorenko, K. S. Novoselov, T. J. Booth, T. Stauber, N. M. Peres, A. K. Geim, *Science* **2008**, *320*, 1308.

[122] C. Xie, C. Mak, X. Tao, F. Yan, *Adv. Func. Mater.* **2016**, *27*, 1603886.

[123] P. Solis-Fernandez, M. Bissett, H. Ago, *Chem. Soc. Rev.* **2017**, *46*, 4572-4613.

[124] O. Lopez-Sanchez, D. Lembke, M. Kayci, A. Radenovic, A. Kis, *Nat. Nanotechnol.* **2013**, *8*, 497-501.

[125] M. Yang, L. Wang, G. Hu, X. Chen, P. L. Gong, X. Cong, Y. Liu, Y. Yang, X. Li, X. Zhao, X. Liu, *Nano Res.* **2021**, *14*, 2241-2246.

[126] W. Zhang, C. P. Chuu, J. K. Huang, C. H. Chen, M. L. Tsai, Y. H. Chang, C. T. Liang, Y. Z. Chen, Y. L. Chueh, J. H. He, M. Y. Chou, L. J. Li, *Sci. Rep.* **2014**, *4*, 3826.

[127] P. Vabbina, N. Choudhary, A. A. Chowdhury, R. Sinha, M. Karabiyik, S. Das, W. Choi, N. Pala, *ACS Appl. Mater. Interfaces* **2015**, *7*, 15206-15213.

[128] C. J. Shih, Q. H. Wang, Y. Son, Z. Jin, D. Blankschtein, M. S. Strano, *ACS Nano* **2014**, *8*, 5790-5798.

[129] H. Li, X. Li, J.-H. Park, L. Tao, K. K. Kim, Y. H. Lee, J.-B. Xu, *Nano Energy* **2019**, *57*, 214-221.

[130] K. Yin, T. Huang, H.-Y. Wu, Y. Si, J.-C. Lian, Y.-W. Xiao, Z. Zhang, W.-Q. Huang, W. Hu, G.-F. Huang, *J. Phys. D: Appl. Phys.* **2021**, *54*, 265302.

[131] S. Singh, C. Espejo, A. H. Romero, *Phys. Rev. B* **2018**, *98*, 155309.

[132] D. Pierucci, H. Henck, J. Avila, A. Balan, C. H. Naylor, G. Patriarche, Y. J. Dappe, M. G. Silly, F. Sirotti, A. T. Johnson, M. C. Asensio, A. Ouerghi, *Nano Lett.* **2016**, *16*, 4054-4061.

[133] B. Liu, L.-J. Wu, Y.-Q. Zhao, L.-Z. Wang, M.-Q. Cai, *RSC Adv.* **2016**, *6*, 60271-60276.

[134] Y. Ma, Y. Dai, M. Guo, C. Niu, B. Huang, *Nanoscale* **2011**, *3*, 3883-3887.

[135] R. L. Anderson, *IBM J. Res. Dev.* **1960**, *4*, 283-287.

[136] Q. Fang, M. Li, X. Zhao, L. Yuan, B. Wang, C. Xia, F. Ma, *Mater. Adv.* **2022**, *3*, 624-631.

[137] a) S. Tongay, W. Fan, J. Kang, J. Park, U. Koldemir, J. Suh, D. S. Narang, K. Liu, J. Ji, J. Li, R. Sinclair, J. Wu, *Nano Lett.* **2014**, *14*, 3185-3190; b) M. Dienwiebel, G. S. Verhoeven, N. Pradeep, J. W. Frenken, J. A. Heimberg, H. W. Zandbergen, *Phys. Rev. Lett.* **2004**, *92*, 126101; c) S. M. Clark, K.-J. Jeon, J.-Y. Chen, C.-S. Yoo, *Solid State Commun.* **2013**, *154*, 15-18.

[138] Y. Li, C. Y. Xu, J. K. Qin, W. Feng, J. Y. Wang, S. Zhang, L. P. Ma, J. Cao, P. A. Hu, W. Ren, L. Zhen, *Adv. Func. Mater.* **2015**, *26*, 293-302.

[139] B. Qiu, X. Zhao, G. Hu, W. Yue, J. Ren, X. Yuan, *Nanomaterials* **2018**, *8*, 962.

[140] H. M. Oh, H. Jeong, G. H. Han, H. Kim, J. H. Kim, S. Y. Lee, S. Y. Jeong, S. Jeong, D. J. Park, K. K. Kim, Y. H. Lee, M. S. Jeong, *ACS Nano* **2016**, *10*, 10446-10453.

[141] M. Vazquez Sulleiro, A. Develioglu, R. Quiros-Ovies, L. Martin-Perez, N. Martin Sabanes, M. L. Gonzalez-Juarez, I. J. Gomez, M. Vera-Hidalgo, V. Sebastian, J. Santamaria, E. Burzuri, E. M. Perez, *Nat. Chem.* **2022**, *14*, 695-700.

[142] X. Chen, M. Assebban, M. Kohring, L. Bao, H. B. Weber, K. C. Knirsch, A. Hirsch, *J. Am. Chem. Soc.* **2022**, *144*, 9645-9650.

[143] R. Rao, A. E. Islam, S. Singh, R. Berry, R. K. Kawakami, B. Maruyama, J. Katoch, *Phys. Rev. B* **2019**, *99*, 195401.

[144] A. C. Ferrari, D. M. Basko, *Nat. Nanotechnol.* **2013**, *8*, 235-246.

[145] R. Beams, L. Gustavo Cancado, L. Novotny, *J. Phys. Condens. Matter* **2015**, *27*, 083002.

[146] A. C. Ferrari, J. C. Meyer, V. Scardaci, C. Casiraghi, M. Lazzeri, F. Mauri, S. Piscanec, D. Jiang, K. S. Novoselov, S. Roth, A. K. Geim, *Phys. Rev. Lett.* **2006**, *97*, 187401.

[147] A. J. Pollard, B. Brennan, H. Stec, B. J. Tyler, M. P. Seah, I. S. Gilmore, D. Roy, *Appl. Phys. Lett.* **2014**, *105*, 253107.

[148] M. M. Lucchese, F. Stavale, E. H. M. Ferreira, C. Vilani, M. V. O. Moutinho, R. B. Capaz, C. A. Achete, A. Jorio, *Carbon* **2010**, *48*, 1592-1597.

[149] P. Vecera, S. Eigler, M. Kolesnik-Gray, V. Krstic, A. Vierck, J. Maultzsch, R. A. Schafer, F. Hauke, A. Hirsch, *Sci. Rep.* **2017**, *7*, 45165.

[150] L. G. Cancado, A. Jorio, E. H. Ferreira, F. Stavale, C. A. Achete, R. B. Capaz, M. V. Moutinho, A. Lombardo, T. S. Kulmala, A. C. Ferrari, *Nano Lett.* **2011**, *11*, 3190-3196.

[151] L. Gustavo Cançado, M. Gomes da Silva, E. H. Martins Ferreira, F. Hof, K. Kampioti, K. Huang, A. Pénicaud, C. Alberto Achete, R. B. Capaz, A. Jorio, *2D Mater.* **2017**, *4*, 025039.

[152] B. Chakraborty, A. Bera, D. V. S. Muthu, S. Bhowmick, U. V. Waghmare, A. K. Sood, *Phys. Rev. B* **2012**, *85*, 161403.

[153] M. Buscema, G. A. Steele, H. S. J. van der Zant, A. Castellanos-Gomez, *Nano Res.* **2015**, *7*, 561-571.

[154] S. Mignuzzi, A. J. Pollard, N. Bonini, B. Brennan, I. S. Gilmore, M. A. Pimenta, D. Richards, D. Roy, *Phys. Rev. B* **2015**, *91*, 195411.

[155] S. Hong, D. Fu, J. Hou, D. Zhou, B. Wang, Y. Sun, P. Liu, K. Liu, *Sci. China Mater.* **2018**, *61*, 1351-1359.

[156] a) H. Li, J. B. Wu, F. Ran, M. L. Lin, X. L. Liu, Y. Zhao, X. Lu, Q. Xiong, J. Zhang, W. Huang, H. Zhang, P. H. Tan, *ACS Nano* **2017**, *11*, 11714-11723; b) K. G. Zhou, F. Withers, Y. Cao, S. Hu, G. Yu, C. Casiraghi, *ACS Nano* **2014**, *8*, 9914-9924.

[157] C. J. Shearer, A. D. Slattery, A. J. Stapleton, J. G. Shapter, C. T. Gibson, *Nanotechnology* **2016**, *27*, 125704.

[158] a) C. H. Lui, L. Liu, K. F. Mak, G. W. Flynn, T. F. Heinz, *Nature* **2009**, *462*, 339-341; b) S. V. Morozov, K. S. Novoselov, M. I. Katsnelson, F. Schedin, D. C. Elias, J. A. Jaszczak, A. K. Geim, *Phys. Rev. Lett.* **2008**, *100*, 016602; c) C.

Dean, A. F. Young, L. Wang, I. Meric, G. H. Lee, K. Watanabe, T. Taniguchi, K. Shepard, P. Kim, J. Hone, *Solid State Commun.* **2012**, *152*, 1275-1282.

[159] a) C. R. Dean, A. F. Young, I. Meric, C. Lee, L. Wang, S. Sorgenfrei, K. Watanabe, T. Taniguchi, P. Kim, K. L. Shepard, J. Hone, *Nat. Nanotechnol.* **2010**, *5*, 722-726; b) Y. Zhang, V. W. Brar, C. Girit, A. Zettl, M. F. Crommie, *Nat. Phys.* **2009**, *5*, 722-726.

[160] K. Watanabe, T. Taniguchi, H. Kanda, *Nat. Mater.* **2004**, *3*, 404-409.

[161] G. Giovannetti, P. A. Khomyakov, G. Brocks, P. J. Kelly, J. van den Brink, *Phys. Rev. B* **2007**, *76*, 073103.

[162] W. Yang, G. Chen, Z. Shi, C. C. Liu, L. Zhang, G. Xie, M. Cheng, D. Wang, R. Yang, D. Shi, K. Watanabe, T. Taniguchi, Y. Yao, Y. Zhang, G. Zhang, *Nat. Mater.* **2013**, *12*, 792-797.

[163] a) X. Zhang, S. Wang, C. K. Lee, C. M. Cheng, J. C. Lan, X. Li, J. Qiao, X. Tao, *Phys. Chem. Chem. Phys.* **2020**, *22*, 21776-21783; b) H. Qiu, T. Xu, Z. Wang, W. Ren, H. Nan, Z. Ni, Q. Chen, S. Yuan, F. Miao, F. Song, G. Long, Y. Shi, L. Sun, J. Wang, X. Wang, *Nat. Commun.* **2013**, *4*, 2642.

[164] Y. Wang, J. Z. Ou, S. Balendhran, A. F. Chrimes, M. Mortazavi, D. D. Yao, M. R. Field, K. Latham, V. Bansal, J. R. Friend, S. Zhuiykov, N. V. Medhekar, M. S. Strano, K. Kalantar-Zadeh, *ACS Nano* **2013**, *7*, 10083-10093.

[165] H. Ardekani, R. Younts, Y. Yu, L. Cao, K. Gundogdu, *ACS Appl. Mater. Interfaces* **2019**, *11*, 38240-38246.

[166] R. Dhall, M. R. Neupane, D. Wickramaratne, M. Mecklenburg, Z. Li, C. Moore, R. K. Lake, S. Cronin, *Adv. Mater.* **2015**, *27*, 1573-1578.

[167] a) J. Jadczak, J. Kutrowska-Girzycka, M. Bieniek, T. Kazimierczuk, P. Kossacki, J. J. Schindler, J. Debus, K. Watanabe, T. Taniguchi, C. H. Ho, A. Wojs, P. Hawrylak, L. Bryja, *Nanotechnology* **2021**, *32*, 145717; b) M. Zhao, P. Song, J. Teng, *ACS Appl. Mater. Interfaces* **2018**, *10*, 44102-44108; c) K. Zhang, T. Zhang, G. Cheng, T. Li, S. Wang, W. Wei, X. Zhou, W. Yu, Y. Sun, P. Wang, D. Zhang, C. Zeng, X. Wang, W. Hu, H. J. Fan, G. Shen, X. Chen, X. Duan, K. Chang, N. Dai, *ACS Nano* **2016**, *10*, 3852-3858.

[168] a) Y. Zhu, X. Li, Q. Cai, Z. Sun, G. Casillas, M. Jose-Yacaman, R. Verduzco, J. M. Tour, *J. Am. Chem. Soc.* **2012**, *134*, 11774-11780; b) N. Sharma, M. Arif, S. Monga, M. Shkir, Y. K. Mishra, A. Singh, *Appl. Surf. Sci.* **2020**, *513*, 145396.

[169] a) X. Wang, L. Jiao, K. Sheng, C. Li, L. Dai, G. Shi, *Sci. Rep.* **2013**, *3*, 1996; b) H.-K. Kim, S.-M. Bak, S. W. Lee, M.-S. Kim, B. Park, S. C. Lee, Y. J. Choi, S. C. Jun, J. T. Han, K.-W. Nam, K. Y. Chung, J. Wang, J. Zhou, X.-Q. Yang, K. C. Roh, K.-B. Kim, *Energy Environ. Sci.* **2016**, *9*, 1270-1281; c) D. Zhou, Y. Cui, P. W. Xiao, M. Y. Jiang, B. H. Han, *Nat. Commun.* **2014**, *5*, 4716.

[170] a) Z. Fan, Q. Zhao, T. Li, J. Yan, Y. Ren, J. Feng, T. Wei, *Carbon* **2012**, *50*, 1699-1703; b) Y. Xu, C. Y. Chen, Z. Zhao, Z. Lin, C. Lee, X. Xu, C. Wang, Y. Huang, M. I. Shakir, X. Duan, *Nano Lett.* **2015**, *15*, 4605-4610.

Acknowledgments

First and foremost, I want to extend my heartfelt gratitude to my supervisor Prof. Dr. Siegfried Eigler for providing me with the opportunity to work and study in our research group. He gave me a lot of trust and freedom to carry out my experiments. I am thankful for his patience, encouragement, support, and guidance throughout my journey.

I would like to thank all my colleagues in AG Eigler for all the help in work and life. They taught me a lot of useful things and gave me a lot of advice. Because of you, I had a lot of good times in Germany.

Thanks to all the collaborators Mira Kreßler and Dr. Patryk Kusch from the Department of Physics at Freie Universität Berlin for the SNOM measurements, Jiajun Dai and Prof. Dr. Beate Paulus from the Institute of Chemistry and Biochemistry at Freie Universität Berlin for the theoretical calculations, and Prof. Dr. Hyeon S. Shin from the Department of Chemistry at Ulsan National Institute of Science and Technology. Thanks to Prof. Dr. Kirill Bolotin from the Department of Physics at Free Universität of Berlin for the shared cleanroom facility. Thanks to Prof. Dr. Stephanie Reich from the Department of Physics at Free Universität of Berlin for the shared facility for the intercalation and Raman measurements.

Thanks to the China Scholarship Council (CSC) for providing me with financial support during my study.

Last but not least, I would like to thank my family for their endless love, understanding, and support all the time. Special thanks to my boyfriend Guixiang. He was always there for me, caring and supportive, and also gave me a lot of encouragement and suggestions in my work. Thanks also to our lovely cat Gulu, making our life full of fun and happiness.

Statement of the Author

I declare on the affidavit that I have written the dissertation independently and have used no sources other than those I have indicated and that there are no facts which make me unworthy of the conduct of a doctoral degree under the provisions of the law governing academic degrees. Further I declare my consent that the electronic version of my dissertation, while maintaining my copyrights and data protection, may be subjected to a separate review regarding the independent preparation of the dissertation. I have not submitted the dissertation anywhere else to obtain an academic degree and have not already passed this or a similar doctoral exam without success.

Berlin, 16.05.2024   _____